Untersuchungen zum Ladungsaufbau und pH-Wert in Silicamesoporen

Brilmayer, Robert Anton Paul

(2020)

DOI (TUprints): https://doi.org/10.25534/tuprints-00012828

Publikationstyp: Dissertation

Fachbereich: 07 Fachbereich Chemie

Quelle des Originals: https://tuprints.ulb.tu-darmstadt.de/12828

Untersuchungen zum Ladungsaufbau und pH-Wert in Silicamesoporen

TECHNISCHE UNIVERSITÄT DARMSTADT

Vom Fachbereich Chemie
der Technischen Universität Darmstadt

zur Erlangung des Grades
Doctor rerum naturalium
(Dr. rer. nat.)

Dissertation von
Robert Anton Paul Brilmayer

Erstgutachterin: Prof. Dr. Annette Andrieu-Brunsen
Zweitgutachter: Prof. Dr. Markus Biesalski

Darmstadt 2020

Tag der Einreichung: 29.05.2020

Tag der mündlichen Prüfung: 13.07.2020

Meinen Eltern - Ulrike und Dietmar

Danksagung

Während meiner Promotion habe ich mit sehr vielen Menschen zusammengearbeitet, ausgiebige Kaffeepausen genossen und eine unvergessliche Zeit während und neben dem Uni-Leben gehabt. Ein umfängliches Projekt, wie eine Promotion abzuschließen, auf diesem schwierigen Weg bedarf es sowohl fachlicher als auch menschlicher Unterstützung. An dieser Stelle möchte ich die Gelegenheit nutzen und mich bei jenen bedanken, die mir in dieser Zeit eine große Stütze waren.

Zuerst möchte ich mich bei meiner Doktormutter *Prof. Dr. Annette Andrieu-Brunsen* für das Vertrauen und die Möglichkeiten bedanken, die ich in ihrer Arbeitsgruppe während meiner Doktorarbeit hatte. Ganz gleich, ob es um neue Kooperationen, Konferenzreisen oder wissenschaftliche Fragestellungen ging, deine Tür war immer offen. Vielen Dank! Ich wünsche dir alles Gute und viel Erfolg bei der Expansion der Smarties.

Bei Herrn *Prof. Dr. Markus Biesalski* möchte ich mich zum einen für die Übernahme des Koreferates bedanken, aber vor allem auch dafür, dass ich mich in deiner Arbeitsgruppe immer willkommen fühlen (und alle Geräte mitbenutzen) durfte.

Den ehemaligen und aktuellen Gruppenmitgliedern der *„Brunsens"* und *„Biesalskies"* möchte ich mich für das stets angenehme Arbeitsklima sowie für die schönen Arbeitsausflüge nach Hirschegg bedanken.

Speziell danke ich *Nicole Herzog*, *Mathias Stanzel* und *Adnan Khalil* - egal, was ich gerade am dringendsten brauchte, ob ein offenes Ohr, wissenschaftliche Diskussionspartner oder sogar Chat- und Aquariensitter, bei euch war ich immer an der richtigen Anlaufstelle!

Für die Hilfe im Kampf mit und gegen kaputte Laborgeräte möchte ich *Martina Ewald* danken.

Ein großer Dank gilt auch meinen Kooperationspartnern *Minh Hai Tran*, *Martin Brodrecht*, *Christoph Kaiser*. Mit euch allen hatte ich das Glück, mit sehr motivierten Wissenschaftlern an spannenden Projekten arbeiten zu dürfen

Ich möchte mich auch bei *Nina Drechsler*, *Dominic Schirra*, *Marius Wolf*, *Marlen Sahlbach*, *Svenja Albus* und *Claire Förster* bedanken, die ich im Laufe der Jahre als Studenten betreut habe, und die mir geholfen haben, meinen Abzug gut auszulasten.

Ich danke meinen Eltern von ganzem Herzen, für die Unterstützung und Förderung, die ihr mir zukommen lasst, solange ich denken kann. Danke, dass ihr immer an mich geglaubt habt!

Meiner Schwester *Clara* möchte für ihre positive Art danken und dafür, dass sie ihren zerstreuten Bruder immer mit Geschenken für die ganze Familie versorgt.

Ganz besonders möchte ich noch *Sharon* danken. Als wir vor über 10 Jahren als junge Studenten auf dem Fluchtbalkon gestanden und über Frankfurt geschaut haben, hätte wohl keiner von uns beiden gedacht, was wir alles zusammen erleben werden. Danke für deine Unterstützung und die schöne Zeit mit dir.

Die vorliegende Arbeit wurde am Ernst-Berl-Institut für Makromolekulare und Technische Chemie der Technischen Universität Darmstadt unter der Leitung von Frau Prof. Dr. Annette Andrieu-Brunsen in der Zeit von März 2016 bis Dezember 2019 durchgeführt.

Teile dieser Arbeit sind bereits veröffentlicht, zur Veröffentlichung eingereicht oder wurden im Rahmen von internationalen Tagungen vorgestellt:

Wissenschaftliche Publikationen als Erstautor:

(1) R. Brilmayer, C. Hess, A. Andrieu-Brunsen, **Influence of Chain Architecture on Nanopore Accessibility in Polyelectrolyte Block-Co-Oligomer Functionalized Mesopores**, *Small*, **2019**, 15, 1902710.

(2) M. H. Tran*, R. Brilmayer*, L. Liu, H. Zhang, C. Hess, A. Andrieu-Brunsen, C. Birkel, **Synthesis of a smart hybrid MXene with switchable conductivity,** *ACS Appl. Nano Mater.*, **2020**, https://doi.org/10.1021/acsanm.0c00118.
*These authors contributed equally to this work

(3) R. Brilmayer, S. Kuebelbeck, A. Khalil, M. Brodrecht, U. Kunz, H.-J. Kleebe, G. Buntkowsky, G. Bayer, A. Andrieu-Brunsen, **Influence of nanoconfinement on the pKa of polyelectrolyte functionalized silica mesopores**, *Adv. Mat. Interf.*, **2020**, 1901914.

(4) R. Brilmayer, M. Brodrecht, C. Kaiser, J. Wachtveitl, G. Buntkowsky, A. Andrieu-Brunsen, **A new dye for ratiometric pH detection inside silica mesopores,** to be submitted.

Wissenschaftliche Publikationen als Übersichtsartikel:

(5) R. Brilmayer*, C. Förster*, L. Zhao*, A. Andrieu-Brunsen, **Trends in Nanopore Polymer Funtionalization**, *Curr. Opin. Biotech.*, **2020**, 63, 200.
*These authors contributed equally to this work

Wissenschaftliche Publikationen aus Kooperationen:

(6) J. Tom, R. Brilmayer, J. Schmidt, A. Andrieu-Brunsen, **Optimisation of Surface-Initiated Photoiniferter-Mediated Polymerisation under Confinement, and the Formation of Block Copolymers in Mesoporous Films**, *Polymers*, **2017**, 9(10), 539.

(7) M. Stanzel, R. Brilmayer, M. Langhans, T. Meckel, A. Andrieu-Brunsen, **FRET-based pH-sensing in mesoporous thin films with tunable detection range**, *Microporous and Mesoporous Materials*, **2019**, 282, 29-37.

(8) N. Herzog, R. Brilmayer, M. Stanzel, A. Kalyta, D. Spiehl, E. Doersam, C. Hess, A. Andrieu-Brunsen, Gravure Printing for Mesoporous Film Preparation, *RSC Adv.*, **2019**, 9, 23570–23578.

(9)

Vorträge:

(1) R. Brilmayer, A. Andrieu-Brunsen, **The influence of chain architecture on polyelectrolyte functionalized mesopore accessibility**, *14. Zsigmondy Kolloquium*, Mainz Germany, **04/2018**.

(2) R. Brilmayer, A. Andrieu-Brunsen, **The influence of chain architecture on polyelectrolyte functionalized mesopore accessibility**, *256. ACS meeting*, Boston USA, **08/2018**.

Poster:

(1) R. Brilmayer, A. Andrieu-Brunsen, **pH-dependent permselectivity of polymer funtionalized mesopores**, *iNAPO Workshop*, Darmstadt Germany, **06/2017**.

(2) R. Brilmayer, A. Andrieu-Brunsen, **pH-dependent permselectivity of polymer funtionalized mesopores**, *648. WE-Heraeus Seminar*, Bremen Germany, **07/2017**.

(3) R. Brilmayer, A. Andrieu-Brunsen, **pH in confinement**, *Doktorandentag FB Chemie*, Darmstadt Germany, **06/2018**.

(4) R. Brilmayer, A. Andrieu-Brunsen, **Influence of nano confinement on the "pH" in functionalized silica mesopores**, Multifuntional, Hybrid and Nanomaterials, Sitges Spain, **03/2019**.

Inhaltsverzeichnis

1. Einleitung

Die Natur und ihre Lebewesen faszinieren Forscher schon seit Jahrhunderten. Das Bestreben, die Natur nachzuempfinden, führte etwa zu bahnbrechenden Entwicklungen wie dem Fliegen, was für das Bestehen der Welt, wie wir sie kennen heute nicht mehr wegzudenken ist. In der heutigen Zeit steht in der technischen Entwicklung z. B. die Miniaturisierung von Geräten im Vordergrund. Fortschritte auf diesem Forschungsgebiet haben bis auf die Nanoskala geführt, wodurch Konzepte wie *Lab on a Chip* möglich geworden sind. Die Nanoskala wirft jedoch auch heute noch Fragen auf, da die begrenzten Materialdimensionen zu Veränderungen von Materialeigenschaften führen. Dies ist allgemeinhin von Goldnanopartikeln bekannt, die, im Unterschied zum makroskopischen Goldbarren, eine rote Farbe aufweisen. In Bezug auf die in dieser Arbeit untersuchten Transportprozesse dienen z.B. in der Natur vorkommende Ionenkanäle als inspirierendes Beispiel. Die Transporteigenschaften natürlicher Ionenkanäle sind im Hinblick auf Selektivität und Transportraten, verglichen mit synthetisch hergestellten Materialien, bis heute unerreicht. Diese Eigenschaften sind im Hinblick auf Technologien wie der Sensorik oder im Kontext von Medikamentenfreisetzung, Wasseraufbereitung und Transportkontrolle in synthetisch hergestellten Nanoporen allerdings von Interesse.[1-2] Biologische Ionenkanäle (Abbildung 1-1) zeigen nicht nur eine in technologischen Poren bisher unerreichte Transportperformance, sondern auch ihr Aufbau ist äußerst komplex. Unterschiedliche Domänen erzeugen geladene/ungeladene oder auch hydrophobe bzw. hydrophile Bereiche in einem Ionenkanal. Dieser im Vergleich zu technologischen porösen Materialien äußerst spezifische Aufbau führt dazu, dass biologische Ionenkanäle im Hinblick auf ihre Transporteigenschaften zwar unerreicht, jedoch für technische Anwendungen durch ihre Fragilität gegenüber äußeren Einflüssen nur sehr bedingt einsetzbar sind.

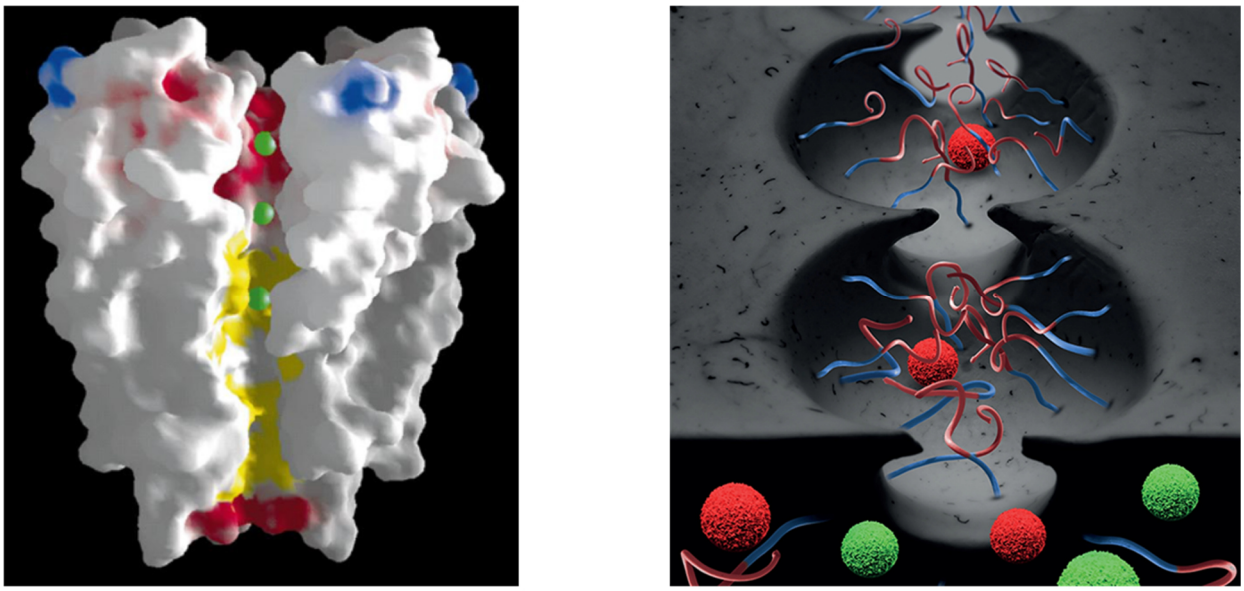

Abbildung 1-1. Links: Struktur eines Kaliumionenkanals. Reprinted with permission from *The American Association for the Advancement of Science* (D. A. Doyle, J. Morais Cabral, R. A. Pfuetzner, A. Kuo, J. M. Gulbis, S. L. Cohen, B. T. Chait, R. MacKinnon, 1998, Science, 280, 69) Rechts: Schematische Darstellung von polymerfunktionalisierten Mesoporen. *Artwork* von Sebastian Keuth. Reprinted with permission from *John Wiley and Sons* (Robert Brilmayer, Christian Hess, Annette Andrieu-Brunsen, Small 41/2019)

Viele Fachgebiete, wie die Materialwissenschaften, die Physik und die Chemie, beschäftigen sich mit der Herstellung synthetischer poröser Materialien u.a. im Kontext von Transportprozessen z. B. für katalytische- oder Trennanwendungen. Hier soll der Fokus v.a. auf geordneten mesoporösen Silicadünnfilmen liegen. Es wurde bereits eine Vielzahl von relativ definierten nanoporösen Materialien hergestellt. Neben ionenspur geätzten Nanokanälen in Polymerfolien oder porösen Polymeren gibt es auch anorganische Strukturen wie poröse Metalloxide oder silicabasierte nanoporöse Materialien.[3-5] Aus dieser Reihe an nanoporösen Materialien haben die silicabasierten mesoporösen Materialien durch Eigenschaften, wie eine relativ hohe chemische und physikalische Beständigkeit, kombiniert mit einer sehr großen spezifischen Oberfläche, einstellbaren Porengrößen und einer variablen Oberflächenchemie bisher mit das größte Interesse erweckt.[6-9] Aus der Vielzahl an möglichen silicabasierten Strukturen und Geometrien sind mesoporöse Silicananopartikel und mesoporöse Silicadünnfilme die am stärksten untersuchten Systeme.[10] Rein anorganische Materialien sind zwar gegenüber Chemikalien und physikalischen Veränderungen wie Druck oder Temperaturschwankungen sehr stabil, bieten aber hinsichtlich Transportsteuerung kaum Selektivität und Anpassungsfähigkeit. Dieser Nachteil lässt sich durch das Einführen von organischen Funktionen in das anorganische Silicanetzwerk verbessern. Organischen Funktionen können in Form von einzelnen Molekülen oder als Polymere über das *Post Grafting* Verfahren oder über die Cokondensation eingeführt werden, um selektive und responsive anorganische-organische Hybridmaterialien zu erzeugen.[11-12] Auf Basis dieser Methoden hat sich das Forschungsfeld der responsiven Materialien (sogenannt: *Smart-Materials*) entwickelt, welches in den letzten 15 Jahren beachtliche Aufmerksamkeit erhalten hat. Bis heute wurden eine Vielzahl an Materialkombinationen entwickelt, die auf externe Stimuli wie pH-, Licht-, Spannungs-,

Ionenkonzentrations- oder Temperaturänderungen reagieren und somit etwa das Transportverhalten des Materials steuern können.[11, 13-20] Neben der eingebrachten Funktion gibt es weitere Parameter, die einen Einfluss auf das Verhalten von Nanomaterialien haben. Der Rolle der räumlichen Ladungsdistribution in Nanomaterialien, welche z.B. durch die Kettenarchitektur der Polymerketten gesteuert werden kann, wurde etwa 2017 von *Szleifer* und Mitarbeitern in theoretischen Studien beschrieben.[14] Zu Beginn dieser Arbeit beschränkten sich die Polymerfunktionalisierungen von Silicamaterialien wie Dünnfilmen oder Nanopartikeln jedoch auf die Anbindung von Homopolymeren und die gezielte Steuerung von Polymerarchitekturen, wie sie in der Lösungspolymerisation üblich ist, war für Nanoporen unerforscht.

Sowohl in Bioporen als auch in synthetisch hergestellten Poren spielen Ladungsgleichgewichte eine essentielle Rolle für die Transportsteuerung. Dies gilt umso mehr, wenn solche Poren mit geladenen Funktionen oder Polymeren funktionalisiert sind. Ein Parameter, der vor allem in wässrigen Lösungen omnipräsent ist und Molekül und Oberflächenladungen bestimmt, ist der pH-Wert. Der pH-Wert lässt sich experimentell sehr leicht steuern, da er einfach über Säure-/Baseregulation einstellbar ist. Allerdings ist der „pH-Wert" in nanoskaligen Räumen, wie etwa in Silicamesoporen, nicht so trivial wie in freier Lösung. In Nanoporen wirken sich in Lösung nicht vorhandene Faktoren, wie die Oberflächenladung der Nanopore oder *Debye*-Radien auf das sich einstellende pH-Gleichgewicht aus.[21-22] In mehreren unabhängigen Studien wurden bisher Unterschiede zwischen dem pH-Wert in Lösung und dem in Nanoporen und Nanokanälen beobachtet.[21, 23-24] Die experimentell durchgeführten Studien beziehen sich bisher jedoch nur auf gelöste Farbstoffe. Erkenntnisse zu pK_s- bzw. pH-Verschiebungen von Molekülen, die kovalent im *nano confinement* angebunden sind und sich somit nicht den Einflüssen entziehen können, gehen bisher nur auf theoretische Studien von *Szleifer* und Mitarbeitern zurück.[24]

Um die ionische Permselektivität, also den Ionentransport von synthetischen Nanoporen, zu beeinflussen, ist die gängigste Methode die Verwendung von ladungsschaltbaren, responsiven Polymeren bzw. Polyelektrolyten. Von allen responsiven Funktionen stellen die pH-schaltbaren die größte und am weitesten verwendete Gruppe dar. Dabei stellt sich natürlich die Frage nach dem Zusammenspiel von geladenem Polymer und nanoskaliger Pore und dessen Einfluss auf den „pH-Wert", oder besser gesagt den pK_s-Wert. Hinsichtlich der Porenfunktionalisierung bieten Polymere den großen Vorteil gegenüber molekularen Oberflächenfunktionalisierungen, mehrere funktionale Gruppen pro Oberflächenanknüpfungspunkt in ein Material einzuführen. Vorarbeiten aus unserer Gruppe haben gezeigt, dass es möglich ist, die Polymermenge in Nanoporen u.a. über kontrollierte radikalische Oberflächenpolymerisationen gezielt einzustellen.[25] Radikalische Polymerisationen zeichnen sich durch die Vielfalt an einsetzbaren Monomeren und schnelle Reaktionszeiten aus.[26] Als Schlüsseltechniken auf diesem Gebiet der Polymerisation sind die *Atom-Transfer Radical Polymerization* (ATRP), die *Reversible Addition Fragmentation Chain Transfer* (RAFT) *Polymerization* und die I*niferter Initiated Polymerization* zu nennen. Bisher haben sich experimentelle Arbeiten zum Einstellen von Ladungen in synthetischen Nanoporen vor allem auf das Einstellen der Kettenlänge und Kettendichte beschränkt. Dass weitere Faktoren wie die

Ladungsverteilung innerhalb der Polymerketten eine erhebliche Rolle für kontrollierten Transport spielen, wurde zwar in einer theoretischen Studie herausgearbeitet, experimentell jedoch noch nicht umgesetzt.[14] Ein möglicher Ansatz zur Gestaltung der Polymerkettenarchitektur ist die Anwendung von kontrollierter Polymerisation in Kombination mit Reinitiation, was zu Beginn dieser Arbeit in Nanoporen <10 nm noch nicht erfolgreich demonstriert werden konnte. Polymere können durch ihren Einfluss auf die Permselektivität von Nanoporen auch für Anwendungen wie die Sensorik eingesetzt werden.[27-28] Hierbei erfolgt die Detektion, wie unter anderem von *Azzaroni* und Mitarbeitern für Ionentransport gezeigt wurde, immer nur indirekt, zum Beispiel über ein Stromsignal.[4, 29]

Eine andere Stoffklasse, welche häufig in der Sensorik eingesetzt wird und direktes Auslesen von z.B. pH-Änderungen ermöglicht, sind Farbstoffe. Farbstoffe sind für sensorische Anwendung sehr gut geeignet, da sie sehr gut erforscht sind, es einige bioverträgliche Farbstoffe gibt, sie in kleinsten Konzentrationen von nM-µM detektierbar sind und Messmethoden wie die Fluoreszenz- oder UV-Vis-Spektroskopie, schnell, exakt und weit verbreitet sind.[30] Die hohe Sensitivität erlaubt in Kombination mit aufwendigen Messaufbauten sogar die Detektion von einzelnen Molekülen. Als molekulare Sensoren, reagieren Farbstoffe, die in Silicagerüsten integriert sind, durch Veränderungen ihres Absorptions-/Emissionsverhaltens. Sie können so direkt auslesbare Veränderungen von z.B. Metallionenkonzentrationen oder vom pH-Wert in Nanoporen direkt anzeigen.[31-36] Die Kombination aus mesoporösen Silicananonadeln und Fluoreszenzmarkern hat gezeigt, dass es möglich ist, einzelne Krebszellen zu detektieren und gleichzeitig einen inkorporierten Wirkstoff in die Zelle zu entlassen.[37-38] Hergestellte responsive Materialen können, z.B. durch eine Veränderung im pH-Wert, einen eingelagerten Wirkstoff freisetzen.[39] Da der pH-Wert in Krebszellen saurer als in gesunden Zellen ist, kann durch die Verwendung von responsiven mesoporösen Silicamaterialien der Wirkstoff gezielt in Krebszellen geführt werden.[11, 40] Bisherige Arbeiten haben vor allem mit Farbstoffen gearbeitet, die im physiologischen pH-Bereich von 6.5 - 7.5 sensitiv sind. Für Silicabasierte Materialien und deren Anwendung in Trennfragestellungen, Sensorik oder auch Enzymstabilisierung ist allerdings vor allem der pH-Bereich, in dem sich die Oberflächensilanolgruppen aufladen (bei pH˜3-4)[41-43], von besonderer Bedeutung, da die Silanolgruppen innerhalb der Nanoporen das Materialverhalten stark beeinflussen.

Trotz der genannten Studien, welche vor allem auf Basis von theoretischen Studien einen großen Einfluss von der Nanoskala auf den pH-Wert nahe legen und einem allgemein breiteren Interesse am pH-Wert in Mesoporen (apparenter pH-Wert),[44-46] ist das direkte Ablesen des apparenten pH-Wertes, bis heute noch nicht ausführlich und ausreichend untersucht worden. Daher stellt die Bestimmung und Vorhersage des pH-Wertes und des pK_s-Wertes von Molekülen in Mesoporen bis heute eine Herausforderung dar. Neue Erkenntnisse in diesem Bereich sind interessant und können zukünftig dazu genutzt werden, Mechanismen in der Arzneimittelfreisetzung oder für Transportmechanismen in Nanomaterialien allgemein besser zu verstehen und sie gezielt einzusetzen.[14]

Auf Basis der vorgestellten Datenlage ergaben sich für die vorliegende Arbeit folgende offenen Forschungsfragen im Kontext des pH-Wertes in nanoskaligen Poren:

- Wie beeinflusst die räumliche Begrenzung im Nanometerbereich den pH-Wert und Moleküle, die sich in Mesoporen <20 nm befinden
- Wie beeinflusst die Ladungsverteilung, einstellbar durch die Polymerkettenarchitektur, das pH-responsive Transportverhalten von Mesoporen

Um diese Fragen adressieren zu können, war allerdings zunächst eine Entwicklung der Polymerfunktionalisierung selbst nötig. Z.B. musste erstmal die Möglichkeit entwickelt werden, Polymerkettenarchitektur in nanoskaligen Poren zu steuern. Um den pH-Wert in Mesporen in-situ auslesen zu können, war ebenfalls zunächst die Entwicklung eines Sensorkonzeptes nötig. Wie im Folgenden dargestellt, kann dies auf molekularen farbstoffbasierten Sensoren/Reportermolekülen beruhen.

2. Stand der Forschung

Im folgenden Kapitel werden die für diese Arbeit wichtigsten Forschungsfelder im Hinblick auf deren Grundlagen und den aktuellen Stand der Literatur vorgestellt.

2.1. Poröse Silicastrukturen als Gerüst zur Herstellung von funktionalen Hybridmaterialien

Poröse Silicamaterialien kommen zum Teil natürlich vor, können aber auch synthetisch hergestellt werden. Nach IUPAC werden poröse Materialien in drei unterschiedliche Klassen eingeteilt: mikroporöse Materialien besitzen einen Porendurchmesser von kleiner 2 nm, mesoporöse einen Durchmesser von 2 – 50 nm und makroporöse besitzen eine Porengröße von > 50 nm (vgl. Tabelle 2.1).[47]

Tabelle 2.1: Porengrößeneinteilung gemäß IUPAC.

Porenbezeichnung	Porendurchmesser	Beispiele
makroporös	>50 nm	Gläser
mesoporös	2-50 nm	Aerogele, Silicananopartikel
mikroporös	<2 nm	Zeolithe, Aktivkohle

Ein Beispiel für natürlich vorkommende Silicastrukturen sind die Zeolithe. Hierbei handelt es sich um eine Stoffgruppe, die 1767 vom schwedischen Mineralogen A.F. Cronstedt entdeckt wurde. Diese Alumosilicat-Gitter haben aufgrund ihrer hohen spezifischen Oberfläche jeher ein großes industrielles Interesse geweckt. Schon in den 1980er Jahren fanden sie Anwendung bei Trennproblemen oder als Katalysatoren[48] und hatten Einzug in die meisten Haushalte in Form von Isolierglas oder als Bestandteil in Kühlsystemen von Kühlschränken gehalten.[49] Zeolithe erreichen die hohe spezifische Oberfläche durch poröse Strukturen, welche in der Regel sehr kleine Porenöffnungen (< 1 nm) besitzen. Diese Eigenschaft macht sie zum einen unzugänglich für größere Moleküle und erschwert zum anderen die Modifikation der inneren Porenoberfläche mit organischen Funktionen, um komplexe Materialien zu generieren. Eine Materialalternative zu den Zeolithen stellen mesoporösen Silicamaterialien (MSM). Die Porengrößen von synthetisch hergestellten MSM können mit kommerziell erhältlichen Templaten im Bereich von 2-10 nm hergestellt werden. Über ein geeignetes Templatdesign wurden jedoch auch schon MSM mit Porengrößen von bis zu 40 nm hergestellt.[50] MSM stellen seit ihrer Entdeckung eine Alternative zu natürlichen Zeolithen für diverse Anwendungsgebiete dar.

Herstellung von mesoporösen Silicamaterialien

Die Entdeckung der templatbasierten Herstellung von geordneten mesoporösen Materialien geht auf die *Mobil Research and Development Cooperation* im Jahr 1992 zurück.[51] Durch die Verwendung von Templaten lassen sich in diesem Verfahren die Porengrößen einstellen. Bis Ende der 1990er Jahre wurden auf Basis von Ionischen- oder Polymertemplaten die bis heute wohl wichtigsten meoporösen Materialien MCM-41 (Mobil Composition of Matter) und SBA-15 (Santa Barbara Amorphous) mit Porengrößen von 3 - 8 nm entwickelt. Eine sehr gängige Templatfamilie, mit der auch die SBA Materialien hergestellt werden, sind die Pluronic © Triblock-co-Polymere. Bei diesen handelt es sich um nicht ionische Polymere auf Basis von Ethylenoxid $(EO)_n$ und Propylenoxid-Einheiten $(PO)_n$. Bei den sehr häufig verwendeten Polymeren Pluronic © F127, P123 oder P103 sind die Blöcke nach $(EO)_n$-$(PO)_n$-$(EO)_n$ angeordnet. [12, 52] Bis heute werden durch Variation der Blocklängen immer neue Porengeometrien und Strukturen entwickelt. Durch die Mischung von verschiedenen Pluronic© Polymeren oder der Erhöhung der Polymerkonzentration ist es gelungen, Porengrößen von > 15 nm zu erzeugen.[9]

Bei der ursprünglichen Synthese von MSM können sich die als Template verwendeten Tenside nach verschiedenen, postulierten Mechanismen wie das t*rue liquid crystal templating* (TLCT) oder *cooperative self assembly* (CLCT) selbst anordnen und die hexagonalen Strukturen ausbilden. Der von *Attard et al.*[53] postulierte Mechanismus des TLCT erfolgt zumeist bei erhöhten Tensidkonzentrationen, wobei sich zunächst sphärische Mizellen bilden, die dann in röhrenförmige Mizellen übergehen. Aus den röhrenförmigen Mizellen entsteht dann direkt die flüssigkristalline Phase. Die Silicapräkusoren können dann die Zwischenräume der Templatstruktur ausfüllen, wodurch die eigentliche Silicastruktur ausgebildet wird.[54-56]

Bei niedrigeren Tensidkonzentrationen ist das CLCT der in der Regel diskutierte Mechanismus für die Ausbildung der Silicastrukturen. Hierbei benötigen die Templatmoleküle die Interaktion mit anderen Molekülen, um eine flüssigkristalline Phase auszubilden. Hierzu dienen in der Regel die Silikapräkusoren, welche sich an die zunächst entstehenden sphärischen oder röhrenförmigen Mizellen anlagern. Nach der Anlagerung der Silicapräkusoren erfolgt direkt die Aggregation zum hexagonalen Porensystem.[54, 56-58] Dabei können durch die Wahl der Syntheseparameter, wie z.B. Templatkonzentration, Luftfeuchtigkeit oder pH-Wert, unterschiedliche Geometrien und Porösitäten der mesoporösen Materialien generiert werden.[6] Ursprünglich wurden so vor allem nano- bis einige hundert Mikrometer große Partikel hergestellt. 1999 veröffentlichte die Gruppe um *Jeffrey Brinker* das *Evaporation-Induced Self-Assembly* (EISA) Verfahren, was die Herstellung von Dünnschichtfilmen ermöglichte.[8, 59] Für den EISA-Prozess zur Erzeugung dünner mesoporöser Filme sind gängige Methoden die in Abbildung 2-1 gezeigte Tauchbeschichtung oder die Sprühbeschichtung. Bei diesen Prozessen werden verdünnte Sol-Gel-Lösungen verwendet. Die Sol-Gel-Lösungen für den EISA Prozess, sind verdünnte, wässrige Systeme, die hauptsächlich den anorganischen Präkursor wie Tetraorthoethoxysilan (TEOS), Templatmoleküle, sowie einen

Katalysator (häufig Säure) beinhalten. Die Selbstanordnung der Templatmoleküle erfolgt ohne weitere äußere Einflüsse, nur durch nichtkovalente Wechselwirkungen, wie elektrostatische-, Van-der-Waals-Anziehungskräfte oder Wasserstoffbrückenbindungen beim Verdampfen des Lösemittels.[60-61] Der anorganische Silicapräkursor härtet während des Verdampfungsprozesses über eine Kondensationsreaktion um die Templatmoleküle herum aus. Die Kondensationsreaktion erfolgt bei einem pH-Wert von 1 - 3 sauer katalysiert.[62] Damit ist die Selbstorganisation jedoch noch nicht abgeschlossen. Während dem *Modulable Steady State* (MSS), was auch als Alterungsprozess bezeichnet wird, kommt es zu einer Reorganisation der Mesophase durch Neuorientierung der Templat-Mizellen.[63-64] Durch anschließendes Kalzinieren wird das Silicagerüst durch vollständige Kondensation stabilisiert und das Templat herausgebrannt.[6, 60, 65, 7]

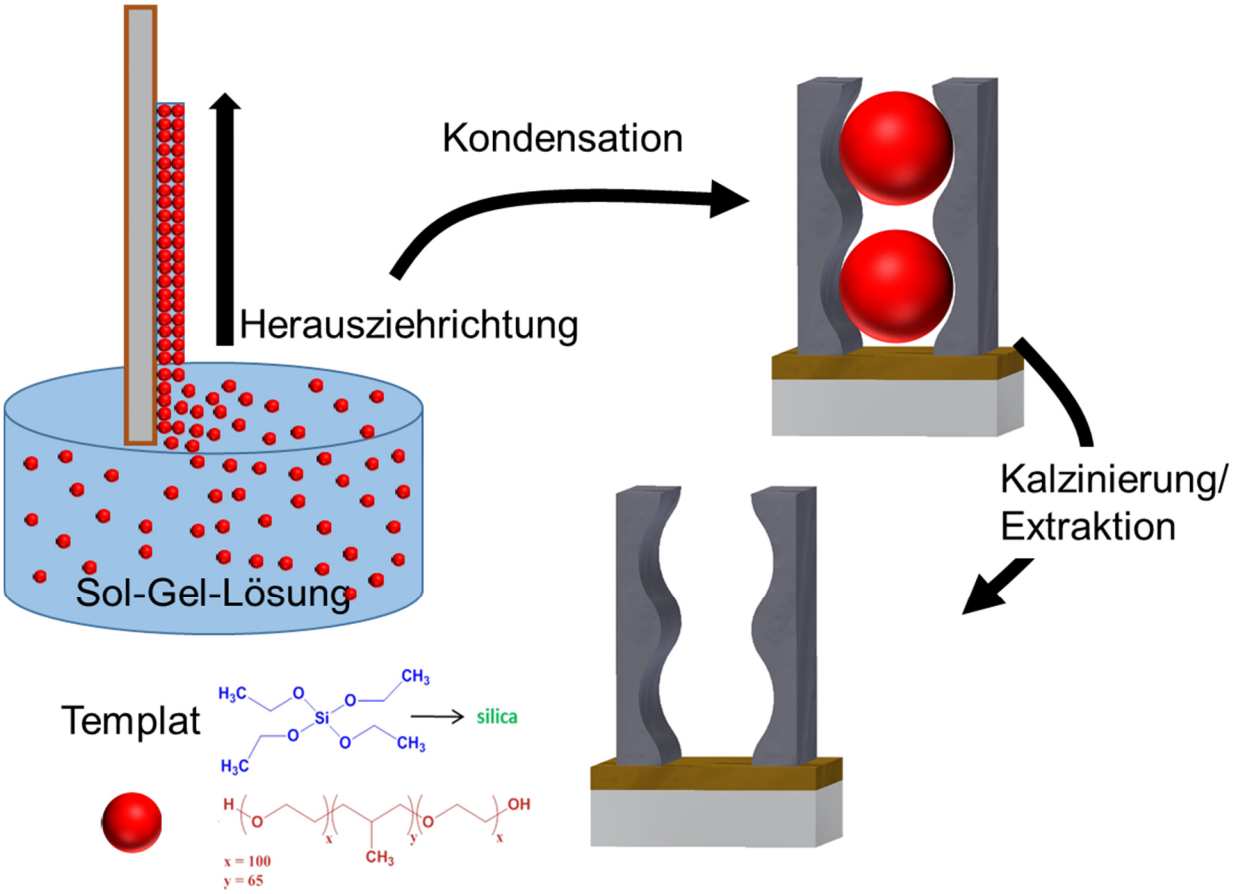

Abbildung 2-1: Schematische Darstellung der Synthese von mesoporösen Silica-Dünnschichtfilmen.

Bei der Herstellung von MSM lassen sich neben der Porenstruktur auch Parameter wie Partikelgröße oder Schichtdicke der Silicamaterialien experimentell sehr gut kontrollieren.[65-68] In den konventionellen Herstellungsprozessen ist man jedoch auf relativ einfache Geometrien, wie sphärische oder planare, beschränkt. Für komplexe Fragestellungen, wie etwa in Trennproblemen, kann es sehr nützlich sein, wenn das MSM zum Beispiel eine durchflussoptimierte Geometrie aufweist.[69] In den letzten Jahren haben sich 3D-Druckverfahren zunehmend etabliert, um neuartige Materialien mit komplexen Geometrien herzustellen.[70-71] Silicabasierte Materialien lassen sich über unterschiedliche Druckverfahren herstellen. Beispiele hierfür sind z.B. 3D-Druck von

fusioniertem Glas,[72] Gravurdruck von mesoporösen Silicafilmen,[68] *layer by layer* Druck von Polydimethylsiloxan[73] oder die Verwendung von Proteinen als strukturdirigierendes Templat[74] zur Erzeugung von naoporösen 3D-Silicagerüsten. Auch wenn die Entwicklung bei der Herstellung von komplexen Silicastrukturen große Fortschritte macht und die Ergebnisse äußerst vielversprechend wirken, bleibt als zu lösendes Problem die Skalierung und Automatisierung der Herstellung sowie die Senkung der Prozesskosten für eine Nutzung in kommerziellen Anwendungen.

2.2. Funktionalisierung von Silicaoberflächen

MSM finden bis heute in vielen Anwendungsbereichen, wie der Sensorik[75-77], Trennprozessen[78-79] oder der Energieumwandlung[80] Verwendung. Dies geht jedoch nicht ausschließlich auf ihre hohe spezifische Oberfläche von mehreren hundert m^2g^{-1}, den günstigen Herstellungsprozess oder die mechanische und chemische Beständigkeit zurück.[54] Vielmehr ist es auch die Funktionalisierung mit organischen Funktionen, die ein solch breites Einsatzspektrum ermöglichen.[11-12] Neben den mesoporösen Silicananopartikeln sind die in dieser Arbeit verwendeten mesoporösen Silicadünnfilme die hinsichtlich der Funktionalisierung am stärksten untersuchten Systeme.[10] Die für die Funktionalisierung verwendeten Moleküle setzen sich meist aus den in Abbildung 2-2 gezeigten Bausteinen zusammen.

Bei der sogenannten Ankergruppe handelt es sich um die Funktion, die die kovalente Anbindung an die Oberfläche erlaubt. Hierbei werden meist Silane vom Typ R-Si$(OMe)_3$, R-Si$(OEt)_3$ oder R-Si$(X)_3$ (X = Cl oder F) verwendet. Die *Spacer*-Einheit dient dazu die gewünschte Funktion räumlich von der Silicaoberfläche zu entfernen, um Wechselwirkungen mit residualen Si-OH Gruppen zu reduzieren und eine gewisse Flexibilität in das System zu bringen. Bei der Kopfgruppe handelt es sich um den Teil des Moleküls, der die gewünschte Funktion trägt, welche das hybride Material auszeichnen soll. Desweiteren ist es möglich z.B. Amin-,Chlor- oder Cyanogruppen zu verwenden, welche als reaktive Endgruppen weiter funktionalisiert werden können.

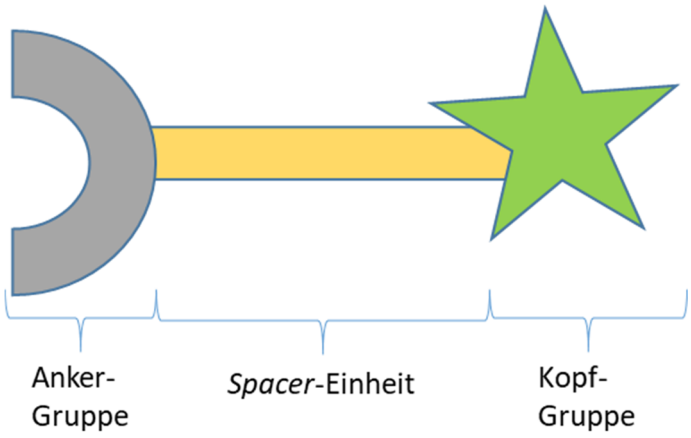

Abbildung 2-2: Schematische Darstellung eines Moleküles zur Funktionalisierung von Silicamaterialien mit jeweils einer Anker-, Spacer- und Kopfgruppe.

Um eine organische Funktion kovalent in das anorganische Silica einzubinden, werden die freien Si-OH Gruppen des Silicapräkursors als Anknüpfungspunkt verwendet um kovalente Bindungen zwischen Funktionalisierungsmolekül und Silicagerüst über eine Kondensationsreaktion herzustellen. Dieser Schritt kann entweder während der Ausbildung der MSM erfolgen (co-Kondensation) oder nachträglich auf dem bereits fertigen MSM erfolgen (postgrafting).

Co-Kondensation

Bei der Co-Kondensation handelt es sich um eine Einschritt-Synthese zur Herstellung von organo-silica Hybridmaterialien, da der organische Linker während der Synthese der MSM eingebaut wird (Schema 2-1). Üblicherweise wird zusätzlich zum TEOS Präkursor ein Organosilan, wie z.B. 3-Aminopropyltriethoxysilan (APTES), hinzugegeben. Durch die Co-Kondensation werden sehr homogene Funktionsverteilung auf der Silicaoberfläche erreicht und die Poren bleiben zugänglich. Allerdings können nicht sämtliche organische Funktionen auf diesem Weg eingeführt werden. Gerade reaktive Spezies, wie (3-Isocyanatopropyl)triethoxysilan oder (3-Chlorpropyl)triethoxysilan, würden beim Herstellungsprozess abreagieren.[56, 81] Zum Anderen nimmt etwa die Porösität der Silicastruktur im Vergleich zu reinen mesoporösen Silicastrukruen erheblich ab und die Porenstruktur ist weniger geordnet, da es durch unterschiedliche Kondensationsgeschwindigkeiten zu Homokondensationen kommen kann. Dies führt häufig dazu, dass die Kopfgruppen auch im Silicanetzwerk mit eingebaut werden. Dies kann die Stabilität des Materials beeinflussen und führt auch dazu, dass nicht alle co-condensierten Funktionen an der Oberfläche zur Verfügung stehen. Ein weiterer inherenter Nachteil der Co-Kondensationsmethode ist, dass bei der Templatentfernung stark darauf geachtet werden muss, die organischen Funktionen nicht zu zerstören. Oftmals ist die Kalzinierung keine valide Option und es muss auf eine chemische Templatextraktion zurückgegriffen werden.[54] Dies kann dazu führen, dass nicht das gesamte Templat aus der Silicastruktur entfernt wird, und dass je nach Extraktionsbedingungen die Silicastruktur beschädigt wird.

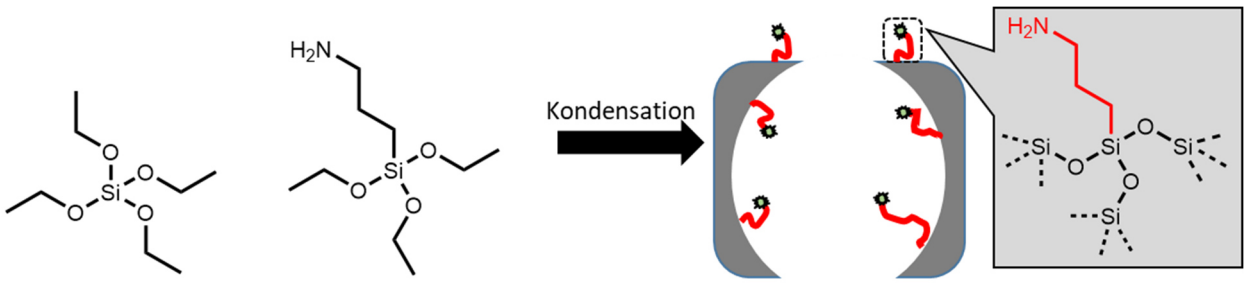

Schema 2-1: Schematische Darstellung der Herstellung einer APTES funktionalisierten Nanopore über den Co-Kondensationsprozess.

Post-Grafting

Bei der postsynthetischen Funktionalisierung, dem *Post-Grafting*, wird ein organisches Molekül (wie in Schema 2-2 für die Anbindung von APTES beispielfhaft gezeigt) an die Oberfläche eines vorab hergestellten Silicagerüstes angebracht. Hierbei ist eine Vielzahl an unterschiedlichen Funktionen verwendbar.[6, 82]

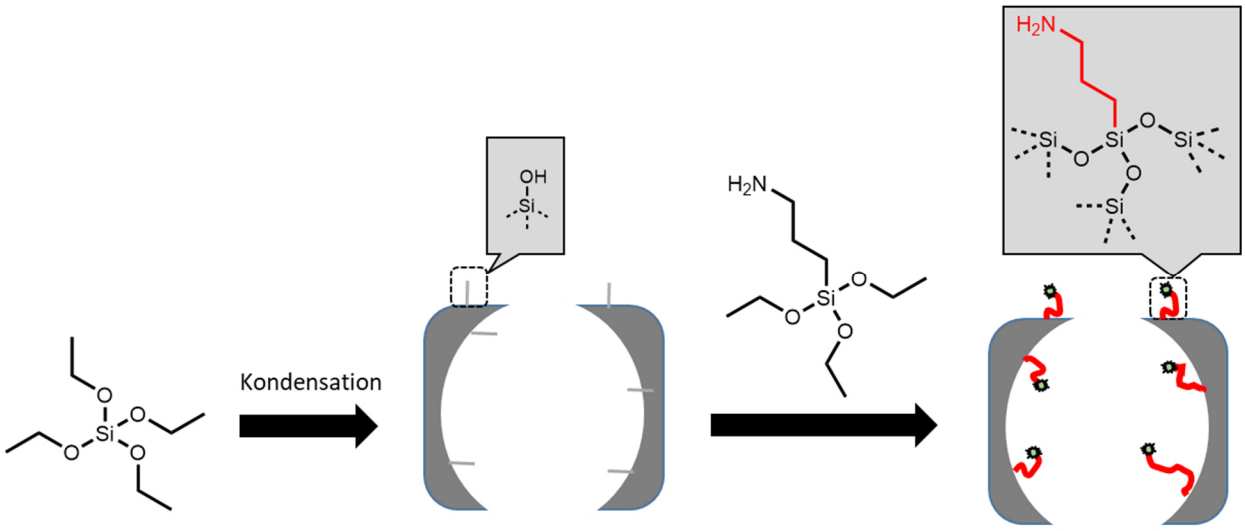

Schema 2-2: Schematische Darstellung der Herstellung einer APTES funktionalisierten Nanopore über das p*ost-grafting*-Verfahren

Die Reaktivität der Abgangsgruppe, also der reaktive Teil der Ankergruppe, spielt hierbei eine entscheidende Rolle für die experimentellen Parameter, siehe Abbildung 2-3. Meistens handelt es sich um eine Kondensationsreaktion zwischen Alkoxy- oder Halogensilanen.[83-84] Können Fluorsilane teilweise aus der Gasphase am Silicagerüst abgeschieden werden, müssen andere Silane aus verdünnten organischen Lösungen angebunden werden. Chlor- und Methoxysilane reagieren bei Raumtemperatur mit den Si-OH-Gruppen, wohingegen Ethoxysilane deutlich unreaktiver sind und erst bei Erwärmen gut kondensieren.

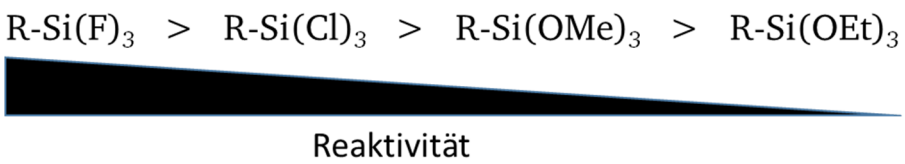

Abbildung 2-3: Reihe der möglichen Silicaankergruppen sortiert abfallend von links nach rechts nach Reaktivität.

Neben der Reaktivität spielt die Anbindungsdauer sowie Konzentration der zur Oberflächenmodifikation eingesetzten Silanverbindung bei der Anbindung eine entscheidende Rolle auf die resultierende Pfropfdichte. Ein Nachteil bei der Verwendung von Organosilanen mit mehreren Abgangsgruppen wie das in Abbildung 2-4 gezeigte Aminopropyltrimethylmethoxysilan (APTMS) ist, dass diese durch Homokondensation Ketten oder Strukturen auf dem Silicagerüst

ausbilden können. Hierbei können zum Beispiel die Porenöffnungen verstopfen, was die Diffusion beeinträchtigen kann und damit zu einer inhomogenen Funktionalisierung des Silicamaterials führt. Um dieses Problem zu umgehen, bietet sich die Verwendung von Organosilanen wie dem Aminopropyldimethylmethoxysilan (APDMS) mit nur einer Abgangsgruppe an.[54, 85]

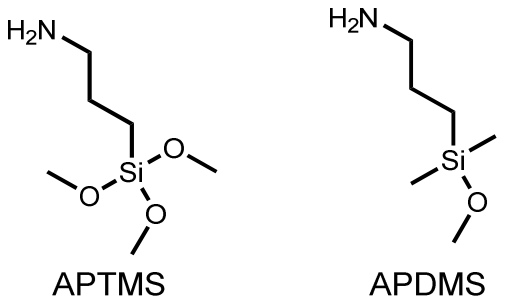

Abbildung 2-4: Strukturformeln der Moleküle APTMS und APDMS.

Durch das breitere Spektrum an möglichen organischen Funktionen und dem Erhalt der Stabilität des Silicagerüstes hat sich die *post-grafting* Methode zunehmend gegenüber der Co-Kondensation behauptet, um funktionale Silicamaterialien herzustellen. Die Co-Kondensation stellt mit einer sehr homogenen Verteilung der Funktionen besonders für simple Funktionalisierungen eine synthetisch sehr gute Alternative dar. Daher sollten bei der Planung neuer hybrider Materialien die Vor- und Nachteile beider Methoden für jeden Anwendungsfall individuell abgewogen werden.

2.3. Polymerisationen in Mesoporen

Kontrollierte Polymerisationen in porösen Materialien werden seit mehr als 20 Jahren erforscht.[86] Neben den üblichen Parametern, die Einfluss auf chemische Reaktionen haben, wie etwa pH-Wert, Temperatur oder Konzentration, kommen in nanoskaligen Umgebungen weitere Faktoren, wie etwa Oberflächenladungen oder die *Debye*-Länge hinzu.[21-22] Da in mesoporösen Materialien mit Porenöffnungen < 10 nm die Diffusion von Makromolekülen stark eingeschränkt ist,[87] wird fast ausschließlich die *grafting-from* Methode in Mesoporen angewendet. Hierbei handelt es sich um eine Polymerisation, bei der die Polymerkette von der Porenwand weg wächst. Polymerisationen von diesem Typ werden auch oberflächeninitiierte Polymerisationen genannt. Um das Wachstum von der Oberfläche zu ermöglichen, muss ein Polymerisationsinitiator an der Oberfläche angebracht werden. Hierbei handelt es sich um kleine Moleküle, die durch die mesoporöse Struktur diffundieren können und somit eine homogene Polymerverteilung gewährleisten. Die überwiegende Mehrheit bestehender Studien zur Polymerfunktionalisierung von mesoporösen Systemen befasst sich mit *grafting from* Polymerisationen. Dies stellt einen entscheidenden Unterschied zur Modifikation von planaren Oberflächen dar. Auf planaren Oberflächen oder in makroporösen Poren findet neben dem *grafting from* auch das *grafting to* häufig Verwendung. Bei der *grafting to* Methode werden fertige Polymerketten, die auf einer Seite eine Ankergruppe besitzen auf die Oberfläche aufgepfropft.[83-85]

Die durch die Nanoskala induzierten Limitierungen haben dazu geführt, dass trotz intensiver Bemühungen bis heute die physikochemischen Eigenschaften in Nanoporen/-kanälen noch nicht vollständig verstanden und Faktoren, die die Leistungsfähigkeit von polymerfunktionalisierten porösen Materialien beeinflussen, wie Molekulargewicht und Pfropfdichte, bis heute offene Fragen beinhalten und experimentell nicht trivial zu lösen sind.[79] Die zu Beginn dieser Arbeit noch nicht bekannte Re-initiation von Polymerisationen in Nanoporen und die Synthese von Block-co-Polymeren ist hierbei beispielhaft zu erwähnen. Block-co-Polymer unterschiedlichster Zusammensetzung werden in Lösung routinemäßig, großtechnisch hergestellt. In Nanoporen <20 nm hingegen ist es jedoch erstmalig im Rahmen dieser Arbeit gelungen, ein Block-co-Oligomer durch Reinitiation zu synthetisieren und nachzuweisen. Deswegen sind sowohl die kontrollierte Funktionalisierung als auch Anstrengungen zum besseren Verständnis von nanoskaligen Effekten auf die Polymersiationsmechanismen und die Polymere in den Nanoporen Gegenstand aktueller Forschung. In den letzten 10 Jahren gab es daher zur Erforschung von Polymerisationen auf (nanoskaligen) Oberflächen einige Studien und Erkenntnisgewinne zu Polymerisationen auf Oberflächen verglichen mit Polymerisationen in Lösung. Gerade das *Confinement* in nanoskaligen Materialien,[79, 88-89] sowie die Form (Wölbung) von Oberflächen haben nachweislich einen starken Einfluss auf die Kinetik von Polymerisationen.[90-92] Zusätzlich zu den erhaltenen experimentellen Erkenntnissen von *Passetto et al.*[93] konnten *molecular dynamics* Simulationen einen starken Effekt der Oberflächenform auf die Initiationseffizienz von Oberflächeninitiierten Polymerisationen sowie auf das Molekulargewicht und die Dispersität der resultierenden Oberflächengebundenen

Polymere vorhersagen. Laut der Studie von *Liu et al.* sind eine höhere Initiationseffizienz und eine niedrigere Dispersität für stark konkav gewölbte Oberflächen zu erwarten, wie sie in kleinen Mesoporen vorliegen.[94]

Auch wenn die Polymerisation in Mesoporen deutlich herausfordernder ist, als etwa auf planaren Oberflächen oder in Lösung, bleiben die grundlegenden Polymerisationstechniken die gleichen. Neben freier radikalischer Polymerisation haben sich schon früh Polymerisationsmethoden der sogenannten kontrollierten radikalischen Oberflächenpolymerisation als eine sehr gute Mesoporenmodifikationstechnik erwiesen.[25] Radikalische Polymerisationen zeichnen sich durch die Vielfalt an einsetzbaren Monomeren und relativ schnelle Reaktionszeiten aus.[26] Als Schlüsseltechniken auf dem Gebiet der kontrollierten radikalischen Polymerisation sind die *Atom-Transfer Radical Polymerization* (ATRP), die *Reversible Addition Fragmentation Chain Transfer* (RAFT) *Polymerization* und die *Iniferter Initiated Polymerization* zu nennen. Bei einem sogenannten *Iniferter* handelt es sich um ein Molekül, das die Polymerisation gleichzeitig initiieren (*Ini*), Ketten transferieren (*fer*) und die Polymerisation terminieren kann (*ter*).[95-96]

Die ATRP ist die wohl am weitesten verbreitete Methode der Oberflächenpolymerisation und kontrollierte Polymersationen bis zu einer Porengröße von 15 nm sind berichtet.[97-100] Die Kontrolle der klassischen ATRP ist abhängig vom Aktivierungs-/Deaktivierungs-Gleichgewicht eines Übergangsmetallkomplexes und einer schlafenden Halogenalkylpolymerkette, welche in der Gegenwart von Monomeren wachsen kann.[101-102] Bei der RAFT Polymerisation basiert die Kontrolle auf einem reversiblen Kettentransfer. Hierbei wird konventionelle freie Radikalik mit einem *Chain Transfer Agent* (CTA), wie etwa Dithiocarbamat, kombiniert. Bei der Oberflächen-RAFT Polymerisation kann entweder der Radikalinitiator oder das CTA an der Oberfläche verankert werden.[103-105] Eine vollständige Zusammenfassung der Oberflächenpolymerisationstypen, sowie den verwendbaren Monomere wurde 2017 von der Gruppe um *Harm-Anton Klok* erstellt, auf die an dieser Stelle verwiesen werden soll.[25] Durch die stetige Weiterentwicklung der Polymerisationsmethoden in Mesoporen lässt sich die gewünschte Polymermenge über unterschiedliche Polymerisationsmethoden wie der SI-PIMP[87], SI-RAFT oder der SI-ATRP[18] mittlerweile sehr gut einstellen.[28-29, 62] Am Beispiel des Monomers DMAEMA wird in Schema 2-4 schematisch eine Übersicht gezeigt, wie über die genannten Methoden in Nanoporen polymerisiert werden kann.

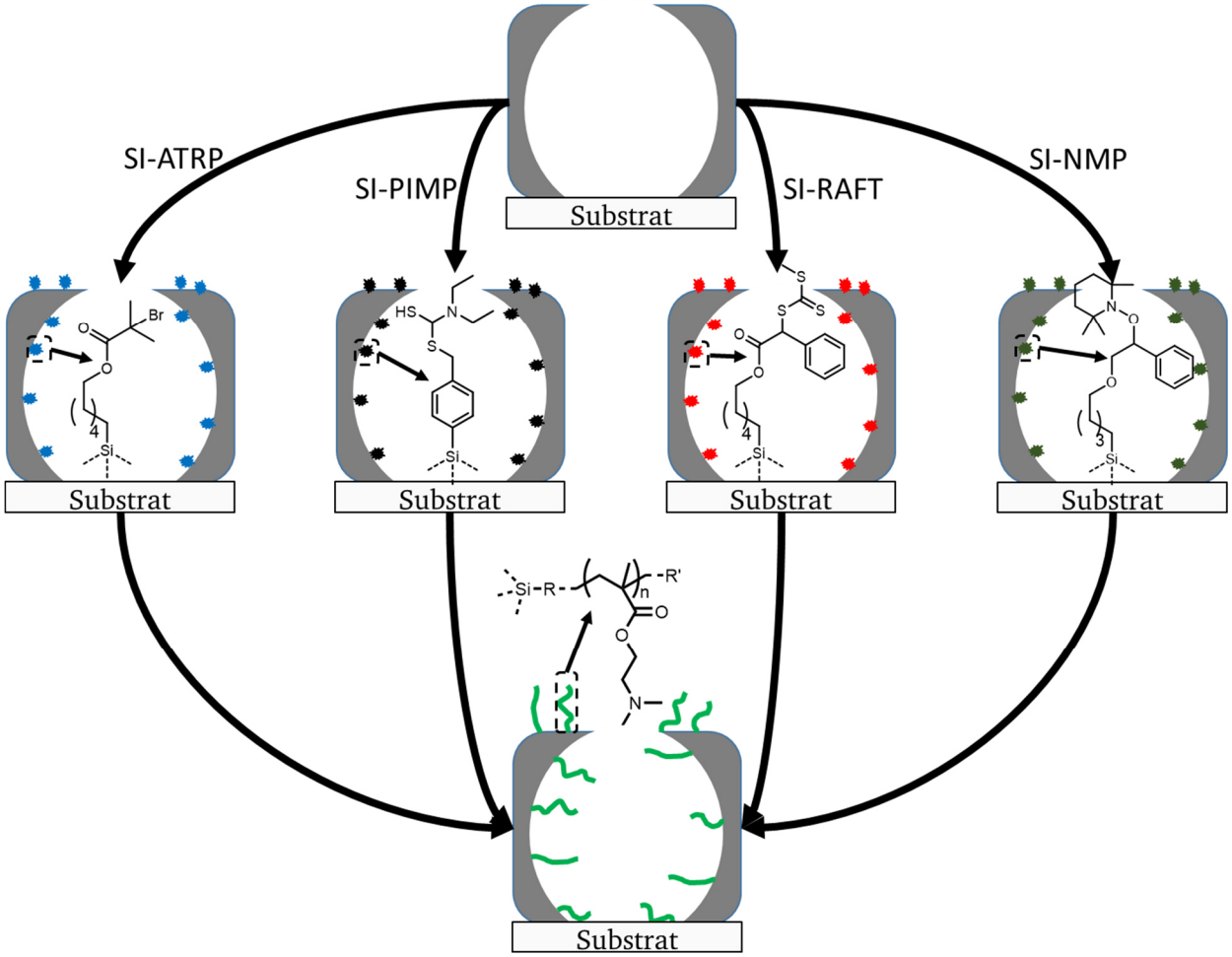

Schema 2-4: Schematische Darstellung der Funktionalisierung von Silicananoporen mit DMAEMA über die Polymerisationsmethoden SI-ATRP, SI-PIMP, SI-RAFT und SI-NMP (Publiziert von Elsevier – © 2020 – mit Genehmigung verwendet; DOI: 10.1016/j.copbio.2020.03.005).

Im Rahmen dieser Arbeit ist ein Übersichtsartikel entstanden, indem die Trends für Polymerfunktionalisierung von Nanoporen im Zeitraum von 2016-2019 zusammengefasst wurden. Mein Beitrag umfasst die Entwicklungen von kontrollierten radikalischen Polymerisationen in Mesoporen.

Zu diesem Kapitel wurde im Rahmen dieser Arbeit ein Übersichtsartikel bei *Current Opinion in Biotechnology* veröffentlicht:

R. Brilmayer*, C. Förster*, L. Zhao*, A. Andrieu-Brunsen, **Trends in Nanopore Polymer Funtionalization**, *Curr. Opin. Biotech.*, **2020**, 63, 200.

*These authors contributed equally to this work

Publiziert von Elsevier –©2020– mit Genehmigung verwendet;

DOI: 10.1016/j.copbio.2020.03.005

Available online at www.sciencedirect.com

ScienceDirect

Current Opinion in Biotechnology

Recent trends in nanopore polymer functionalization

Robert Brilmayer, Claire Förster, Lucy Zhao and Annette Andrieu-Brunsen

Functional nanopores play an essential role in many biotechnological applications such as sensing, or drug delivery. Prominent examples are polymer functionalized ceramic or solid state nanopores. Intensive research efforts led to a discovery of a plethora of polymer functionalized nanopores demonstrating gated molecular transport upon basically all common stimuli. Nevertheless, nature's biological pore transport precision is unreached. This can be, among others, ascribed to limits in design precision especially with respect to functionalization. Recent trends in polymer functionalized nanopores address the role of confinement and polymerization control, strategies toward more sustainable reaction conditions, such as visible light initiation and strategies toward nanoscale local placement of polymer functionalization. The resulting multi-stimuli responsive nanopore performance enables concerted release or transport, side selective separation and selective detection.

Address
Technische Universitat Darmstadt, Germany

Corresponding author:
Andrieu-Brunsen, Annette (andrieu-brunsen@smartmem.tu-darmstadt.de)

Current Opinion in Biotechnology 2020, **63**:200–209

This review comes from a themed issue on **Nanobiotechnology**

Edited by **Beatrix Süß** and **Thomas Hermann**

https://doi.org/10.1016/j.copbio.2020.03.005

Introduction

Biological ion channels exhibit selective and spatiotemporal transport control. With this nature has set the unmatched standard for nanopore transport in terms of complexity, regulated selectivity, directional permeability, and temporal control. To advance biotechnology, for example, drug delivery, sensing, or separation, nature's performance has to be implemented into robust technological nanopores [1–5]. This requires nanoporous materials with highly defined porous structure and precise functionalization. Within the last two decades a large portfolio of functional nanoporous materials has been explored. Examples are mesoporous silica, or ion track etched nanopores. The combination of these nanoporous materials with responsive molecules, and above all responsive polymers, has led to a plethora of transport gating functional nanopores. Especially porous silica materials have been transformed into a diversity of functional hybrid materials and served to push the limits of polymer functionalization because of their versatile surface chemistry. Using responsive polymers all common stimuli, such as pH, temperature, light, or voltage have been demonstrated to gate molecular transport (Figure 1). Many reviews, including very recent ones [6–9], summarize achievements in functional nanopores, their transport characteristics, and application potential. In spite of many examples of switchable nanopores transport selectivity, spatiotemporal transport control, or transport direction remains a challenge but at the same time represents a key step towards complex nanosystem design and biotechnological applications. Both are a current driving force to advance precision of polymer functionalization in nanoporous materials which then become multi-stimuli responsive, multifunctional, and serve a specific application such as drug delivery or sensing even down to single molecule detection. At the same time polymerizations in nanopores itself are heavily investigated with respect to understanding confinement effects and to increase sustainability of synthesis procedures. In this review we highlight recent trends in polymer nanopore functionalization, which could help to further approach the precision level of transport control in nature and to design complex, multifunctional nanosystems for biotechnology.

Controlled polymerization in nanopores

Polymers carry multiple functions per surface anchor point and can be stimuli-responsive. This allows to induce time-dependent gating of nanopores based on changes in charge density, wettability, or ligand binding. Thereby nanopore filling, or polymer composition strongly determine the nanopore properties such as molecular transport. Highest polymer amount and nanopore filling control in nanopores has been achieved using grafting from polymerizations. In addition, control over polymer chain architecture has recently become accessible through surface-initiated controlled radical polymerizations (SI-CRP). With respect to detailed reviews on SI-CRP in solution and on surfaces we refer the interested reader to reviews by the group of *Klok* [14••,15••] and further reviews on *Atom-Transfer Radical Polymerization* (ATRP) [16], *Reversible Addition Fragmentation Chain Transfer polymerization* (RAFT) [17] and photo *iniferter mediated polymerization* (PIMP) polymerizations [18]. The most important polymerization techniques applied in nanopores are ATRP, RAFT and PIMP (Figure 2).

Figure 1

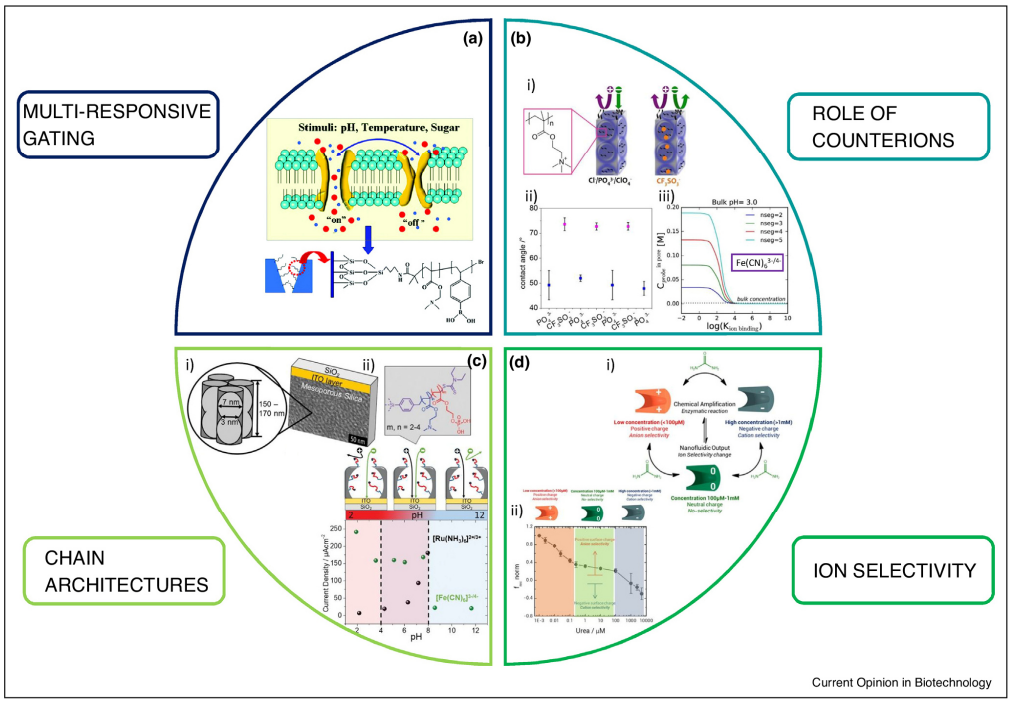

(a) A triple-responsive nanofluidic diode under external stimuli including temperature, pH and sugar. The multi-responsive copolymer poly(*N,N*-dimethylamino ethyl methacrylate-*co*-4-vinyl benzene boric acid) (P(DMAEMA-*co*-VPBA)) was polymerized onto the interior surface of a single glass conical nanochannel and allows switching the nanochannel between high and low ion conducting states. Reprinted with permission from *Nanoscale*, **2017**, 9, 433 [10], Copyright (2017), American Chemical Society. **(b)** (i) Effect of different counterions on the wetting and ionic transport in poly(2-(methacryloyloxy)ethyltrimethylammonium chloride)-functionalized silica mesopores. Ionic pore accessibility is strongly dependent on the counterion. (ii) Measuring contact angles on such modified mesoporous silica thin films, a reversible switching of the advancing contact angle between PO_4^{3-} and ClO_4^- can be observed. (iii) Averaged in-pore concentration of $Fe(CN)_6^{3-/4-}$ as a function of the log of the binding constant at pH 3, showing how to adjust the pores from positively charged when no ion binding occurs to negatively charged (from the deprotonation of surface silanol groups) when binding is strong. Reprinted with permission from *Langmuir*, **2018**, 34, 20, 5943–5953 [11•], Copyright (2018), American Chemical Society. **(c)** (i) Responsive 2-dimethylamino)ethyl methacrylate)-*block*-2-methacryloyloxy)ethyl phosphate (DMAEMA-*b*-MEP)-functionalized mesoporous silica films show complex gating behavior. (ii) Measured ion permselectivity (of $Fe(CN)_6^{3-/4-}$) of such modified silica films can be gradually adjusted from anion selective at acidic pH (red area) over an open state between approximately pH 4–8 to a cation selective nanopore at basic pH (blue area). Reprinted with permission from *Small*, **2019**, 15, 1902710 [12•], Copyright (2019), The Authors. Published by WILEY-VCH Verlag GmbH and Co. KGaA, Weinheim. **(d)** Urea-dependent behavior of the PET/PAH/Ur (polyethylene terephthalate/poly(allylamine)/urease) modified nanochannel. (i) With increasing amount of urea in solution, the nanofluidic system shifts progressively from anion selectivity to cation selectivity, or from positive to negative rectifications, which can be shown by the (ii) rectification efficiencies (f_{rec}) varying with urea concentration. Reprinted with permission from *Nano Lett.*, **2018**, 18, 3303–3310 [13•], Copyright (2018), American Chemical Society.

Surface Initiated Atom Transfer Radical Polymerization (SI-ATRP)

In the last years, different efforts turning SI-ATRP into a more environmentally friendly method are pursued. Since 2007 [16] common Cu(0)-catalysts are used while performing the polymerization under ambient conditions. Yan *et al.* [19,20•] used this technique to polymerize poly (2-methacryloyloxyethyl phosphorylcholine) (PMPC) brushes on larger scale surfaces. Huang *et al.* [21] used photoATRP with $FeBr_3$ for surface modification of mesoporous silica. Even though SI-ATRP is widely used for many years in nanopores and has been systematically investigated in nanoporous silica [22] not every aspect is fully understood yet, especially regarding nanoconfinement with pore diameters below 15 nm. Regarding confinement effects Chen *et al.* [23,24] showed that

Figure 2

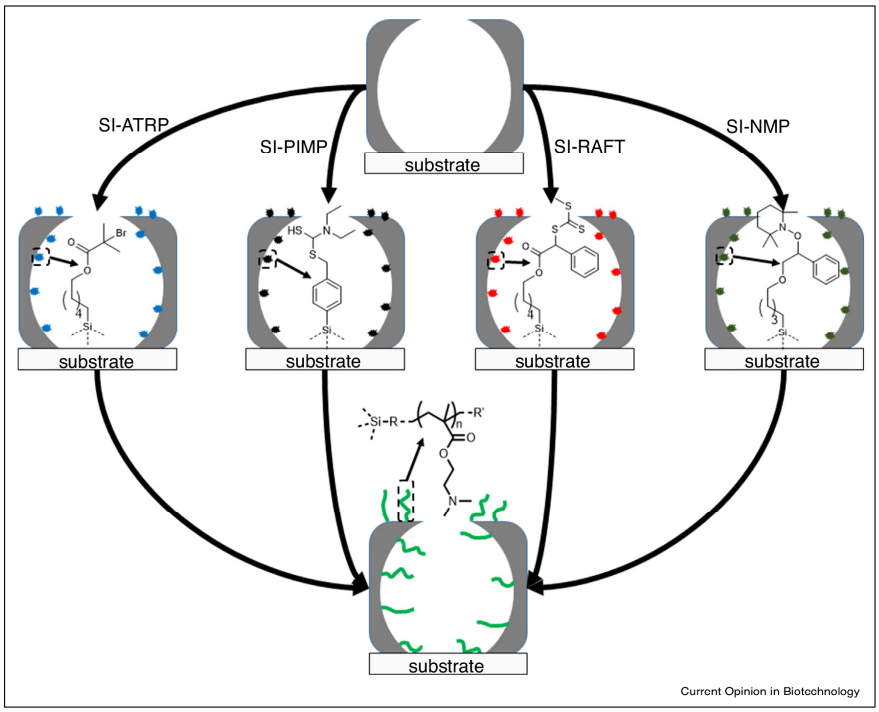

Schematic illustration of DMAEMA grafting from polymerization in a mesopore by SI-ATRP, SI-PIMP, SI-RAFT and SI-NMP (from left to right) at the pore wall. Polymerization control in ATRP is dependent on an activation-deactivation equilibrium depending on the presence of a transition metal complex and a dormant alkyl halide terminated polymer chain and monomers which all have to diffuse into the nanopore. The feature of PIMP polymerizations is that no further additives are needed since the iniferter is able to initiate the polymerization transFER the chains and TERminate (INI-FER-TER) the polymerization. The RAFT polymerization resembles mainly a conventional free radical polymerization with the addition of a *Chain Transfer Agent* (CTA), such as dithiocarbamate to enhance control. For a SI-RAFT either the initiator or the CTA can be attached to the surface. NMP uses a nitroxide radical to reversibly activate–deactivate the propagating polymer chain.

polymerization of styrene in mesoporous materials such as SBA-15 or MCM-41 lead to higher molecular weight, polydispersity, and glass transition temperature (T_g). Most recently, SI-ATRP has been employed to produce dual stimuli, pH and light responsive nanocarriers based on mesoporous silica particles [25•] or multi-stimuli responsive nanopores [10], low fouling nanoparticles with reduces cell uptake [26], and antimicrobical surfaces [27]. Polymer modification by SI-ATRP has also led to silica nanoparticles that are more salt tolerant and temperature stable [28], and a combination of MCM-41 mesoporous silica particles with polymer coated, silica covered magnetic nanoparticles was used to detect salmonella in milk samples [29]. That large scale production of polymer brush functionalized surfaces has been demonstrated by Sato *et al.* [30•] using a sol-gel based roll-to roll or wire-bar coating process, which in combination with a technique developed by Herzog *et al.* [31•] can be transferred to nanoporous materials in the near future.

Surface Initiated Reversible Addition-Fragmentation Chain Transfer (SI-RAFT) and Photo Iniferter Mediated Polymerization (SI-PIMP)

For SI-RAFT and SI-PIMP numerous recent examples of nanopore and especially mesoporous silica functionalization are reported. A strong focus of current research is dedicated towards a better understanding of the surface-initiated polymerizations as well as to create more complex surfaces. Zheng *et al.* [32] grafted chloroprene to silica nanoparticles by SI-RAFT and demonstrated that even on particles surfaces SI-RAFT of cloroprene is slower than free RAFT polymerization. Silies *et al.* [11•,33] successfully polymerized

2-(methacryloyloxy)ethyl-trimethylammonium chloride by SI-PIMP in silica mesopores (pore diameter <10 nm) while controlling pore filling. Investigating the influence of counter ions on ion transport and wetting, modulation of wetting from hydrophilic to hydrophobic and modulation of transport from closed to open nanopores was demonstrated. Using the same iniferter Tom *et al.* [12•,34••] achieved high pore filling degrees, successfully re-initiated the polymerizations and thus graft multi-stimuli responsive block-cooligomers in silica mesopores with a diameter of less than 10 nm. Interestingly, these mesopores do not show bipolar ion exclusion [12•] as observed for zwitterionically charged nanopores [35,36]. Chen *et al.* [37••,38] used light induced SI-RAFT to successfully graft zwitterionic and thermoresponsive monomers on fluorescent silica nanoparticles in the presence of oxygen. Although not surface initiated, Xu *et al.* [39•] used silica SBA-15 of pore sizes between 8–27 nm as micro-reactors for RAFT polymerizations and showed, that the spatial confinement leads to narrower molecular weight distributions. Magnetic mesoporous silica particles were modified with disulfide bonds by Hegazy *et al.* [40•] and the thermo responsive polymer poly(2-nitrobenzyl acrylate) via RAFT polymerization to create a dual stimuli drug release platform. Wang *et al.* [41] produced antimicrobial surfaces on mesoporous silica by the formation of poly (3-acrylamidopropyl) trimethylammonium chloride brushes by SI-RAFT polymerizations.

Non radical controlled surface initiated polymerizations

Other controlled polymerization techniques such as SI-Nitroxide-Mediated Polymerization (SI-NMP), ring-opening metathesis polymerization (ROMP) or ionic polymerization play only a minor role for nanopore functionalization especially regarding nanoporous silica. Although anionic polymerization has been applied to silica surfaces [42] the reactive nature of the silica surface hydroxyl groups, the remaining water traces and the synthetically demanding ionic polymerization offer no attractive alternative to SI-CRP techniques. ROMP on the other hand offers mild reaction conditions and can be used to generate block copolymers and complex polymer achitectures on surfaces [43] but reaction control on surfaces remains limited. In addition, ROMP allows the synthesis of polymers which are inaccessible by radical polymerization, such as for example, light-responsive spiropyran homopolymers. Krohm *et al.* [44] grafted norbornene-based polymers with a spiropyran side and spirooxazine side chain *from* mesoporous silica thin films using SI-ROMP. Eder *et al.* [45] used SI-ROMP in a *grafting-to* approach to combine norbornene-functionalized mesoporous silica with different derivates of poly(ferrocene) using a Schrock-initiator.

Visible light induced polymer functionalization of nanopores

Not only with respect to sustainable polymerization but as well regarding miniaturization and improved local resolution as well as for complex nanosystem design visible light induced polymerization is an emerging topic. Within the last years, most of the common polymerization techniques have been made visible light compatible. It has to be noted that visible light refers to a very broad wavelength range and even polymerizations initiated below 380 nm are sometimes categorized as visible light initiated. Here, we refer to visible light for wavelength larger than 380 nm. The majority of visible light polymerizations has been developed and optimized in solution.

Available wavelengths for visible light induced polymerization

In solution, the probably most investigated visible light-initiated polymerization reaction is ATRP. Recent developments show ATRP initiation at 392 nm in aqueous solution using a copper catalyst [46]. The initiation wavelength has been further shifted to 464 nm by Zhu and coworkers [47] using $[Ir(ppy)_3]$ as photoredoxcatalyst, the catalyst has been recycled after polymerization. Instead of recycling the catalyst Yagci and coworkers [48•] performed a metal-free ATRP with the use of perylene under irradiation of 400–500 nm. Besides ATRP, several radical and ionic polymerizations are reported to be initiated by visible light. Recently, a radical-promoted cationic polymerization, initiated by 400–500 nm was achieved using an acylsilane photoinitiator at room temperature [49]. Kaya *et al.* [50] demonstrated free radical-promoted cationic polymerizations using organotellurium compounds in the presence of diphenyliodonium hexafluorophosphate initiated at 450 nm. Even ROMP initiated at 450–480 nm has been reported: Boydston and coworkers[51] used divinyl ether initiators and a photoredox catalyst to polymerize norbornene with blue light (450–480 nm). Rovis and coworkers [52•] reported a blue light controlled ROMP and photolithographic olefin metathesis polymerization (PLOMP) with 2,4,6-triphenylpyrylium tetrafluoroborate and $[RuCl_2(CHPh)(IMes)_2]$ as catalysts.

It has to be noted that only few examples demonstrate initiation at higher wavelength between 500 nm and 700 nm. Polymerization suitable for initiation in this wavelength range is, for example, a Photo-induced Electron Transfer (PET)-RAFT [53], which was used to polymerize *o*-nitrobenzyl methacrylate under irradiation of red (635 nm) and yellow (590 nm) light. Another example are dye-sensitized polymerizations, in which the wavelength is determined by choosing the dye, for example, to 660 nm using methylene blue. A significant number of visible light initiated polymerizations has been transferred to planar surfaces including RAFT [54–59] and ATRP [60–62].

Visible light induced nanopore functionalization

Functionalization of nanopores using visible light-initiated polymerizations is much less explored. To avoid scattering this requires sufficiently small pore-sizes or refractive index matching. The group of Cai [63] used

the RAFT agent 4-cyano-4-(ethylsulfanylthiocarbonylsulfanyl)pentanoic acid (CEP) for a visible light mediated RAFT at 420 nm with polymerization-induced self-assembly to synthesize hydrogen-bonded pore-switchable cylindrical vesicles. Analyzing the polymer amount and pH-dependent porosity they show that nanotubes have a more sensitive switchable porosity as compared to vesicles. Wei and coworkers [37••] functionalized mesoporous silica nanoparticles with zwitterionic polymers using RAFT with CEP as RAFT agent at 480 nm. Fan *et al.* [64••] reported functionalized microcapsules, which impart a self-healing to hydrogels using a visible light induced PET-ATRP with rhodamine B as catalyst to functionalize porous carbon nanospheres with poly(4-vinylpyridine). Ma *et al.* [65] achieved a visible light (380 nm) induced SI-ATRP on SBA-15 using the photocatalyst 10-phenylphenothiazine (PTH). By functionalization with PMMA improved adsorption capacity for toluene could be observed. Recently, the group of Silván [66••] described a visible light assisted organosilane assembly (VLAO) on mesoporous silicon by irradiation with 700 nm. Visible light supports the surface oxidation of the mesoporous silicon allowing a reaction with organosilanes (in this case 3-aminopropyl-triethoxy-silane and *1H,1H,2H,2H*-perfluorodecyl-triethoxy-silane). Functionalization of mesoporous silica thin films at wavelength between 400−700 nm was demonstrated using coinitiator (e.g. tertiary amine)/dye systems. This system is especially advantageous because it allows tuning the initiation wavelength by selecting suitable dyes. Polymerizations were successfully carried out at wavelength of 390 nm while using 2-chlorothioxanthone or with 660 nm while using methylene blue as dye [67].

Nanolocal placement and asymmetric design of functional nanopores

Precise local functional placement on surfaces and especially in nanopores is expected to improve complex nanosystem design by allowing multifunctionality and locally controlled multiresponsivity, nanoscale gradients, or nanoscale pattern formation. To induce precise local placement of molecules and polymers into nanopores with ideally nanoscale precision functionalization technology beyond photolithography or soft lithography is required. Concerning planar surfaces and microchips Rühe [68•] gives an overview on nanofabrication techniques.

Asymmetric design of nanoporous materials

Regarding nanopores already asymmetric shape in ion-track etched nanopores shows interesting diode like (side-selective) transport on a single nanopore level [69–71]. By introducing asymmetry into geometry (e.g. conical nanopores), but as well into functionalization, side-selective and multiresponsive, double-gated and multiresponsive ion transport has been demonstrated [68•,72,73]. Interestingly, these activities have not been intensified within the last years. Instead, research on doublelayer or multilayer membranes was strongly pursued. Prominent examples are Janus membranes and diode-like nanochannel membranes. Jiang and coworkers presented PET/PTFE-based Janus membranes for side-selective oil water separation (Figure 3a) [74••] as well as PSS (poly)styrenesulfonate)/AAO (anodic alumina oxide)-based and kaolinite-based Janus membranes for selective ion transport in the context of osmotic-energy based energy conversion [75•,76]. In accordance with these examples various Janus membranes demonstrating side-selective oil-water separation [77•] and osmosis transport [78••] have been developed within the last two years. Functionalizing only the outer planar surface of mesoporous films allows to investigate the interplay of orthogonally functionalized layers. As a recent example PNIPAM-capped mesoporous thin films have been equipped with thermosensitive cation-selectivity based on such concerted function [79]. Further developments discuss *in situ* functionalized mesoporous silica [80••] for multilayer film generation. As an example, Bathfield *et al.* [81] synthesized PEO-*b*-PNIPAM from a PEO macroinitiator and subsequent RAFT polymerization, and applied them as templates to produce thermosensitive drug-loaded OMS (silica-based ordered mesoporous materials). The mesoporosity of these materials was then created by water washing below the LCST of PNIPAM. The approach of local *in situ* functionalization in combination with printing processes [31•] bares great potential for model system design to understand nanopore performance in hierarchical materials. Understanding the role of nanopores and their distribution within hierarchical materials is essential to understand material function as has been demonstrated for paper wetting and paper based fluidics by Nau *et al.* [82•]. Blocking fiber swelling and nanopore accessibility using a thin silica coating results in side selective oil-/water permeation.

Nanoscale local functionalization

Besides multilayer Janus membrane generation and ion-track etched single pore functionalization material deposition and resulting orthogonal surface chemistry have been used as well recently to achieve local resolution. One recent example is the synthesis of an ordered, vertically aligned mesoporous silica thin film with propyl–copper–phosphonate or propyl–silver–carbonate groups localized exclusively at the pores bottom (Figure 3b) [83••]. Going beyond double layer formation nanolocal placement of polymers into nanopores with high precision is an ongoing challenge. Nanoscale local functionalization on surfaces has been achieved, for example, by dip-pen-lithography and two-photon lithography. While dip-pen lithography remains limited to monolayers, and is time-consuming, scanning near-field optical microscopy (SNOM) and beam-pen lithography, in combination with two-photon polymerizations or cross-linking reactions, incorporate challenges, such as writing speed, difficulty in controlling the amount of light and the development of

Figure 3

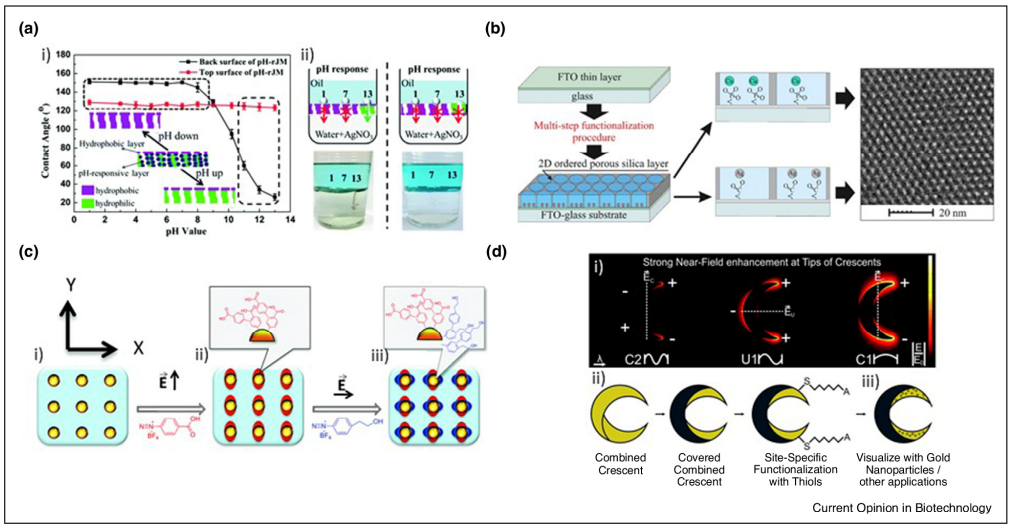

(a) pH responsive Janus membrane realizing selective permeation of water droplets in oil. (i) pH dependent water contact angle at the top and the bottom of the Janus membrane. (ii) Illustrations and photographs confirming selective, pH dependent permeation of water doplets (pH = 1, 7, 13. left); water droplets with different pH values were blocked after inverting the pH responsive Janus membrane (right). Reprinted with permission from *Nanoscale Horiz.*, **2018**, 3, 53-57 [74••], Copyright (2017), The Royal Society of Chemistry. **(b)** Multi-step synthesized ordered porous silica thin layer with vertically alligned pores containing copper and silver ion binding groups exclusively at the pores bottom. Reprinted from with permission from *Microporous and Mesoporous Materials*, **2019**, 274, 356–362 [83••], Copyright (2018), Elsevier. **(c)** Nanolocal multifunctionalization of gold nanodiscs under irradiation with polarized light. (i) The nanostructures were incubated in an aqueous solution of carboxyphenyl diazonium salt and (ii) irradiated with a polarized laser in y-direction, followed by (iii) incubating those nanostructures in an aqueous solution of hydroxyethyl phenyl diazonium salt under laser irradiation in x-direction. Reprinted with permission from *Nanoscale Horiz.*, **2018**, 3, 53–57 [89••], Copyright (2018), The Royal Society of Chemistry. **(d)** Nanolocal functionalization in the regions of plasmon enhancement of gold nanocrescents. (i) Nanocrescents can evoke the fundamental dipole resonance (C1), the first order resonance (U1) and the second order resonance (C2). (ii) First, a combined crescent with extended contour via two gold deposition steps is produced. Subsequently, the nanocrescents are partially covered by evaporating a blocking layer. Finally, the structure can be functionalized with thiols, which exclusively binds to the free gold surface. (iii) The successful site-specific functionalization is demonstrated by electrostatically adsorb gold nanoparticles. Reprinted with permission from *Nanoscale Adv.*, **2020**, Advance Article [90••], Copyright (2020), The Royal Society of Chemistry.

suitable polymerization systems, but could potentially be combined with nanoporous materials and especially films. Another very promising concept to confine nanopore functionalization and polymerization to the nanoscale, and thus below the diffraction limit, is the use of localized near fields such as surface plasmons [84]. Pioneering work by Kreiter [84,85] and Soppera [86], exploiting the excitation of locally enhanced optical near-field of silver nanoparticles achieving a sub 10 nm optical resolution of photopolymerization at metal nanoparticles using visible light. Thereby the required polymerization wavelength which is determined by the near-field generating metal and usually is located within the visible or even infrared wavelength range remains a challenge but recently becomes accessible. The first example of surface plasmon-induced polymerization with mesoporous silica thin films was presented by Herzog *et al.* [87] still not showing nanolocal control. Nevertheless, these films provide polymer controlled ionic permselectivity. Structured chemical surface functionalization with nanoscale local resolution was demonstrated by Nguyen *et al.* [88] through aryl film grafting covalently bonded on gold nanostripes. Additionally, using polarized light for plasmon excitation allows regioselective multifunctionalization of gold nanodisks (Figure 3c) [89••]. By exploiting the strong near-field enhancement at the tips of crescent-shaped nanostructures, they were site-selectively modified (Figure 3d) [90••]. These recent advances in precise, nanoscale arrangement of functionalizations can be expected to be transferred to nanopores in the near future.

Conclusion

Responsive polymer functionalized nanopores have made first steps toward nature inspired nanopore performance accessible and hold promise for the design of complex nanosystems in the context of biotechnology. Functionalization

concepts have been demonstrated to enable transport gating upon basically all common stimuli, gradual transport control, side selective transport in Janus membranes, and concerted transport control in double layer architectures. Recent developments in nanopore polymer functionalization focus on more sustainable functionalization, for example, using visible light, enhanced control and understanding of confinement effects as well as precise local placement of polymers into nanopores. Functional asymmetry is envisioned to transform side selective transport into precisely directed, selective transport. These activities will not only result in new synthesis technologies, but as well push the development of complex nanosystems and alongside this, enable and improve technologies such as drug delivery, sensing, water management and energy conversion.

Conflict of interest statement

Nothing declared.

CRediT authorship contribution statement

Robert Brilmayer: Writing - original draft, Visualization, Investigation. **Claire Förster:** Writing - original draft, Visualization, Investigation. **Lucy Zhao:** Writing - original draft, Visualization, Investigation. **Annette Andrieu-Brunsen:** Conceptualization, Validation, Supervision, Funding acquisition, Project administration.

Acknowledgement

We thank Maria Ochs for providing literature and expertise with respect to ROMP in solution, on surfaces and in pores.

References and recommended reading

Papers of particular interest, published within the period of review, have been highlighted as:

- • of special interest
- •• of outstanding interest

1. Castillo RR, Lozano D, Gonzalez B, Manzano M, Izquierdo-Barba I, Vallet-Regi M: **Advances in mesoporous silica nanoparticles for targeted stimuli-responsive drug delivery: an update**. *Expert Opin Drug Deliv* 2019, **16**:415-439.
2. Wang Y, Sun S, Zhang Z, Shi D: **Nanomaterials for cancer precision medicine**. *Adv Mater* 2018, **30**:1705660.
3. Knežević NŽ, Gadjanski I, Durand J-O: **Magnetic nanoarchitectures for cancer sensing, imaging and therapy**. *J Mater Chem B* 2019, **7**:9-23.
4. Nasir T, Herzog G, Hebrant M, Despas C, Liu L, Walcarius A: **Mesoporous silica thin films for improved electrochemical detection of paraquat**. *ACS Sens* 2018, **3**:484-493.
5. Zhang H, Tian Y, Jiang L: **Fundamental studies and practical applications of bio-inspired smart solid-state nanopores and nanochannels**. *Nano Today* 2016, **11**:61-81.
6. Fu L, Zhai J: **Biomimetic stimuli-responsive nanochannels and their applications**. *Electrophoresis* 2019, **40**:2058-2074.
7. Zhu Z, Wang D, Tian Y, Jiang L: **Ion/molecule transportation in nanopores and nanochannels: from critical principles to diverse functions**. *J Am Chem Soc* 2019, **141**:8658-8669.
8. Perez-Mitta G, Toimil-Molares ME, Trautmann C, Marmisolle WA, Azzaroni O: **Molecular design of solid-state nanopores: fundamental concepts and applications**. *Adv Mater* 2019, **31**:e1901483.
9. Zhang Z, Huang X, Qian Y, Chen W, Wen L, Jiang L: **Engineering smart nanofluidic systems for artificial ion channels and ion pumps: from single-pore to multichannel membranes**. *Adv Mater* 2019:1904351.
10. Zheng YB, Zhao S, Cao SH, Cai SL, Cai XH, Li YQ: **A temperature, pH and sugar triple-stimuli-responsive nanofluidic diode**. *Nanoscale* 2017, **9**:433-439.
11. • Silies L, Gonzalez Solveyra E, Szleifer I, Andrieu-Brunsen A: **Insights into the role of counterions on polyelectrolyte-modified nanopore accessibility**. *Langmuir* 2018, **34**:5943-5953.
This study considers external influences on nanopores, which is extremely important in real applications.
12. • Brilmayer R, Hess C, Andrieu-Brunsen A: **Influence of chain architecture on nanopore accessibility in polyelectrolyte block-co-oligomer functionalized mesopores**. *Small* 2019:1902710.
This study represents the first systematic investigation of block-co-polymer/oligomer synthesis and resulting transport in nanopores.
13. • Perez-Mitta G, Peinetti AS, Cortez ML, Toimil-Molares ME, Trautmann C, Azzaroni O: **Highly sensitive biosensing with solid-state nanopores displaying enzymatically reconfigurable rectification properties**. *Nano Lett* 2018, **18**:3303-3310.
This study is an example of bioinspired smart nanopores and demonstrating the versatility of nanopore application in sensing.
14. •• Zoppe JO, Ataman NC, Mocny P, Wang J, Moraes J, Klok HA: **Surface-initiated controlled radical polymerization: state-of-the-art, opportunities, and challenges in surface and interface engineering with polymer brushes**. *Chem Rev* 2017, **117**:1105-1318.
This review provides in depth information on the state of SI-CRP with all basic information.
15. •• Badoux M, Billing M, Klok H-A: **Polymer brush interfaces for protein biosensing prepared by surface-initiated controlled radical polymerization**. *Polym Chem* 2019, **10**:2925-2951.
This review provides in depth information on the state of SI-CRP with all basic information.
16. Matyjaszewski K, Dong H, Jakubowski W, Pietrasik J, Kusumo A: **Grafting from surfaces for "everyone": ARGET ATRP in the presence of air**. *Langmuir* 2007, **23**:4528-4531.
17. Christopher BK, DT P, HJP A, SM H, Philipp V, Michael W: **RAFTing down under: tales of missing radicals, fancy architectures, and mysterious holes**. *J Polym Sci Part A Polym Chem* 2003, **41**:365-375.
18. Otsu T: **Iniferter concept and living radical polymerization**. *J Polym Sci Part A Polym Chem* 2000, **38**:2121-2136.
19. Yan W, Fantin M, Spencer ND, Matyjaszewski K, Benetti EM: **Translating surface-initiated atom transfer radical polymerization into technology: the mechanism of Cu0-mediated SI-ATRP under environmental conditions**. *ACS Macro Lett* 2019, **8**:865-870.
20. • Yan W, Fantin M, Ramakrishna S, Spencer ND, Matyjaszewski K, Benetti EM: **Growing polymer brushes from a variety of substrates under ambient conditions by Cu(0)-mediated surface-initiated ATRP**. *ACS Appl Mater Interfaces* 2019, **11**:27470-27477.
This studies (Refs. [19] and [20•]) explore SI-ATRP aiming for its use in technical application.
21. Huang L, Liu M, Mao L, Huang Q, Huang H, Zeng G, Tian J, Wen Y, Zhang X, Wei Y: **A facile FeBr3 based photoATRP for surface modification of mesoporous silica nanoparticles for controlled delivery cisplatin**. *Appl Surf Sci* 2018, **434**:204-210.
22. Kruk M: **Surface-initiated controlled radical polymerization in ordered mesoporous silicas**. *Isr J Chem* 2012, **52**:246-255.
23. Chen M, Qin L, Wei Y, Liu Y, Zhang F: **Confinement effect of mesoporous silica reactors on electron transfer atom transfer radical polymerization of styrene**. *J Porous Mater* 2018, **26**:7-17.
24. Chen M, Qin L, Liu Y, Zhang F: **Controllable preparation of polymer brushes from mesoporous silica SBA-15 via surface-initiated ARGET ATRP**. *Microporous Mesoporous Mater* 2018, **263**:158-164.

25. • Wang C, Isaacson SG, Wang Y, Lionti K, Volksen W, Magbitang TP, Chowdhury M, Priestley RD, Dubois G, Dauskardt RH: **Surface chemical functionalization to achieve extreme levels of molecular confinement in hybrid nanocomposites**. *Adv Funct Mater* 2019, **29**.
This study is an interesting example for the versatility of nanopore-polymer combinations for complex system design.

26. Encinas N, Angulo M, Astorga C, Colilla M, Izquierdo-Barba I, Vallet-Regi M: **Mixed-charge pseudo-zwitterionic mesoporous silica nanoparticles with low-fouling and reduced cell uptake properties**. *Acta Biomater* 2019, **84**:317-327.

27. Oh YJ, Khan ES, Campo AD, Hinterdorfer P, Li B: **Nanoscale Characteristics and Antimicrobial Properties of (SI-ATRP)-seeded polymer brush surfaces**. *ACS Appl Mater Interfaces* 2019, **11**:29312-29319.

28. Ma L, Luo P, He Y, Zhang L, Fan Y, Jiang Z: **Ultra-stable silica nanoparticles as nano-plugging additive for shale exploitation in harsh environments**. *Nanomaterials* 2019, **9**.

29. Bayramoglu G, Ozalp VC, Dincbal U, Arica MY: **Fast and sensitive detection of salmonella in milk samples using aptamer-functionalized magnetic silica solid phase and MCM-41-aptamer gate system**. *ACS Biomater Sci Eng* 2018, **4**:1437-1444.

30. • Sato T, Dunderdale GJ, Urata C, Hozumi A: **Sol–gel preparation of initiator layers for surface-initiated ATRP: large-scale formation of polymer brushes is not a dream**. *Macromolecules* 2018, **51**:10065-10073.
This study explores the scalability of polymer functionalization in mesoporous materials by SI-ATRP, which is needed for technological applications.

31. • Herzog N, Brilmayer R, Stanzel M, Kalyta A, Spiehl D, Dörsam E, Hess C, Andrieu-Brunsen A: **Gravure printing for mesoporous film preparation**. *RSC Adv* 2019, **9**:23570-23578.
This study explores the scalability of mesoporous film preparation using gravure printing which is relevant for fast and defined multilayer formation.

32. Zheng Y, Abbas ZM, Sarkar A, Marsh Z, Stefik M, Benicewicz BC: **Surface-initiated reversible addition-fragmentation chain transfer polymerization of chloroprene and mechanical properties of matrix-free polychloroprene nanocomposites**. *Polymer* 2018, **135**:193-199.

33. Silies L, Didzoleit H, Hess C, Stühn B, Andrieu-Brunsen A: **Mesoporous thin films, zwitterionic monomers, and iniferter-initiated polymerization: polymerization in a confined space**. *Chem Mater* 2015, **27**:1971-1981.

34. •• Tom J, Brilmayer R, Schmidt J, Andrieu-Brunsen A: **Optimisation of surface-initiated photoiniferter-mediated polymerisation under confinement, and the formation of block copolymers in mesoporous films**. *Polymers* 2017, **9**:539.
This study presents the first block-co-oligomer formation by reinitiation in nanopores sub 10 nm.

35. Silies L, Andrieu-Brunsen A: **Programming ionic pore accessibility in zwitterionic polymer modified nanopores**. *Langmuir* 2018, **34**:807-816.

36. Calvo A, Yameen B, Williams FJ, Soler-Illia GJ, Azzaroni O: **Mesoporous films and polymer brushes helping each other to modulate ionic transport in nanoconfined environments. An interesting example of synergism in functional hybrid assemblies**. *J Am Chem Soc* 2009, **131**:10866-10868.

37. •• Chen J, Liu M, Huang L, Huang H, Wan Q, Tian J, Wen Y, Deng F, Zhang X, Wei Y: **Preparation of zwitterionic polymers functionalized fluorescent mesoporous silica nanoparticles through photoinduced surface initiated RAFT polymerization in the presence of oxygen**. *J Taiwan Inst Chem Eng* 2018, **91**:570-577.
This study provides one of the very few examples of (complex) nanopore functionalization using visible light.

38. Chen J, Liu M, Huang H, Deng F, Mao L, Wen Y, Huang L, Tian J, Zhang X, Wei Y: **Facile preparation of thermoresponsive fluorescent silica nanopaprticles based composites through the oxygen tolerance light-induced RAFT polymerization**. *J Mol Liq* 2018, **259**:179-185.

39. • Xu X, Zeng Y, Yu C, Zhang F: **Controlled RAFT polymerization of MMA in confined space of various pore sizes of SBA-15**. *J Porous Mater* 2019.
This study explores the use of mesoporous silica particles as microreactors for RAFT polymerizations.

40. • Hegazy M, Zhou P, Rahoui N, Wu GY, Taloub N, Lin YP, Huang X, Huang YD: **A facile design of smart silica nanocarriers via surface-initiated RAFT polymerization as a dual-stimuli drug release platform**. *Colloids Surf A Physicochem Eng Aspects* 2019, **581**.
This study is an interesting example for complex system design, using RAFT polymerization to create a dual stimuli responsive drug release platform.

41. Wang Y, Yin M, Lin X, Li L, Li Z, Ren X, Sun Y: **Tailored synthesis of polymer-brush-grafted mesoporous silicas with N-halamine and quaternary ammonium groups for antimicrobial applications**. *J Colloid Interface Sci* 2019, **533**:604-611.

42. Kim CJ, Sondergeld K, Mazurowski M, Gallei M, Rehahn M, Spehr T, Frielinghaus H, Stühn B: **Synthesis and characterization of polystyrene chains on the surface of silica nanoparticles: comparison of SANS, SAXS, and DLS results**. *Colloid Polym Sci* 2013, **291**:2087-2099.

43. Cao E, Pichavant L, Prouzet E, Héroguez V: **The formation and study of poly(ethylene oxide)-poly(norbornene) block-copolymers on the surface of titanium-dioxide particles: a novel approach towards application of si-ROMP to larger surface modification**. *Polym Chem* 2016, **7**:2751-2758.

44. Krohm F, Kind J, Savka R, Alcaraz Janßen M, Herold D, Plenio H, Thiele CM, Andrieu-Brunsen A: **Photochromic spiropyran- and spirooxazine-homopolymers in mesoporous thin films by surface initiated ROMP**. *J Mater Chem C* 2016, **4**:4067-4076.

45. Eder K, Reichel E, Schottenberger H, Huber CG, Buchmeiser MR: **Alkyne metathesis graft polymerization: synthesis of poly (ferricinium)-based silica supports for anion-exchange chromatography of oligonucleotides**. *Macromolecules* 2001, **34**:4334-4341.

46. Pan X, Malhotra N, Simakova A, Wang Z, Konkolewicz D, Matyjaszewski K: **Photoinduced atom transfer radical polymerization with ppm-level Cu catalyst by visible light in aqueous media**. *J Am Chem Soc* 2015, **137**:15430-15433.

47. Liu X, Ni Y, Wu J, Jiang H, Zhang Z, Zhang L, Cheng Z, Zhu X: **A sustainable photocontrolled ATRP strategy: facile separation and recycling of a visible-light-mediated catalyst fac-[Ir(ppy)3]**. *Polym Chem* 2018, **9**:584-592.

48. • Aydogan C, Yilmaz G, Yagci Y: **Synthesis of hyperbranched polymers by photoinduced metal-free ATRP**. *Macromolecules* 2017, **50**:9115-9120.
This study provides a recent example for the development of environmentally friendly polymerization.

49. Sari E, Mitterbauer M, Liska R, Yagci Y: **Visible light induced free radical promoted cationic polymerization using acylsilanes**. *Prog Organ Coat* 2019, **132**:139-143.

50. Kaya K, Seba M, Fujita T, Yamago S, Yagci Y: **Visible light-induced free radical promoted cationic polymerization using organotellurium compounds**. *Polym Chem* 2018, **9**:5639-5643.

51. Lu P, Alrashdi NM, Boydston AJ: **Bidirectional metal-free ROMP from difunctional organic initiators**. *J Polym Sci Part A Polym Chem* 2017, **55**:2977-2982.

52. • Theunissen C, Ashley MA, Rovis T: **Visible-light-controlled ruthenium-catalyzed olefin metathesis**. *J Am Chem Soc* 2019, **141**:6791-6796.
This study presents an interesting new synthesis strategy by merging olefin metathesis and photoredox catalysis.

53. Bagheri A, Yeow J, Arandiyan H, Xu J, Boyer C, Lim M: **Polymerization of a photocleavable monomer using visible light**. *Macromol Rapid Commun* 2016, **37**:905-910.

54. Li M, Fromel M, Ranaweera D, Rocha S, Boyer C, Pester CW: **SI-PET-RAFT: surface-initiated photoinduced electron transfer-reversible addition–fragmentation chain transfer polymerization**. *ACS Macro Lett* 2019, **8**:374-380.

55. Seo SE, Discekici EH, Zhang Y, Bates CM, Hawker CJ: **Surface-initiated PET-RAFT polymerization under metal-free and**

ambient conditions using enzyme degassing. *J Polym Sci* 2020, **58**:70-76.

56. Bagheri A, Arandiyan H, Adnan NNM, Boyer C, Lim M: **Controlled direct growth of polymer shell on upconversion nanoparticle surface via visible light regulated polymerization**. *Macromolecules* 2017, **50**:7137-7147.

57. Tucker BS, Coughlin ML, Figg CA, Sumerlin BS: **Grafting-from proteins using metal-free PET–RAFT polymerizations under mild visible-light irradiation**. *ACS Macro Lett* 2017, **6**:452-457.

58. Li X, Ye S, Huang Y, Li JL, Cai T: **Precise growth of polymer brushes on silica-based nanocomposites via visible-light-regulated controlled radical polymerization**. *J Mater Chem A* 2019, **7**:6173-6179.

59. Bagheri A, Sadrearhami Z, Adnan NNM, Boyer C, Lim M: **Surface functionalization of upconversion nanoparticles using visible light-mediated polymerization**. *Polymer* 2018, **151**:6-14.

60. Yang Y, Liu X, Ye G, Zhu S, Wang Z, Huo X, Matyjaszewski K, Lu Y, Chen J: **Metal-free photoinduced electron transfer–atom transfer radical polymerization integrated with bioinspired polydopamine chemistry as a green strategy for surface engineering of magnetic nanoparticles**. *ACS Appl Mater Interfaces* 2017, **9**:13637-13646.

61. Discekici EH, Pester CW, Treat NJ, Lawrence J, Mattson KM, Narupai B, Toumayan EP, Luo Y, McGrath AJ, Clark PG *et al.*: **Simple benchtop approach to polymer brush nanostructures using visible-light-mediated metal-free atom transfer radical polymerization**. *ACS Macro Lett* 2016, **5**:258-262.

62. Ma A, Zhang J, Wang N, Bai L, Chen H, Wang W, Yang H, Yang L, Niu Y, Wei D: **Surface-initiated metal-free photoinduced ATRP of 4-vinylpyridine from SiO2 via visible light photocatalysis for self-healing hydrogels**. *Ind Eng Chem Res* 2018, **57**:17417-17429.

63. Gao P, Cao H, Ding Y, Cai M, Cui Z, Lu X, Cai Y: **Synthesis of hydrogen-bonded pore-switchable cylindrical vesicles via visible-light-mediated RAFT Room-temperature aqueous dispersion polymerization**. *ACS Macro Lett* 2016, **5**:1327-1331.

64. •• Fan D, Wang G, Ma A, Wang W, Chen H, Bai L, Yang H, Wei D, Yang L: **Surface engineering of porous carbon for self-healing nanocomposite hydrogels by mussel-inspired chemistry and PET-ATRP**. *ACS Appl Mater Interfaces* 2019, **11**:38126-38135.
This study is one of the first examples transferring environmentally friendly ATRP with visible light to controlled surface functionalization of porous carbon.

65. Ma L, Li N, Zhu J, Chen X: **Visible light-induced metal free surface initiated atom transfer radical polymerization of methyl methacrylate on SBA-15**. *Polymers* 2017, **9**:58.

66. •• Rodriguez C, Muñoz Noval A, Torres-Costa V, Ceccone G, Manso Silván M: **Visible light assisted organosilane assembly on mesoporous silicon films and particles**. *Materials* 2019, **12**:131.
This study is an interesting example of advanced pore functionalization by using visible light.

67. Herzog N, Kind J, Hess C, Andrieu-Brunsen A: **Surface plasmon & visible light for polymer functionalization of mesopores and manipulation of ionic permselectivity**. *Chem Commun* 2015, **51**:11697-11700.

68. • Rühe J: **And there was light: prospects for the creation of micro- and nanostructures through maskless photolithography**. *ACS Nano* 2017, **11**:8537-8541.
This review provides an overview of nanofabrication processes.

69. Huang X, Kong X-Y, Wen L, Jiang L: **Bioinspired ionic diodes: from unipolar to bipolar**. *Adv Funct Mater* 2018, **28**.

70. Zhang H, Tian Y, Jiang L: **From symmetric to asymmetric design of bio-inspired smart single nanochannels**. *Chem Commun (Camb)* 2013, **49**:10048-10063.

71. Hou X, Zhang H, Jiang L: **Building bio-inspired artificial functional nanochannels: from symmetric to asymmetric modification**. *Angew Chem Int Ed Engl* 2012, **51**:5296-5307.

72. Ermis M, Antmen E, Hasirci V: **Micro and nanofabrication methods to control cell-substrate interactions and cell behavior: a review from the tissue engineering perspective**. *Bioact Mater* 2018, **3**:355-369.

73. Zhou H, Guo Z: **Superwetting Janus membranes: focusing on unidirectional transport behaviors and multiple applications**. *J Mater Chem A* 2019, **7**:12921-12950.

74. •• Wang Z, Yang X, Cheng Z, Liu Y, Shao L, Jiang L: **Simply realizing "water diode" Janus membranes for multifunctional smart applications**. *Mater Horiz* 2017, **4**:701-708.
This study represents the first prominent example of Janus membranes, which allow pH-switchable side-selective oil-water separation.

75. • Sui X, Zhang Z, Li C, Gao L, Zhao Y, Yang L, Wen L, Jiang L: **Engineered nanochannel membranes with diode-like behavior for energy conversion over a wide pH range**. *ACS Appl Mater Interfaces* 2019, **11**:23815-23821.
This study demonstrates the applicability of local and hierarchical nanoporous material design for energy conversion.

76. Cheng H, Zhou Y, Feng Y, Geng W, Liu Q, Guo W, Jiang L: **Electrokinetic energy conversion in self-assembled 2D nanofluidic channels with Janus nanobuilding blocks**. *Adv Mater* 2017, **29**.

77. • Yang J, Li H-N, Chen Z-X, He A, Zhong Q-Z, Xu Z-K: **Janus membranes with controllable asymmetric configurations for highly efficient separation of oil-in-water emulsions**. *J Mater Chem A* 2019, **7**:7907-7917.
In this study novel demulsification-type Janus membranes with controllable asymmetric configurations lead to high separation efficiency.

78. •• Zhou S, Xiong Z, Liu F, Lin H, Wang J, Li T, Han Q, Fang Q: **Novel Janus membrane with unprecedented osmosis transport performance**. *J Mater Chem A* 2019, **7**:632-638.
This study represents a novel Janus membrane with unprecedented osmotic water permeability and nearly complete salt rejection through asymmetrical porous structure and wettability design.

79. Schmidt S, Alberti S, Vana P, Soler-Illia G, Azzaroni O: **Thermosensitive cation-selective mesochannels: PNIPAM-capped mesoporous thin films as bioinspired interfacial architectures with concerted functions**. *Chemistry* 2017, **23**:14500-14506.

80. •• Tom JC, Appel C, Andrieu-Brunsen A: **Fabrication and in situ functionalisation of mesoporous silica films by the physical entrapment of functional and responsive block copolymer structuring agents**. *Soft Matter* 2019, **15**:8077-8083.
This study presents an innovative and simple design of multilayered porous systems with different stimuli-responsive functions via *in situ* functionalization.

81. Bathfield M, Reboul J, Cacciaguerra T, Lacroix-Desmazes P, Gérardin C: **Thermosensitive and drug-loaded ordered mesoporous silica: a direct and effective synthesis using PEO-b-PNIPAM block copolymers**. *Chem Mater* 2016, **28**:3374-3384.

82. • Nau M, Herzog N, Schmidt J, Meckel T, Andrieu-Brunsen A, Biesalski M: **Janus-type hybrid paper membranes**. *Adv Mater Interfaces* 2019, **6**.
In this study, the combination of nanopores and their distribution within hierarchical materials realized novel side-selective permeation properties.

83. •• Laskowski Ł, Laskowska M, Dulski M, Zubko M, Jelonkiewicz J, Perzanowski M, Vila N, Walcarius A: **Multi-step functionalization procedure for fabrication of vertically aligned mesoporous silica thin films with metal-containing molecules localized at the pores bottom**. *Microporous Mesoporous Mater* 2019, **274**:356-362.
This study belongs to the first examples demonstrating local placement of functional units into nanopores which is an essential requirement for complex system design and transport control therein.

84. Dostert KH, Alvarez M, Koynov K, del Campo A, Butt HJ, Kreiter M: **Near field guided chemical nanopatterning**. *Langmuir* 2012, **28**:3699-3703.

85. Álvarez M, Best A, Unger A, Alonso JM, del Campo A, Schmelzeisen M, Koynov K, Kreiter M: **Near-field lithography by two-photon induced photocleavage of organic monolayers**. *Adv Funct Mater* 2010, **20**:4265-4272.

86. Deeb C, Ecoffet C, Bachelot R, Plain J, Bouhelier A, Soppera O: **Plasmon-based free-radical photopolymerization: effect of**

diffusion on nanolithography processes. *J Am Chem Soc* 2011, **133**:10535-10542.

87. Herzog N, Kind J, Hess C, Andrieu-Brunsen A: **Surface plasmon & visible light for polymer functionalization of mesopores and manipulation of ionic permselectivity**. *Chem Commun (Camb)* 2015, **51**:11697-11700.

88. Nguyen M, Lamouri A, Salameh C, Levi G, Grand J, Boubekeur-Lecaque L, Mangeney C, Felidj N: **Plasmon-mediated chemical surface functionalization at the nanoscale**. *Nanoscale* 2016, **8**:8633-8640.

89. •• Tijunelyte I, Kherbouche I, Gam-Derouich S, Nguyen M, Lidgi-Guigui N, de la Chapelle ML, Lamouri A, Lévi G, Aubard J, Chevillot-Biraud A *et al.*: **Multi-functionalization of lithographically designed gold nanodisks by plasmon-mediated reduction of aryl diazonium salts**. *Nanoscale Horiz* 2018, **3**:53-57.
This study realized precise local multifunctionalization of gold nanodisks using near-field methods.

90. •• Goerlitzer ESA, Speichermann LE, Mirza TA, Mohammadi R, Vogel N: **Addressing the plasmonic hotspot region by site-specific functionalization of nanostructures**. *Nanoscale Adv* 2020.
In this study further advancements regarding precise, nanoscale arrangement of functionalization of crescent-shaped nanostructures are presented.

Da im Rahmen dieser Arbeit ausschließlich mit Iniferter-initiierten Polymerisationen gearbeitet wurde, wird im Weiteren für Details zur ATRP auf zwei sehr ausführliche Artikel vom Erfinder der ATRP *Krzysztof Matyjaszewski*[106-107] und für die RAFT Polymerisation auf eine Publikation aus der Gruppe um *Michael Whittaker*[108] verwiesen. Für diese Arbeit wurde ein Iniferter-basiertes Polymerisationssystem ausgewählt, da es mit möglichst wenigen Komponenten auskommt und Licht als Initiationsstimulus auch ohne Probleme in sehr kleine Poren eindiffundieren kann.

Iniferter-initiierte Polymerisation in Mesoporen

Photoiniferter basierte Polymerisationen wurden bereits vor über 30 Jahren von *Otsu et al.* beschrieben.[109] Mit Hilfe des Iniferters Thiuramdisulfid wurde in diesen ersten Arbeiten Styrol polymerisiert. Wie auch für andere lichtkontrollierte Polymerisationen bekannt, lässt sich die Polymermenge bei Photoiniferter initiierten Polymerisationen sehr gut zeitlich und räumlich kontrollieren.[25, 110] Durch die präzise Steuerung der Polymerisation hat sich ein Iniferter basiertes Polymerisationssystem besonders angeboten, um die Forschungsfrage der einstellbaren Porenfüllung und Kettenarchitektur in Mesoporen zu adressieren. Im folgenden Abschnitt wird daher der in dieser Arbeit verwendete Photoiniferter (N,N(diethylamino)dithiocarbamoyl-benzyl(trimethoxy)silan (SBDC) sowie der Polymerisationsmechanismus vorgestellt.

Der Zerfall des Iniferters Benzylditethyldithiocarbamat (BDC) unter UV Licht ist beispielhaft in Schema 2-5 dargestellt.

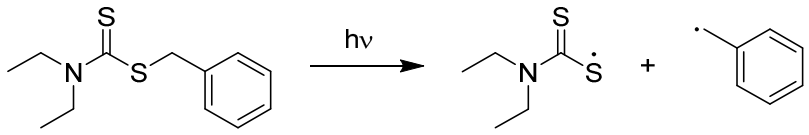

Schema 2-5: Photodissoziation des Iniferters BDC.

Das entstehende Benzylradikal, welches als Kettenstarter dient, weist dabei eine höhere Reaktivität auf als das Thionylradikal. Das Thionylradikal ist das Transferreagenz und kann immer wieder an ein reaktives Kettenende kuppeln und so die schlafende Spezies herstellen. Durch eine Silanankergruppe wurde der BDC Iniferter im Jahr 2000 von *de Boer et al.* so weiterentwickelt, dass er auf Oberflächen kovalent angebunden werden kann (Schema 2-6).[111]

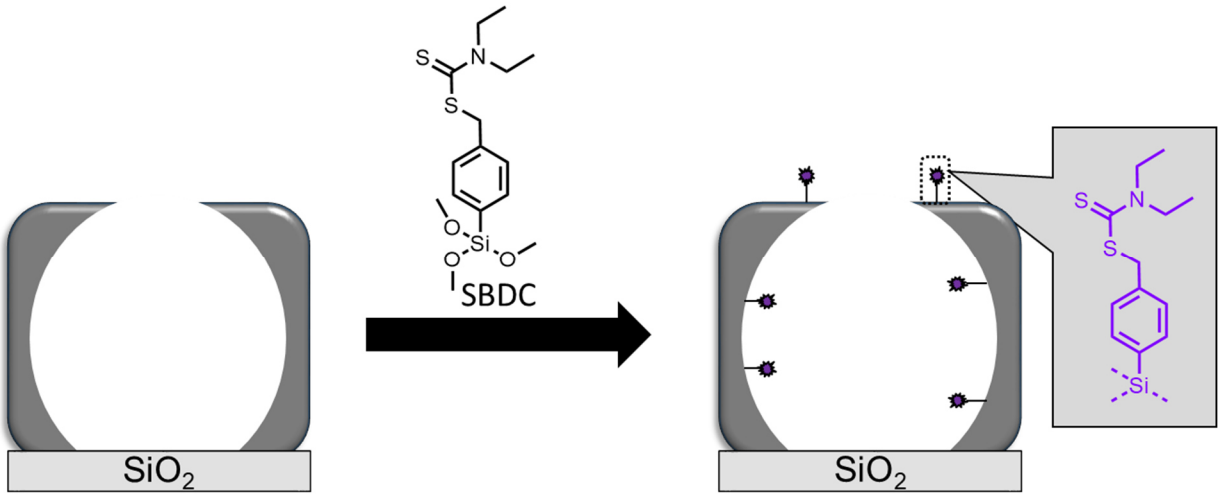

Schema 2-6: Molekularstruktur des Photoiniferters SBDC und schematische Anbindung von SBDC an eine Silicananopore.

Der Polymerisationsmechanismus ist im nachfolgenden Schema 2-7 am Beispiel des an einer Oberfläche verankerten (SBDC) dargestellt.

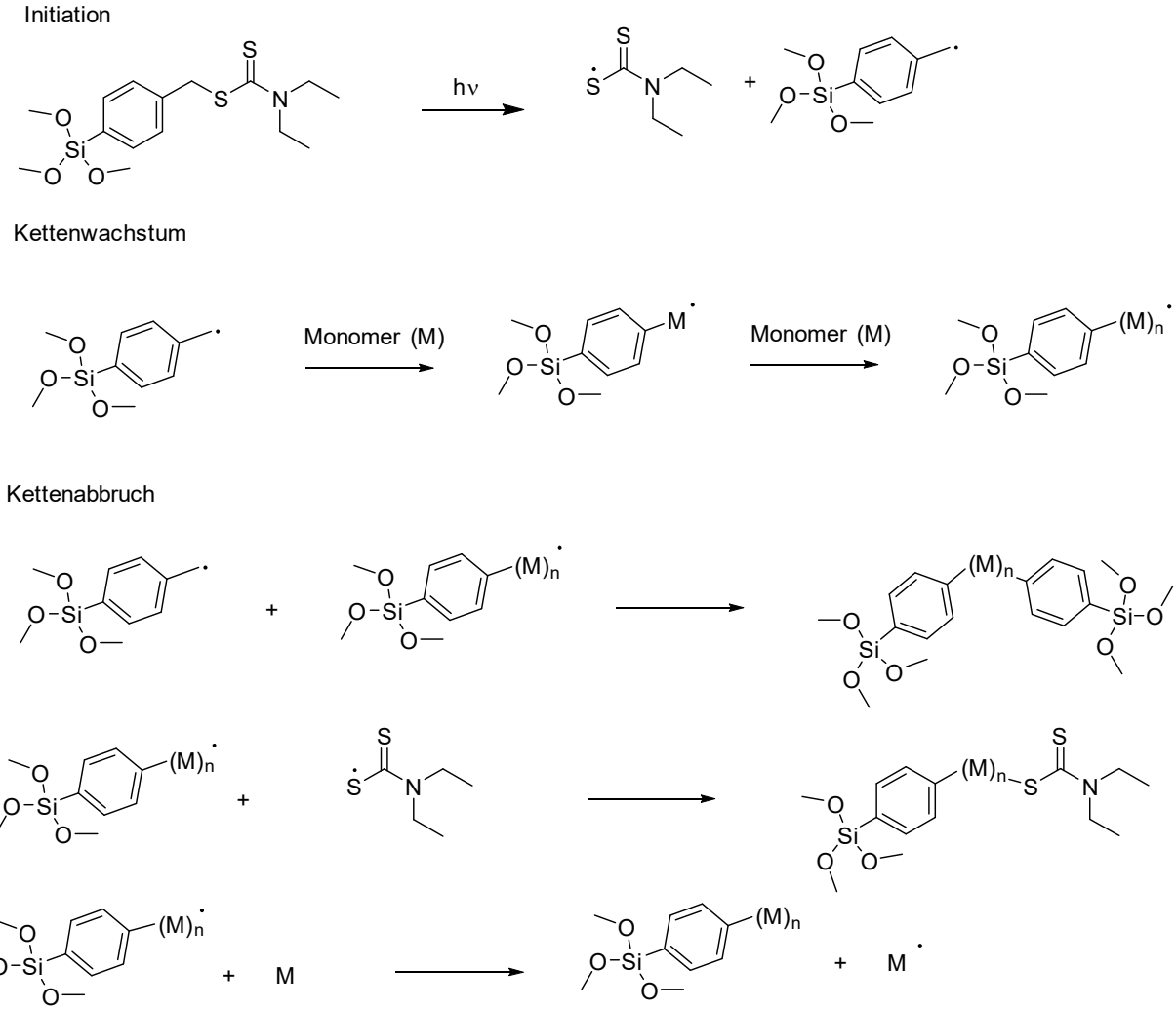

Schema 2-7: Schematische Darstellung der Iniferter-initiierten Polymerisation mit SBDC als Iniferter.

Die Polymerisation wird durch die Bestrahlung mit Licht (365 nm) initiiert, wodurch sich das Dithiocarbamat unter Radikalbildung vom Benzylrest abspaltet. Da das Benzylradikal nicht stabilisiert ist, ist es sehr reaktiv, kann vorhandene Monomere angreifen und startet damit das Kettenwachstum von der Oberfläche aus. Ein Vorteil der oberflächeninitiierten Polymerisation auf planaren Oberflächen oder auf Nanopartikeln verglichen mit Lösungspolymerisationen ist, dass ein Kettenabbruch durch Rekombination von zwei Ketten unwahrscheinlicher ist und nur mit benachbarten Ketten passieren könnte. Sobald die Bestrahlung mit Licht unterbrochen wird, spalten sich Ketten, an die das Dithiocarbamatradikal angebunden hat, nicht erneut und die Polymerisation endet. Die daraus resultierende, schlafende Spezies kann in einer weiteren Reaktion reaktiviert werden, wodurch die Synthese von Block-*co*-polymeren möglich ist.

2.4. Responsive/Schaltbare mesoporöse Silicamaterialien

Die Funktionalisierung von Silicamaterialien führt in der Regel zu einer statischen Veränderung der physikalischen und chemischen Eigenschaften. Beispielsweise lassen sich hydrophile Silicafilme mit Perfluorosilanen zu stark hydrophoben Oberflächen umfunktionieren, indem die Benetzungseigenschaften von der organischen Funktion dominiert werden.[112] Bei Anwendungen, wie der Wirkstofffreisetzung oder in der Sensorik, reichen solche statischen Funktionalitäten allerdings nicht aus. Es wird von dem hergestellten und verwendeten Material erwartet, dass dieses genau zum richtigen Zeitpunkt den eingelagerten Wirkstoff freisetzt oder die Gegenwart bzw. Abwesenheit eines Zielmoleküls anzeigt. Um diese Anforderungen zu erfüllen hat sich das Forschungsfeld der responsiven Materialien (sogenannt: *Smart-Materials*) entwickelt. Beispiele für stimuli responsive Silicamaterialien wurden in den letzten 15 Jahren viele berichtet.[11, 13-20]

An dieser Stelle seien besonders die zahlreichen hybriden Materialien erwähnt, die auf externe Stimuli wie pH-Wert, Licht oder Konzentrationsänderungen reagieren.[6, 62] Beispielhaft seien hier hybride Silicamaterialien erwähnt, die als molekulare Sensoren verwendet werden können. Hierzu werden etwa Farbstoffe in das Silicagerüst integriert, welche durch Veränderungen ihres Absorptions-/Emissionsverhaltens Metallionen detektieren können.[31-36] Ein anderes Feld sind mesoporöse Silicananopartikel, die für die Wirkstofffreisetzung verwendet werden. Ein Ansatz dabei ist, die Silicapartikel mit einem Polymerfilm, der kovalent angebunden ist, zu umschließen. Durch ein Stimuli, wie z.B. eine Veränderung im pH-Wert, kann diese Polymerhülle aufquellen und der Wirkstoff freigesetzt werden.[39] pH-responsive Wirkstofffreisetzung ist daher von großem Interesse für die Tumorbehandlung, da der pH-Wert in Krebszellen (pH 4-6) saurer als in gesunden Zellen (pH 7.4) ist.[113] Dieser pH-Unterschied ermöglicht es responsiven MSM, den Wirkstoff gezielt in Krebszellen freizusetzen.[11, 40] Schema 2-3 zeigt das Prinzip von geschaltetem Transport in funktionalisierten Silicamesoporen.

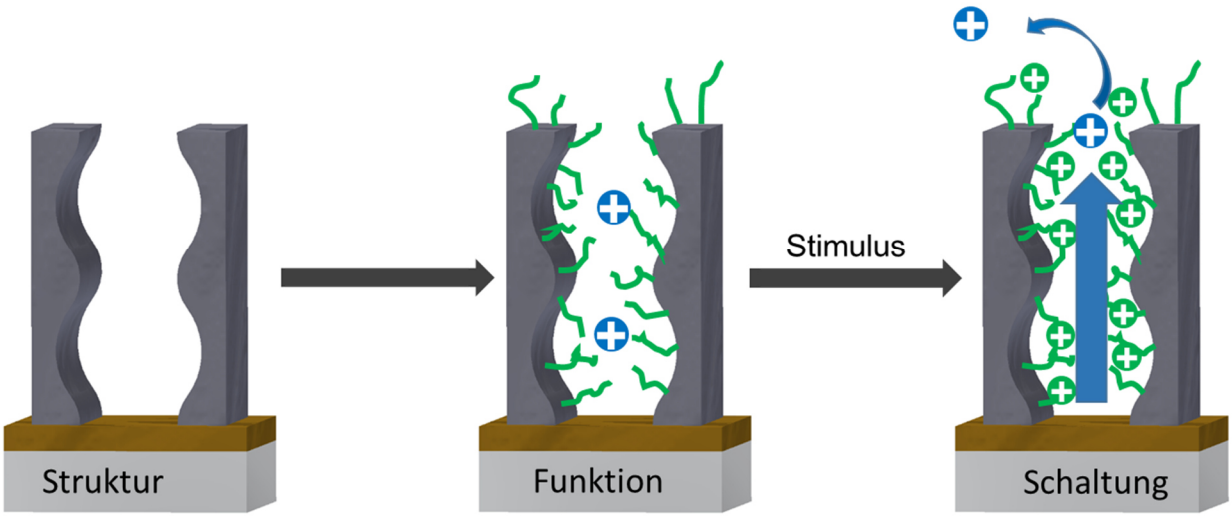

Schema 2-3: Schematische einer unfunktionalisierten Silicananopore (links), welche mit einem responsiven Polymer funktionalisiert wird (mitte) um responsiv den Transport von Ionen zu steuern (rechts).

Polymermodifikationen in Mesoporen zur Transportsteuerung

In unterschiedlichen Anwendungsgebieten, wie etwa der Wasseraufbereitung oder der Medikamentenfreisetzung, spielen Polymerfunktionalisierungen von mesoporösem Silica eine entscheidende Rolle, um die gewünschten Molekül- bzw. Ionentransporteigenschaften zu erreichen. Die bisher erreichte Transportkontrolle von funktionalisierten mesoporösen Silicamaterialien, zum Beispiel inspiriert von Ionenkanälen aus der Natur, ist jedoch noch recht weit vom Vorbild entfernt, da man sich im Gegensatz zu z.B. natürlichen Ionenkanälen zwischen Selektivität und Durchsatz entscheiden muss. Um den Transport zu steuern, werden externe Stimuli wie Licht, Temperatur, elektrische Spannung, Ionen oder Moleküle verwendet. Neben dem Übersichtsartikel von *Zoppe et al.*[25] hat es aus der Gruppe um *Lei Jiang* in den letzten Jahren ausführliche Übersichtsartikel zu steuerbaren, polymerfunktionalisierten Nanoporen und Nanokanälen gegeben.[15, 114-116] Aus diesem Grund, und weil der Fokus dieser Arbeit auf den pH-Wert gelegt ist, befasst sich das folgende Kapitel vor allem mit der Entwicklung von pH-schaltbaren Polymeren in Silicamesoporen.

pH-responsive Polymere in mesoporösen Materialien sind im Vergleich zu anderen stimuliresponsiven Polymeren besonders gut erforscht. Eine Vielzahl von pH-schaltbaren Monomeren wurden bisher erfolgreich genutzt, um Mesoporen zu funktionalisieren. pH-responsive Monomere können an der Art und Anzahl der möglichen Ladung pro Molekül unterschieden werden. An Monomeren, die eine einzelne Ladung pro Monomereinheit tragen können, wurden beispielsweise Poly(vinylpyridin) (PVP), Poly(2-(Dimethylamino)ethylmethacrylat) (PDMAEMA) und Poly(acrylsäure) (PAA) polymerisiert.[117-120] Zusätzlich konnten mehrfach aufladbare Polymere, wie (2-(methacryloyloxy)ethylphosphat) (MEP) oder zwitterionische Monomere wie Carboxybetainmethacrylat (CBMA), in mesoporösen Materialien polymerisiert werden.[4, 21, 28-29, 120] Die so funktionalisierten Mesoporen wurden zusätzlich hinsichtlich ihrer pH-abhängigen Transportschaltung untersucht, wobei in allen Fällen das Transportverhalten in Abhängigkeit vom Lösungs-pH-Wert gesteuert werden konnte.[117-118, 121] Diese experimentellen Studien untersuchen alle nur jeweils einen Polymertyp, teilweise mit variierender Polymermenge. Dass die Steuerung von Transport in funktionalisierten Nanoporen deutlich komplexer aufgebaut werden kann, wurde kürzlich in einer theoretischen Arbeit von *Szleifer* und Mitarbeitern gezeigt.[14] Die Ergebnisse zeigen, dass das präzise Design von Monomersequenzen in Polymerketten ein entscheidender Schritt zum Erhalt naturnaher, schaltbarer Mesoporen mit präziserer Transportkontrolle sein kann.[14] Diese Erkenntnis führte dazu, dass ein Hauptaugenmerk auf möglichst komplexe Porendesigns gelegt wurde. Komplex bedeutet in diesem Zusammenhang die Inkorporation von einer oder mehrerer funktionellen Gruppen in eine Mesopore, wodurch das resultierende Material auf mehr als nur einen Stimulus reagieren kann (Multistimuliresponsiv). Als Beispiel für synthetisch hergestellte, multifunktionale Materialien kann die von *Hegazy et al.* veröffentlichte Studie genannt werden. In dieser Studie wurden die mesoporösen Silicapartikel sowohl mit dem thermo responsiven Polymer Poly(2-nitrobenzyl acrylat) als auch mit

Disulfidbrücken modifiziert, wodurch es gelungen ist, eine Wirkstofffreisetzungsplattform zu erzeugen, die auf zwei Stimuli reagieren kann.[122] Ein anderer Ansatz ist es, komplexe Polymerarchitekturen in die Mesoporen zu integrieren, die auf mehrere Stimuli oder pH-Werte reagieren können. Ein Beispiel hierfür ist das PMEP, welches zum Einen zwei pk_s-Werte aufweist und zum Anderen zweiwertige Ionen wie Kalzium chelatisieren kann.[4, 28] Neben der Verwendung von dual stimuli responsiven Homopolymeren wie dem PMEP, welches auf die stoffspezifische Stimuluskombination beschränkt ist, ist es unter anderem im Rahmen dieser Arbeit gelungen, auch multistimuliresponsive Copolymere in nanoskaligen Poren zu synthetisieren. Die in dieser Arbeit mit PDMAEMA-co-PMEP funktionalisierten Silicamesoporen sind Temperatur-, pH- und ionenresponsiv.[27] In einem weiteren Beispiel wurde durch die Immobilisierung von Poly[2-(dimethylamino)ethyl methacrylat]-*co*-[4-vinyl phenylboronsäure] (P(DMAEMA-*co*-VPBA)) in einem konischen Nanokanal aus Glas eine Diode erzeugt, welche auf Temperatur, den pH-Wert und Zucker reagieren kann (Tristimuliresponsiv).[123] Da der Aufbau solcher Polymerstrukturen in Nanoporen synthetisch anspruchsvoll und neu ist, wurden in älteren Studien andere Ansätze verfolgt. Eine Möglichkeit für die Herstellung von multistimuliresponsiven Hybridmaterialien besteht darin asymmetrische Materialien zu synthetisieren. Bei assymetrisch funktionalisierten Materialien, werden einfach stimuliresponsive Gruppen räumlich voneinander getrennt auf ein Material angebracht. Die Kombination von PAA und PVP auf gegenüberliegenden Seiten eines Nanokanals wurde von *Zhang et al.*[119] genutzt um eine Ionenpumpe herzustellen. Eine andere Möglichkeit stellt die Verwendung von *Janus*-Membranen dar, die eine seitenselektive oder steuerbare Öl-Wasser Separation ermöglichen. Die ist vor allem im Hinblick auf komplexe Zusammenspiele von Faktoren wie Benetzung und Ionenselektivität interessant.[13, 114-115, 124-126]

Die hier genannten Beispiele zeigen das breite Anwendungspotential von multistimuliresponsiven mesoporösen Silicamaterialien auf. Die bisher erreichte Transportkontrolle und Selektivität von synthetisch hergestellten Nanoporen und –kanälen ist jedoch noch recht weit von den aus der Natur bekannten Vorbildern entfernt. Die Entwicklung der vergangenen Jahre hin zu multistimuli responsiven Materialien die Leistungsfähigkeit und Möglichkeiten erheblich verbessert. Durch weitere synthetische Bemühungen sollte es in den kommenden Jahren möglich sein die Lücke zwischen synthetischen Materialien und ihren natürlichen Vorbildern immer weiter zu schließen.

2.5. pH-Detektion auf der Nanoskala

Aufgrund der großen räumlichen Begrenzung in nanoskaligen Poren können Effekte, wie Oberflächenladungen, die Materialeigenschaften (Transportverhalten, Benetzung) stärker beeinflussen als auf planaren Oberflächen. Die durch die Nanoskala induzierten Veränderungen im Materialverhalten werden gemeinhin als *Confinement* Effekte bezeichnet und beschreiben die Verschiebung von chemischen Gleichgewichten in Nanoporen. Ein wichtiges Gleichgewicht, das stark durch das *Confinement* beeinflusst wird, ist der pH-Wert. Wie bereits in Kapitel 1 (Einleitung) erläutert spielt der pH-Wert in unterschiedlichen Anwendungen von stimuli responsiven Nanomaterialien, wie etwa der Wirkstofffreisetzung aus Nanopartikeln oder der Transportsteuerung durch Membrane, eine entscheidende Rolle. Im Laufe der vergangenen Jahre wurden immer wieder messbare Unterschiede zwischen $pH_{Lösung}$ und $pH_{Confinement}$ beschrieben.[44, 127-129] Bisherige experimentelle Untersuchungen im Zusammenhang des pH-Wertes im *Nanoconfinement* sind unter anderem im Zusammenhang mit polymerfunktionalisierten Nanokanälen gemacht worden. Die Abschätzungen zu pH-Wert-, beziehungsweise pK_s-Wert-Verschiebungen beziehen sich allerdings auf indirekte elektrochemische Messungen, da vor allem das Transportverhalten der funktionalisierten Nanokanäle im Vordergrund der durchgeführten Studien stand.[21, 130] Neben den experimentellen Studien konnte die Gruppe um *Szleifer*[127] in theoretischen Studien zeigen, dass sich durch Funktionalisieren eines mesoporösen Silicafilms mit Polyacrylsäurebürsten der pH-Wert in den funktionalisierten Mesoporen um bis zu zwei Einheiten von dem desselben Polymers in Bulk-Lösung unterscheidet. Dieser pH-Wert in Mesoporen wird häufig als apparenter pH-Wert bezeichnet. Mit Verschiebung des pH-Wertes gehen auch Veränderungen der pK_s-Werte, immer im Vergleich zu den korrespondierenden pK_s-Werten in Lösung, von Molekülen in Mesoporen einher. Die Verschiebung von pK_s-Werten ist auf elektrostatische Abstoßungen zwischen z.B. Polymerketten und deren Ladungsregulation zurückzuführen.[24, 127] Den Zusammenhang zwischen pK_s- und pH-Werten kann und muss man sich zu Nutze machen, um pH-Werte auf der Nanoskala zu messen. Aufgrund der kleinen Räume lassen sich keine handelsüblichen pH-Elektroden verwenden. Neben dieser praktischen Einschränkung kommt erschwerend dazu, dass der pH-Wert definitionsgemäß eine Bulkeigenschaft darstellt, definiert als der negative dekadische Logarithmus der Konzentration (bzw. der nicht experimentell messbaren Aktivität) von H^+-Ionen in einer wässrigen Lösung.

$$pH = -\lg a(H^+) = -\lg[H^+]$$

Die Angabe von Konzentrationen in der Einheit mol/l muss in Nanoporen mit Volumina von 10 – 100 nm^3 und Teilchenzahlen von < 100 Molekülen pro Pore vorsichtig verwendet werden, da diese Zahlen im Vergleich zu der Größenordnung von $6{,}02214076 \times 10^{23}$ Teilchen pro Liter eine extreme Extrapolation darstellen. Zusätzlich führt der starke Einfluss der Nanoporenoberfläche zur

Ausbildung einer *Stern*-Schicht und dadurch zu einer inhomogenen Ladungsverteilungen von H^+-Ionen innerhalb der Nanopore.[131-132] Viel einfacher und sinnvoller erscheint es daher, die H^+-Ionen abhängige, stoffspezifische Größe des pK_s-Wertes zu verwenden, um Vergleiche zwischen Bulklösungen und Nanoporen zu ziehen.

Eine Stoffgruppe, die sich für die experimentelle Bestimmung von pK_s-Werten im *Confinement* besonders anbietet, sind pH-responsive Farbstoffe. Farbstoffe bieten den Vorteil, dass sie sehr gut erforscht sind, es einige bioverträgliche Farbstoffe gibt, sie in kleinsten Konzentrationen von nM-µM detektierbar und Messmethoden, wie die Fluoreszenz- oder UV-Vis-Spektroskopie, schnell, exakt und weit verbreitet sind.[30] Bisher gibt es nur wenige Studien, die sich unter Verwendung von pH-responsiven Farbstoffen wie dem carboxy-SNARF-1 (Seminaphtharhodafluor) oder 8-aminopyrene-1,3,6-trisulfonate (APTS) direkt den pH-Wert in Nanokanälen angeschaut haben.[23, 129] Zudem waren die Farbstoffe in diesen Studien nicht kovalent an die Oberflächen der Nanokanäle angebunden. Durch die *Stern*-Schicht und die damit einhergehende Abstoßung der Farbstoffe von der Oberfläche hin zur Kanalmitte, wo die pH-Verschiebung schwächer ist, wurden die bestimmten pH-Verschiebungen in der Studie von *Bottenus et al.* vermutlich unterschätzt.[23] In der Studie von *Yamaguchi et al.* wurde dieses Problem durch attraktive elektrostatische Wechselwirkung zwischen Farbstoff und Porenwand reduziert.[129] Durch die Aufladung der Porenwand wird allerdings auch das chemische Verhalten und die Ausbildung der natürlichen Stern-Schicht unterdrückt, wodurch die resultierenden Ergebnisse nicht die pH-Situation in unfuntionalen Silicamesoporen darstellen. Das direkte Ablesen des apparenten pH-Wertes, also dem pH-Wert in Mesoporen durch kovalent in das mesoporöse System angebundene molekulare Sensoren, war vor dieser Arbeit nicht experimentell untersucht worden, obwohl die pH-Detektion in Mesoporen in den letzten Jahren immer mehr an Bedeutung gewonnen hat.[44-46] Die Bestimmung und Vorhersage des pH-Wertes in Mesoporen stellt eine Herausforderung dar und kann zukünftig dazu eingesetzt werden, um Mechanismen, wie etwa der Arzneimittelfreisetzung- oder generell Transportmechanismen in Nanomaterialien, besser zu verstehen.[14] Die hohe Sensitivität erlaubt in Kombination mit aufwendigen Messaufbauten sogar die Detektion von einzelnen Molekülen und könnte damit potentiell radiale Verteilungen, die bisher exp. nicht zugänglich sind, messbar machen.

Fluoreszenz

Fluoreszenz beschreibt die spontane Emission von Licht infolge der elektronischen Anregung eines Fluorophors in ein höheres Energieniveau durch Absorption von Photonen. In der folgenden Abbildung 2-5 sind die zum Verständnis von Fluoreszenz wichtigen Übergänge dargestellt

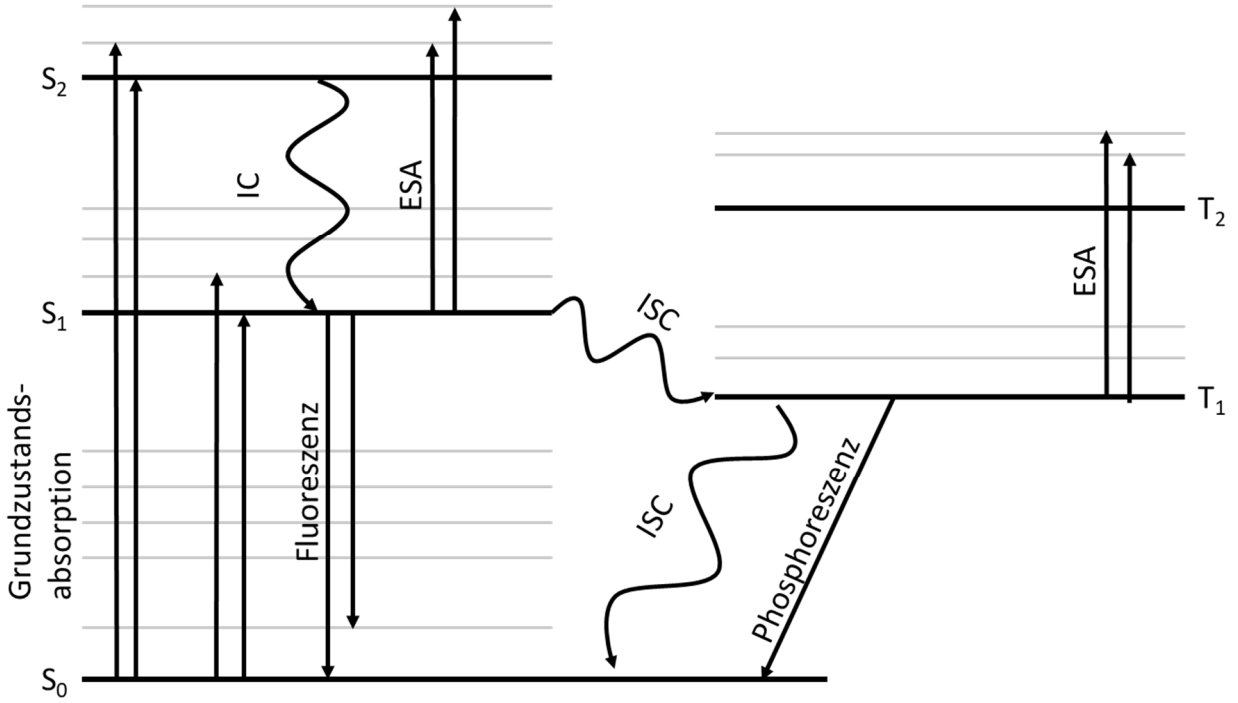

Abbildung 2-5: Jablonski-Diagramm zu Erklärung der Fluoreszenz. IC *Internal conversion*, ESA *excited state aborption*, ISC *intersystem crossing*.

Durch die Anregungsenergie werden Elektronen aus dem elektronischen Grundzustand in einen schwingungsangeregten Zustand eines angeregten elektronischen Zustandes überführt. Erfolgt ein strahlungsloser Übergang (*vibrational cooling*) eines Elektrons von einem angeregten Zustand in den Schwingungsgrundzustand des elektronisch angeregten Zustandes wieder in den elektronischen Grundzustand zurück, können verschiedene Prozesse ablaufen: Bei der *Internal conversion* wird der strahlungslose thermische Übergang des Elektrons von einem angeregten Singulettzustand in den darunterliegenden angeregten vibronischen Zustand beschrieben. Beim Übergang des ersten elektronischen angeregten Zustands in den elektronischen Grundzustand wird Energie frei, die aufgrund des strahlungslosen Übergangs der Elektronen in den S_1 Zustand (*Internal conversion*) kleiner ist als diejenige, die bei der Absorption durch das eingestrahlte Licht aufgenommen wurde. Diese Reststrahlung wird emittiert, sodass die Fluoreszenz eines Fluorophors stets rotverschoben zum absorbierten Licht erscheint. Bei allen Übergängen behalten die Elektronen ihren Spinzustand bei.[133-134]

Neben der Fluoreszenz selbst, spielt auch das sogenannte Quenching eine wichtige Rolle für diese Anwendungen von Fluoreszenzfarbstoffen. Quenching bezeichnet einen Prozess der Fluoreszenzauslöschung. Dabei wird strahlungslos Energie von einem angeregten Fluorophor auf ein zweites anwesendes Molekül („Quencher“) übertragen. Sauerstoffmoleküle sind die bekanntesten Fluoreszenzlöscher. Durch Sauerstoff kann die Fluoreszenz fast aller bereits bekannten Fluorophore über Kollisionen oder radikalisch gequencht werden. Ein weiteres Beispiel für Fluoreszenzauslöschung in Gegenwart eines “Quencher“-Moleküls, ist die Wechselwirkung in Form von Komplexbildung (Abbildung 2-6). Der Komplex aus Fluorophor und „Quencher“ zeichnet

sich dann dadurch aus, dass er nicht bzw. sehr schwach fluoresziert und somit die Fluoreszenzintensität insgesamt verringert wird.[135] Die Zugabe von Metallionen wie Kupfer, Cadmium, Quecksilber und Mangan führt dazu, dass Elektronen vom Fluoreszenzfarbstoff dem fluoreszenzlöschenden Molekül übertragen werden und somit die Fluoreszenzintensität geschwächt wird.[135-137] Neben „Quencher"-Molekülen können auch Veränderungen in einem Molekül, die etwa durch protonierung/deprotonierung bei pH-Änderungen induziert werden, herbeiführen. Durch pH- abhängige Fluoreszenzintensität können Flourophore als pH-Detektor eingesetzt werden. Als Beispiel sei hier das der Fluorophor Fluorescein (pK_s ~6.4) genannt. Bei pH-Werten unterhalb von 7 nimmt die Fluoreszenzintensität von Fluorescein stark ab, wodurch pH-Änderungen in einem Bereich von etwa 5-9 detektiert werden können.

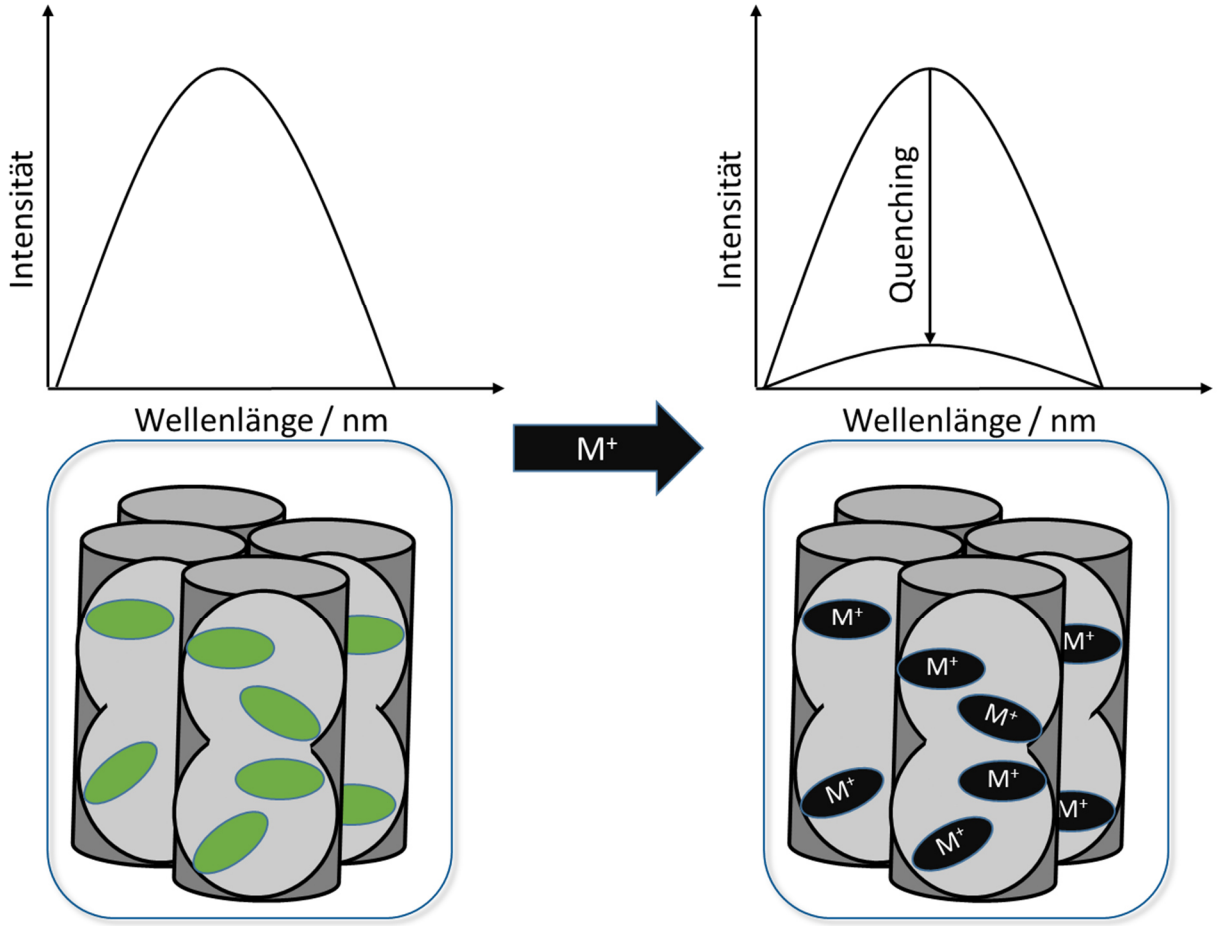

Abbildung 2-6: In dieser Abbildung ist der Mechanismus des *Quenchings* durch Komplexierung schematisch dargestellt. Durch die Komplexierung des Metallions M^+ kommt es zu einer Auslöschung der Fluoreszenz.

Ein großer Vorteil des Fluoreszenzquenchings besteht darin, dass nicht jeder bekannte *Quencher* die Fluoreszenz jedes Fluorophors gleichermaßen verringert. Dies macht *Quenching* z. B. sehr interessant für den selektiven Nachweis von Metallionen in wässrigen Lösungen.[138] Ebenso findet dieses Verfahren in der Sauerstoffsensorik (pO_2-Optrode) Verwendung.[135] Im Gegensatz zum *Quenching* ist die Photobleichung ein irreversibler Prozess. Dabei handelt es sich um einen Prozess,

bei dem die Struktur des Fluorophors aufgrund der Lichteinstrahlung zerstört wird und somit seine Fluoreszenz verliert.[137]

pH-responsive Farbstoffe als molekulare pH-Reporter

Ein sehr großes Anwendungsgebiet von Fluorophoren stellt die pH-Detektion dar,[139-143] vor allem die pH-Detektion in Zellen, z. B. im Kontext der pH-Änderungen von Krebszellen wurde sie in den letzten Jahren ausgiebig untersucht.[144-149] Bisher sind allerdings nur wenige Arbeiten veröffentlicht, die pH-sensitive Fluorophore als pH-Reporter mit nanoskaligen Poren kombiniert haben.[128, 150-151]

Um einen Farbstoff als quantitativen pH-Sensor verwenden zu können, müssen bestimmte Rahmenbedingungen beachtet werden. Da Farbstoffe im pH-Bereich um ihren pK_s-Wert besonders empfindlich auf pH-Änderungen reagieren, aber bei Entfernung vom pK_s-Wert an Empfindlichkeit verlieren, muss der zu untersuchende pH-Bereich vorab bekannt sein und ein kompatibler Farbstoff ausgesucht werden. Zudem lässt sich, wie im Folgenden beschrieben, nicht jeder pH-responsive Farbstoff als pH-Sonde verwenden, der mit nur einer Messung einen definierten Wert ausgibt. Die am weitesten verbreitete Farbstoffmolekülfamilie für pH-abhängige Untersuchungen sind Fluoreszeinderivate.[152] Fluorescein ist pH-responsiv, da die Fluoreszenz im pH-Bereich unterhalb des pK_s von 6.4 stark abnimmt. Dieses Verhalten ermöglicht allerdings keine quantitative pH-Bestimmung, da Fluoreszenz von weiteren äußeren Einflüssen, wie beispielsweise der Temperatur, beeinflusst wird. Quantitative Auswertungen sind somit in der Praxis nicht möglich,[153] da Picosekunden-zeitaufgelöste Messungen notwendig wären.[152]

Fluoreszein bietet trotzdem die Möglichkeit quantitative pH-Bestimmung durchzuführen, da es mit dem Farbstoff Rhodamin B ein sogenanntes Försterresonanzenergiertransfer (FRET)-Paar bildet. Beim FRET findet eine Energieübertragung vom z.B. dem Fluoreszein zu einem Akzeptor-Farbstoff (Rhodamin B) statt. Dies ist möglich, da das Absorptionsspektrum des Rhodamin B mit dem Emissionsspektrum des Fluoreszeins überlappt (Abbildung 2-7).

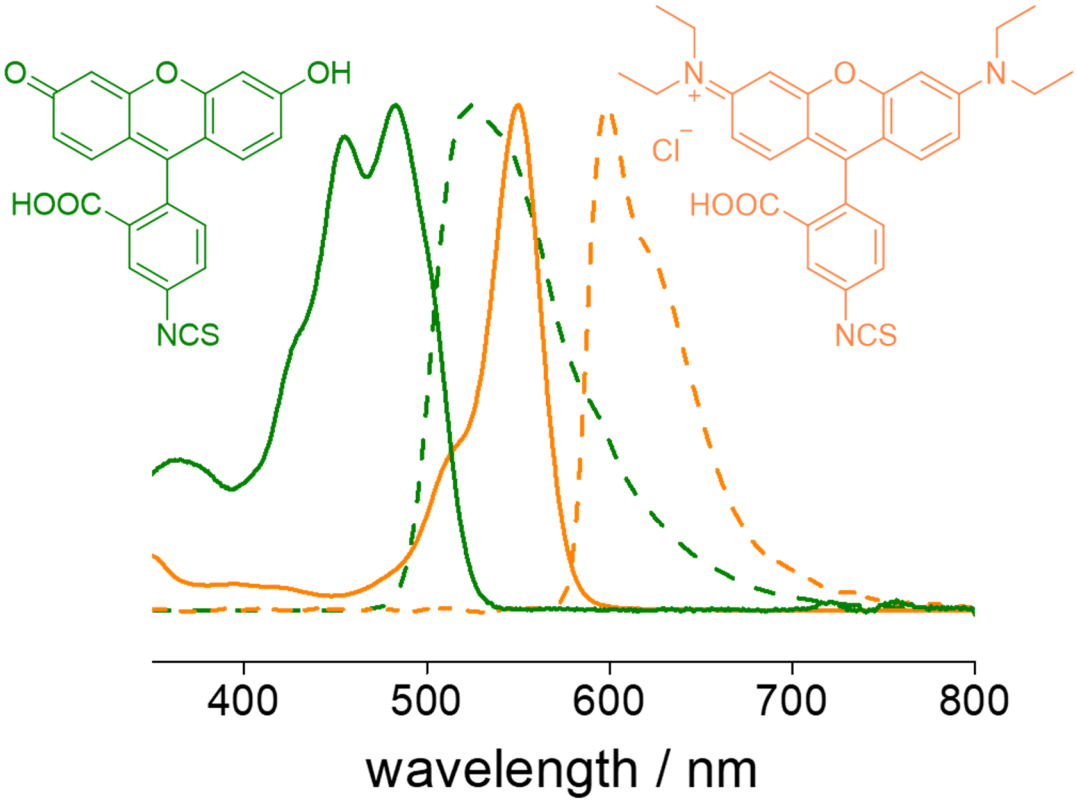

Abbildung 2-7: Molekularsturktur des FRET-Paares FITC (grün) und RITC (rot) und die korrespondierenden Absorptions- (durchgezogene Linien) und Emissionsspektren (gestrichelte Linien) (Publiziert von Elsevier – © 2019 – mit Genehmigung verwendet; DOI: 10.1016/j.micromeso.2019.03.009).

Die Energieübertragung ist dabei abhängig vom Abstand der beiden Fluoreszenzfarbstoffe. Der Energieübertrag erfolgt über Dipol-Wechselwirkungen und ist nur dann erlaubt, wenn der Spin beim Übergang zum Akzeptormolekül erhalten bleibt.[134, 137, 154-155] Die Kombination von silicabasierten Nanomaterialien, wie Partikeln und Dünnschichtfilmen mit FRET-Farbstoffpaaren, wurde bereits erfolgreich eingesetzt, um den pH-Wert der Umgebung auszulesen.[45, 156]

Beispielsweise wurden von WIDMER *et. al.*[140] farbstofffunktionalisierte mesoporöse Silicapartikel hergestellt. Hierzu wurde das FRET-Farbstoffpaar Fluorescein und Rhodamin B durch einen Cokondensationsprozess in die Silicamatrix integriert. Dieser Prozess hat jedoch den intrinsischen Nachteil, dass Farbstoffmoleküle in das Silicagerüst eingebettet werden, wie in Kapitel 2.2 diskutiert. Die so eingelagerten Moleküle sind chemisch für eine Messlösung nicht zugänglich und verfälschen somit die Messungen.[140] Ein anderer Ansatz wurde von GAO *et. al.*[141] verfolgt. In dieser Studie wurden Kern-Schale-Silicananopartikel verwendet, die Fluorescein im Silicanetzwerk beinhaltet haben. Neben Fluorescein wurde das pH-unempfindliche Fluorophor Phenosafranin als Referenzsignal verwendet. Die so funktionalisierten Kern-Schale-Silica-Nanopartikel haben sich als biokompatibel und sehr stabil herausgestellt, wodurch sie für Anwendungsgebiete wie der Bioanalytik relevant sind. Einflüsse auf den pH-Wert durch *Nanoconfinement* wurden in dieser Studie noch nicht berücksichtigt. Untersuchungen von *Confinement* Effekten durch FRET-Farbstoffpaare sind bisher wenige bekannt. Eine von unserer Gruppe veröffentliche Studie hat

zudem gezeigt, dass Vergleiche zwischen Confinement und freier Lösung durch den Einsatz von FRET-Farbstoffpaaren nur schwer möglich sind, da FRET in Lösung mit unkontrolliertem Farbstoffabstand und -orientierung erfolgt und keine Vergleichskalibrationskurve erstellt werden kann.[44]

Eine Alternative zur FRET-basierten pH-Detektion stellt die Verwendung von ratiometrischen Farbstoffen dar.[46, 142] Ratiometrische Farbstoffe besitzen jeweils für die protonierte und deprotonierte Form getrennte Absorptions-/Emissionswellenlängen. Über das Intensitätsverhältnis der unterschiedlichen Maxima kann der korrespondierende pH-Wert bestimmt werden, sobald die Absorptionsmaximaverhältnisse bei bekannten pH-Werten bestimmt wurden.[144] Die Kalibrierung erfolgt also intern. Ratiometrische Farbstoffe besitzen einen isosbestischen Punkt, in welchem keine Änderung der Absorbanz mit der Reaktionszeit auftritt.[152, 157] Der isosbestische Punkt beschreibt somit den Schnittpunkt der unterschiedlichen Absorptionsspektren, Unabhängigkeit von der Konzentration, Änderungen in der Anregung oder Verblassen von Fluoreszenz.

$$pH = \frac{[Dye - H+]}{[Dye]}$$

Eine ratiometrische pH-Detektion ist unempfindlich gegenüber Faktoren wie Konzentrationsschwankungen,[157] Quellintensität und Photobleichung.[139]

Von den ratiometrischen Farbstoffen ist SNARF der am intensivsten untersuchte Farbstoff, der aufgrund seines pK_s-Wertes von etwa 7.5 für intrazelluläre Anwendungen interessant ist .[144, 158-160] SNARF-1 wurde zudem bereits als Fluoreszenzsensor in Nanoporen zur Bestimmung des pH-Wertes verwendet.[161] In der Studie von *Mori et al.* wurden Nanoporen durch Eintauchen in eine Farbstofflösung mit SNARF-1 beschichtet und nachfolgend mittels konfokaler Mikroskopie auf Fluoreszenz untersucht. Es konnte gezeigt werden, dass eine Verschiebung des apparenten pH-Wertes von bis zu 0.7 pH-Einheiten, verglichen mit dem pH-Wert der Lösung, detektiert werden konnte. Es wurden jedoch keine Untersuchungen zur pH-Schaltung in der Nanopore durchgeführt und der Farbstoff SNARF-1 war nicht kovalent an die Nanopartikel angebunden. Neben dem diskutierten Farbstoff SNARF gibt es auch andere, etablierte ratiometrische Farbstoffe. Von *Shen et al.* wurde ein pH-sensitives Copolymer mit einem ratiometrischen Fluoreszenzsensor synthetisiert und für pH-Messungen in den Polymerketten eingesetzt.[139] Das den Fluoreszenzsensor enthaltende Copolymer konnte anschließend in Mikrobioreaktoren eingesetzt werden, um den den pH-Wert zu verfolgen. Ähnlich zum SNARF hat auch dieser Farbstoff pH-abhängige Absorptions- und Fluoreszenzemissionsmaxima. Im pH-Bereich von 1.7 und 4.5 konnten zwei isosbestische Punkte beobachtet werden. Die unterschiedlichen Protonierungsformen sind in Schema 2-8 dargestellt.

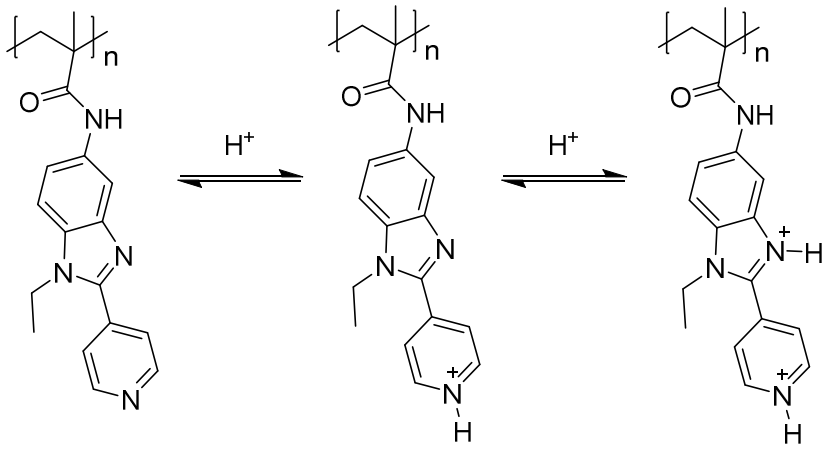

Schema 2-8: Protonierungsstufen des von SHEN *et.al.*[40] verwendeten Fluoreszenzsensors.

Die Inkorporation solcher komplexen Polymerarchitekturen in Nanoporen sind Gegenstand aktueller Forschung.[27, 120] Bisher sind Farbstoff-beinhaltende Copolymere in Nanoporen allerdings nicht bekannt, stellen jedoch eine sehr interessante Möglichkeit dar, um pH-responsive, selektive Nanomaterialien mit eingebauter Auslesefunktion zu erzeugen.

Eine weitere Farbstoffgruppe wurde 2006 von *Yan et al.*[46] entwickelt. Dabei handelt es sich um die Fluorophore 5-Methoxy-2-(2-, 3- oder 4-pyridyl)-thiazol, die im Weiteren mit 2-, 3- oder 4-MPT abgekürzt werden. Die Farbstoffe zeigen alle eine pH-abhängige Absorption und Fluoreszenzemission. Der abgedeckte, sensitive pH-Bereich liegt etwa zwischen pH 1-6. Dieser pH-Bereich ist vor allem im Hinblick auf die Kombination mit silicabasierten Materialien interessant, da die Oberflächen-Silanolgruppen in diesem pH-Bereich protoniert/deprotoniert werden.[41-43, 162] Durch die Unterschiede zwischen dem pH-Wert in Mesoporen und dem in Lösung, sind MPT-Farbstoffe für viele Anwendungsgebiete interessant, zum Beispiel für die Entwicklung von Biosensoren zur Membranherstellung mit hochselektivem Transport.[127-128] In der folgenden Abbildung 2-8 sind die drei Fluorophore aufgezeigt:

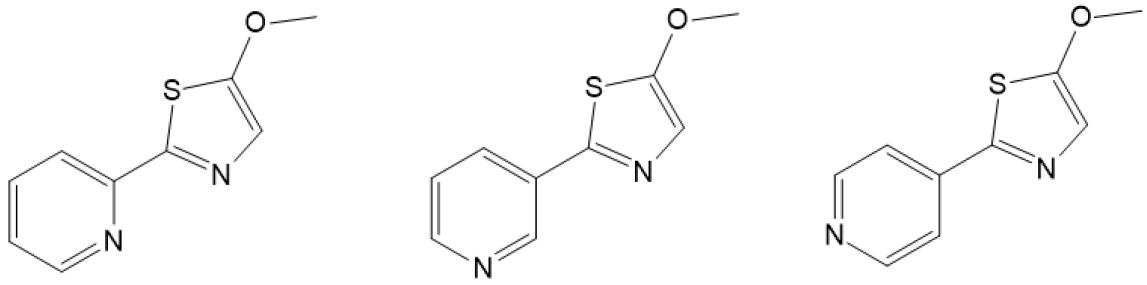

2-MPT 3-MPT 4-MPT

Abbildung 2-8: Strukturformeln der Fluorophore 2-MPT (links), 3-MPT (mitte), 4-MPT (rechts).

Yan et al.[46] konnten durch Absorptions- und Fluoreszenzmessungen folgende Regel bei den MPT-Farbstoffen aufzeigen: je saurer der pH-Wert in der Lösung ist, desto stärker verschiebt sich sowohl die Fluoreszenz als auch die Absorption in den langwelligen roten Bereich des Spektrums. Ebenfalls ist für jedes Derivat des Farbstoffes ein isosbestischer Punkt gegeben, der das Säure-Base-Gleichgewicht der jeweils protonierten und deprotonierten Form aufzeigt.[46] Die Protonierung von Farbstoffen kann in einer Veränderung des π-Systems resultieren, wodurch die Absorption bzw. die Fluoreszenz beeinflusst werden können. Eine solche pH-abhängige Beeinflussung kann über UV/Vis- und Fluoreszenzuntersuchungen analysiert werden.

Damit bieten diese Farbstoffe ein großes Potential für die ratiometrische pH-Detektion in Silica mesoporen. Für das Farbstoffderivat 2-MPT wurde ebenfalls untersucht, ob sich dieses zur Detektion von Metallionen benutzen lässt. In einer nachfolgenden Studie derselben Gruppe konnte zudem gezeigt werden, dass 2-MPT an Silicaoberflächen kovalent angebunden und als Cu-Sensor verwendet werden kann.

2.6. Charakterisierung funktionalisierter Silicahybridmaterialien mittels Cyclo Voltammetrie

Die Cyclovoltammetrie (CV) wurde in dieser Arbeit genutzt, um die pH-abhängige Mesoporenzugänglichkeit von funktionalisierten und unfunktionalisierten Silicadünnfilmen für Ionen zu untersuchen. Auf diese Weise sollten Rückschlüsse auf die durch das *Nanoconfinement und Polymerfunktionalisierung* induzierten pH- und pK_s-Verschiebungen sowie die resultierende ionische Zugänglichkeit in den Mesoporen erhalten werden. Zu diesem Zweck wurden die Silicafilme auf Indium-Zinnoxid (ITO) beschichteten Glassubstraten abgeschieden (siehe Abbildung 2-10). Als Testmoleküle wurden die gut etablierten, redoxaktiven Komplexe $[Ru(NH_3)_6]^{2+/3+}$ und $[Fe(CN)_6]^{3-/4-}$ verwendet.[3] Bei der Cyclovoltammetrie wird die Stromstärke unter Variation der Spannung gemessen. Hierbei wird die Spannung linear auf einen Zielwert erhöht (U_2), bevor sie wieder zur Ausgangsspannung (U_1) verringert wird.[163-164] Die Änderung der Spannung pro Zeit wird als *Scanrate* bezeichnet. Ein beispielhaftes Cyclovoltammogramm einer reversiblen Redoxreaktion wird in Abbildung 2-9 abgebildet.

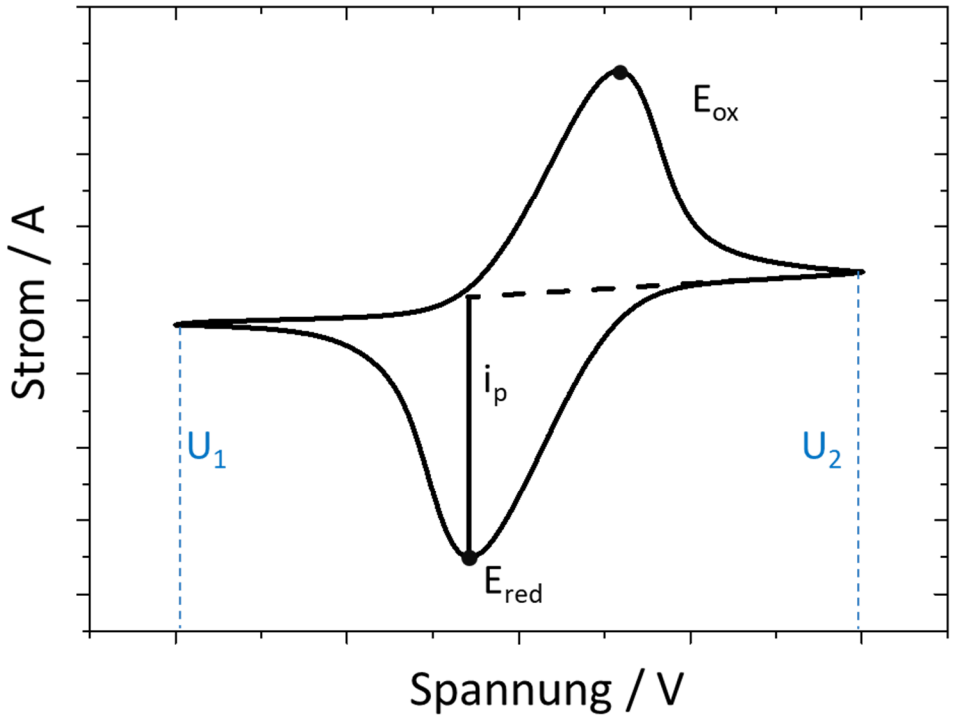

Abbildung 2-9: Schematische Darstellung des Cyclovoltammogramms einer reversiblen Redoxreaktion.

U_1 und U_2 stellen die oben beschrieben Umkehrpunkte der Spannung dar, zwischen denen in mehreren Scanraten gewechselt wird. Folgende *Scanraten* Sequenz wurde in dieser Arbeit

eingesetzt: 200, 100, 25, 300, 500/1000, 200 mVs^{-1}. Nur wenn beide 200 mVs^{-1} Scanrates vergleichbar sind, kann von einem Gleichgewichtszustand ausgegangen werden, der notwendig ist um die Messung verwenden zu können. E_{ox} und E_{red} stellen das Oxidations- bzw. das Reduktionspotential dar, welches Testmolekül-abhängig ist und an der Arbeitselektrode detektiert wird. Der für die Auswertung relevante Spitzenstrom wird mit i_p bezeichnet. Er kann mit Hilfe der *Randles-Sevcik*-Beziehung beschrieben werden, welche die Korrelation zwischen i_p und dem Diffusionskoeffizienten ermöglicht:

$$i_p = (2{,}69 \cdot 10^5) \cdot \sqrt{n^3} \cdot A \cdot \sqrt{D} \cdot c \cdot \sqrt{v}$$

$n =$ Anzahl der übertragenen Elektronen
$A =$ Elektrodenfläche
$D =$ Diffusionskoeffizient
$c =$ Konzentration des redoxaktiven Testmoleküls
$v =$ Scanrate

Messaufbau

Für die Messungen wird ein drei Elektroden Aufbau verwendet, bestehend aus einer Arbeitselektrode, einer Referenzelektrode und einer Gegenelektrode. Die Elektrodenfläche der Arbeitselektrode ist kreisförmig und hat eine definierte Fläche von 0.21 cm^2. Mit einem Potentiostat wird die Spannung an der Arbeitselektrode in Abhängigkeit des Potentials an der Referenzelektrode gesteuert. Die Gegenelektrode dient zum Ausgleich der gemessenen und angelegten Spannungen.[165] Der Messaufbau ist schematisch in Abbildung 2-10 illustriert.

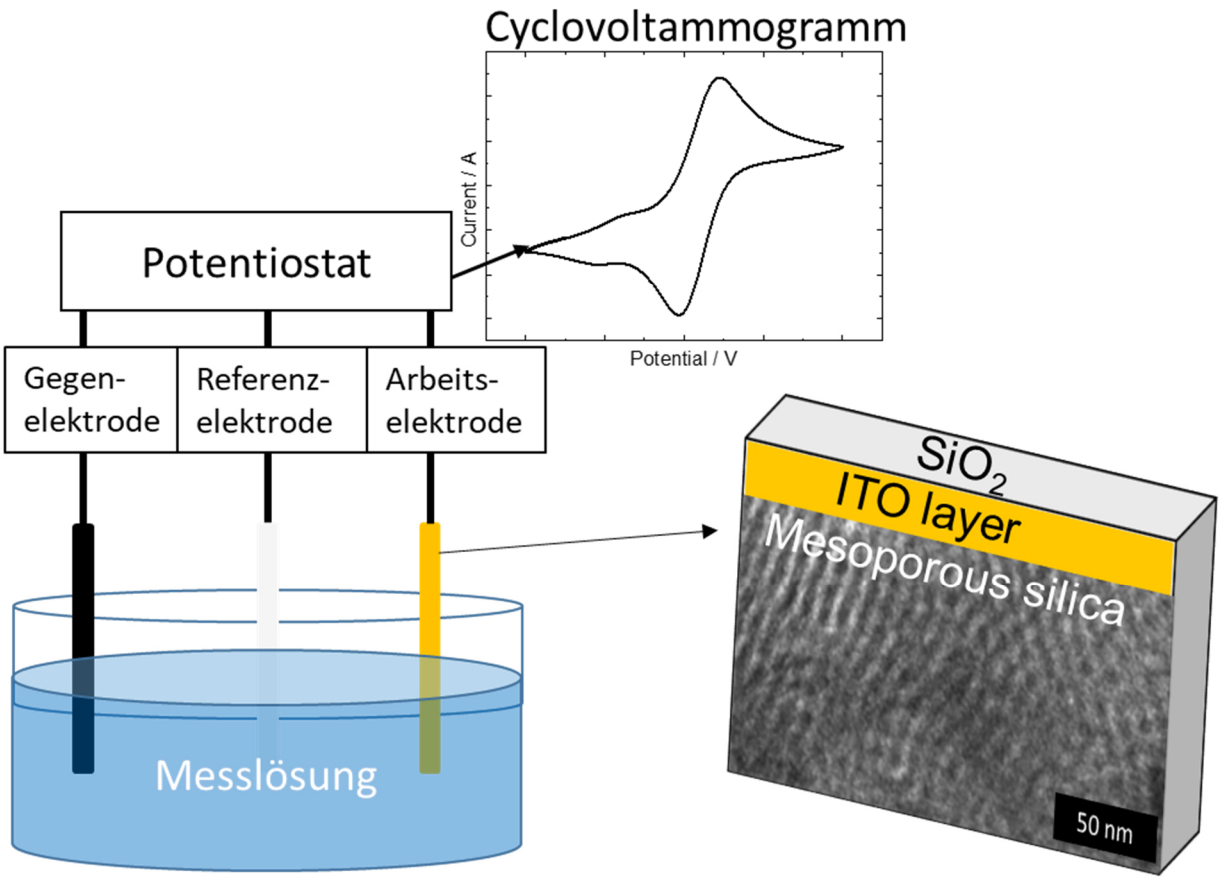

Abbildung 2-10: Schematische Darstellung des Messaufbaus für Cyclovoltammetriemessungen in dieser Arbeit.

Wie bereits erwähnt, wurde in dieser Arbeit als Arbeitselektrode eine ITO-Schicht verwendet. Als Referenzelektrode diente eine Ag/AgCl Elektrode und als Gegenelektrode eine Graphitelektrode. Wenn ein redoxaktives Testmolekül den mesoporösen Film, der auf der ITO-Schicht aufgebracht ist, durchquert, wird es an der Elektrode oxidiert bzw. reduziert, wodurch ein Signal durch Änderung des Stroms detektiert werden kann. Dadurch sind Rückschlüsse auf die Poren-/Filmzugänglichkeit möglich, da attraktive bzw. repulsive Wechselwirkungen zwischen (funktionalisierten) Film und Testmolekülen die Testmolekülkonzentration an der Arbeitselektrode beeinflussen. Bei den in dieser Arbeit angewendeten Cyclovoltammetriemessungen handelt es sich um eine etablierte Methode, um poröse Dünnfilme zu charakterisieren und deren Permselektivitätsverhalten zu untersuchen.[3, 28, 166-167] Zusätzlich zu der in der Literatur bekannten Probenpräparation wurde im Zuge dieser Arbeit festgestellt, dass gerade für polymerfunktionalisierte Filme einige Punkte beachtet werden müssen, um repräsentative Messwerte zu erhalten:

Zunächst ist es wichtig die Filme zwischen der Polymerisation und der Messung nicht eintrocknen zu lassen, durch das Eintrocknen kollabieren die Polymere: wird dann sofort eine CV-Messung gestartet, sind die erhaltenen Rückschlüsse auf die Porenzugänglichkeit verfälscht. Die Polymere können zwar durch Inkubation der Filme in wässriger Lösung wieder aufgequollen werden, dieser

Schritt bringt allerdings einen erheblichen Zeitverlust mit sich und stellt eine Unsicherheitskomponente für die erhaltenen Messwerte dar. Bei sehr hohen Porenfüllgraden muss zudem stark darauf geachtet werden, dass sich das Messgleichgewicht eingestellt hat. Hierfür können mehrere Messzyklen erforderlich sein, bevor die definierten Qualitätsstandards erfüllt sind.

Das Konzentrationsverhältnis der oxidierten (c_{ox}) und reduzierten (c_{red}) Spezies können bei reversiblen Elektrodenprozessen mit Hilfe der *Nernst*-Gleichung bestimmt werden:

$$E = E^0 + \frac{RT}{zF} \log\left(\frac{c_{ox}}{c_{red}}\right)$$

E beschreibt hierbei die Elektrodenspannung, E^0 die Standard-Elektrodenspannung, R die ideale Gaskonstante, T die Temperatur in Kelvin, z die übertragenen Elektronen und F ist die Faraday-Konstante. Der Spitzenstrom (I_p) kann über Gleichung 3 bestimmt werden. Hierbei werden die Anzahl der pro Molekül reagierenden Elektronen n, die Elektrodenoberfläche A, der Diffusionskoeffizient D_0, die Scanrate v und die Konzentration der redoxaktiven Spezies C_0 einbezogen.

$$I_p = (2{,}69 \cdot 10^5) \cdot n^{\frac{2}{3}} \cdot A \cdot {D_0}^{\frac{1}{2}} \cdot v^{\frac{1}{2}} \cdot C_0$$

Messlösung

Da Wasser intrinsisch ein Isolator ist, muss in die Messlösung neben dem Testmolekül auch ein sogenanntes Hintergrundsalz hinzugegeben werden, um eine leitfähige Lösung herzustellen. Wie in der Literatur üblich, wurden für die Messungen zunächst wässrige 100 mM KCl-Lösungen mit 1 mM Testmolekül verwendet. Für Messungen bei unspezifischen pH-Werten ist diese Art Messlösung gut geeignet. Für die in dieser Arbeit durchgeführten Titrationsexperimente allerdings nicht, da keine stabilen pH-Werte eingestellt werden können. Da die Ionenspezies eine signifikante Rolle auf CV-Messungen haben,[168] kann nicht für jeden pH-Bereich ein optimales, aber variierendes Puffersystem verwendet werden. Aus diesem Grund bot sich das sogenannte *Phosphat buffered saline* (PBS) Puffersystem an. Das Salzgemisch beinhaltet K^+, Na^+, sowie Cl^- und $H_xPO_4^{3-x}$ (x=0-2) Ionen, besitzt 2 pK_s-Werte bei ~5.5 und ~7.5 und deckt somit ausreichend den für diese Arbeit relevanten pH-Bereich von ca. 1.5-10 ab. Wenn nicht anders erwähnt, wurde auf die weit verbreitete 1xPBS Salzkonzentration zurückgegriffen, welche eine Gesamtmolarität von ca. 150 mM besitzt. Alternativ wurde 1/3xPBS verwendet, was einer Salzkonzentration von ca. 50 mM entspricht.

2.7. Polymerfunktionalisierung von MXenen

Bei MXenen handelt es sich um eine relativ neue Art von (polymer)funktionalisierbaren 2D Materialien, welche sich durch veränderte elektronische, optische, mechanische und thermische Eigenschaften im Vergleich zu den korrespondierenden Bulkmaterialien auszeichnen. Seit der Entdeckung von 2D Ti_3C_2 in 2011[169] erzeugte die Stoffklasse der MXene enorm großes Interesse im Bereich der Materialwissenschaften, Physik und Chemie. Innerhalb der letzten 10 Jahre wurde so aus einem MXen eine Materialfamilie von ca. 70 Derivaten, wobei das Potential an unterschiedlichen Materialzusammensetzungen noch lange nicht erschöpft ist.[170-172] MXene folgen der allgemeinen Zusammensetzung $M_{n+1}X_nT_x$, wobei M ein frühes Übergangsmetall wie Sc, Ti, Zr, Hf, V, Nb, Ta, Cr, Mo etc.), darstellt. X steht für Kohlen- oder Stickstoff und bei T handelt es sich um die terminierende Oberflächenfunktion, typischerweise –OH, -O oder –F, wenn mit fluorhaltigen Mitteln exfoliert wird.[173] Durch diese interessante Elementzusammensetzung weisen MXene eine einzigartige Kombination aus Leitfähigkeit auf, bedingt durch die freien Elektronen der Übergangsmetalle und Hydrophilie, welche aus den Oberflächenfunktionen hervorgeht. Diese Eigenschaften machen MXene für Anwendungen wie Energiespeicherung,[174] transparente Stromleiter,[175-176] Gas- und Drucksensoren,[177-179] Wasseraufbereitung[180-182] bis hin zur Photo- und Elektrokatalyse interessant.[183-184]

Herstellung und Oberflächenchemie von MXenen

MXene werden aus ihren MAX-Phasen-Vorstufen durch selektives Ätzen der A-Elemente gewonnen. Hierbei wird die Selektivität von HF-basierten Ätzmitteln zunutze gemacht.[185] Die metallischen M-A-Bindungen sind in einer fluoridhaltigen Lösung reaktiver als die gemischten M-X-Bindungen.[173, 186] Aufgrund der unangenehmen Handhabung von konzentrierter HF-Säure gibt es auch Ansätze diese Chemikalie mit LiF und HCl-Säure zu substituieren,[187-189] oder ein hydrothermales Ätzverfahren anzuwenden.[190] Da die MXen-Herstellung jedoch nicht Bestandteil dieser Arbeit war, wird an dieser Stelle auf ein detailliertes Syntheseprotokoll zur Herstellung von $Ti_0C_2T_X$ verwiesen.[191]

Bedingt durch den für die Herstellung notwendigen Ätzprozess, ist die Oberfläche üblicherweise durch eine Mischung aus –F, -OH, und –O-Gruppen terminiert. Die gezielte Oberflächenterminierung stellt bis heute eine Herausforderung dar und ist noch nicht vollständig verstanden.[170, 173] Für die Charakterisierung der Oberfläche werden verschiedenste Methoden verwendet, wie etwa Röntgenphotoelektronenspektroskopie (XPS)[192-193] oder Kombinationen aus thermogravimiterischer Analyse (TGA) und Massenspektrometrie (MS).[194] Da die MXen-Oberfläche komplex ist und sich je nach Übergangsmetall stark unterscheidet, fokussieren sich aktuelle Oberflächenuntersuchungen hauptsächlich auf titanhaltige MXene.[171]

Neben der Herstellung neuer MXen-Varianten stellt auch die Verbesserung der chemischen und physikalischen Eigenschaften bestehender MXene ein großes Forschungsgebiet dar. Der bisher verbreitetste Ansatz ist hierbei die Herstellung von Kompositmaterialien.[172] Durch Vermischen der MXene mit Polymeren wie Polyvinylalkohol lassen sich etwa freistehende, leitende und gleichzeitig flexible Materialien herstellen.[195] Die Polymere können zwischen die MXen-Schichten interkalieren und durch Quellung responsiv die Materialeigenschaften verändern.[196] Für eine detaillierte Übersicht der verschiedenen MXen basierten Kompositmaterialien, deren Herstellung und Anwendung wird an dieser Stelle auf einen ausführlichen Übersichtsartikel von *Hong et al.* verwiesen.[172] Neben der Herstellung von physikalischen Gemischen aus Polymeren und MXenen, lassen sich über die Oberflächen –OH-Funktionen auch chemische Modifikationen einfügen. Bisher haben sich die Oberflächenmodifikationen von MXenen hauptsächlich auf molekulare Modifikationen beschränkt. Polymermodifikationen, wie für andere Materialklassen (z.B. silicabasierte Oberflächen) üblich, sind bisher kaum erforscht. Ein Ansatz zur Polymerfunktionalisierung von MXenen, welcher in dieser Arbeit angewendet wurde, erfolgt analog zur Synthese für andere bereits etablierten anorganischen-organischen Hybridmaterialien, wie etwa Organosilicamaterialien. In Abbildung 2-11 ist schematisch die Herstellung von MXenen mit anschließender Polymerfunktionalisierung gezeigt.

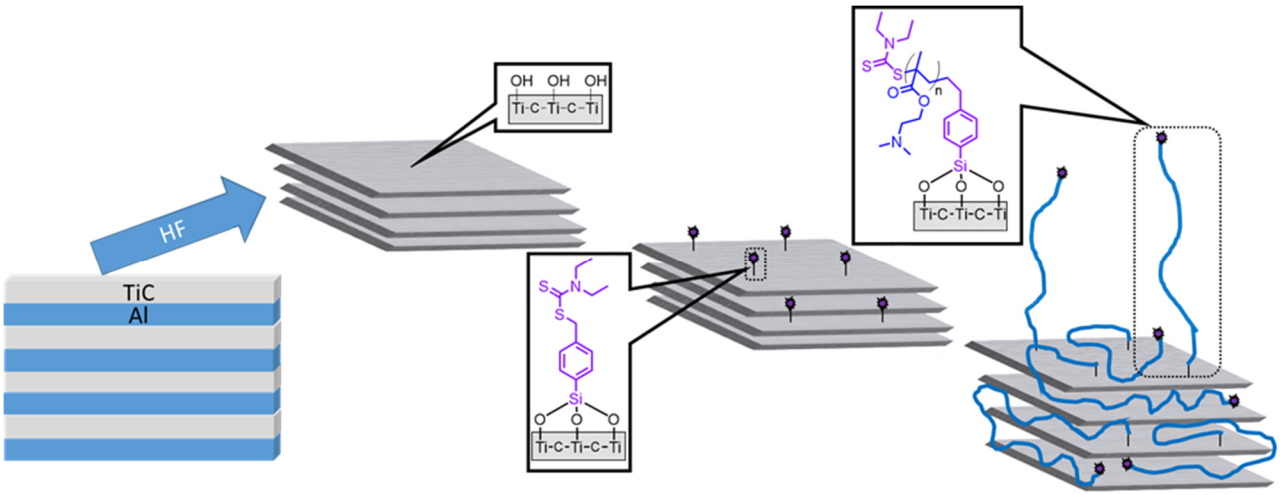

Abbildung 2-11: Schematische Darstellung der Herstellung eines TiC-MXen aus der MAX-Phase und die anschließende Funktionalisierung mit dem responsiven Polymer PDMAEMA.

Das Potential von Polymer-MXen-Materialien wurde zuerst von *Chen et al.* erkannt, denen es erstmals 2015 gelang, eine kovalente Polymerfunktionalisierung auf MXenen anzubringen.[197] Durch die Kombination von V_2CT_x mit PDMAEMA ist es gelungen, ein CO_2- und temperaturresponsives MXen-Hybridmaterial herzustellen. Des Weiteren ist es *Ye et al.* Gelungen, Polystyrol auf Ti_4AlN_3 Microblättchen über eine selbst initierende, photografting-photopolymerisation (SIPGP) herzustellen.[198] In diesen ersten Studien ist es zwar gelungen, die

MXene mit Polymer zu modifizieren, die Polymerisationen erfolgten aber recht unkontrolliert. In einer jüngeren Arbeit konnten *Tao et al.* einen kontrollierteren Ansatz zur Polymerfunktionalisierung von MXenen aufzeigen. Über den Ätzprozess ist es gelungen Hydroxylradikale auf der MXen-Oberfläche zu erzeugen, welche eine *grafting from* Polymerisation von unterschiedlichen Acrylaten ermöglichten. Die so entstandenen NIPAM@$Ti_3C_2T_x$-Nanoblättchen zeigten ein responsives Verhalten in Gegenwart von Nah-Infrarotlicht.[199]

In einer Kooperation mit der Arbeitsgruppe von Christina Birkel und Houlong Zhuang (beide Arizona State University, USA) ist es gelungen mit SI-PIMP erstmals eine traditionelle, kontrollierte Polymerisationsmethode auf MXenen anzuwenden. Die erzeugten PDMAEMA@TiC_2T_x Hybridmaterialien zeigen ein temperaturabhängiges Leitfähigkeitsverhalten auf.[200]

3. Ziele und Strategie

In dem folgenden Kapitel wird die Strategie vorgestellt, welche im Rahmen dieser Arbeit genutzt wurde, um die in Kapitel 1 definierten Forschungsfragen zu beantworten.

- Wie beeinflusst die Nanoskala den pH-Wert und Moleküle, die sich in Mesoporen <20 nm befinden
- Wie beeinflusst die Ladungsverteilung, einstellbar durch die Polymerkettenarchitektur, das pH-responsive Transportverhalten von Mesoporen

Zur Untersuchung dieser Fragen mussten Oberflächenfunktionalisierungen mit einer möglichst hohen Funktionalisierungsdichte auf Silicadünnfilmen hergestellt werden. Die unterschiedlichen Funktionalisierungstypen in Form von Farbstoff- und Polymerfunktionalisierung (Schema 3-1) sollten dazu dienen, ein möglichst breites Spektrum an Oberflächenfunktionen abzudecken. Aus den Einzelmessungen sollte ein finales Gesamtbild erstellt werden, welches den Einfluss von *Nano Confinement* auf den pK_s-Wert der unterschiedlichen Detektionsmoleküle darstellt. Diese Zusammenstellung sollte es ermöglichen, den pH-Wert in Nanoporen in Abhängigkeit von Parametern wie Porengröße oder Salzkonzentrationen besser verstehen zu können.

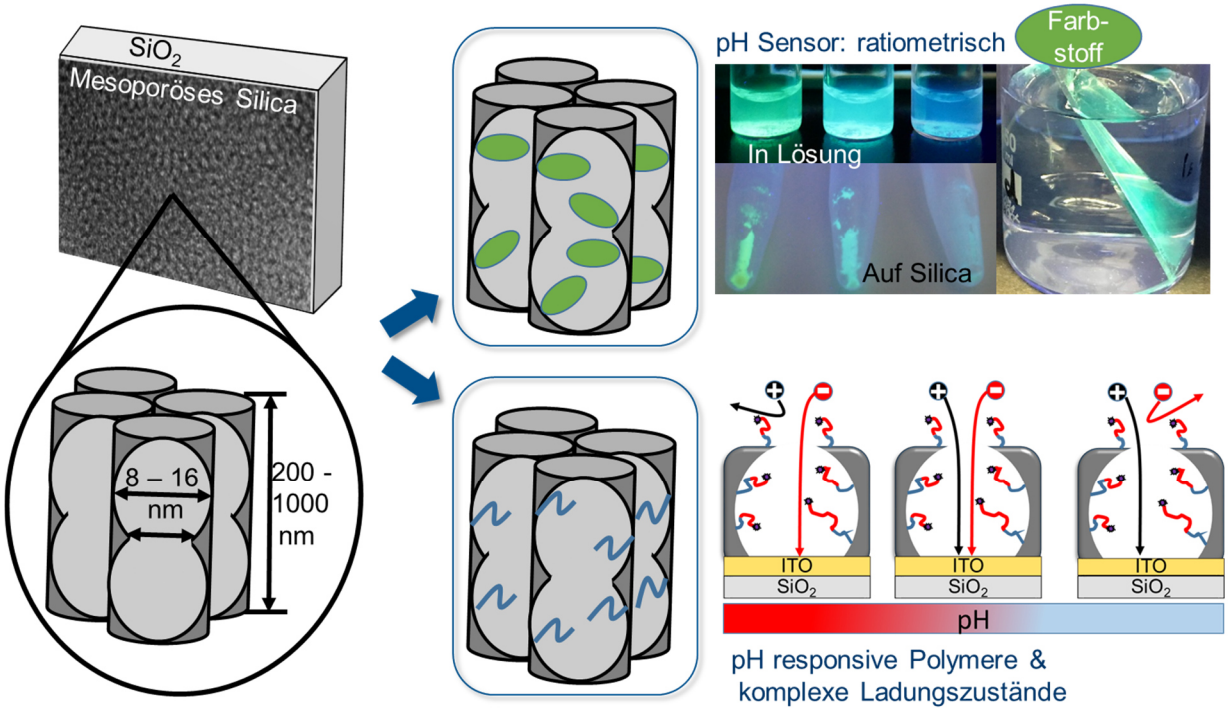

Schema 3-1: Schematische Darstellung der unterschiedlichen Untersuchungsansätze zur pH Detektion in Silicamesoporen, welche in dieser Arbeit verfolgt wurden.

Im ersten Teil dieser Arbeit wurden daher zunächst mesoporöse Silicafilme hergestellt. Da die gängigsten mesoporösen Silicamaterialien wie etwa SBA-15 und MCM-41 Porengrößen von ca. 3-

8 nm Durchmesser haben, ist die Menge und Größe von Molekülen bzw. Polymerketten stark limitiert. Deshalb wurden möglichst großporigere mesoporöse Silicafilme mit einer hohen Porösität benötigt, die eine höhere Beladung mit organischen Funktionen erlauben als konventionelle Silicamaterialien.

Um den Einfluss von mehrfachladbaren Polymersystemen in Silicamesoporen zu untersuchen, wurde zunächst die kontrollierte Photoinferter basierte Homopolymersynthese von PDMAEMA (multiresponsiv) und PMEP (2 pK_s-Werte) hinsichtlich der Porenfüllung und Polymermenge in Abhängigkeit von Polymersiationszeit untersucht. Die so hergestellten Silicafilme wurden elektrochemisch hinsichtlich ihres Permselektivitätsverhaltens in Abhängigkeit von Porengröße und Hintergrundelektrolytkonzentration untersucht, um die apparenten pK_s-Werte der Polymerfunktionen zu bestimmen.

Die erhaltenen Erkenntnisse über die Polymerisation von PDMAEMA und PMEP wurden anschließend genutzt, um durch Reinitiation der Polymerisation PDMAEMA-co-PMEP block-co-oligomere herzustellen. Diese Funktionalisierungsstrategie konnte in Kooperation mit der Arbeitsgruppe von Prof. Hess (TU Darmstadt) durch Röntgenphotoelektronenspektroskopie (XPS)-Messungen erfolgreich nachgewiesen werden. Die PDMAEMA-co-PMEP funktionalisierten Filme wurden dann analog zu den homopolymerfunktionalisierten Silicafilmen elektrochemisch untersucht. Hierbei zeigten sich große Unterschiede zu anderen mehrfach- und orthogonal geladenen polymerfunktionalisierten Silicafilmen, wie z. B. zwitterionisch geladenen PCBMA funktionalisierten Silicamesoporen.[201] Dadurch konnte die Rolle der Kettenarchitektur und der Ladungsverteilung innerhalb von Mesoporen herausgearbeitet werden.

Zur Untersuchung des pH-Wertes in Mesoporen und des Einflusses der Nanoskala auf darin angebundene Moleküle wurde ein pH-responsives Farbstoffsystem ausgewählt. Als Grundgerüst diente ein etabliertes Pyridylthiazolgerüst. Da das Grundgerüst vor allem im UV-Bereich absorbiert und emittiert, wurde es um einen Phenylrest erweitert. Gleichzeitig wurde so auch eine Ankergruppe mit in das Farbstoffmolekül eingeführt, wodurch eine kovalente Anbindung an das Silicagerüst ermöglicht wurde. Der erhaltene Farbstoff wurde dann über eine Amidbindung kovalent in ein Aminosilikagerüst angebunden. Die erfolgreiche Anbindung wurde in Kooperation mit der AG Bunkowsky per Festkörper-NMR nachgewiesen. Anschließend wurden Titrationsexperimente vom Farbstoff in Lösung und dem Farbstoff in den Mesoporen durchgeführt und verglichen.

4. Ergebnisse und Diskussion

In diesem Kapitel werden die wissenschaftlichen Ergebnisse vorgestellt und diskutiert, die im Rahmen dieser Arbeit entstanden sind. Die vorgestellten Ergebnisse sind teilweise in wissenschaftlichen Fachartikeln publiziert und teilweise noch unveröffentlicht. Daraus ergibt sich eine Gliederung in folgende Unterkapitel:

I. Herstellung mesoporöser Silicadünnfilme mit unterschiedlichen Porendurchmessern (Abschnitt 4.1)
II. Iniferter-initierte, kontrollierte Polymerisation von PMEP und PDMAEMA in mesoporösen Silicadünnfilmen (Abschnitt 4.2)
III. Synthese und elektrochemische Untersuchung zum pH-abhängigen Permselektivitätsverhalten von PDMAEMA-co-PMEP funktionalisierten Silicamesoporen (Abschnitt 4.3)
IV. Synthese und Verwendung von Farbstoffen zur pH-Detektion in Silicamesoporen (Abschnitt 4.4)
V. Polymerfunktionalisierung zur Herstellung von responsiven Ti2CTx-PDMAEMA MXen-Materialien (Abschnitt 4.5)

Kapitel 4.1 beschreibt hierbei die Entwicklung und Herstellung der benötigten mesoporösen Silicamaterialien.
In Kapitel 4.2 und 4.3 werden anschließend die Polymerfunktionalisierungen, sowie die elektrochemischen Permselektivitätsuntersuchungen dargestellt, um den Einfluss von Ladungsverteilung und Polymerkettenarchitektur in Silicamesoporen zu untersuchen.
Kapitel 4.4 beschreibt die Synthese eines Farbstoffbasierten pH-Reportermoleküls und dessen Anbindung an Silicamesoporen, um den Einfluss der Nanoskala auf angebundene Moleküle zu untersuchen.
Kapitel 4.5 beschreibt schließlich die Polymerfunktionalisierung der neuartigen Stoffgruppe der MXene. Hierbei werden die für auf Silica bekannten Oberflächenpolymerisationstechniken auf eine neue Materialklasse übertragen.

4.1. Herstellung mesoporöser Silicadünnfilme mit unterschiedlichen Porendurchmessern

In diesem Abschnitt wird die Herstellung von unterschiedlichen mesoporösen Silicafilmen über Tauchbeschichtung und Tiefdruck beschrieben. Die beiden Methoden werden im Hinblick auf die resultierenden mesoporösen Silicafilme verglichen. Dabei wurden zum Einen mesoporöse Silicafilme mit den sehr oft verwendeten, durch Pluronic F127 templatierten Porendurchmessern von ca. 8 nm und Porenverbindungen von ca. 3 nm Durchmesser verwendet.[28, 87, 202] Zum Anderen wurden auch in einer Arbeit von *Dunphy et al.*[9] inspirierte mesoporöse Silicafilme mit Porengrößen von bis zu 16 nm verwendet.

Zur Untersuchung von kontrollierter Polymerisation in Poren und zur Untersuchung von *Confinement*-Effekten waren, neben den vor dieser Arbeit in der Gruppe eingesetzten mesoporösen Silicafilmen mit Porengrößen von 3-8 nm, auch mesoporöse Silicafilme mit Porengrößen zwischen 10 und 20 nm relevant. Angeregt durch Arbeiten von *Dunphy et al.*[9] wurden diese zunächst über klassische Tauchbeschichtung hergestellt. Die erhaltenen Filme zeigten Porositäten von bis zu 70 vol%. Um mesoporöse Silicafilme für Anwendungen als Grundgerüst interessant zu machen, müssen die Filme sehr homogen, schnell und in großen Mengen produziert werden können. Etablierte Verfahren wie die *Tauchbeschichtung* sind hierbei in der Größe nicht beliebig skalierbar und aufwändig in der Präparation. Zudem ist die Filmdicke an den Substraträndern nicht homogen. Druckprozesse hingegen sind bereits etabliert, um dünne Filme und Beschichtungen auf Oberflächen aufzubringen. In Zusammenarbeit mit Dieter Spiehl (AG Dörsam, FB Maschinenbau, TU-Darmstadt) und mit Nicole Herzog und Anastasia Kalyta aus unserer Arbeitsgruppe stellte sich das Tiefdruckverfahren für diese Art Lösungen als besonders geeignet heraus. Über das Tiefdruckverfahren ist es gelungen, die in dieser Arbeit verwendeten mesoporösen Filme in wenigen Sekunden, sehr homogen auf Flächen von 6 x 20 cm^2 zu drucken. Die Filmdicke konnte beim Tiefdruck, wie auch beim *Dip-Coat*-Verfahren, durch Variation von Präparationsparametern wie Anpressdruck und Zylindervolumen bzw. der Herausziehgeschwindigkeit, in einem Bereich von wenigen zehn bis mehreren hundert Nanometer kontrolliert eingestellt werden. Die im Druckverfahren hergestellten Filme stellten sich zudem als homogener heraus und zeigten nicht das vom Tauchbeschichten bekannte Problem an den Aussenrändern sehr uneben zu sein.

Die Ausgangslösung für die von *Dunphy et al.* inspirierten mesoporösen Filme mit etwas größeren Porendurchmessern zwischen 10-20 nm reagierte empfindlicher auf Veränderungen im Herstellungsprozess, wodurch Filmdicken von 250-1000 nm in einem Herstellungsschritt möglich waren, was einer Variation der Filmdicke von 750 nm entspricht. Zusätzlich wurde das Tiefdruckverfahren erfolgreich zur Herstellung von komplexen Filmarchitekturen genutzt, indem konsekutiv ein Film auf einen bereits vorhandenen Film draufgedruckt wurde. Hierbei zeigte sich, dass die Poren untereinander vernetzt sind, wodurch Ionentransport entlang der Filmdichte (z-

Richtung des Films) zwischen und durch die beiden unterschiedlichen Filmtypen (Filme mit 8 nm bzw. 16 nm großen Poren) möglich ist. Letztlich wurden die mittels Tauchbeschichtung und Tiefdruck hergestellten Filme hinsichtlich ihrer Eigenschaften verglichen. Zudem wurde untersucht, inwieweit sich die Vorgehensweise der Templatentfernung auf die pH-abhängige Permselektivität auswirkt. Verglichen wurde hierzu die Kalzinierung des Polymertemplates durch Herauslösen in wässriger HCl-Lösung. In dieser Veröffentlichung konnte gezeigt werden, dass das Tiefdruckverfahren einige Vorteile gegenüber dem etablierten *dip-coating* besitzt, ohne an Flexibilität zu verlieren, was die Variation der Filmdicke oder Verwendung von unterschiedlichen Sol-Gel-Lösungen betrifft.

Mein Beitrag zu dieser Veröffentlichung beinhaltet die Entwicklung von unterschiedlichen Sol-Zusammensetzungen und deren Anwendung in der Tauchbeschichtung zur Herstellung von mesoporösen Filmen mit einstellbaren Schichtdicken und Porengrößen. Zusätzlich wurden von mir die pH-abhängigen Cyclovoltammetrie-Messungen durchgeführt, durch die der Einfluss der Templatentfernungsmethode auf die Anzahl der resultierenden Oberflächen OH-Gruppen untersucht wurde.

Die Ergebnisse dieses Abschnittes sind in ***RSC Advances*** veröffentlicht:

Nicole Herzog, Robert Brilmayer, Mathias Stanzel, Anastasia Kalyta, Dieter Spiehl, Edgar Dörsam, Christian Hess, Annette Andrieu-Brunsen. **Gravure printing for mesoporous film preparation**, *RSC Advances,* **2019**, 9, 23570.

Die *Supporting Information* ist nicht abgedruckt, aber in der elektronischen Version dieses Artikels (DOI: 10.1039/c9ra04266k) verfügbar.

RSC Advances

PAPER

View Article Online
View Journal | View Issue

Cite this: *RSC Adv.*, 2019, **9**, 23570

Gravure printing for mesoporous film preparation†

Nicole Herzog,[a] Robert Brilmayer,[a] Mathias Stanzel,[a] Anastasia Kalyta,[a] Dieter Spiehl,[b] Edgar Dörsam,[b] Christian Hess[c] and Annette Andrieu-Brunsen*[a]

Received 6th June 2019
Accepted 19th July 2019

DOI: 10.1039/c9ra04266k

rsc.li/rsc-advances

This study presents gravure printing as a new strategy for rapid printing of ceramic mesoporous films and highlights its advantages over conventional mesoporous film preparation using evaporation induced self-assembly together with dip-coating. By varying the printing process parameters, the mesoporous coating thicknesses can be adjusted between 20 and 200 nm while maintaining a very high film homogeneity allowing the printing of ultrathin mesoporous films. Step gradients in film composition are accessible by consecutively printing two different "inks". Thereby, gravure printing is a much faster process than mesoporous single- and multilayer preparation using conventional dip-coating because lower amounts of solution are transferred and dissolution of previously deposited layers is avoided. The effect of printing process parameters on resulting film characteristics as well as the resulting mesoporous film's ionic accessibility is systematically investigated.

Introduction

Printing is a powerful tool for manufacturing thin films and coatings. Mesoporous ceramic coatings or thin films are of special interest because they provide an ordered porous framework able to include a variety of functional molecules, resulting in hybrid materials with organized and specific features such as a large surface area and functionalized mesopore walls. These features enable tuning of material characteristics such as ionic permselectivity or optical properties.[1–3] Therefore, functional mesoporous materials and coatings play a key role in many technological applications such as nanoscale reaction vessels, sensors, optics, separation, catalysis or lab on chip devices.[4–12] Commonly, mesoporous ceramic coatings are prepared by Evaporation-Induced Self-Assembly (EISA) and sol–gel chemistry using a dip- or spin-coating process.[13] Within this process mesoporous film characteristics, especially the film thickness, can be easily adjusted by varying the solvent or withdrawal speed and by varying the geometry of the solution level within the solution reservoir.[14,15] Despite this versatility, the fabrication of structured or patterned films as well as the automated fabrication of complex coating architectures or ultrathin films of interest *e.g.* in electronic applications, is not easily possible and film homogeneity, especially with respect to film thickness, varies significantly within the coating. For example, composition control along the film thickness by dip-coating requires multiple dip-coating steps with intermediate temperature-stabilization, to avoid dissolution of previous layers. Aside from being very time consuming, this procedure affects film homogeneity along the film thickness. In addition, substrate rims induce film inhomogeneities, limiting the fabrication of small patterns, for example those desired in microelectronic devices. As another example ultrathin mesoporous films with film thicknesses down to 10 nm, of interest *e.g.* in electronic devices, have been recently prepared by wet-etching previously deposited films.[16] Printing such films would be much faster and allow much more precise local control. Interestingly, only a few examples of ink-jet printed, structured mesoporous coatings are reported. A technology allowing the construction of highly defined multiple layer and step gradient coatings with the potential for scale up is still missing.[17–19] Nevertheless, porous structures with well controlled compositions along the film thickness are of special interest in advanced molecular transport control and porous material compartmentalization, and thus in technologies such as sensors, separation or energy conversion. Consequently, a technology allowing homogeneous large area coatings as well as structured deposition while being scalable to an industrial scale that is fast and allows well defined multilayer generation at the nanoscale is required.

These criteria are fulfilled by printing technologies. With respect to mesoporous materials, printing is mainly based on paste printing usually to fabricate net-like macroscopic architectures of mesoporous silica, mostly intended to be used for cell growth.[20,21] Thereby ordered mesoporous structures such as

[a]*Ernst-Berl Institut für Technische und Makromolekulare Chemie, Technische Universität Darmstadt, Alarich-Weiss-Str. 4, D-64287 Darmstadt, Germany. E-mail: andrieu-brunsen@smartmem.tu-darmstadt.de*

[b]*Institute of Printing Science and Technology, Technische Universität Darmstadt, Magdalenenstr. 2, D 64289 Darmstadt, Germany*

[c]*Eduard-Zintl-Institut für Anorganische und Physikalische Chemie, Technische Universität Darmstadt, Alarich-Weiss-Str. 8, D-64287 Darmstadt, Germany*

† Electronic supplementary information (ESI) available. See DOI: 10.1039/c9ra04266k

hexagonally arranged mesopores have been demonstrated.[20] Only a few studies focus on printing with higher local resolution. For example, Kotz *et al.* show the possibility to print fused silica 3D structures by using stereolithography.[22] Instead of a sol used for EISA-based dip-coating, SiO_2 particles within a UV-curable polymer are applied. Thereby, the polymer matrix stabilizes the 3D structure upon hardening with UV-light followed by sintering resulting in a silica structure. This approach allows the design of transparent 3D silica structures but does not directly allow printing of ordered mesoporous 3D materials. Other experiments to create a 3D ceramic structure are based on ink-jet printing using a layer-by-layer approach, depositing ceramic suspension micro droplets ejected *via* nozzles.[23–25] Additionally, the group of Brinker demonstrated silica nanostructures prepared by micro-pen lithography and ink-jet printing. Printing is performed with functional organosilanes on patterned self-assembly monolayers, which leads to functional, hierarchically organized structures.[17] Unfortunately, ink-jet printing of microdot arrays of mesoporous silica is limited by the homogeneity of the dots. For optimal results this technique is limited to hydrophobic organosilanes as co-condensates.[26] The hydrophobic organosilanes are required to avoid clogging of the nozzle aperture.[27]

Currently, gravure printing is explored as an alternative fabrication process to be combined with sol–gel chemistry. A recent study published in 2018 demonstrates gravure printing of silica nanoparticles for metal oxide thin film formation.[28] Gravure printing has not yet been used to generate ordered mesoporous silica coatings. Thereby, gravure printing of mesoporous architectures bares a strong potential for automated thin film production with highly defined composition. As a roll to roll process it allows relatively high manufacturing speed of up to 15 ms^{-1} at up to 4 m width.[29] For example, literature describes gravure printing as a good candidate for thin film production in electronics as it allows high throughput, high control of film characteristics and provides the opportunity to print well-defined multiple layers.[30] With respect to production of complex mesoporous film architectures, gravure printing bares the potential to generate more homogeneous films in much shorter production time as compared to established EISA using dip- or spin-coating and ink-jet printing. In addition, standardization and automation of the film preparation process as well as complex film architecture fabrication should be relatively easy. Combining structuring by gravure printing with different sol inks and co-condensation approaches, known from conventional sol–gel chemistry, and using subsequent post-functionalization strategies further supports complex film architecture design. In general, gravure printing allows nanoscale adjustment of film thickness and film homogeneity based on the substrate, ink viscosity, cell volume, printing speed and printing force. Consequently, smart process design is expected to not only allow the deposition of nanometer thick, homogeneous, and structured mesoporous film architecture in an automated fashion but also layer selective functional placement.

Here, we establish gravure printing as a rapid and scalable process to prepare homogeneous mesoporous thin film architectures with nanoscale thickness resolution, including multilayer and thus step gradient design, using layer-selective *in situ* functionalization exemplified for co-condensation of amine functional groups. The gravure printed mesoporous silica film properties, especially ionic mesopore accessibility, are compared to films prepared *via* conventional dip-coating based evaporation induced self-assembly. The gravure printing process has been optimized by exploring different curing processes and their influence on functional film properties. Regarding functional film properties mesopore ionic permselectivity and the apparent pK_a values of silanol groups in the confinement of printed mesopores have been explored.

Results and discussion

The mesoporous silica film preparation process combining evaporation induced self-assembly (EISA) and gravure printing is schematically shown in Fig. 1 and compared to conventionally used dip-coating. The working principle of the gravure printing process starts with filling the cells of the rotating gravure cylinder in an inking unit. A doctor blade removes excess ink so that a defined amount of ink remains within the cells. The layout of the cells determines the printed layout. After further rotation of the cylinder, the cells come into contact with the substrate and most of the ink is transferred onto it. On the substrate, these transferred dots of ink start to merge into a homogeneous layer and the solvent evaporates. Thereby the influence of process parameters such as the cell volume, printing force, withdrawal speed and co-condensate solution composition are systematically controlled and the effect on film characteristics such as film thickness, porosity, and morphology is investigated. In general, gravure printing produces very homogeneous mesoporous silica films on large areas (here 6 × 20 cm^2) in an automated fashion. Micrometerscale patches are accessible printing individual spots (Fig. S1b†).

Gravure printed *versus* dip-coated mesoporous film characterization

Structural characterization by transmission electron microscopy (TEM) reveals similar mesoporous structures with pores 6–8 nm in diameter (Fig. 2a and b) for dip-coated and gravure printed mesoporous films. Furthermore, SEM images (ESI Fig. S2†) do not show any microscale cracks or structural defects. Gravure printed films appear to be very homogeneous microscopically as well as macroscopically as deduced from very homogeneous optical interference colors (Fig. 2d). Notably, substrate rim effects resulting in thicker films close to the substrate rims are absent when using gravure printing, as observed in electron microscopy and based on the reflected interference color visible for mesoporous films printed onto silicon wafer substrates (Fig. 2e and f). This makes gravure printing a versatile technique to print homogeneous microscopically small area mesoporous film architectures. In contrast to dip-coating, gravure printing easily allows for film thickness and film composition patterns and gradients by adjusting

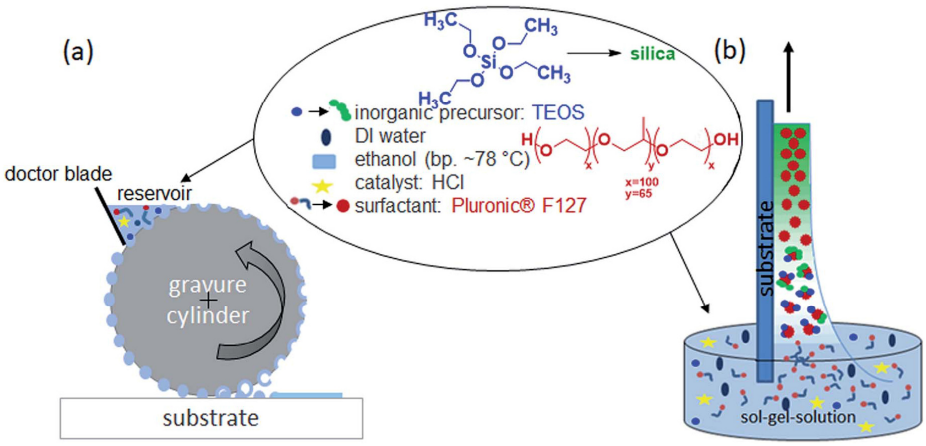

Fig. 1 Comparison of the two mesoporous film preparation strategies, evaporation-induced self-assembly (EISA) by dip-coating or gravure printing. (a) Gravure printing using a metal cylinder transferring the "ink" (sol–gel-solution) to the substrate. The ink is filled out of a reservoir into the cells of the gravure cylinder and directly transferred to the substrate. Excess ink is scraped off by a doctor blade. The cells are not completely emptied, as it comes to a film splitting. The settled fluid spots on the substrate extend to a surface at appropriate ratios of the surface tension of fluid and substrate. The arrangement of the cells specifies the layout to be printed film. The layout repeats after one cylinder revolution. (b) Conventional dip-coating process based on withdrawing a substrate with a defined speed from the sol–gel-solution. The film thickness and quality mainly depends on the used withdrawal speed, solution viscosity and substrate wetting.

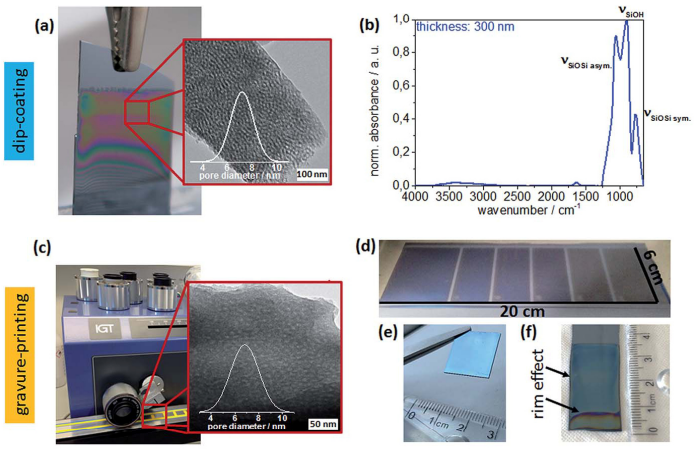

Fig. 2 Comparison of dip-coating (a, b and f) and gravure printing (c–e) as a mesoporous thin film preparation process. (a) Photograph of the dip-coating process as well as TEM image of a mesoporous silica film prepared by dip-coating with a withdrawal speed of 2 mm s^{-1} and template calcination at 350 °C showing a statistic pore distribution (7.2 ± 0.8 nm). (b) Infrared spectra of the mesoporous film after template calcination at 350 °C measured directly on a glass substrate. (c) Photograph of gravure printed mesoporous silica films and a TEM image of mesoporous silica prepared by gravure printing and calcination at 350 °C using a cylinder with a cell volume of 8.5 mL m^{-2} with a statistic pore distribution (6.8 ± 1.2 nm). (d) Photograph showing the homogeneity of gravure printed mesoporous silica films with different cylinder cell volume field (9.19 mL m^{-2}, 8.3 mL m^{-2}, 5.98 mL m^{-2}, 4.71 mL m^{-2}, 2.72 mL m^{-2} and 1.67 mL m^{-2} from left to right). By using gravure printing, it is possible to print mm-scale patterns. Substrate size is demonstrated with 6 cm × 20 cm. The different film thickness is visible by the different interference colors. (e) Image of a printed homogeneous mesoporous silica film prepared with a cell volume of 8.5 mL m^{-2}. (f) Image of a dip-coated mesoporous silica film prepared with 2 mm s^{-1} withdrawal speed. Inhomogeneity's because of edge effects are indicated by the black arrow and are visible by a colour change at the end of the substrate indicating a different film thickness originating from drop formation during dip-coating (rim effects).

gravure cylinder cell volume and sol composition (ink), respectively. Without special optimization, our experiments allow resolution down to 10–20 nm for film thickness while maintaining film homogeneity (Fig. 3) allowing to homogeneously print ultrathin mesoporous films. In accordance with literature, film thicknesses between 60 nm and 400 nm are achieved by dip-coating upon varying the withdrawal speed between 0.05 and 30 mm s^{-1} as shown in Fig. 2b.[31] In gravure printing, the film thicknesses and homogeneity is mainly determined by the cell volume of the grounded cylinders (we used a range from 1.6 to 24 mL cm^{-2}) resulting in film thickness variation between 20–240 nm (Fig. 3b) for a contact force of 500 N. In addition, film thickness can be tuned by varying the contact force between gravure cylinder and substrate. Increasing contact force from 500 N to 700 N leads to increasing film thickness of 10–20 nm (ESI, Fig. S3†). Consequently, gravure printing yields thinner homogeneous films compared to dip-coating. Porosity (pore volume) of 40–45 vol% as calculated from ellipsometry data (refractive index) using Brüggemann effective medium approximation (please refer to the ESI, Tables S1–S3†) is detected for dip-coated as well as gravure printed films. High refractive indices resulting in low porosities of below 20 vol% are observed only when very small cell volumes of less than 1.67 mL cm^{-2} are used. This can be attributed to insufficient ink transfer resulting in inhomogeneous film formation (ESI, Fig. S1†), which is supported by SEM and microscopy results. Using a critical cell volume (above 2 mL cm^{-2}) seems to be crucial for obtaining homogeneous mesoporous silica films by gravure printing with a comparable pore volume to dip-coated mesoporous silica films.

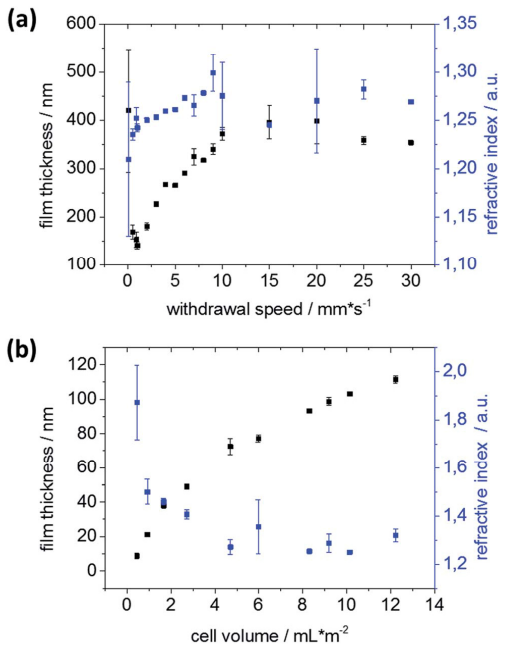

Fig. 3 (a) Film thickness (black) and refractive index (blue) determined by ellipsometry in dependence of the dip-coating withdrawal speed. (b) Film thickness (black) and refractive index (blue) determined by ellipsometry in dependence of the cell volume of the used gravure printing cylinder.

Changing the ink composition can introduce functional groups into the mesopore wall (co-condensation) and produce films with varying pore diameters. Here, we demonstrate pore diameters of about 16 nm instead of about 8 nm. These films show higher film thickness under identical gravure printing or dip-coating conditions and the calculated pore volume is slightly larger reaching up to 70 vol% (ESI, Tables S4 and S5†). Interestingly, film thickness variation for these films is more sensitive to withdrawal speed and cylinder volume (ESI, Fig. S2†) allowing a thickness variation range of 750 nm between film thickness of 250–1000 nm.

Functional integrity is characterized by using ATR-IR of 350 °C calcinated mesoporous silica films deposited on glass substrates. Three different silica stretching vibrational bands are observed (Fig. 2b):[32] the asymmetric stretching vibration of bridged Si–O–Si at 1260–1000 cm^{-1} and the symmetric stretching vibration of Si–O–Si ring structure at around 800 cm^{-1}, both originating from the silica network Si–O–Si as well as the stretching vibrational band of free silanol (Si–OH) groups in the range of 900–980 cm^{-1}. Based on these ATR-IR results no significant difference within the chemical structures, such as degree of silica condensation, can be observed for mesoporous silica films prepared under different process conditions or location on the supporting substrate (compare as well Fig. S4†).

Gravure printed mesoporous film performance

With respect to technological applications, such as separation, sensing, or catalysis, performance-limiting mesoporous film characteristics are mesopore accessibility and ionic permselectivity. Mesoporous silica ionic permselectivity and mesoporous silica film ionic uptake capability is mainly determined by structural characteristics such as pore size and porosity, together with pore wall functionalisation depending interface characteristics such as charge but might as well be affected by mesoporous film thickness. Walcarius and co-workers for example demonstrate an increasing peak current in cyclic voltammetry, representing, according to Nernst equation, an increasing molecule concentration, with increasing number of mesoporous silica layers produced by dip-coating.[33] As gravure printing allows very precise adjustment of homogeneous mesoporous layer thickness the correlation of film thickness and ionic permselectivity is shown in Fig. 4 as detected by the maximum peak current density deduced from cyclic voltammetry. Ionic mesopore accessibility of gravure printed and dip-coated mesoporous silica thin films with increasing film thickness using anionic and cationic probe molecules $[Fe(CN_6)]^{3-/4-}$ and $[Ru(NH_3)_6]^{2+/3+}$ at acidic and basic pH are compared. Thereby film stability has to be considered as recently demonstrated by Alberti *et al.*[34] Within the discussed experiments, cycling time has always been kept below 6

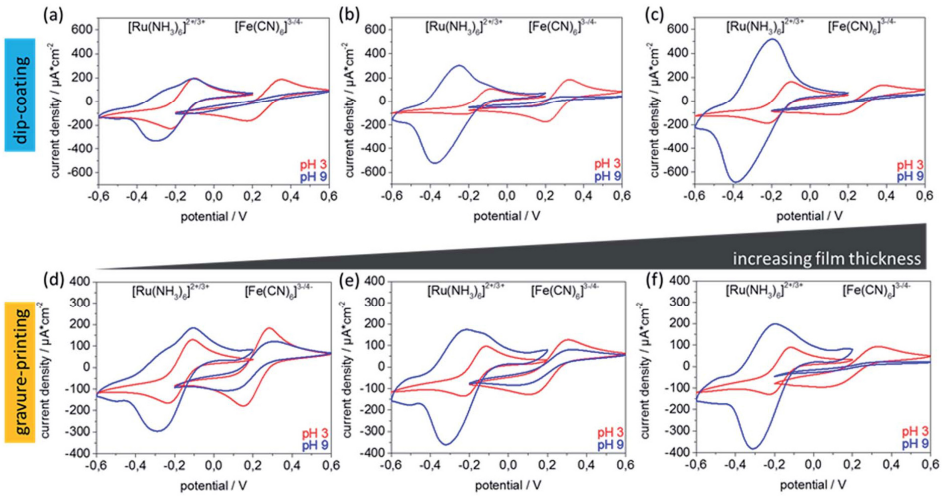

Fig. 4 Cyclic voltammograms of mesoporous silica thin films using $[Ru(NH_3)_6]^{2+/3+}$ (−0.6 to + 0.2 V) and $[Fe(CN)_6]^{3-/4-}$ (−0.2 to +0.6 V) as an ionic redox probes at pH 3 (red) and 9 (blue). The dip-coated mesoporous silica films are prepared with different withdrawal speeds (a) 0.5 mm s^{-1} (b) 2 mm s^{-1} and (c) 10 mm s^{-1} resulting in film thicknesses of (a) 140 nm (47 vol% porosity), (b) 180 nm (44 vol% porosity), (c) 300 nm (39 vol% porosity). Mesoporous silica films prepared by gravure printing are prepared using different cell volumes of (d) 8.5 mL m^{-2} (e) 16.3 mL m^{-2} and (f) 24 mL m^{-2} resulting in film thicknesses of (d) 100 nm (48 vol% porosity), (e) 162 nm (40 vol% porosity), (f) 250 nm (48 vol% porosity).

minutes and a strict data quality control has been applied ensuring stable and reproducible cyclic voltammograms as described in Experimental section and Fig. S13.† At basic pH values (Fig. 4a–c blue) the silica mesopore wall is negatively charged due to deprotonated silanol groups. Under these conditions an exclusion of $[Fe(CN_6)]^{3-/4-}$ due to overlapping Debye screening layers reflected by zero maximum peak current density (j_p) as well as a preconcentration of positively charged $[Ru(NH_3)_6]^{2+/3+}$ in the silica mesopores reflected by increased maximum peak-current densities and peak broadening is expected. At acidic pH, and thus neutral pore wall charge, no ion discrimination in pore accessibility and thus similar j_p is expected. In accordance with this expectation both probe molecules show similar, and thickness independent, maximum peak currents at acidic pH (Fig. 4, red). As well in accordance with expectation, electrostatic exclusion of $[Fe(CN_6)]^{3-/4-}$ at basic pH is observed indicating a defect-free film structure. Except for very thin films with a film thickness of below 100 nm a thickness dependent peak current reduction is observed (Fig. 4d–f). Interestingly, the preconcentration of $[Ru(NH_3)_6]^{2+/3+}$ at basic pH and the simultaneously observed broadening of the cyclic voltammograms seems to be film thickness and thus preparation process dependent, although no direct correlation can be drawn due to the dependence on multiple parameters especially on the free electrode area which is not directly accessible. Reference measurements of unmodified ITO electrodes are shown in Fig. S5.† These are not showing any peak broadening or preconcentration at basic or acidic pH values. In addition, the ATR-IR spectra (Fig. S4†) do not show differences in the Si–O–Si to Si–OH ratio in dependence of film thickness or preparation process, and ellipsometry indicates comparable pore volumes for all investigated films. Together, this indicates that the variation of $Si–O–Si_{asym./sym.}$ to Si–OH band intensity with varying cylinder volume is probably caused by the mesoporous film thickness but not by a difference in Si–OH concentration and thus charge density at the mesopore wall. In addition, data evaluation using Randles–Sevcik's equation (Fig. S6†) indicates that non-diffusional transport becomes significant for mesoporous films thicker than 250 nm for basic pH values and positively charged probe molecule and thus with existing attractive electrostatic interaction between pore wall and diffusing ions. This is reflected by a non-linear correlation of peak currents to the square root of scan rates. All these results indicate good accessibility and a comparable behavior for gravure printed to dip-coated mesoporous silica films.

Gravure printing of complex mesoporous film architectures

Besides the opportunity of printing different inks and thus creating gradient architectures, an advantage of mesoporous film gravure printing is the rapidity of the printing process itself. The very short contact time between supporting substrate and the sol–gel solution leads to fast drying, avoiding penetration of sol into a pre-printed layer and thus facilitating complex but homogeneous, defect-free multilayer fabrication. This allows printing of multiple mesoporous silica layers directly on top of one another without using stabilizing temperature treatments between layer deposition steps, which may negatively affect film homogeneity. Specifically, two-layer

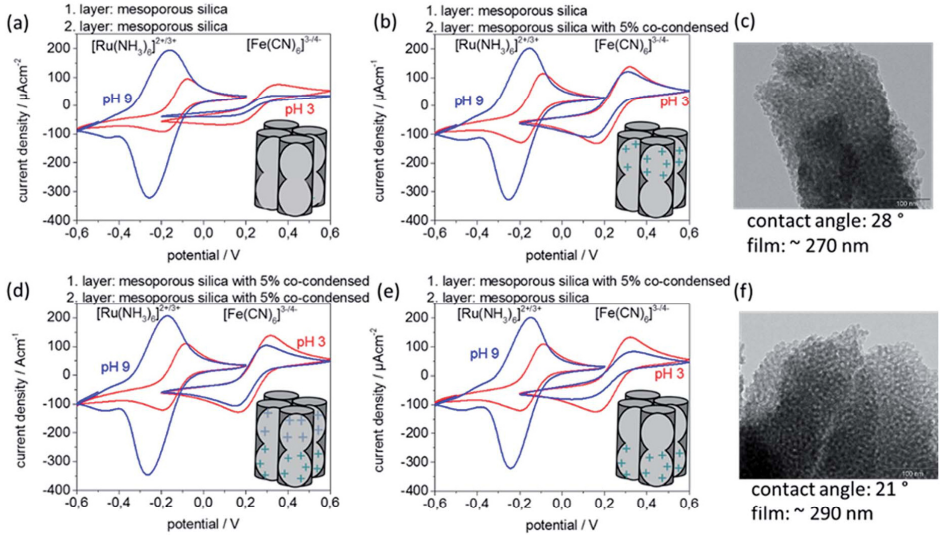

Fig. 5 Cyclic voltammograms of mesoporous silica thin films using $[Ru(NH_3)_6]^{2+/3+}$ and $[Fe(CN)_6]^{3-/4-}$ as ionic redox probes at pH 3 (red) and 9 (blue). Mesoporous silica films prepared by gravure printing are prepared using the cell volumes 8.5 mL m^{-2} resulting in film thicknesses 150 nm for one layer and 300 nm for two layers. (a) Two gravure printed layers of unfunctionalized mesoporous silica. (b) Two gravure printed layers consisting of a first mesoporous silica layer and a second mesoporous silica layer containing 5 mol% co-condensed (bis(2-hydroxyethyl)-3-aminopropyl-triethoxysilane) (c) TEM image of a two-layer mesoporous silica film prepared by gravure printing with two different inks corresponding to (b). (d) Two gravure printed layers of 5 mol% co-condensed mesoporous silica. (e) Two gravure printed layers consisting of a first mesoporous silica layer containing 5 mol% co-condensed (bis(2-hydroxyethyl)-3-aminopropyl-triethoxysilane) and a second mesoporous silica layer, (f) TEM image of a two-layer mesoporous silica film prepared by gravure printing with two different inks. The first layer consists of mesoporous silica with 5 mol% co-condensed (bis(2-hydroxyethyl)-3-aminopropyl-triethoxysilane) and a second layer of unfunctionalized mesoporous silica. The mesoporous films are thermally treated up to 200 °C and template extracted with acidic ethanol.

gravure printed mesoporous silica films using two different inks resulting in two different functional layers are prepared (Fig. 5). The corresponding characterization concerning porosity, contact angles, temperature treatment dependent ionic permselectivity, and morphology are summarized within the ESI (Fig. S9–S11 and Table S6†). Thereby it must be considered that layer functionalization by co-condensation of organic functional groups limits the maximum applicable temperatures, here to 200 °C. Successful multilayer step gradient preparation is as well supported by XPS measurements (ESI, Fig. S12 and Table S7†). XPS results show one nitrogen atom per seven Si-atoms after printing two layers of 5 mol% co-condensed mesoporous silica. When printing one layer of 5 mol% mesoporous co-condensed silica followed by a second top layer of mesoporous silica only one nitrogen atom per 32 Si-atoms is detected by XPS. Printing 5 mol% mesoporous co-condensed silica on top of mesoporous silica leads to one nitrogen atom per 17 Si-atoms. The reference sample of two printed mesoporous silica layers shows no nitrogen within the XPS. The discussed double layer gravure printed films (Fig. 5) have a film thickness around 280 nm. According to this estimation XPS detects around 10 nm of the entire film.[35]

In Fig. 5 cyclic voltammetry measurements of double layer gravure printed films consisting of one mesoporous silica layer and one mesoporous silica containing 5 mol% of co-condensed (bis(2-hydroxyethyl)-3-aminopropyl-triethoxysilane) are depicted. The cyclic voltammograms for two layer films consisting of two identical layers of mesoporous silica, measured as reference, are comparable to those shown above for one layer with a comparable film thickness (Fig. 5a and 4d) co-condensation of (bis(2-hydroxyethyl)-3-aminopropyl-triethoxysilane) results into inclusion of amino groups with a pK_a value around 8 inducing a change of the mesopore wall charge. This results in a reduced exclusion of the negatively charged probe molecule $[Fe(CN)_6]^{3-/4-}$ at pH 9 visible by a detected j_p of 100 μA cm^{-2} instead of 30 μA cm^{-2} for unmodified mesoporous silica (Fig. 5d). When printing two layers as a step gradient with different functional composition and individual film thicknesses of 140 nm, here mesoporous silica and 5% co-condensed mesoporous silica (Fig. 5b and c), the top layer which is in contact with the probe molecule solution seems to determine the overall transport characteristics. When the 5 mol% co-condensed mesoporous silica film is located on top (Fig. 5b) the observed pore accessibility is very similar to the pure 5 mol% co-condensed mesoporous silica layers (Fig. 5d) showing no exclusion of $[Fe(CN)_6]^{3-/4-}$ at pH 9. But when the unmodified mesoporous silica layer is located on top of a 5 mol% co-condensed mesoporous film the exclusion of negatively charged $[Fe(CN)_6]^{3-/4-}$ at pH 9 is again observed (Fig. 5e).

Experimental section

Mesoporous silica film preparation

Mesoporous silica films are synthesized *via* sol–gel-chemistry using tetraethyl orthosilicate (TEOS) in the presence of the template Pluronic® F127. The precursor solutions (1TEOS : 0.0075F127 : 40EtOH : 10H_2O : 0.2HCl) resulting in 8 nm mesopores or (1TEOS : 0.02F127 : 40EtOH : 34.5H_2O : 0.08HCl)[36] resulting in 16 nm mesopores or ((1 − *x*)TEOS : *x*(bis(2-hydroxyethyl)-3-aminopropyl-triethoxysilane) : 0.0075F127 : 40EtOH : 10H_2O : 0.2HCl) with *x* being between 0 and 25 mol% are stirred for 24 h at room temperature before being used to produce mesoporous silica films by evaporation induced self-assembly (EISA)[13] on silicon wafer, glass, or indium tin oxide coated glass substrates at 40–50% relative humidity and 298 K.

Dip-coating

The mesoporous silica films are dip-coated using varying withdrawal speeds between 0.1 and 30 mm s^{-1}. After deposition the films were kept at 50% relative humidity for 1 h followed by a stabilizing thermal treatment and extraction like for films treated to 200 °C. After successful film deposition a stabilizing thermal treatment is carried out in two successive 1 h steps at 60 and 130 °C. Consecutively, the temperature is increased to 350 °C, or to 200 °C, with a gradient of 1 °C min^{-1}. This final film stabilization temperature is applied for 2 h. Finally, the films treated up to 350 °C are rinsed with ethanol and stored under ambient conditions. Template extraction of the films, treated only up to 200 °C, are treated with acidic ethanol (0.01 M HCl in abs. ethanol) for 3 days to remove the mesopore template.

Gravure printing

The mesoporous silica films are gravure printed using a laboratory scale gravure printing machine G1-5 (IGT Testing Systems) with different gravure cylinder cell volumes between 0.2 and 24 mL m^{-2}. A printing speed of 0.6 m s^{-1} and a printing force of 700 N are used. Freshly deposited films are stored at 50% relative humidity for 1 h. In case of printing two layers the cylinder with 8.5 mL m^{-2} cell volume was used. Between the first and the second layer an aging time of 10 min is used. After deposition of the second layer films were kept at 50% relative humidity for 1 h followed by an identical stabilizing thermal treatment and chemical template extraction used for dip-coated films treated up to 200 °C: after successful film deposition a stabilizing thermal treatment is carried out in two successive 1 h steps at 60 and 130 °C. Consecutively, the temperature is increased to 350 °C, or to 200 °C in case of co-condensed mesoporous silica films, with a gradient of 1 °C min^{-1}. This final film stabilization temperature is applied for 2 h. Finally, the films treated up to 350 °C are rinsed with ethanol and stored under ambient conditions. Template extraction of the films with co-condensed organic groups, treated only up to 200 °C, are treated with acidic ethanol (0.01 M HCl in abs. ethanol) for 3 days to remove the mesopore template.

Infrared spectroscopy (IR)

IR is performed using a Spectrum One (PerkinElmer) instrument in attenuated total reflection mode. The measured spectra are automatically background corrected, measured at glass surface and normalized to the Si–OH vibrational band at 912 cm^{-1}.

Ellipsometry

Film thicknesses and refractive indices are determined on silicon wafer substrates using a Nanofilm EP3 imaging ellipsometer. One zone angle of incidence (AOI) variation measurements are captured between AOIs of 38 and 68° using a 658 nm laser. The relative humidity is constantly adjusted to 15% using a humidity control (ACEflow, Solgelway). The apparent film thickness and refractive indices are calculated from the measured angles Ψ and Δ using the EP4 analysis software supplied with the instrument. The fitting parameters for the silicon oxide layer thickness on the wafer substrate ($d(SiO_x)$ = 2.8 nm) are measured separately. The measured data is fitted with a one-layer box model. The fitting program is allowed to vary film thickness of the mesoporous silica thin films between 100 and 500 nm and the refractive index between 1.1 and 1.7. All films are measured at three defined positions before and after each functionalization step. Changes in film thickness and refractive index are calculated for each specific position. Error bars result from the changes in *n* and *d* at these three different positions. To determine the porosity from refractive indices the Brüggemann effective medium approximation was used as discussed elsewhere.[37,38]

Transmission electron microscopy (TEM)

TEM measurements are recorded using a FEI CM20 TEM microscope with a maximum resolution of 2.3 Å, equipped with a LAB-6 cathode and a charge coupled device camera (Olympus), using an acceleration voltage of 200 kV. Samples are scratched from substrate, dispersed in ethanol and sonicated. Subsequently, the suspension is placed onto a TEM grid.

Scanning electron microscopy (SEM)

Scanning electron microscopy (SEM) micrographs were acquired using a Philips XL30 FEG scanning electron microscope operated at an acceleration voltage of 30 kV. Samples are sputtered prior to analysis with a platinum/palladium layer of 3 nm using a Sputter Coater 208 HR comprising a thickness controller MTM-20 (both Cressington).

Cyclic voltammetry (CV)

Quantitative variations of ionic mesopore permselectivity are studied by following the changes of voltammetric peak currents associated with cationic $[Ru(NH_3)_6]^{2+/3+}$ and anionic $[Fe(CN)_6]^{3-/4-}$ redox probes. Cyclic voltammograms and thus maximum peak currents, are recorded using an Autolab PGSTAT302N (Metrohm). All probe molecule solutions are prepared with a concentration of 1 mM in 100 mM KCl as supporting electrolyte resulting in a pH 5–6 solution besides

measurements shown in ESI (Fig. S7†) which are measured in 150 mmol PBS solution as supporting electrolyte. Acidic or basic conditions (pH 3 and pH 9) are adjusted by adding a drop of a concentrated HCl or NaOH solution directly before starting the measurement. Mesoporous silica films are prepared on indium tin oxide (ITO) coated glass substrates being used as working electrode. An Ag/AgCl electrode (BASi RE-6) serves as reference electrode, and a carbon electrode as counter electrode. Various scan rates between 25 and 1000 mV s^{-1} are measured. The electrode area is 0.21 cm^2. Cyclic voltammetry data are strongly quality controlled by measuring the scanrate of 200 mV s^{-1} at the beginning and at the end of each scanrate variation. Only if both scans are comparable the data are further evaluated. In addition each scanrate is measured three times and the data is only further evaluated if these scans are comparable. Finally, the first pH-value is re-measured for all scanrates after screening all pH-values in between and the data are only further evaluated if the first and the last measurement of one pH series are comparable. For an example please refer as well to Fig. S13 (ESI†).

Contact angle

Macroscopic static contact angle measurements are performed using model TBU90E from company Dataphysics Instruments GmbH with the Program SCA-Software. The static contact angles are measured using a 1 μL s^{-1} rate with a final DI water drop volume of 2 μL.

X-ray photoelectron spectroscopy (XPS)

XP spectra were recorded on a SSX 100 ESCA spectrometer (Surface Science Laboratories Inc.) equipped with a monochromatic Al Kα X-ray source (100 W). XPS analysis reveals peaks at around 103 eV, 154 eV, 200 eV, 285 eV, 400 eV, 533 eV, and 1073 eV, which are attributed to Si2p, Si2s, Cl2p, C1s, N1s, O1s, and Na1s photoemissions, respectively.[39] The observed Si2p, Si2s and O1s peaks are consistent with the presence of silica, whereas the N1s peak originates from the nitrogen in the co-initiator. The presence of small amounts of K, Na, indium and Cl may result from indium-thin-oxide coated glass support substrate.

Conclusions

In summary, this study demonstrates the versatility of gravure printing for preparation of homogeneous, large area and complex architecture mesoporous coatings in comparison to conventionally used dip-coating. The resulting printed mesoporous silica films are more homogeneous and show no substrate rim effects even on very large areas. The fabrication of ultrathin homogeneous films down to a film thickness of 20 nm is possible and film thickness can be tuned by adjusting process parameters such as the printing cylinder cell depth and the contact force. Fast and homogeneous multilayer fabrication with nanoscale thickness resolution has been demonstrated relying on preventing sol incubation into bottom, pre-printed layers due to the controlled, low solution volume applied to the substrate. Thereby, the achieved film properties, such as high porosity and pH-dependent ionic permselectivity, are comparable to dip-coated films. Using co-condensation and different sol compositions for gravure printing enables the fabrication of homogeneous multi-layer films with nanoscale step gradient in porosity, pore size, or layer functionalization and thus charge density. For such multilayer films the ionic permselectivity is influenced by the condensation degree of the mesoporous silica (due to temperature treatment), film thickness, and in case of double layer films with pore sizes below the Debye screening length and layer thicknesses of about 280 nm, seems to be determined by the second layer which is in contact with the probe molecule solution. Based on the advantages of gravure printing for mesoporous film preparation and its potential for automation and complex film architecture design we expect these results to impact scale up and application potential of mesoporous films.

Conflicts of interest

There are no conflicts to declare.

Acknowledgements

The authors acknowledge the Adolf-Messer Stiftung and the DFG grant BR-4806/4-1 for recognition and financial support of this work. The authors thank Karl Kopp for performing XPS-measurements. We especially thank Ulrike Kunz and Prof. Kleebe from the Material Science Department of the Technische Universität Darmstadt for their support with TEM measurements. Prof. Markus Biesalski for access to interface characterization facilities and the Merck Lab @ TU Darmstadt for access to gravure printing machine and sputter coater. Janine Herzog is acknowledged for calculation of pore size distribution. Robert Brilmayer further acknowledges support in the frame of the LOEWE project iNAPO by the Hessen State Ministry of Higher Education, Research and the Arts. Dieter Spiehl thanks the Merck KGaA for financial support through the Merck Lab @ TU Darmstadt. The German Research Foundation (DFG) funded Collaborative Research Centre 1194 "Interaction between Transport and Wetting Processes", Project "C04, C01" is kindly acknowledged for enabling fruitful discussion. This study represents initial work for an ERC Starting Grant (grant agreement number 803758). We acknowledge support by the German Research Foundation and the Open Access Publishing Fund of Technische Universität Darmstadt.

Notes and references

1 A. Walcarius, *Chem. Soc. Rev.*, 2013, **42**, 4098–4140.
2 P. Innocenzi and L. Malfatti, *Chem. Soc. Rev.*, 2013, **42**, 4198–4216.
3 G. J. Soler-Illia and O. Azzaroni, *Chem. Soc. Rev.*, 2011, **40**, 1107–1150.
4 M. E. Davis, *Nature*, 2002, **417**, 813–821.
5 G. M. Whitesides, *Small*, 2005, **1**, 172–179.

6 C. Burda, X. Chen, R. Narayanan and M. A. El-Sayed, *Chem. Rev.*, 2005, **105**, 1025–1102.
7 Y. Piao, A. Burns, J. Kim, U. Wiesner and T. Hyeon, *Adv. Funct. Mater.*, 2008, **18**, 3745–3758.
8 D. Grosso, F. Cagnol, G. J. A. A. Soler-Illia, E. L. Crepaldi, H. Amenitsch, A. Brunet Bruneau, A. Bourgeois and C. Sanchez, *Adv. Funct. Mater.*, 2004, **14**, 309–322.
9 J. Hwang, N. Shoji, A. Endo and H. Daiguji, *Langmuir*, 2014, **30**, 15550–15559.
10 A. Brunsen, A. Calvo, F. J. Williams, G. J. Soler-Illia and O. Azzaroni, *Langmuir*, 2011, **27**, 4328–4333.
11 A. Brunsen, J. Cui, M. Ceolin, A. del Campo, G. J. Soler-Illia and O. Azzaroni, *Chem. Commun.*, 2012, **48**, 1422–1424.
12 C. Sanchez, P. Belleville, M. Popall and L. Nicole, *Chem. Soc. Rev.*, 2011, **40**, 696–753.
13 C. J. Brinker, Y. Lu, A. Sellinger and H. Fan, *Adv. Mater.*, 1999, **11**, 579–585.
14 M. Faustini, C. Boissière, L. Nicole and D. Grosso, *Chem. Mater.*, 2013, **26**, 709–723.
15 E. Bindini, G. Naudin, M. Faustini, D. Grosso and C. Boissière, *J. Phys. Chem. C*, 2017, **121**, 14572–14580.
16 M. Kobayashi, K. Susuki, T. Otani, S. Enomoto, H. Otsuji, Y. Kuroda, H. Wada, A. Shimojima, T. Homma and K. Kuroda, *Nanoscale*, 2017, **9**, 8321–8329.
17 H. Fan, Y. Lu, A. Stump, S. T. Reed, T. Baer, R. Schunk, V. Perez-Luna, G. P. López and C. J. Brinker, *Nature*, 2000, **405**, 56–60.
18 T. Homola, M. Shekargoftar, P. Dzik, R. Krumpolec, Z. Ďurašová, M. Veselý and M. Černák, *Flexible Printed Electron.*, 2017, **2**, 035010.
19 T. T. Baby, M. Rommel, F. von Seggern, P. Friederich, C. Reitz, S. Dehm, C. Kubel, W. Wenzel, H. Hahn and S. Dasgupta, *Adv. Mater.*, 2017, **29**, 1603858.
20 F. Putz, S. Scherer, M. Ober, R. Morak, O. Paris and N. Hüsing, *Adv. Mater. Technol.*, 2018, 1800060, DOI: 10.1002/admt.201800060.
21 E. B. Duoss, M. Twardowski and J. A. Lewis, *Adv. Mater.*, 2007, **19**, 3485–3489.
22 F. Kotz, K. Arnold, W. Bauer, D. Schild, N. Keller, K. Sachsenheimer, T. M. Nargang, C. Richter, D. Helmer and B. E. Rapp, *Nature*, 2017, **544**, 337–339.
23 G. Senlis, M. Dubarry, M. Lejeune and T. Chartier, *Ferroelectrics*, 2002, **273**, 279–284.
24 R. Noguera, C. Dossou-Yovo, M. Lejeune and T. Chartier, *J. Eur. Ceram. Soc.*, 2005, **126**, 133–137.
25 R. Noguera, M. Lejeune and T. Chartier, *J. Eur. Ceram. Soc.*, 2005, **25**, 2055–2059.
26 M. Mougenot, M. Lejeune, J. F. Baumard, C. Boissiere, F. Ribot, D. Grosso, C. Sanchez and R. Noguera, *J. Am. Ceram. Soc.*, 2006, **89**, 1876–1882.
27 B. Fousseret, M. Mougenot, F. Rossignol, J.-F. o. Baumard, B. Soulestin, C. d. Boissière, F. o. Ribot, D. Jalabert, C. Carrion, C. m. Sanchez and M. Lejeune, *Chem. Mater.*, 2010, **22**, 3875–3883.
28 G. Sico, M. Montanino, C. T. Prontera, A. De Girolamo Del Mauro and C. Minarini, *Ceram. Int.*, 2018, **44**, 19526–19534.
29 R. Wilken, I. Pollex, S. Stahl, E. Dörsam, R. Klein and M. Miletić, *Handbook of Paper and Board*, Wiley-VCH Verlag GmbH & Co. KGaA, Weinheim, Germany, 2nd edn, 2013.
30 D. Spiehl, M. Haming, H. M. Sauer, K. Bonrad and E. Dorsam, *IEEE Trans. Electron Devices*, 2015, **62**, 2871–2877.
31 M. Faustini, D. R. Ceratti, B. Louis, M. Boudot, P. A. Albouy, C. Boissiere and D. Grosso, *ACS Appl. Mater. Interfaces*, 2014, **6**, 17102–17110.
32 R. F. S. Lenza and M. L. Vasconcelos, *Mater. Res.*, 2001, **4**, 189–194.
33 G. Giordano, N. Vilà, E. Aubert, J. Ghanbaja and A. Walcarius, *Electrochim. Acta*, 2017, **237**, 227–236.
34 S. Alberti, P. Y. Steinberg, G. Giménez, H. Amenitsch, G. Ybarra, O. Azzaroni, P. C. Angelomé and G. J. A. A. Soler-Illia, *Langmuir*, 2019, **35**, 6279–6287.
35 A. Calvo, P. C. Angelomé, C. Sanchez, D. A. Scherlis, F. J. Williams and G. J. A. A. Soler-Illia, *Chem. Mater.*, 2008, **20**, 4661–4668.
36 D. R. Dunphy, P. H. Sheth, F. L. Garcia and C. J. Brinker, *Chem. Mater.*, 2015, **27**, 75–84.
37 C. Boissiere, D. Grosso, S. Lepoutre, L. Nicole, A. Brunet Bruneau and C. Sanchez, *Langmuir*, 2005, **21**, 12362–12371.
38 J. E. Spanier and I. P. Herman, *Phys. Rev. B: Condens. Matter Mater. Phys.*, 2000, **61**, 10437–10450.
39 J. F. Moulder, W. F. Stickle, P. E. Sobol and K. D. Bomben, *Handbook of X-ray Photoelectron Spectroscopy*, Physical Electronics Inc., USA, 1995.

4.2. Iniferter initierte, kontrollierte Polymerisation von PMEP und PDMAEMA in mesoporösen Silicadünnfilmen

Mesoporöse Silicadünnfilme und deren Modifikation mit organischen Funktionalitäten haben sich in den letzten Jahren zu einem faszinierenden Forschungsfeld entwickelt, um Fragestellungen in der Sensorik, der Medikamentenfreisetzung oder auch bei Trennprozessen zu adressieren.[6, 203] In vielen Anwendungen sogenannter *Smart Materials* spielt die Steuerung von Transport, von z.B. Ionen oder Molekülen, eine Schlüsselrolle. Um hybride mesoporöse Silicafilme nutzen zu können, bedarf es jedoch eines sehr präzisen Porendesigns hinsichtlich der Porenfüllung und der Ladungsdichte in den Mesoporen. Um diese Anforderungen zu erfüllen, wurden die in Kapitel 4.1 hergestellten Silicafilme im weiteren Verlauf dieser Arbeit als Basismaterial zur Funktionalisierung mit pH-responsiven Polymeren eingesetzt. pH-responsive Polymermodifikationen werden häufig für die kontrollierte Steuerung von Transport auf der Nanoskala eingesetzt (siehe auch Kapitel 2.3 und 2.4).[15] Ein wichtiger Aspekt bei der Herstellung von funktionalen Silicamaterialien ist neben der Wahl der chemischen Funktion, die in das Silica eingebracht wird, auch die Zahl der funktionalen Gruppen, um damit die Porenfüllung zu kontrollieren. Hierfür eignen sich besonders polymerbasierte Funktionalisierungen, da nicht nur die Pfropfdichte, sondern auch die Kettenlänge zur Anzahl an funktionalen Gruppen im Silicamaterial beiträgt. Die mit pH-responsiven Polymeren funktionalisierten mesoporösen Silicafilme wurden abschließend durch cyclovoltammetrische Untersuchungen hinsichtlich ihres pH-abhängigen Ladungsaufbaus untersucht. Das pH-abhängige Verhalten von Polymerketten in Mesoporen hinsichtlich ihres Ladungsaufbaus ist insofern interessant, dass es durch die nanoskalige Umgebung zu Verschiebungen des apparenten pH-Wertes kommt. Das bedeutet, dass sich der pH-Wert in einer Mesopore deutlich von dem pH-Wert einer die Mesopore umgebenden Bulklösung unterscheiden kann.[21, 24] Der apparente pH-Wert führt in der Konsequenz zu verschobenen Säure-Base-Gleichgewichten. Um diese besser verstehen und vorhersagen zu können, müssen polymermodifizierte Silicamesoporen experimentell untersucht werden. Cyclovoltammetriemessungen können indirekt dazu verwendet werden, die durch das Nanoconfinement induzierte Verschiebung der Polymer pK_s-Werte im Vergleich zu den Monomer pK_s-Werten zu bestimmen, indem von der ermittelten Permselektivität Rückschlüsse auf den Ladungszustand geschlossen werden.

Auf Basis von Vorarbeiten durch Laura Silies[87] wurde die auf dem Photoiniferter (N,N(diethylamino)dithiocarbamoyl-benzyl(trimethoxy)silane (SBDC) basierte Polymerisation ausgewählt, da sich über dieses Polymerisationssystem die Polymermenge in den Silicamesoporen sehr gut steuern lässt. Als Monomere wurden, aufgrund ihrer Multiresponsivität sowie Mehrfachladung, das pH- und temperaturresponsive Poly(2-(dimethylamino)ethylmethacrylat (PDMAEMA) und das zweifache Ladung tragende, pH-responsive Poly(2-(methacryloxy)ethylphosphat) (PMEP) ausgewählt.

Im ersten Schritt wurde der Iniferter SBDC über *post grafting* in das mesoporöse Silica eingebracht. Im nächsten Schritt konnte gezeigt werden, dass die Monomere DMAEMA und MEP in organischen Lösemitteln und in wässriger Lösung hinsichtlich der Polymermenge kontrolliert polymerisiert werden können, wodurch es möglich ist, die Porenfüllung graduell einzustellen. Die Kontrolle der Polymermenge gelang in unterschiedlichen Mesoporengrößen mit Porendurchmessern von ca. 8 bzw. 16 nm. Die Polymermenge konnte durch Variation der Reaktionsparameter Monomerkonzentration und Belichtungsdauer zwsichen 5 und 20 Minuten gesteuert werden. Hinsichtlich nachhaltigerer Reaktionsführung konnte gezeigt werden, dass unter Verwendung des Iniferters SBDC in wässriger Lösung MEP durch Bestrahlung der Probe mit Sonnenlicht polymerisiert werden kann. Dies bietet eine Alternative, in Zukunft Polymerisationen auf Oberflächen ohne Einbringen von künstlich hergestellter Energie zu realisieren.

Um nachzuweisen, dass die Polymerfunktionalisierung nicht nur in der Nähe der Filmoberfläche, sondern entlang der gesamten z-Achse (Filmdicke) des mesoporösen Silicafilmes stattfindet, wurde in einer Kooperation mit der BASF SE erstmalig durch eine Kombination aus Kryo-Transmissionselektronenmikroskopie-(TEM)-Messungen und Energiedispersiver Röntgenspektroskopie (EDX)-*Mapping* gezeigt, dass Photoinferter basierte Polymerisationen in den verwendeten mesoporösen Silicafilmen zu einer homogenen Polymerverteilung des phosphathaltigen PMEP entlang der Filmdicke des mesoporösen Films führt.

Die hergestellten und charakterisierten PDMAEMA und PMEP funktionalisierten mesoporösen Silicafilme wurden dann eingesetzt, um zu untersuchen, wie nanoskalige Umgebungen den pH-Wert und die apparenten pK_s-Werte der Polymerwiederholungseinheiten beeinflussen. Hierzu wurden die funktionalisierten mesoporösen Silicadünnfilme auf einem leitenden ITO-Substrat hergestellt, wodurch es möglich ist, sie für cyclovoltammetrische Messungen (siehe Kap 2.6) zu verwenden. Werden die Silicafilme in wässriger Lösung inkubiert und die ITO-Schicht benetzt, ist in diesem Verfahren eine relative Bestimmung der Probenmolekülkonzentration an der ITO-Elektrode, also hinter dem Silicafilm, sehr gut möglich. Die verwendeten Monomere DMAEMA und MEP sind beide pH-responsiv und besitzen in Lösung pK_s-Werte von respektive 7.6 und 4.5/7.5. Die Verwendung von orthogonal zu den Wiederholungseinheiten geladenen Probenmolekülen erlaubt es so, die Permselektivität in Abhängigkeit vom pH-Wert zu untersuchen und die apparenten pK_s-Werte zu bestimmen. Diese Untersuchungen zeigten, sowohl für PDMAEMA als auch für PMEP modifizierte Silicafilme, dass der Aufbau von Ladung von den Systemen vermieden wurde. Dies zeigte sich in einer Verschiebung der bestimmten pK_s-Werte von 1-2 pH-Einheiten (pK_s PDMAEMA 8.4 → 7.7; pK_{s1} PMEP 4.5 → 6.6). Für das PMEP war der zweite pK_s-Wert durch diese Methode nicht mehr bestimmbar, was bedeutet, dass der Aufbau einer zweiten Ladung energetisch so ungünstig ist, dass der zweite pK_s-Wert zu pH-Werten außerhalb des Messbereichs verschoben wird. Die Beobachtungen, dass sich die apparenten pK_s-Werte im räumlichen Confinement zu extremen pH-Werten verschieben, decken sich auch mit Simulationen der Szleifer-Gruppe. In der Arbeit von *Gilles et al.* wird für PMEP-Gruppen in einem Nanokanal mit einem

Diameter von ~10-290 nm der apparente pK_s-Wert berechnet, wobei Unterschiede zwischen Bulk und apparentem pKs-Wert von 1-2 pH-Einheiten vorhergesagt werden (pK_{s1} 4.5 →5.8 und pK_{s2} 7.7 →9.7).[24] Da die von mir verwendeten Mesoporen noch deutlich kleiner sind als der simulierte Nanokanal, ist es nicht verwunderlich, dass für die pK_s-Werte der MEP-Gruppen eine noch größere Verschiebung des apparenten pK_s-Wertes beobachtet wird.

Für die in meiner Arbeit durchgeführten Untersuchungen zur Verschiebung des apparenten pK_s-Wertes der PDMAEMA Wiederholungseinheiten gibt es keine Vergleichsstudien. Da in diesem Fall der apparente pK_s-Wert des PDMAEMA in den Silicamesoporen jedoch in die entgegengesetzte Richtung verschoben wird als für die PMEP Funktionalisierung, folgen auch diese Ergebnisse den Erwartungen. Im Weiteren wurden für die PDMAEMA modifizierten mesoporösen Silicafilme der Einfluss von unterschiedlicher Polymermenge und Salzkonzentration der Messlösung untersucht. Beide Parameter zeigten einen messbaren Einfluss auf die Verschiebung des pK_s-Wertes. Sowohl eine hohe Porenfüllung als auch eine niedrige Salzkonzentration der Messlösung verstärken den *Confinement*-Effekt und führen im Vergleich zu den initialen Experimenten zu einer noch stärkeren Verschiebung des apparenten pK_s-Wertes.

In einer Kooperation mit der BASF SE konnte zudem in ersten Versuchen die Relevanz des Einflusses von nanoskaliger Umgebung auf Moleküle, die für Anwendungen in Silicamesoporen inkorporiert sind, gezeigt werden. Am Beispiel der Lipase *Aspergillus oryzae,* welche von Adnan Khalil (AG Andrieu-Brunsen, TU Darmstadt) in Nanopartikeln eingelagert wurden, konnte von Sonja Kübelbeck (BASF SE) gezeigt werden, dass das Enzym nach Einlagerung in Silicamesoporen bei einem pH-Wert, der bei dem das Enzym in Lösung stabil ist, einen enormen Aktivitätsverlust aufzeigte.

Mein Beitrag zu der Veröffentlichung beinhaltet die Herstellung der mesoporösen Filmen mit einstellbaren Porengrößen und deren Polymermodifikation mit PMEP und PDMAEMA. Zusätzlich wurden von mir die Proben für die in der BASF durchgeführten Kryo-TEM/EDX-Messungen präpariert. Von mir wurden auch sämtliche pH-abhängigen Cyclovoltammetrie-Messungen durchgeführt, durch die die Ermittlung der apparenten pK_s-Werte von PDMAEMA und PMEP in Silicamesoporen möglich waren.

Die Ergebnisse des Abschnittes 4.2 sind in *Advanced Materials Interfaces* veröffentlicht:

R. Brilmayer, S. Kuebelbeck, A. Khalil, M. Brodrecht, U. Kunz, H.-J. Kleebe, G. Buntkowsky, G. Bayer, A. Andrieu-Brunsen, **Influence of nanoconfinement on the pKa of polyelectrolyte functionalized silica mesopores**, *Adv. Mat. Interf.*, **2020**, 1901914.

Die *Supporting Information* ist nicht abgedruckt, aber in der elektronischen Version dieses Artikels (DOI: 10.1002/admi.201901914) verfügbar.

ADVANCED MATERIALS INTERFACES
www.advmatinterfaces.de

Influence of Nanoconfinement on the pKa of Polyelectrolyte Functionalized Silica Mesopores

*Robert Brilmayer, Sonja Kübelbeck, Adnan Khalil, Martin Brodrecht, Ulrike Kunz, Hans-Joachim Kleebe, Gerd Buntkowsky, Grit Baier, and Annette Andrieu-Brunsen**

Functionalized ordered mesoporous materials are relevant in technologies, such as drug release, sensing, and separation. To design functionality, the silica framework can be functionalized with responsive molecules or polymers. Often, the pH value in those hybrid materials determines performance. Even though pH/pKa differences between polymers in bulk solutions and nanoscale confinement have been observed, the influence of confinement on pH- and pore filling dependent polyelectrolyte oligomer chain charge has yet not been investigated systematically. Here, mesoporous silica films are functionalized with (2-dimethylamino) ethyl methacrylate) (DMAEMA) and 2-(methacryloyloxy)ethyl phosphate (MEP) oligomers using photoiniferter initiated polymerization. This approach allows a controlled and environmentally friendly mesopore functionalization in water. The obtained oligomer functionalized pores are tunable with respect to pore filling. For both, poly(2-(dimethylamino) ethyl methacrylate) (PDMAEMA) and poly(2-(methacryloxy)ethyl phosphate) (PMEP), the charge generation inside mesopore confinement is significantly delayed toward harsher pH conditions resulting in pKa shifts of 1–2 pH units. Polymer amount and ionic strength show to further influence the pKa of PDMAEMA in mesopores. The technological importance of the pH value in confinement and its effect on enzyme stabilization is demonstrated. Lipase from *Aspergillus oryzae* loses its activity upon encapsulation in silica nanoparticles at pH values where the enzyme is stable in bulk solution.

1. Introduction

Mesoporous silica materials have been established in various technologies, such as water management or biomedical applications.[1] Its high and tunable stability makes silica an ideal host for active ingredients or enzymes. Rendering a variety of applications, such as drug delivery or biocatalysis accessible.[2] In addition, mesoporous silica offers a wide variety of transport characteristics achieved by introducing organic functions into the silica framework. Those silica hybrid materials are a common motive in separation processes, drug delivery, or sensor technology.[3] Key properties, such as high specific surface area, stability, adjustable pore geometries, as well as high diversity regarding surface chemistry allow their application in such diverse areas.[4]

Especially the responsive, so-called smart, organo–silica materials have been established as a new fascinating field of research over the last decades.[5] Using responsive polymers, gates are created in silica nanopores which react to triggers, such as light,[6] pH,[7] or temperature[8] and thus control pore accessibility, transport, or the release of drugs.[9] Applications for mesoporous silica strongly depend on charge generation and the corresponding gating behavior of the mesopores, which result from interactions with pH adjusted solutions.

Controlled polymerization and thus precise control on pore filling and charge density in nanopores has been demonstrated by atom transfer radical polymerization, reversible addition-fragmentation chain transfer, or surface initiated photoiniferter polymerization.[10] Only very recently it has been shown that not only the amount of polymer but also the architecture of the polymer chains can be controlled and block-cooligomers in pores can be generated.[10a,11] Thereby, pH responsive polymers

R. Brilmayer, A. Khalil, Prof. A. Andrieu-Brunsen
Ernst-Berl-Institut für Technische und Makromolekulare Chemie
Technische Universität Darmstadt
Alarich-Weiss-Str. 12, 64287 Darmstadt, Germany
E-mail: andrieu-brunsen@smartmem.tu-darmstadt.de

The ORCID identification number(s) for the author(s) of this article can be found under https://doi.org/10.1002/admi.201901914.

DOI: 10.1002/admi.201901914

S. Kübelbeck, Dr. G. Baier
BASF SE
67056 Ludwigshafen, Germany
Dr. M. Brodrecht, Prof. G. Buntkowsky
Eduard-Zintl-Institut für Anorganische und Physikalische Chemie
Technische Universität Darmstadt
Alarich-Weiss-Str. 8, 64287 Darmstadt, Germany
U. Kunz, Prof. H.-J. Kleebe
Institut für Angewandte Geowissenschaften
Technische Universität Darmstadt
Schnittspahnstraße 9, 64287 Darmstadt, Germany

are most extensively investigated.[5c,12] A wide range of pH responsive polymers, such as poly(vinylpyridine) (PVP), poly(2-(dimethylamino)ethyl methacrylate) (PDMAEMA), poly(acrylic acid) (PAA) are reported. Additionally multicharged polymers, such as (2-(methacryloyloxy)ethyl phosphate) (MEP), carboxybetaine methyl acrylate (CBMA) or block copolymers of PDMAEMA-*b*-PMEP have been polymerized in nanoporous materials and their gating properties have been studied in detail.[5d,e,9c,d,10a,11–13] They have also been proven to be particularly suitable for drug-release applications, as differences in the physiological pH value can be used and no additional external stimulus is required.[14] Due to the importance and the influence of spatial confinement on the pH-value and thus on the performance of silica hybrid material mesopores it is essential to be able to understand and predict the charge density in nanoscale pores. Although within the last years several studies have observed pH differences between nanoscale confinement and bulk solutions,[5d,15] it is not yet possible to exactly predict or measure pKa values in functional mesopores. Very recently Szleifer and co-workers have theoretically investigated protonation equilibria of PMEP brushes in nanochannels in detail.[9b] Additionally, Vilà et al. showed by cyclic voltammetry measurements the influence of pH and ionic strength toward transport through unmodified mesoporous silica films.[16] Inspired by those studies and the relevance of pH in various applications we herein experimentally address mesopore charge generation of weak polyelectrolyte oligomer filled silica mesopores in dependence of solution pH through electrochemical cyclic voltammetry studies. The use of cyclic voltammetry together with probe molecules, such as, $[Fe(CN)_6]^{3-/4-}$ and $[Ru(NH_3)_6]^{2+/3+}$ is a well-established method to investigate perm selectivity of mesoporous silica materials and has been employed for more than a decade.[16,17] As polymers we choose PMEP and PDMAEMA, representing a negatively, and positively chargeable polyelectrolyte, demonstrate their controlled polymerization in silica mesopores (pores <16 nm) and present a green chemistry approach using sun light as light source and water as solvent. The mesoporous silica films are structurally equivalent to SBA-15 silica nanoparticles that are commonly used as drug or enzyme carriers.[2b,18] Using lipase from *Aspergillus oryzae*, we also show an exemplified impact of confinement-based pH-shift as the enzyme activity is lost through encapsulation in mesoporous silica nanoparticles under conditions in which the enzyme is actually stable in solution.

2. Mesoporous Silica Thin Film Preparation

To investigate solution pH-dependent charge density and thus pKa in spatial confinement mesoporous silica thin films were functionalized with the pH responsive polymers polydimethylaminoethyl methacrylate and poly 2-(methacryloyloxy) ethyl phosphate (**Figure 1**). Mesoporous silica thin films with two different pore sizes were used, generated through variation of the Pluronic F127 template concentration, adapting a method from Dunphy et al. to film preparation by evaporation induced self-assembly and dip-coating.[4d] Transmission electron microscopy (TEM) images (Figure 1) show the enlarged pore openings of ≈12 nm for the so-called big pore (BP) films, produced with higher Pluronic F127 template concentration, while the structure for a film produced with a lower template concentration results in small pore (SP) openings of ≈3 nm. The mesoporous silica films were produced through dip coating with a withdrawal speed of 2 mm s^{-1}, leading to significantly different film thicknesses of around 200 nm for SP films and 500–600 nm for BP films. In addition to the film thickness the porosity of the SP and BP films

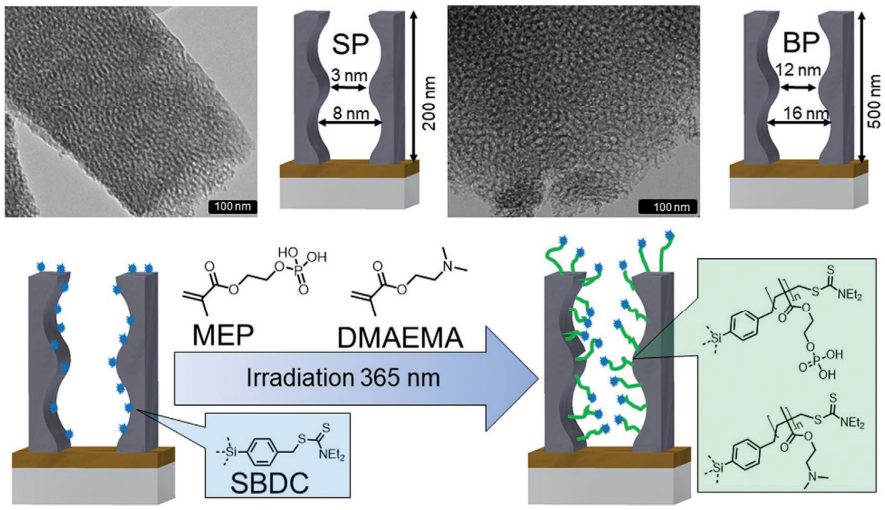

Figure 1. TEM images and schematic illustration of the different mesoporous silica films used in this study (left side SP films, right side BP films). Bottom: Schematic illustration of the polymer modification, of mesoporous silica with photoiniferter initiated polymerization using MEP and DMAEMA as monomers. The schematic illustration of the film structure is simplified, see Figure 2a.

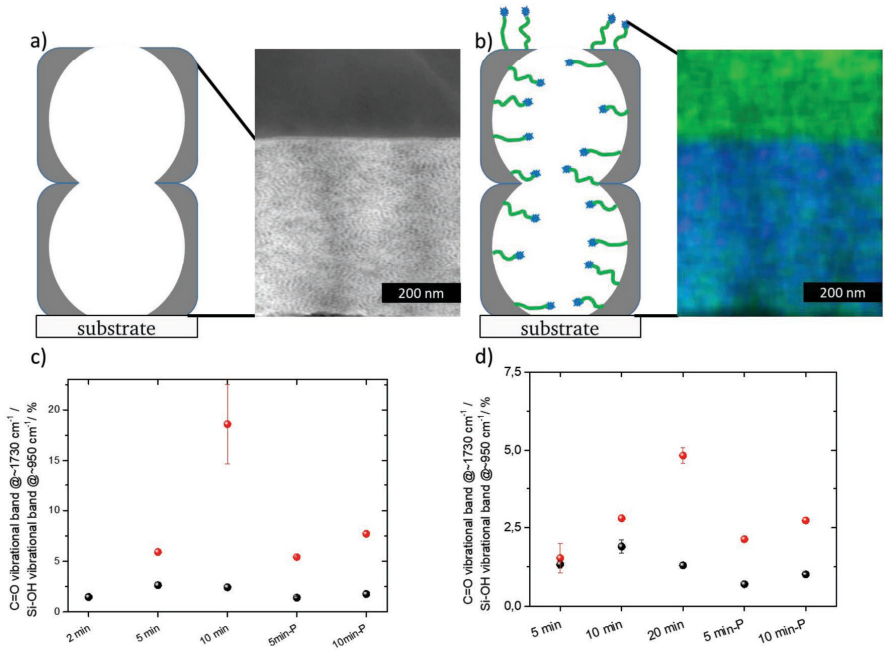

Figure 2. a) HAADF-TEM image of the cross-section of an SP mesoporous silica thin film. b) EDX Mapping of the cross section of a PMEP modified mesoporous silica SP film (green color: phosphorous; blue color: sulfur). c,d) Black spheres correspond to polymer amount in SP films; red spheres correspond to polymer amount in BP films; -P correspond to CO_2-Plasma treated films. c) Polymer amounts achieved by variation of polymerization conditions using PMEP as monomer in water. d) Polymer amounts achieved by variation of polymerization conditions using PMEP as monomer in DMF. The schematic illustration of the film structure is simplified, see (a).

were determined by ellipsometry using the effective medium approximation.[19] As systematically investigated in a previous study, porosity is not affected by withdrawal speed and film thickness[20] and was here determined to be in the range of 68 vol% for BP films and in the range of 40–50 vol% for SP films (Tables S1 and S2, Supporting Information).

3. Polymer Functionalization of Mesoporous Silica Thin Films

To explore the influence of spatial confinement on charging of mesopores and thus on the apparent pKa value of weak polyelectrolyte functionalized mesopores PDMAEMA and PMEP functionalized mesopores were prepared. DMAEMA was chosen as positively charged monomer, while the negatively chargeable MEP was chosen since theoretical data on pKa shifts are available from Gilles et al.,[9b] and because it can carry two charges per repetition unit allowing to investigate complex charge situation within the spatial confinement of mesopores. (N,N(diethylamino) dithiocarbamoylbenzyl(trimethoxy)silane (SBDC) as photoiniferter was covalently grafted to the silica mesopore wall following a previously reported and well-established procedure allowing a controlled polymerization in nanoconfined pores.[10a,b,11] This grafting process resulted into a photoiniferter density of 0.7 molecules*nm^{-2} as already reported in a previous study.[11] Besides initiator density the polymer distribution is essential for subsequent transport and pH investigations. **Figure 2**a) shows a BP mesoporous silica thin film which was functionalized with PMEP, transferred from an indium tin oxide (ITO)-coated glass substrate to a polyethylene terephthalate (PET) foil, following a procedure by Lin et al.,[21] subsequently characterized by TEM and energy-dispersive X-ray spectroscopy (EDX) mapping of thin microtome cuts. Through combination of TEM and EDX it was possible to individually visualize the sulfur atoms of the SBDC iniferter (blue color, Figure 2b) and the phosphorous of the PMEP (Figure 2b, green color). The image clearly shows a mixture of blue and green inside the mesoporous film, indicating rather short chains and the presence of the iniferter SBDC as well after PMEP functionalization. In contrast to the mesopore walls the outer surface of the mesoporous silica film the predominant color is green indicating longer oligomer chains and thus a larger relative amount of phosphorous as compared to inside the mesopores. Simultaneously this indicates that the iniferter end group appears to diffuse into the solution resulting in a reduced concentration of detected sulfur. This dilution of terminating end group would lead to reduced control over the polymerization on the outer film surface.

Additionally, Figure 2d shows the increase of the PMEP amount with increasing irradiation time using SP films. The time dependence applies to SP mesoporous silica films with photoiniferter grafted on top as well as inside the mesoporous film and to mesoporous films which have been subjected to a CO_2-plasma treatment after SBDC grafting, removing the organic moieties on the outer mesoporous film surface (named "-P" in Figure 2c,d). The polymer amount was determined by ATR-IR measurements comparing the polymer C=O vibrational band (1720 cm^{-1}) to the Si–OH vibrational band (950 cm^{-1}) originating from the mesoporous silica film supported on glass substrates. Regardless of the polymerization solvent (dimethylformamide (DMF) and H_2O were investigated in depth) the polymer amount did increase already for short polymerization time between 5 and 10 min under the applied reaction conditions. For the SP films (black spheres in Figure 2d,c) a maximum C=O vibrational band intensity and thus a maximum PMEP amount was obtained at around 2.5% relative to the Si–OH band at 950 cm^{-1}, while the BP films reached up to 5% in DMF and in water even up to 20%. As shown in Tables S1 and S2 (Supporting Information) the porosity and polymer pore filling of the mesopores was determined by ellipsometry measurements using a one layer fitting model. The SP films showed porosities of 40–50 vol%. Applying polymerization times of 5 and 10 min pore fillings of 50–60 vol% were obtained. This correlates with ATR-IR measurements, showing very similar C=O band intensities of 2.5% for those two samples (Figure 2c). Even higher pore fillings could be achieved using the very porous (70 vol%) BP films. After 10 min of irradiation the mesopores were filled by 80 vol%. Besides polymerization time the concentration of the monomer in the polymerization solution can be easily adjusted. A DMF solution of 0.6 M MEP was irradiated 10 min using a BP and a SP film (Figure S2, Supporting Information). The polymer amount for the SP film did only increase marginally compared to the otherwise applied 0.125 M MEP concentration. On the other hand, using the BP film the polymer amount did almost triple using 0.6 M MEP resulting in a relative polymer C=O stretching band intensity of 7% as compared to the 2.5% using a 0.125 M MEP concentration.

With diminishing natural resources sustainability of chemical reactions should be improved. Ionic methacrylates are well soluble in water, whereas SBDC or its analogon BDC are not water soluble. Through surface attachment this problem is easily avoided, since the iniferter is homogeneously distributed along the silica film, and covalently attached. The combination of SBDC functionalized mesoporous silica films and MEP dissolved in water did allow to perform a homogeneous polymerization with the same degree of control (Figure 2c) compared to conventional solvents, such as DMF (Figure 2d). In addition, it was possible to produce responsive hybrid materials by subjecting the iniferter modified mesoporous silica film in a water solution in the sun light which did lead to large amounts of PMEP on SP and BP mesoporous silica films with C=O stretching band as high as 120% relative to the Si–OH band of the glass substrate. By combining water and sun light it has thus been possible to enhance the ecological footprint in regards to two key parameters of polymerizations.

4. pH-Dependent Mesopore Accessibility: pH in Confinement

pH-dependent mesopore accessibility was studied with cyclic voltammetry measurements while titrating the solution pH. The different charged states of PMEP grafted silica mesopores and thus their permselectivity toward positively charged ions are illustrated in **Figure 3**a). At acidic solution pH the mesopore is expected to be neutral and gradual increase of the solution pH value leads to the MEP monomers carrying one negative charge per monomer (monomer $pKa_1 = 4.5$) and finally two charges per monomer ($pKa_2 = 7.7$).[9h] The pH dependent cyclic voltammograms for PMEP functionalized mesoporous Silica films are shown in Figures S4–S6 (Supporting Information). Measurements were conducted with solution pH values ranging from 2 to 11 (Figure 2b) and using $[Ru(NH_3)_6]^{2+/3+}$ as probe molecule to investigate the gating behavior toward cations. Measuring time was adjusted to below 10 min to guarantee stability.[22] The obtained peak current density (j_p) values were plotted against the adjusted solution pH value and subjected to an empirical Boltzmann-fit (for details see Tables S3–S5, Supporting Information). The resulting turning point of the fit was set equal to the pKa value of the MEP polymer modification (Figure 3c). Using this method different polymerization times as well as BP and SP films were investigated and resulted in a median mesopore pKa_1 value of 6.9 ± 0.5, corresponding to a higher pKa shift of 2.5 pH units compared to solution pKa. This shift is even higher than predicted in theoretical studies by Gilles et al. who observed a shift of 1.2 pH units for the first pKa value (apparent pKa1 = 5.81, pKa2 = 9.67).[9b] The observed difference might result from differences between the here presented experimental study and the used parameters within the theoretical study by Gilles et al.,[9b] such as a slight difference in polymer chain length and background electrolyte. In addition, our experimental results clearly do not show a 2nd increase of the j_p values in the range of pKa_2. This might be due to an even further shifted 2nd pKa of PMEP in the mesoporous silica and thus even the solution with the highest pH of 11 was not sufficiently basic to generate the second PMEP charge, or the charge generation of both forms are merged and are not distinguishable from each other. The signal broadening observed for basic pH values indicates strong electrostatic interactions between the PMEP and the countercharged $[Ru(NH_3)_6]^{2+/3+}$ probe molecule. Due to the limited pH-stability of silica at pH values >9 samples with even higher basic pH-values could not be investigated.

To investigate the effect of positive charge generation within the spatial confinement of silica mesopores, PDMAEMA was selected. PDMAEMA represents an ideal second candidate for this model since it is a widely used polymer in the context of responsive surface modifications.[10d,23] The pH-dependent charging and the corresponding gating behavior of PDMAEMA modified mesoporous silica is shown in **Figure 4**a. Each DMAEMA repetition unit can generate one positive charge. Since DMAEMA is orthogonally charged to eventually remaining silanol groups from the mesopore walls, the silanol groups may reduce the obtained j_p values. By performing cyclic voltammetry measurements using the negatively charged $[Fe(CN)_6]^{3-/4-}$ probe molecule, the observed preconcentration at

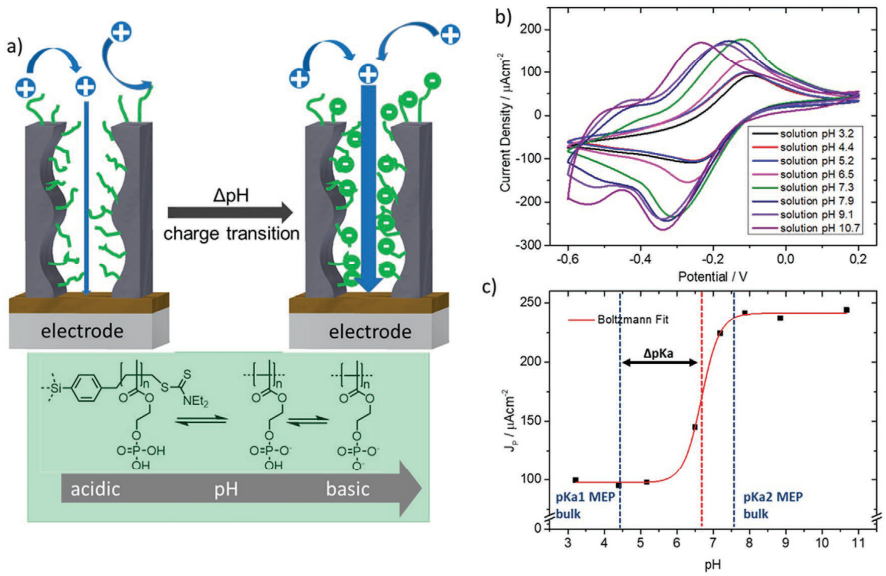

Figure 3. a) Schematic illustration of cation selectivity for a PMEP modified mesoporous silica film for different charge states. b) Cyclic voltammograms of a PMEP modified mesoporous silica film at different pH values using 1×10^{-3} M $[Ru(NH_3)_6]^{2+/3+}$ as probe molecule. Scanrate 100 mVs^{-1}. c) j_p values obtained from measurements in Figure 2b) plotted against the measurement solution pH. PMEP pka values indicated with blue dashed line and apparent pka value, obtained from Boltzmann Fit, indicated with red dashed line. The schematic illustration of the film structure is simplified, see Figure 2a.

acidic pH (Figure 4c,d j_p@pH 1.8 >> j_p@pH 10.4) can clearly be attributed to the positive DMAEMA charges. The pH response and thus the ionic pore accessibility of PDMAEMA modified SP film was investigated by gradually changing the solution pH, which is shown in Figure 4b). As shown in Figure S15 (Supporting Information) during the short measurement times applied at extreme pH values the film remains stable and can be reversibly switched between the charged and uncharged state. Starting at basic solution pH of 10.4, at which PDMAEMA are expected to be mostly neutral a peak current density (j_p) of only 30 µA cm^{-2} is detected, indicating that barely any probe molecules are infiltrating the mesopores reaching the below located electrode. Upon pH variation toward acidic solution pH the j_p gradually increases by a factor of >20 to reach a current peak density of 700 µA cm^{-2} at pH 1.8. In addition, the redox peak potential shifts slightly, which indicates electrostatic attraction between the functionalized mesopore and the countercharged probe molecules. The charge transition occurs over a very broad pH range of almost 5 pH units, which is, in accordance with the theoretical studies by Szleifer and co-workers,[5d] attributed to the nanoscale confinement. Performing a Boltzmann Fit (Table S6, Supporting Information) (red line in Figure 4c), of the obtained j_p values plotted against the measurement solution pH, an apparent pK_a of 7.7 is determined (red dashed line Figure 4c). This indicates a shift of the DMAEMA pK_a compared to the one of DMAEMA in bulk solution (pK_a = 8.4) of almost 1 pH unit toward more acidic pH. Performing this type of experiment for different polymerization conditions did lead to pK_a values of 7.6–7.9 (Figures S9 and S10, Supporting Information) indicating a slightly stronger pK_a shift with increasing polymer amount. Although a change in the polymer amount did lead to distinguishable pK_a values it has to be noted that the variation is not very pronounced and difficult to separate from the error of pKa determination. Based on previous findings this only minor influence of polymer amount variation has to be expected since the chain length variation of oligomers in SP mesoporous systems between a median filled pore (≈50%) and highly filled pores (>90%) is not larger than 2–3 repetition units as determined in a previous study.[10b,11] Additionally, since the mesopore necks are only ≈3 nm wide and very probably partially blocked by polymer regardless of the polymer amount and pore filling degree ions that enter the pore are in the range of the Debye screening length and thus subjected to the strong influence of the electric double layer.[15] To reduce or to enhance the influence of the electric double layer two different parameters of this model system were further investigated: As a first approach pore size of the mesoporous silica films was varied in the sub 20 nm domain comparing SP and BP films as mentioned above. As a second parameter the ionic strength of the pH solution was reduced from 150×10^{-3} M to 30×10^{-3} M which leads to an increase of the electric double layer from ≈0.9 to ≈1.8 nm.

In Figure S14 (Supporting Information), the pH-dependent permselectivity of SP and BP films with different polymer amounts or ionic strength are depicted. Figure S14a, Supporting Information) shows the obtained peak current density of a SP

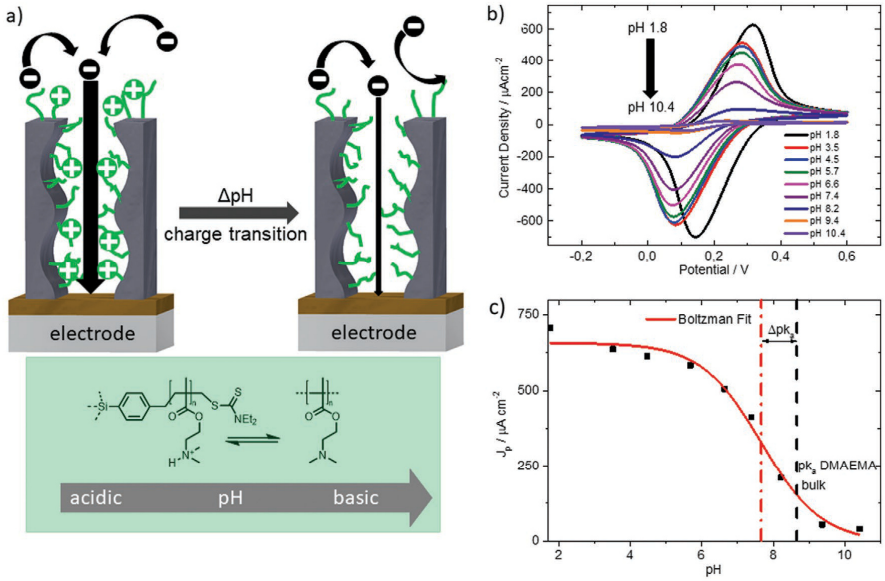

Figure 4. a) Schematic illustration of cation selectivity for a DMAEMA modified mesoporous silica film for different charge states. b) Cyclic voltammograms of a PMEP modified mesoporous silica film at different pH values using 1×10^{-3} M $[Fe(CN)_6]^{3-/4-}$ as probe molecule. Scanrate 100 mVs^{-1}. c) j_p values obtained from measurements in b) plotted against the measurement solution pH. DMAEMA pKa value indicated with blue dashed line and apparent pka value, obtained from Boltzmann Fit, indicated with red dashed line. The schematic illustration of the film structure is simplified, see Figure 2a.

film with 1.5 % C=O vibrational band intensity (Figure S14a, black spheres, Supporting Information) and 4.1% (Figure S14a, blue spheres, Supporting Information) in dependence of the solution pH. A significant shift between the black and blue curve in Figure S14a (Supporting Information) is observed. In addition, the peak current density of the higher PDMAEMA amount (Figure S14a, blue spheres, Supporting Information) starts to increase at slightly higher pH values as compared to the lower PDMAEMA amount (Figure S14a, black spheres, Supporting Information). The obtained pKa values of 7.9 and 7.6, respectively, correspond to this observation and indicate the effect and correlation of spatial confinement and polymer amount/pore filling. The observed trends are in accordance with theoretical results[9b] related to PMEP modified nanochannels and show that higher charge densities in nanoscale confinement are energetically less favored and thus more difficult to establish as compared to bulk solution. This explains the observed pKa-shift with increasing PDMAEMA amount by 0.3 pH units toward more acidic conditions.

The BP films were investigated in a similar experiment. The pH-dependent peak current density depicted in Figure S14b (Supporting Information) correspond again to different PDMAEMA amounts C=O vibrational band intensity of 4.9% (Figure S14b, black spheres, Supporting Information) and 15.7% (Figure S14b, blue spheres, Supporting Information). The difference in the pH-dependent peak current density upon increasing relative PDMAEMA amount is much less pronounced as compared to the smaller mesopores (Figure S14a, Supporting Information). Nevertheless, two different pKa values of 7.3 and 7.5 for the lower and higher PDMAEMA amount were obtained. Two conclusions can be drawn from the comparison between PDMAEMA amounts and pore sizes: The maximum current density increases with increasing relative amount of PDMAEMA in the mesopores by a factor of 3 in the case of the SP films and by almost a factor of 5 for the BP films at acidic pH. This shows that with increasing PDMAEMA amount the number of charges increases resulting in an increase of electrostatically attracted counter charged probe molecules which are not hindered to enter the pores albeit the increasing pore filling. This observation is in agreement with previous work of our group related to strong polyelectrolyte poly([2-(methacryloyloxy)ethyl]trimethyl ammonium chloride) (PMETAC) and polycarboxybetaine methyl acrylate (PCBMA).[7a,10b,24] As a second conclusion, the overall median pKa shift for the BP films with two different PDMAEMA amounts is larger (7.4) than for the SP films (7.7). For the investigated porous systems (SP and BP films) with variable polymer amounts, according to C=O vibrational band intensities (1.5–15.7%) influences the apparent pKa of PDMAEMA by a smaller degree than the PDMAEMA being subjected to nanoconfinement.

Finally, the ionic strength of the phosphate buffered saline (PBS) background electrolyte was varied. PDMAEMA was grafted to the BP mesoporous silica film containing ≈16% PDMAEMA. The resulting film has been subjected to cyclic voltammetry measurements between pH values of 1.5–11 using a 1x PBS (corresponds to 150×10^{-3} M) and a 0.2x PBS (corresponds to 30×10^{-3} M) solution as background electrolyte. The

concentration of the $[Fe(CN)_6]^{3-/4-}$ probe molecule has been kept constant at 1×10^{-3} M. As shown in Figure S8c (Supporting Information) the pH-dependent PDMAEMA charge generation within the mesoporous film is further shifted to higher (more basic) pH-values in case of lower ionic strength (Figure S14c, red dots, Supporting Information) of 30×10^{-3} M as compared to an ionic strength of 150×10^{-3} M. For better comparison the peak current density values are plotted relative to the highest measured current density peak within the pH-dependent series, e.g., $\frac{jp@pH}{jp@pH\ 2.5}$. Up to a pH of above 8 the pH-dependent peak current densities between 150×10^{-3} M and 30×10^{-3} M ionic strength are comparable and are independent of pH. At a pH of 7.5 an increase of peak current density up to 50% of the maximum (highest) value at pH 2 is observed for the 150×10^{-3} M measurement solution. In presence of a 30×10^{-3} M background PBS electrolyte a peak current density of 50% of the maximum detected value at pH 2 is reached at a slightly more acidic pH-value of 7.0 (Figure S14c, red, Supporting Information). This shift within the pH-dependent peak current density of 0.5 pH units remains up to a relative peak current density value of 75% of the maximum peak current density at pH 2 and is also reflected in the apparent pKa values. For the measurements at 30×10^{-3} M ionic strength the PDMAEMA shifts to 7.1 compared to 150×10^{-3} M ionic strength that has been otherwise used in this study (apparent pka 7.5). The variation of the ionic strength from the background electrolyte leads to an expansion of the Debye screening length, which should result in a lower concentration of ions within the mesopores. This is probably the reason for a stronger pKa shift in the measurements with an ionic strength of 30×10^{-3} M as compared to an ionic strength of 150×10^{-3} M.

5. Enzyme Encapsulation in Mesoporous Silica Particles

The pore accessibility investigations of polyelectrolyte modified mesoporous silica films indicate pK_a shifts of at least 1 pH unit toward more acidic (PDMAEMA) or more basic (PMEP) pH conditions. The direction of the shift is determined by the type of the molecule charge incorporated in the silica mesopores and is directed toward harsher pH conditions. A shift of 1 pH unit corresponds to a theoretical increase of the $[H^+]$ concentration by 10-fold. This should not be neglected, while investigating pH sensitive processes, such as protein binding or drug delivery inside or outside of mesoporous silica, as shown in the encapsulation of lipase from *Aspergillus oryzae* (**Figure 5** top).

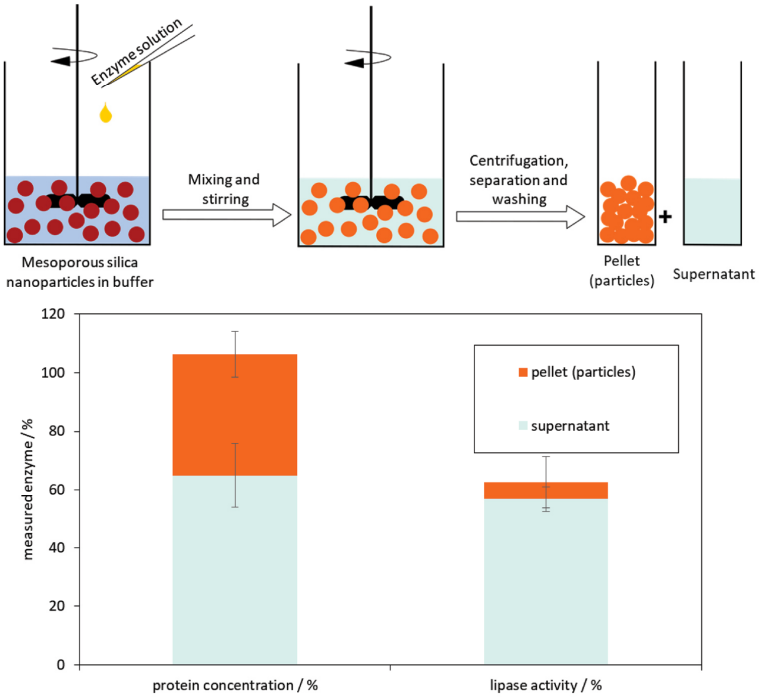

Figure 5. Top: Schematic illustration of enzyme adsorption on the mesoporous silica particles (SBA-15 and SBA-NH_2 as well as TEOS and BTSE based particles). Bottom: Mean value using the different types of mesoporous silica particles of lipase activity and protein concentration detected in the pellets and the supernatant, respectively.

Enzyme encapsulations were studied in different types of mesoporous silica nanoparticles SBA-15 (Santa Barbara amorphous silica-15) and SBA-NH_2 as well as TEOS (tetraethoxy-ortho silane) and BTSE (1,2-bis(triethoxysilyl)ethane) based particles before and after calcination. Due to lipase´s isoelectric point of about 5, highest lipase encapsulation efficiencies were obtained at buffered pH values of 4. Here, enzyme loadings of about 500 mg lipase per gram silica were determined by measuring the protein content in supernatant and particle pellet. However, lipase activity of encapsulated enzyme was reduced significantly: a maximum of 20% of successfully encapsulated lipase remained active (Figure 5 bottom). Accordingly, large parts of the enzyme were denatured upon encapsulation into the mesoporous silica. The lipase itself was stable under the terms of immobilization as measured lipase activities in the supernatant largely corresponded to determined protein concentrations (Figure 5 bottom). Furthermore, it is unlikely that the presence of charges on the silica surface was responsible for the activity loss.[25] Accordingly, it can be assumed that the nanoconfinement and its influence on the apparent pH value inside the mesopores as well as the resulting shift on the pK_a value of encapsulated molecules affected the lipase stability. Low lipase activities could be a result of a lower pH value in the pore as a significant lipase stability difference between pH 3 and 4 occurs.

6. Conclusion

In order to investigate ion accessibility with the aid of cyclic voltammetry, mesopore filling between 50 and 80 vol% of polymer functionalized mesoporous thin films were used. By measuring the preconcentration of the metal complexes $[Fe(CN)_6]^{3-/4-}$ and $[Ru(NH_3)_6]^{2+/3+}$ at an electrode below the hybrid silica film, it was possible to investigate the charge generation in dependence of the measurement solution pH value. The results obtained show significant shifts in the pKa values of the polyelectrolytes PDMAEMA and PMEP. Those differences between pKa(bulk) and pKa(confinement) are due to the nature of nanoconfinement that has a significant influence on the pH value in, e.g., nanopores. A pKa shift of 1 as observed for PDMAEMA functionalized mesopores indicates a 10 times higher proton concentration inside the mesopores than in the adjusted pH value of the bulk solution. In order to investigate further influences on the charge situation in nanoconfinement, measurements were carried out in the lower and middle size range of the mesopore scale (8–16 nm). It was found that the importance of pore size in this region decreases with increasing polymer content of the hybrid material. A measurable but small influence on the pKa value could also be achieved by varying the ionic strength of the measurement solution, which can be explained by the widening of the Debye screening length.

In addition, the application relevance of the pH confinement effects could be demonstrated. The high degree of denaturing of the lipase from *Aspergillus oryzae* took place by encapsulation in mesoporous silica nanoparticles at a solution pH of 4, a pH at which the enzyme is stable in bulk solution. The influences on polyelectrolytes and enzymes in silica mesopores shown here illustrate the importance of confinement affecting pH. If fully understood, those confinement effects can be used as another tool to precisely design responsive nanopores. In any case, these effect must not be neglected when using mesoporous materials in protic media.

7. Experimental Section

Preparation of 1x PBS Buffer Solution: In 1000 mL distilled water 8.00 g (136.9 mmol) NaCl, 0.20 g (2.7 mmol) KCl, 1.42 g Na2HPO_4 (10.0 mmol), 0.27 g (2.0 mmol) KH_2PO_4 were dissolved and the solution was stirred for 24 h before being used for cyclic voltammetry measurements.

Preparation of Mesoporous Silica Thin Films: The mesoporous silica films were prepared via sol–gel chemistry using tetraethoxysilane (TEOS) as an inorganic precursor. The sol contained an amphiphilic triblock copolymer, Pluronic F127 (BioReagent, Sigma-Aldrich, 13 800 g mol^{-1}) in different ratios, which undergoes micellization upon solvent evaporation resulting in the formation of a porous inorganic network. A typical synthesis of films with 8 nm (or 16 nm) pores used 1.37 g (2.61 g) of Pluronic F127, which was dissolved in 33.8 mL (24.0 mL) of absolute ethanol and 5.22 mL of H2O, 0.33 mL of 37% HCl (6.4 mL of 0.05 M HCl). After which, 6.55 mL (4.88 mL) of TEOS was added to the mixture, and the solution was then stirred overnight under ambient conditions before being used to prepare films through evaporation-induced self-assembly (EISA). Dip-coating was performed in a climate-controlled chamber at a temperature of 23 °C and a relative humidity of 50%, at a withdrawal speed of 2 mm s^{-1}. After aging the films for 1 h at 50% relative humidity and at 23 °C they were subjected to the following thermal treatment: Two 1 h steps at 60 and 130 °C followed by heating to 350 °C with a heating rate of 1 °C min^{-1}. Finally, the films were stabilized at 350 °C for 2 h before cooling to room temperature.

Surface Grafting of N,N-(diethylamino)dithiocarbamoylbenzyl (trimethoxy)silane) (SBDC): The iniferter SBDC synthesis and grafting was performed according to previous literature protocols.[10f,11]

1.71 g (10.0 mmol) Sodium N,N-diethyldithiocarbamate trihydrate (STC) was recrystallized from Methanol and dried under high vacuum. Under Schlenk condition the purified STC was dissolved in 10 mL dry THF and added dropwise to a stirred solution of 2.12 g (8.59 mmol) p-(chloromethyl)-phenyltrimethoxysilane in 10 mL dry THF. After stirring for 16 h at room temperature the precipitated NaCl was filtered off and the resulting mixture dried under reduced pressure. The obtained crude product was purified using a "Kugelrohr"-destillation apparature at 160 °C to yield pure SBDC as a yellow oil (yield: 78%).

^{1}H NMR (300 MHz, $CDCl_3$): δ 7,60 (d, J = 8,1 Hz, 2H), 7,42 (d, J = 7,9 Hz, 2H), 4,56 (s, 2H), 4,05 (q, J = 7,1 Hz, 2H), 3,73 (q, J = 7,0 Hz, 2H), 3,62 (s, 9H), 1,29 (t, J = 7,1 Hz, 6H).

The prepared mesoporous silica films were postgrafted with SBDC under an inert atmosphere. SBDC 7.2 mg (0.02 mmol) was dissolved in absolute toluene (20.0 mL). The mixture was heated to 80 °C for 60 min in the presence of the mesoporous films. The films were subsequently extracted through multiple washings with toluene.

PMEP Modification of Mesoporous Silica Films: For the surface-functionalization with PMEP a 0.125 M/0.6 M monomer solution of MEP (0.55/2.5 g in 20 mL distilled H_2O) was prepared. To this solution a SBDC functionalized mesoporous silica film on a waver or ITO-coated glass substrate was added before the mixture was sealed with a rubber septum and deoxygenated by nitrogen bubbling for 20 min before irradiation using a Bio-Link BLX by Vilber Lourmat (t = 10–15 min, λ = 365 nm, P = 40 W). The substrates were then extracted in a distilled water bath overnight.

PDMAEMA Modification of Mesoporous Silica Films: DMAEMA (1.0 mL, 5.9 mmol) was dissolved in DMF (8 mL) and the reaction mixture was deoxygenated by nitrogen bubbling under light protection for 5 min. The deoxygenated monomer solution was transferred

under nitrogen atmosphere to a sealed flask containing the SBDC-functionalized mesoporous films on an ITO-coated glass substrate. After addition of the monomer solution the flask was irradiated using a Bio-Link BLX by Vilber Lourmat (t = 10 min, λ = 365 nm, P = 40 W). The films were extracted in THF at least 3 times to remove any physisorbed material before drying under ambient conditions for further characterization.

Cyclic Voltammetry: The electrochemical pore accessibility properties of the mesoporous silica thin films were investigated by cyclic voltammetry. $[Fe(CN)_6]^{3-/4-}$ and $[Ru(NH_3)_6]^{2+/3+}$ were used as negatively- and positively charged probe molecules, respectively. Measurements were recorded using a Metrohm Autolab PGSTAT302N potentiostat. Mesoporous films prepared on ITO-coated glass substrates were characterized using a 1×10^{-3} M solution of either $[Fe(CN)_6]^{3-/4-}$ (0.31 mg mL^{-1}) or $[Ru(NH_3)_6]^{2+/3+}$ (0.27 mg mL^{-1}) in a 1x (0.15 M), 1/3x (0.05 M) or 1/5x (0.03 M) PBS electrolyte solution. The pH-dependent ionic permselectivity was investigated by adjusting the solution pH between pH 2 and pH 12 by the addition of either aqueous 1 M NaOH or 3 M HCl to the prepared solutions. The pH was determined using pH-meter pH110 (VWR). A three-electrode setup was used with an Ag/AgCl reference electrode (BASi RE-6), a graphite counter electrode, and the mesoporous film carrying ITO-coated glass substrate as working electrode. The measured electrode coated with mesoporous film was 0.21 cm^2. Each pH was measured using a scan rate sequence of 200, 100, 25, 300, 1000 or 500, and 200 mV s^{-1}, with each scan rate cycled 3 times. If equilibrium was not reached after the first scan cycle, a second has been performed immediately after. All cyclic voltammograms shown correspond to a scan rate of 100 mV s^{-1}.

Supporting Information

Supporting Information is available from the Wiley Online Library or from the author.

Acknowledgements

The authors acknowledge funding in the frame of the LOEWE project iNAPO by the Hessen State Ministry of Higher Education, Research and the Arts. In addition Adnan Khalil and Annette Andrieu-Brunsen acknowledge the financial support by the German Research Foundation (DFG) within the Collaborative Research Centre 1194 "Interaction between Transport and Wetting Processes", Project <C04>. They especially thank Dr. Ute Heinemeyer and Ronald Walter from BASF for HAADF-TEM measurements shown in Figure 2. Additionally the authors thank Prof. Markus Biesalski for access to interface characterization facilities. Nina Drechsler is acknowledged for synthesis of SBDC and Niels Postulka for his support with CAD drawing.

Conflict of Interest

The authors declare no conflict of interest.

Keywords

iniferter polymerization, mesoporous silica, nanoconfinement, pKa value, poly electrolyte

Received: November 13, 2019
Revised: December 17, 2019
Published online: February 13, 2020

[1] a) D. M. Mitrano, E. Rimmele, A. Wichser, R. Erni, M. Height, B. Nowack, *ACS Nano* **2014**, *8*, 7208; b) D. A. Doyle, J. M. Cabral, R. A. Pfuetzner, A. Kuo, J. M. Gulbis, S. L. Cohen, B. T. Chait, R. MacKinnon, *Science* **1998**, *280*, 69.
[2] a) Z. Zhou, M. Hartmann, *Chem. Soc. Rev.* **2013**, *42*, 3894; b) S. Lu, Z. An, J. Li, J. He, *J. Phys. Chem. B* **2011**, *115*, 13695; c) I. I. Slowing, J. L. Vivero-Escoto, C. W. Wu, V. S. Lin, *Adv. Drug Delivery Rev.* **2008**, *60*, 1278; d) N. Carlsson, H. Gustafsson, C. Thorn, L. Olsson, K. Holmberg, B. Akerman, *Adv. Colloid Interface Sci.* **2014**, *205*, 339.
[3] a) M. H. Sun, S. Z. Huang, L. H. Chen, Y. Li, X. Y. Yang, Z. Y. Yuan, B. L. Su, *Chem. Soc. Rev.* **2016**, *45*, 3479; b) Z. Zhang, X. Sui, P. Li, G. Xie, X. Y. Kong, K. Xiao, L. Gao, L. Wen, L. Jiang, *J. Am. Chem. Soc.* **2017**, *139*, 8905.
[4] a) G. J. Soler-Illia, O. Azzaroni, *Chem. Soc. Rev.* **2011**, *40*, 1107; b) L. Nicole, C. Boissière, D. Grosso, A. Quach, C. Sanchez, *J. Mater. Chem.* **2005**, *15*, 3598; c) C. J. Brinker, Y. Lu, A. Sellinger, H. Fan, *Adv. Mater.* **1999**, *11*, 579; d) D. R. Dunphy, P. H. Sheth, F. L. Garcia, C. J. Brinker, *Chem. Mater.* **2015**, *27*, 75; e) I. I. Slowing, B. G. Trewyn, S. Giri, V. S. Y. Lin, *Adv. Funct. Mater.* **2007**, *17*, 1225.
[5] a) H. Zhang, Y. Tian, L. Jiang, *Nano Today* **2016**, *11*, 61; b) F. Xia, L. Jiang, *Adv. Mater.* **2008**, *20*, 2842; c) X. Hou, W. Guo, L. Jiang, *Chem. Soc. Rev.* **2011**, *40*, 2385; d) M. Tagliazucchi, O. Azzaroni, I. Szleifer, *J. Am. Chem. Soc.* **2010**, *132*, 12404; e) M. Ulbricht, *Polymer* **2006**, *47*, 2217.
[6] C. Chiappini, J. O. Martinez, E. De Rosa, C. S. Almeida, E. Tasciotti, M. M. Stevens, *ACS Nano* **2015**, *9*, 5500.
[7] a) L. Silies, A. Andrieu-Brunsen, *Langmuir* **2018**, *34*, 807; b) L.-L. Li, H. Sun, C.-J. Fang, J. Xu, J.-Y. Jin, C.-H. Yan, *J. Mater. Chem.* **2007**, *17*, 4492.
[8] M. Nakayama, T. Okano, T. Miyazaki, F. Kohori, K. Sakai, M. Yokoyama, *J. Controlled Release* **2006**, *115*, 46.
[9] a) G. Perez-Mitta, W. A. Marmisolle, A. G. Albesa, M. E. Toimil-Molares, C. Trautmann, O. Azzaroni, *Small* **2017**, *14*, 1702131; b) F. M. Gilles, M. Tagliazucchi, O. Azzaroni, I. Szleifer, *J. Phys. Chem. C* **2016**, *120*, 4789; c) A. Brunsen, C. Diaz, L. I. Pietrasanta, B. Yameen, M. Ceolin, G. J. Soler-Illia, O. Azzaroni, *Langmuir* **2012**, *28*, 3583; d) H. Zhang, X. Hou, L. Zeng, F. Yang, L. Li, D. Yan, Y. Tian, L. Jiang, *J. Am. Chem. Soc.* **2013**, *135*, 16102.
[10] a) J. Tom, R. Brilmayer, J. Schmidt, A. Andrieu-Brunsen, *Polymers* **2017**, *9*, 539; b) L. Silies, H. Didzoleit, C. Hess, B. Stühn, A. Andrieu-Brunsen, *Chem. Mater.* **2015**, *27*, 1971; c) M. Kruk, *Isr. J. Chem.* **2012**, *52*, 246; d) J. O. Zoppe, N. C. Ataman, P. Mocny, J. Wang, J. Moraes, H. A. Klok, *Chem. Rev.* **2017**, *117*, 1105; e) E. M. Benetti, C. Kang, J. Mandal, M. Divandari, N. D. Spencer, *Macromolecules* **2017**, *50*, 5711; f) B. de Boer, H. K. Simon, M. P. L. Werts, E. W. van der Vegte, G. Hadziioannou, *Macromolecules* **2000**, *33*, 349; g) J. Jiang, X. Xiao, P. Zhao, H. Tian, *J. Polym. Sci., Part A: Polym. Chem.* **2010**, *48*, 1551; h) J. Elbert, M. Gallei, C. Rüttiger, A. Brunsen, H. Didzoleit, B. Stühn, M. Rehahn, *Organometallics* **2013**, *32*, 5873; i) T. Otsu, A. Kuriyama, *J. Macromol. Sci., Part A: Chem.* **1984**, *21*, 961; j) K. Matyjaszewski, *Macromolecules* **2012**, *45*, 4015; k) L. Cao, M. Kruk, *Polym. Chem.* **2010**, *1*, 97; l) C. B.-K., D. Thomas, J. P. A. Heuts, M. H. Stenzel, P. Vana, M. Whittaker, *J. Polym. Sci., Part A: Polym. Chem.* **2003**, *41*, 365.
[11] R. Brilmayer, C. Hess, A. Andrieu-Brunsen, *Small* **2019**, *15*, 1902710.
[12] a) B. Yameen, M. Ali, R. Neumann, W. Ensinger, W. Knoll, O. Azzaroni, *Chem. Commun.* **2010**, *46*, 1908; b) M. A. Basit Yameen, R. Neumann, W. Ensinger, W. Knoll, O. Azzaroni, *J. Am. Chem. Soc.* **2009**, *131*, 2070; c) G. Chen, S. Das, *J. Appl. Phys.* **2015**, *117*.
[13] a) S. P. Adiga, D. W. Brenner, *J. Funct. Biomater.* **2012**, *3*, 239; b) D. F. Stamatialis, B. J. Papenburg, M. Gironés, S. Saiful, S. N. M. Bettahalli, S. Schmitmeier, M. Wessling, *J. Membr. Sci.* **2008**, *308*, 1.

[14] a) J. Wen, K. Yang, F. Liu, H. Li, Y. Xu, S. Sun, *Chem. Soc. Rev.* **2017**, *46*, 6024; b) Y. Wang, Q. Zhao, N. Han, L. Bai, J. Li, J. Liu, E. Che, L. Hu, Q. Zhang, T. Jiang, S. Wang, *Nanomed. Nanotechnol. Biol. Med.* **2015**, *11*, 313; c) Q. He, Y. Gao, L. Zhang, Z. Zhang, F. Gao, X. Ji, Y. Li, J. Shi, *Biomaterials* **2011**, *32*, 7711; d) C. H. Lee, S. H. Cheng, I. P. Huang, J. S. Souris, C. S. Yang, C. Y. Mou, L. W. Lo, *Angew. Chem., Int. Ed.* **2010**, *49*, 8214.
[15] D. Bottenus, Y. J. Oh, S. M. Han, C. F. Ivory, *Lab Chip* **2009**, *9*, 219.
[16] N. Vilà, P. de Oliveira, A. Walcarius, I. M. Mbomekallé, *Electrochim. Acta* **2019**, *309*, 209.
[17] a) A. Goux, J. Ghanbaja, A. Walcarius, *J. Mater. Sci.* **2009**, *44*, 6601; b) F. Yan, W. Zheng, L. Yao, B. Su, *Chem. Commun.* **2015**, *51*, 17736; c) D. Fattakhova-Rohlfing, M. Wark, J. Rathouský, *Chem. Mater.* **2007**, *19*, 1640.
[18] M. Vallet-Regi, F. Balas, D. Arcos, *Angew. Chem., Int. Ed.* **2007**, *46*, 7548.
[19] C. Boissiere, S. Lepoutre, L. Nicole, A. B. Bruneau, C. Sanchez, *Langmuir* **2005**, *21*, 12362.
[20] N. Herzog, R. Brilmayer, M. Stanzel, A. Kalyta, D. Spiehl, E. Dörsam, C. Hess, A. Andrieu-Brunsen, *RSC Adv.* **2019**, *9*, 23570.
[21] X. Lin, Q. Yang, L. Ding, B. Su, *ACS Nano* **2015**, *9*, 11266.
[22] S. Alberti, P. Y. Steinberg, G. Gimenez, H. Amenitsch, G. Ybarra, O. Azzaroni, P. C. Angelome, G. Soler-Illia, *Langmuir* **2019**, *35*, 6279.
[23] a) P. Pasetto, H. Blas, F. Audouin, C. Boissière, C. Sanchez, M. Save, B. Charleux, *Macromolecules* **2009**, *42*, 5983; b) X. Huang, D. Appelhans, P. Formanek, F. Simon, B. Voit, *ACS Nano* **2012**, *6*, 9718; c) A. Zengin, G. Karakose, T. Caykara, *Eur. Polym. J.* **2013**, *49*, 3350; d) F. Yu, X. Tang, M. Pei, *Microporous Mesoporous Mater.* **2013**, *173*, 64.
[24] L. Silies, A. Andrieu-Brunsen, *Langmuir* **2017**, *3*, 807.
[25] S. Y. Zaitsev, I. V. Gorokhova, T. V. Kashtigo, A. Zintchenko, H. Dautzenberg, *Colloids Surf. A* **2003**, *221*, 209.

4.3. Synthese und elektrochemische Untersuchung zum pH-abhängigen Permselektivitätsverhalten von PDMAEMA-co-PMEP funktionalisierten Silicamesoporen

Neben der in Kapitel 4.2 beschriebenen Porenfüllung und Ladungsdichte spielen auch weitere Faktoren, wie etwa die Kettenarchitektur und die damit einhergehende Ladungsverteilung innnerhalb der Pore, eine entscheidende Rolle, um das Transportverhalten von nanoskaligen Hybridmaterialien zu modellieren.[14] Kontrollierte Porenfüllung von Mesoporen lässt sich über unterschiedliche Polymerisationsmethoden wie der ATRP, RAFT oder auch über Iniferter basierte Systeme umsetzen.[25] Auf der Nanoskala wurden bisher gewisse Parameter, die für Polymerisationen in Bulklösungen bekannt sind, noch nicht untersucht. Einer dieser Parameter ist die Rolle von Opferinifertern bei Oberflächen-initiierten Polymerisationen in Silicamesoporen. Bei Opferinifertern handelt es sich um Inifertermoleküle, welche zusätzlich zu den an der Oberfläche verankerten Inifertermolekülen in die Polymerisationslösung gegeben werden. Opferiniferter werden in der Polymerchemie üblicherweise dazu verwendet, homogenere Polydispersitäten zu erreichen. Jessica C. Tom konnte jedoch für die in dieser Arbeit verwendeten mesoporösen Silicafilme zeigen, dass die Präsenz von BDC als Opferiniferter zusätzlich zum auf der Oberfläche angebunden SBDC zu weniger Polymer in den Mesoporen führt. Dieser Unterschied zwischen Polymerisationen in Lösung und der im Nanoconfinement von Mesoporen, sowie die Frage nach dem Einfluss der Ladungsverteilung auf pH-Wert und Transporteigenschaften, motivierte die Untersuchung zur Herstellung von Block-co-oligomeren in Silicamesoporen. Analog zu Lösungspolymerisationen wurde durch Reinitiation der Polymerisation nach Wechsel der Monomerlösung versucht, blockartig strukturierte Copolymere/Cooligomere in Mesoporen mit einem Durchmesser kleiner als 10 nm zu generieren. Die erfolgreiche Synthese konnte durch Ellipsommetriemessungen verfolgt werden. Zusätzlich wurde durch eine Kooperation mit der Arbeitsgruppe von Prof. Hess (TU Darmstadt) die Präsenz beider Blöcke mittels Röntgenphotoelektronenspektroskopie (XPS) nachgewiesen.

Das Design der neuartigen PDMAEMA-co-PMEP Polymerstrukturen wurde dann verwendet, um den Einfluss der Kettenarchitektur und der daraus resultierenden Ladungszusammensetzung zu untersuchen. Dies war von Interesse, da für zwitterionische Polymere in Arbeiten aus unserer Gruppe von *Silies et al.* bipolare Poren bekannt sind.[201] Diese lassen bei Vorhandensein zwitterionischer Ladung (also einer positiven sowie einer negativen Ladung pro Monomer) weder positiv noch negativ geladene Ionen in die Poren diffundieren. Die Frage war also, ob sich Ketten, die ähnliche Mengen positive und negative Ladung tragen, allerdings nicht in jedem Monomer sondern in jedem Block, ähnlich verhalten. Hierzu wurden analog zu den Experimenten aus Kapitel 4.2 hinsichtlich der pH-abhängigen Permselektivität Untersuchungen durchgeführt. Hierbei konnte gezeigt werden, dass die blockartige Kettenarchitektur einen erheblichen Einfluss auf die Permselektivität hat. Im pH-Bereich, in dem beide Blöcke geladen vorliegen, zeigte sich ein invertiertes Transportverhalten, verglichen mit anderen mehrfach, orthogonal geladenen

Systemen, wie etwa Zwitterionen. Zudem stellte sich heraus, das Kalziumionen als Signalverstärker für dieses System dienen, wodurch diese Art der Systeme in Zukunft für die Sensorik relevant werden kann.

Mein Beitrag zu der Veröffentlichung in Polymers 2017, 9, 539 beinhaltet die Synthese des PDMAEMA-co-PMEP Block-co-Oligomers in Silicamesoporen sowie die Verfolgung der Synthese durch Ellipsommetriemessungen.
Mein Beitrag zu der Veröffentlichung in Small 2019, 15, 1902710 beinhaltet die Synthese des PDMAEMA-co-PMEP Block-co-Oligomers in Silicamesoporen. Zusätzlich wurden von mir die pH-abhängigen Cyclovoltammetrie-Messungen durchgeführt, durch die das Perm-selektivitätsverhalten der funktionalisierten Silicamesoporen untersucht wurde.

Die Ergebnisse des Abschnittes 4.3 sind in *Polymers* und *Small* veröffentlicht:
J. Tom, R. Brilmayer, J. Schmidt, A. Andrieu-Brunsen, **Optimisation of Surface-Initiated Photoiniferter-Mediated Polymerisation under Confinement, and the Formation of Block Copolymers in Mesoporous Films**, *Polymers*, **2017**, 9(10), 539.

R. Brilmayer, C. Hess, A. Andrieu-Brunsen, **Influence of Chain Architecture on Nanopore Accessibility in Polyelectrolyte Block-Co-Oligomer Functionalized Mesopores**, *Small*, **2019**, 15, 1902710.

Die *Supporting Information* ist nicht abgedruckt, aber in der elektronischen Version dieses Artikels (DOI: 10.3390/polym9100539; 10.1002/smll.201902710) verfügbar.

polymers

MDPI

Article

Optimisation of Surface-Initiated Photoiniferter-Mediated Polymerisation under Confinement, and the Formation of Block Copolymers in Mesoporous Films

Jessica C. Tom [1], Robert Brilmayer [1], Johannes Schmidt [2] and Annette Andrieu-Brunsen [1,*]

[1] Ernst-Berl Institut für Technische und Makromolekulare Chemie, Technische Universität Darmstadt, Alarich-Weiss-Straße 4, 64287 Darmstadt, Germany; jessica.c.h.tom@gmail.com (J.C.T.); brilmayer@cellulose.tu-darmstadt.de (R.B.)

[2] Technische Universität Berlin, Fakultät II, Institut für Chemie, Hardenbergstr. 40, 10623 Berlin, Germany; johannes.schmidt@tu-berlin.de

* Correspondence: brunsen@cellulose.tu-darmstadt.de; Tel.: +49-6151-162-3742

Received: 18 September 2017; Accepted: 17 October 2017; Published: 23 October 2017

Abstract: Nature as the ultimate inspiration can direct, gate, and selectively transport species across channels to fulfil a specific targeted function. Harnessing such precision over local structure and functionality at the nanoscale is expected to lead to indispensable developments in synthetic channels for application in catalysis, filtration and sensing, and in drug delivery. By combining mesoporous materials with localised charge-switchable poly(2-(dimethylamino)ethyl methacrylate) (PDMAEMA) brushes, precisely controlling pore filling and exploring the possibility of incorporating two different responsive polymers, we hope to approach the precision control of natural systems in the absence of an external force. Here, we report a simple one-step approach to prepare a mesoporous silica thin film with ~8 nm pores functionalised with a photoiniferter by combining sol–gel chemistry and evaporation-induced self-assembly (EISA). We show that surface-initiated photoiniferter-mediated polymerisation (SI-PIMP) allows the incorporation of a high polymer content up to geometrical pore blocking by the simple application of UV light in the presence of a monomer and solvent, proceeding in a controlled manner in pore sizes below 10 nm, with the potential to tune the material properties through the formation of surface-grafted block copolymers.

Keywords: grafting from; surface-initiated; photoiniferter; photoinitiated; block copolymers; mesoporous silica; ionic permselectivity; local functionalisation

1. Introduction

The high degree of control exercised in biological channels to regulate key processes including ionic flow and molecular transport across cell membranes is the ultimate inspiration and key motivator for the material scientist to mimic in synthetic materials [1,2]. To achieve this, precise control over the structure, functional density, and ideally local placement is required [2].

Ordered mesoporous silicas (OMSs) are an ideal support structure due to their high specific surface area, dimensional stability, and their uniform, ordered channel structure with tuneable pore size and geometry [3,4]. Furthermore, the rich surface hydroxyl groups available on the silica surface are a convenient handle for various synthetic transformations [3]. These properties have afforded OMSs significant research interest over the last several decades, attracting attention for application in a broad range of fields from catalysis to controlled drug delivery [2,4–8].

The incorporation of polymeric architectures offers the greatest amount of versatility and a high degree of functionality; e.g., a high density of chargeable groups can be incorporated into the

porous structure [9]. The incorporation of a polymer coating further permits the intelligent design of hybrid materials. For example, the careful selection of monomers can endow the hybrid material with sensitivity towards a number of external stimuli including pH, redox potential, temperature, solvent, salt concentration, and even light to create "smart" materials, changing their transport behaviour by altering the ion–pore wall interactions [2,9].

Such responsive materials possess great potential for various applications [5]: catalysis and nanoreactors [10], energy storage [11], molecular separation and filtration [12–14], controlled drug delivery and release [15], and in microfluidic devices from chemical sensing and biosensing [2] to lab-on-chip devices (pre-concentration, enrichment/extraction for analysis, e.g., pesticides) [16].

Polymerisation in spatially confined mesoporous materials is a key technology that has been widely investigated over the last decade with advances in both soft chemistry and controlled/"living" radical polymerisation (CLRP) techniques [7,8,17,18]. A number of CLRP techniques have been successfully applied to the functionalisation of mesoporous silica including atom transfer radical polymerisation (ATRP) [19–21], reversible addition-fragmentation chain transfer (RAFT) polymerisation [22], nitroxide-mediated radical polymerisation (NMP) [23], and photoiniferter-mediated polymerisation (PIMP) [23,24] through a grafting from or surface-initiated approach. While the successful grafting of pre-formed polymer to the interior and exterior surface has been reported in large-pore (15 nm) membranes [25], this approach is preferred for gated membranes with sterics limiting the molecular weight, grafting density, and pore filling achievable [8,17,22,26].

The formation of polymer brushes from the interior surface of mesopores through surface-initiated polymerisation, while synthetically more viable than post-grafting pre-formed polymers to the surface, remains synthetically challenging when compared to planar or spherical surfaces [17,27]. This is particularly true for pores less than 10 nm in diameter [17]. Polymer-functionalised pores below 10 nm generally become inaccessible, and the grafted polymer is generally multimodal with a broad molecular weight distribution [17].

Surface-initiated atom transfer radical polymerisation (SI-ATRP) remains the most widely investigated technique due to its wide range of polymerisable monomers with controllable molecular weight and narrow dispersities, chemical tolerance, and mild polymerisation conditions [3,18]. While several techniques such as initiators for continuous activator regeneration (ICAR) [3] and activators (re)generated by electron transfer (A(R)GET) [10] have been implemented to reduce the concentration of the copper catalyst that contaminates the final material, ATRP systems are more onerous, requiring numerous components to mediate a controlled polymerisation. This could severely limit the pore size that can be functionalised in terms of the control achievable and the polymer content.

Photoinitiated systems such as photoiniferter-mediated polymerisation (PIMP) are becoming increasingly popular in material functionalisation [18,23,24,28]. PIMP is advantageous in its synthetic simplicity, requiring minimal reaction components and proceeding by the simple application of UV irradiation. PIMP is also versatile, being effectively applied in surface functionalisation with a number of functional monomers including styrene [29], methyl methacrylate (MMA) [10,29], 2-(dimethylamino)ethyl methacrylate (DMAEMA) [30], [2-(methacryloyloxy)ethyl] trimethylammonium chloride (METAC) [24], and zwitterionic monomers [19,30]. Surface-initiated polymerisation (SIP) activated by UV irradiation also permits spatial and temporal control over the surface functionalisation to specify the location, degree of functionalisation, and even allowing surface patterning [18,23,28,30]. For a more detailed overview of the various SIP techniques applied to functionalise surfaces and the impact of surface curvature, the reader is referred to a recent and comprehensive review by Klok and co-workers [18].

While it is possible to functionalise small pores below 10 nm via SI-CLRP techniques, it is rather challenging to control the polymerisation kinetics, resulting in poorly accessible pores [17]. Consequently, selective functionalisation of the external surface has taken precedence in many studies. For instance, no current reports have attempted the formation of block copolymers within mesoporous materials. Although several reports have incorporated block copolymers selectively to the exterior

surface of mesoporous silica nanoparticles for gating and controlled drug release [15,31]. To design and fabricate well-controlled uniform and responsive polymer coatings under the confines of mesopores below 10 nm, it is essential to understand how confinement impacts the polymerisation kinetics. Our research group previously reported an iniferter-initiated polymerisation of a zwitterionic monomer, carboxybetaine methacrylate (CBMA), from the interior and exterior surface of mesoporous silica with pores ranging from 2 to 115 nm in diameter, focussing on the effect of pore size, grafting density, and initiator on the SIP from iniferters that were post-grafted to the mesoporous silica surface through a terminal trimethoxysilane moiety [24]. In this system, a certain degree of control over the polymer content was achieved; however, the pore filling ratio was limited under the conditions used, and the post-grafting strategy of the iniferter does not permit localised polymer functionalisation.

Herein, we report a simple one-step approach to functionalise mesoporous silica films with a responsive polymer through surface-initiated photoiniferter-mediated living radical polymerisation (SI-PIMP). We further explore the effect of confinement on the polymerisation kinetics of 2-(dimethylamino)ethyl methacrylate (DMAEMA), and its impact on the amount of polymer formed within the mesopores, including the use and effect of a sacrificial iniferter on film functionalisation, and how this impacts the wetting and ionic permselectivity behaviour of the hybrid materials. Our approach involves the incorporation of a photoiniferter, *N*,*N*-(diethylamino)dithiocarbamoyl-benzyl (trimethoxy)silane) (SBDC), in a one-pot procedure through co-condensation with an inorganic precursor combining sol–gel chemistry and evaporation-induced self-assembly (EISA) to prepare a functional mesoporous thin film through dip-coating that is capable of undergoing polymerisation on exposure to UV light in the presence of a monomer as depicted in Scheme 1. We will further demonstrate that the formation of block copolymers is possible under confinement.

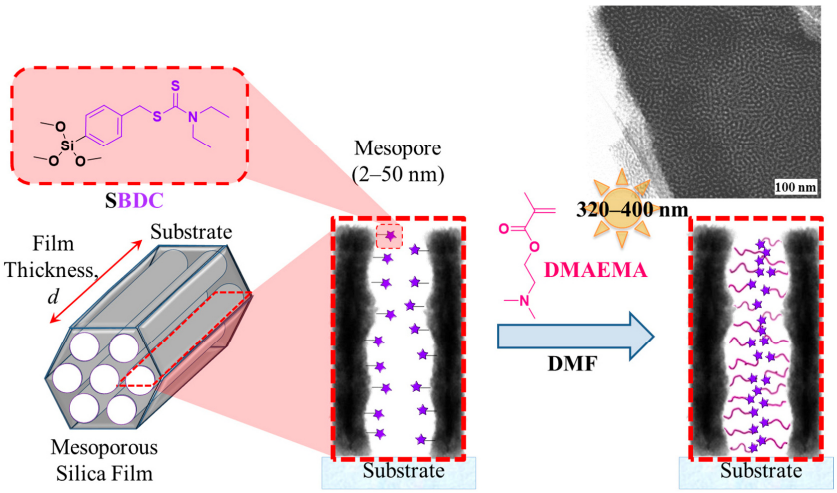

Scheme 1. Mesoporous silica thin films functionalised with an organosilane bearing a terminal trimethoxysilane (*N*,*N*-(diethylamino)dithiocarbamoyl-benzyl(trimethoxy)silane, SBDC) can be easily functionalised in the presence of a functional monomer, UV light, and solvent (*N*,*N*-dimethylformamide, DMF).

2. Materials and Methods

2.1. Materials

All materials and solvents were purchased from Sigma-Aldrich (Darmstadt, Germany) and used as received unless stated otherwise. The impact of a sacrificial iniferter was examined by the addition of benzyl diethyldithiocarbamate (BDC), a structural mimic of *N*,*N*-(diethylamino) dithiocarbamoyl-benzyl(trimethoxy)silane) (SBDC), which were synthesised according to a previous literature protocol [29]. The monomer used to study the photoiniferter polymerisations from BDC and/or SBDC, 2-(dimethylamino)ethyl methacrylate (DMAEMA, 98%) was passed over neutral alumina immediately prior to use to remove the hydroquinone monomethyl ether (MEHQ) inhibitor, and the solvent *N*,*N*-dimethylformamide (DMF, anhydrous, 99.8%) was used as received. For re-initiation studies, 2-(methacryloyloxy)ethyl phosphate (MEP) was used as received.

The precursor solutions for dip-coating mesoporous films were prepared using the inorganic precursor tetraethoxysilane (TEOS, Acros Organics, 98%, Geel, Belgium) alone or in combination with an organosilane such as SBDC, in dry tetrahydrofuran (THF, Merck, SeccoSolv, Darmstadt, Germany) or absolute ethanol (EtOH, Merck, ≥99.5%), with a hydrochloric acid catalyst (HCl, 37%) and Milli-Q water. Pluronic® F-127 (F127, BioReagent, Sigma-Aldrich, 13,800 g mol^{-1}) was used as a structuring agent in the sol, which was used as received at a molar ratio of 0.0050 or 0.0075 relative to the silane precursor to control the porosity of the mesoporous films prepared. The microscope slides (VWR, glass, cut edges) were cleaned in a mixture of detergent and water prior to rinsing with ethanol and drying under ambient conditions. The silicon wafers (Si-Mat, Kaufering, Germany, 100 mm diameter, 525 ± 25 μm thickness, type P/Bor, <100> orientation, CZ growth method, 2–5 Ω resistivity, polished on 1 side) and indium tin oxide (ITO, Delta Technologies, Ltd., Loveland, CO, USA, polished float glass, 150 × 150 × 1.1 mm, SiO_2 passivated/Indium Tin Oxide coated one surface, R_S = 4–8 Ω, cut edges) were cut to an appropriate size using a diamond cutter, cleaned using technical grade ethanol, and dried under ambient conditions prior to dip-coating.

2.2. Characterisation

2.2.1. Ellipsometry

Ellipsometry measurements of mesoporous films prepared on silicon wafer substrates (Si-Mat, Kaufering, Germany) were obtained from at least three spots per film to determine the average film thickness and refractive index using a Nanofilm EP3 imaging ellipsometer equipped with a 658 nm laser. Measurements were recorded at a fixed humidity of 15% at room temperature, and the angle of incidence (AOI) was varied from 38° to 66° in one zone in 2° increments. The EP4 analysis software supplied with the instrument was used to calculate the film thickness and refractive index from the measured amplitude and phase difference, Ψ and Δ, respectively. The data was fit using a one-layer box model, assuming an oxide layer on the silicon wafer was present between the substrate and mesoporous film, and this was fixed at 2.2 nm from previous measurements and fitting. The film thickness was allowed to vary between 10 and 300 nm, with a refractive index between 1 and 1.7. The Brüggemann effective medium approximation was used to calculate the volume porosity from the fitted refractive index [32,33]. Detailed calculations are provided in the Supplementary Materials (Section 5, Scheme S1).

2.2.2. Cyclic Voltammetry (CV)

The electrochemical and transport properties of the mesoporous materials was investigated via cyclic voltammetry using $Fe(CN)_6^{4-/3-}$ and $Ru(NH_3)_6^{2+/3+}$ as negative and positive probe molecules, respectively. Measurements were recorded using a Metrohm Autolab PGSTAT302N potentiostat (Metrohm, Utrecht, The Netherlands). Mesoporous films prepared on ITO substrates were characterised using a 2 mM solution of either the positive or negative probe molecule in a 100 mM KCl

electrolyte solution. The pH-dependent permselectivity was investigated by adjusting the solution pH between 2 and 11 by the addition of either aqueous NaOH or HCl to the prepared solutions. The pH was determined using pH-Fix 0–14 indicator sticks (Laborbedarf, Article No. 0549, Carl Roth, Karlsruhe, Germany). A Ag/AgCl reference electrode (BASi RE-6) and graphite counter electrode was used in the sample cell. The electrode area was 0.21 cm^2; however, all measurements reported here correspond to the peak currents in μA. Each pH was measured using a scan rate sequence of 200, 100, 25, 300, 1000, and 200 mV s^{-1}, with each scan rate cycled three times. All voltammograms shown here were measured at 100 mV s^{-1} from the last cycle recorded, and bare ITO was measured as a reference on each measurement day for comparison.

2.2.3. Static Contact Angle (CA)

CA measurements of the prepared films were measured using a DataPhysics OCA35 instrument (DataPhysics Instruments GmbH, Filderstadt, Germany) and evaluated using SCA20 software (Version 4.5.15 build 1064, DataPhysics Instruments GmbH, Filderstadt, Germany, 1998–2013) through the sessile drop method. All measurements were conducted within a climate-controlled room with a temperature of 25 °C and a relative humidity of 50%. Contact angles were determined within 30 s of applying a 2 μL water droplet onto the surface at a rate of 2 μL s^{-1}. All values reported arise from averaging at least 3–5 measurements across each film surface, and are reported with a standard deviation. Before each film was measured, it was stored under the measurement conditions within the climate-controlled room for several hours or overnight.

2.2.4. Attenuated Total Reflectance Fourier Transform Infrared Spectroscopy (ATR-FTIR)

Infrared spectra of the prepared mesoporous films on glass or ITO substrates were performed using a Perkin Elmer Instrument One Spectrum FT-IR Spectrometer equipped with a Universal ATR Polarization Accessory (Waltham, MA, USA). All spectra shown were averaged from at least 3 spots and normalised to the Si–O–Si band at ~1085 cm^{-1}. The spectra were recorded using the Spectrum Software (Version 10.5.4.738, PerkinElmer, Inc., Waltham, MA, USA, 2016) between 4000 and 650 cm^{-1} with a resolution of 4 cm^{-1}, and a background correction was automatically applied. All further data corrections were performed in OriginPro9 (ADDITIVE Soft- und Hardware für Technik und Wissenschaft GmbH, Friedrichsdorf, Germany, 2012).

2.2.5. Transmission Electron Microscopy (TEM)

Electron micrographs were recorded using a Philips FEI CM-20 transmission electron microscope (Philips, Amsterdam, The Netherlands) equipped with a LAB-6 cathode and Olympus CCD camera, and with a maximum resolution of 2.3 Å operating at an accelerating voltage of 200 kV. Samples were prepared by scratching the mesoporous films off the substrate and dispersing in filtered ethanol with 10 min of sonication before being drop cast onto 3.05 mm Cu grids (mesh size 200) with a Lacey carbon film (Plano GmbH, article number S166-2). The samples were then dried under ambient conditions.

2.2.6. Scanning Electron Microscopy (SEM)

SEM spectra were obtained using a Philips XL30 FEG scanning electron microscope equipped with a tungsten cathode and a back scattered electron yttrium aluminium garnet (BSE YAG) detector with an accelerating voltage of 15–25 kV, a 30 μm aperture, and a spot size of 4–5. The samples were sputter-coated with a 5 nm coating of Pt/Pd. The digital micrographs were recorded over a range of magnifications at a working distance of approximately 10 nm using an SE2 detector.

2.2.7. ^1H Nuclear Magnetic Resonance (^1H NMR) Spectroscopy

^1H NMR spectra were recorded on a 300 MHz Bruker AVANCE NMR spectrometer (Billerica, MA, USA) in deuterated chloroform ($CDCl_3$, 99.8% D), methanol (MeOD-d_4, 99.8% D) or dimethyl

sulfoxide (DMSO-d_6, 99.8% D) unless specified otherwise. The solvent residual peak was used as an internal reference.

2.2.8. Size Exclusion Chromatography (SEC)

SEC (Agilent Scientific Instruments, Santa Clara, CA, USA) was performed using a PSS-Agilent 1200 equipped with a 1200 Agilent RID and an autosampler (100 µL). The filtered samples were passed through a GRAM 10 µm pre-column (8 × 50 mm) and a PSS GRAM LINEAR 10 µm column (8 × 300 mm) using *N*,*N*-dimethylformamide (DMF) with 3 g L^{-1} LiCl at a flow rate of 0.5 mL min^{-1} at 25 °C. The molecular weight and molecular weight distribution was determined using WinGPC UniChrom software (Version 8.20 build 4815, PSS Polymer Standards Service GmbH, Mainz, Germay, 1992–2014) by conventional calibration with linear poly(methyl methacrylate) standards ranging between 2.2 × 10^2 and 1.6 × 10^6 g·mol^{-1}.

2.2.9. Krypton BET Adsorption

Krypton sorption and desorption measurements were performed at 77 K using an Autosorb iQ2 from Quantachrome. The samples were degassed for 12 h prior to measurement, and the BET surface area was calculated in the relative pressure range of 0.1 to 0.3.

2.3. Experimental

2.3.1. Synthesis of *N*,*N*-(Diethylamino)dithiocarbamoyl-benzyl(trimethoxy)silane) (SBDC), a Silane Terminated Iniferter

Sodium *N*,*N*-diethyldithiocarbamate trihydrate (STC) was dissolved in an excess of hot methanol to remove insoluble impurities. The solution was then dried over molecular sieves before being concentrated on a rotary evaporator and dried under high vacuum to remove any water or residual solvent. The purified sodium *N*,*N*-diethyldithiocarbamate (1.51 g, 8.81 mmol) was dissolved in dry THF (10 mL) before being added dropwise via syringe to a solution of *p*-(chloromethyl)-phenyltrimethoxysilane (1.93 mL, 8.76 mmol) in dry THF (10 mL) under a nitrogen atmosphere. The solution was then stirred at room temperature for 4 h before being filtered to remove the sodium chloride and dried under reduced pressure to remove the THF to yield crude SDBC (2) as a pale yellow liquid (76% crude yield). The crude product was then vacuum distilled at 160 °C using a Kugelrohr to yield pure SBDC as a yellow liquid (64% yield). ^1H NMR (300 MHz, $CDCl_3$, ppm): δ 7.53 (d, 2H, C_6H_4), 7.35 (d, 2H, C_6H_4), 4.49 (s, 2H, –CH_2S–), 3.98 (q, 2H, –NCH_2–), 3.66 (q, 2H, –NCH_2–), 3.55 (s, 9H, –Si(OCH_3)$_3$), 1.22 (t, 6H, –NCH$_2$CH_3). MS (ES)$^+$: *m*/*z* (%) calcd. for $C_{15}H_{25}O_3NS_2Si$ $[M^{\cdot}]^+$ 359, found 359 (100) $[M^{\cdot}]^+$, 360 (23) $[M + 1]^+$, 361 (16) $[M + 2]^+$, 362 (4) $[M + 3]^+$, 363 (1) $[M + 4]^+$. Assigned NMR and MS spectra are provided in the Supplementary Materials (Figures S1 and S4).

2.3.2. Synthesis of Benzyl Diethyldithiocarbamate (BDC), a Sacrificial Iniferter and SBDC Mimic

Recrystallised *N*,*N*-diethyldithiocarbamate (1.50 g, 8.77 mmol) was dissolved in dry THF (10 mL). This solution was then added dropwise via syringe to a solution of benzyl chloride (1105 µL, 9.62 mmol) in dry THF (10 mL) under a nitrogen atmosphere. The solution was then stirred for 3 h before being filtered to remove the sodium chloride. The filtrate was then dried under reduced pressure to remove the THF to yield crude BDC as a dark yellow-brown liquid (66% yield). The crude product was then vacuum distilled at 60–100 16C at 5 × 10^{-1} mbar using a Kugelrohr. ^1H NMR (300 MHz, $CDCl_3$, ppm): δ 7.33–7.16 (m, 5H, C_6H_5), 4.47 (s, 2H, –SCH_2Ph), 3.97 (q, 2H, –NCH_2CH$_3$), 3.65 (q, 2H, –NCH_2CH$_3$), 1.21 (t, 6H, –NCH$_2$CH_3). MS (ES)$^+$: *m*/*z* (%) calcd. for $C_{15}H_{25}O_3NS_2Si$ $[M^{\cdot}]^+$ 239, found 239 (100) $[M^{\cdot}]^+$, 240 (16) $[M + 1]^+$, 241 (10) $[M + 2]^+$, 242 (1) $[M + 3]^+$. Assigned NMR and MS spectra are provided in the Supplementary Materials (Figures S2, S3 and S5).

2.3.3. Preparation of Mesoporous Silica Thin Films

The mesoporous silica films were prepared via sol–gel chemistry using tetraethoxysilane (TEOS) as an inorganic precursor either alone or in combination with a functional organosilane (SBDC) in order to perform a photo-initiated polymerisation. The sol contained an amphiphilic triblock copolymer, F127, which undergoes micellisation upon solvent evaporation resulting in the formation of a porous inorganic network. The precursor solutions were stirred for 24 h under ambient conditions before being used to prepare films through evaporation-induced self-assembly (EISA). Dip-coating was performed in a climate-controlled chamber at a temperature of 25 °C and a relative humidity of 50%, at a withdrawal speed of 2 mm s^{-1} unless stated otherwise. The precursor solution used to prepare mesoporous silica with 5 mol % SBDC (5SBDCSi) contained a final TEOS:SDBC:F127:THF:H_2O:HCl molar ratio of 0.95:0.05:0.0075:20:5.2:0.28, and these films were prepared at a reduced temperature of 15 °C. After aging the films for 24 h under climate-controlled conditions, the films were subjected to a stabilising thermal treatment: 60 °C for 24 h, 130 °C for 24 h, and then finally at 200 °C for 1–2 h. The F127 template was then removed by immersion into a 0.01 M HCl ethanoic solution for 3 days with stirring. Detailed optimisation of the film preparation conditions including the withdrawal speed, temperature, and relative humidity are provided in the Supplementary Materials (Figures S8 and S9), as well as the full structural characterisation of the final 5SBDCSi films used in this study (Figure S10).

2.3.4. Surface-Initiated Photoiniferter-Mediated Polymerisation (SI-PIMP) from SBDC-Functionalised Mesoporous Silica

BDC (0.057 g, 0.24 mmol) and DMAEMA (1.0 mL, 5.9 mmol) were dissolved in DMF (8 mL), and the reaction mixture deoxygenated by nitrogen bubbling under light protection. The solution was then transferred via a deoxygenated syringe to a sealed flask containing the SBDC-functionalised mesoporous films on either glass, silicon wafer, or ITO substrates, which had been previously dried in vacuo, and deoxygenated using 3 vacuum–nitrogen cycles before being placed under a slight underpressure. The flask was then irradiated with UV light (320–400 nm) for various periods of time before exposure to air to quench the polymerisation. The free polymer formed was collected, dried under reduced pressure, and characterised by ^1H NMR spectroscopy and SEC to determine the conversion and molecular weight, respectively. The films were extracted in THF at least 3 times to remove any physisorbed material before drying under ambient conditions for further characterisation. Unless otherwise stated, the DMAEMA:BDC molar ratio was maintained at 25:1, with a monomer to solvent ratio of 1:8 (v/v). Investigations in the absence of sacrificial iniferter were carried out in a similar fashion with an identical monomer concentration. A Lumatec UV-Technik Superlite 410 lamp was used as the light source in all photoiniferter polymerisations unless stated otherwise. The wavelength ranged from 320 to 400 nm (UVA) with an intensity of ~6 mW cm^{-2} (see Supplementary Materials, Figure S6). Each polymerisation was carried out in a specially designed Schlenk flask with rectangular sides, and positioned ~10 cm away from the light source in an aluminium foil-lined box.

2.3.5. CO_2 Plasma Treatment

The organic functional groups present on the exterior surface of the mesoporous silica films were removed by applying a CO_2 plasma treatment using a Diener Femto plasma cleaner (Diener electronic, Ebhausen, Germany) at a pressure of 0.4 mbar and power of 20% for 12 s according to a previously published protocol by Babu et al. [34].

3. Results and Discussion

3.1. Controlling a Confined Polymerisation

Successful and well-controlled polymerisation within a porous material depends on a number of additional factors when compared to a solution polymerisation: the accessibility of the reagents and pore blocking [18], initiator grafting density [35], exterior surface [24], surface curvature [18,19],

and polymerisation time. To tune the amount of polymer incorporated within mesoporous materials and the level of control obtained—i.e., the molecular weight and corresponding molecular weight distribution of the surface-fixed polymers—these factors must be considered.

Photoiniferter-mediated polymerisation (PIMP) offers great potential to tune the surface properties, and hence the ionic permselectivity, of mesoporous films simply by exposure to UV light and appropriate monomers as depicted in Scheme 1 [22,28]. To achieve this, a functional organosilane (SBDC) bearing an iniferter group was co-condensed with TEOS in the presence of a templating agent (F127). The electron micrograph in Scheme 1 clearly shows a mesoporous structure formed with an approximate pore size of 8 nm. The polymerisable films have an average thickness of 232 nm and porosity of 21% from ellipsometry; and are characterised by a low specific surface area of approximately 4.9 m^2/g according to BET measurements taken from substrate-supported films. Despite this low specific surface area arising from the incorporation of SBDC into the silica framework through co-condensation, the films display good permselectivity towards both positive and negative species (see Figure S10 and Table S1 in the Supplementary Materials for complete characterisation of the prepared films).

Co-condensation is an advantageous route over post-grafting onto a pre-formed mesoporous material; it ensures a uniform surface modification [7,36], and the successful co-condensation of an initiating group offers the potential to confine the initiating species to a specific layer in multilayer films for local polymer functionalisation. Previous approaches to functionalise mesoporous silica with functional polymers such as dual-responsive poly(2-(dimethylamino)ethyl methacrylate) (PDMAEMA) are labour-intensive involving multiple steps, and local polymer functionalisation is not conceivable [22,24]. This is the first report where an iniferter has been incorporated through co-condensation successfully.

The iniferter concentration was maintained at 5 mol % relative to TEOS to avoid significant disruptions during the self-assembly process [37–39]. Further details regarding the co-condensation conditions and the effect on the prepared material are provided in the Supplementary Materials (Section 3a). Furthermore, a low iniferter concentration minimises the radical concentration within the mesopores to suppress irreversible termination [24], as well as circumventing radical migration often observed in SI-RAFT-type systems that results in premature termination [40].

3.1.1. Pore Accessibility

Our previous findings [24] suggest that slowing the polymerisation rate is key to the mediation of a controlled polymerisation under confinement; i.e., the radical concentration must be reduced to prevent premature termination due to the close proximity of radicals at concave surfaces. We employed several strategies to achieve this including a low concentration of surface-fixed iniferters, and high dilution. Consequently, the polymerisation was first studied in solution using a free or sacrificial iniferter (SI), BDC, which is structurally similar to SBDC (Scheme 2). The solution polymerisation proceeds in a controlled fashion using a monomer to initiator ratio of 25:1, and a monomer to solvent ratio of 1:8 (v/v) over a 4 h period under ambient temperature and constant irradiation with UV light (320–400 nm, 6 mW cm^{-2}). The solvent, *N*,*N*-dimethylformamide (DMF), was selected to solubilise the iniferter, monomer, and polymer in our initial kinetic studies. Under these conditions, a monomer conversion up to 60% is reached within 4 h with a corresponding dispersity exceeding 1.6 (see Supplementary Materials, Figure S7). These results are in agreement with general observations of iniferter-initiated polymerisations in which polymers synthesised in the presence of a photoiniferter are typically characterised by dispersities greater than 1.5, whilst dispersities of 1.1–1.4 are typical for their thermally-initiated counterparts [41].

The monomer and solvent must also be able to diffuse freely into the pores to access the initiating sites to successfully functionalise the inner pore walls of the mesoporous material. A CO_2 plasma was applied prior to polymerisation to confirm that the SBDC initiating sites are accessible on the surface, and that the monomer can indeed access the mesopores and undergo polymerisation from the pore

wall [34]. The optimised solution polymerisation was then applied directly to a mesoporous silica film co-condensed with 5 mol % SBDC relative to TEOS, the inorganic precursor, denoted 5SBDCSi (Scheme 2). After 4 h of irradiation, the free polymer formed in solution from the free iniferter reached a conversion of 58%, with a corresponding dispersity of 1.63.

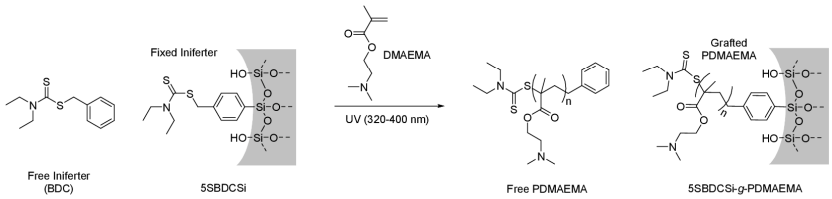

Scheme 2. Proof of pore accessibility and the surface-initiated photoiniferter-mediated polymerisation (SI-PIMP) of 2-(dimethylamino)ethyl methacrylate (DMAEMA) from available *N*,*N*-(diethylamino) dithiocarbamoyl-benzyl(trimethoxy)silane (SBDC) surface groups within a mesoporous material in the presence of a sacrificial iniferter, benzyl diethyldithiocarbamate (BDC). Reaction conditions: [DMAEMA]:[BDC] = 25:1, DMAEMA:DMF = 1:8 (*v*/*v*), 4 h, 320–400 nm. Surface-initiated polymerisation (SIP) confined to pores by pre-treating the 5SBDCSi films with a CO_2 plasma.

The appearance of a C=O stretching band at approximately 1730 cm^{-1} is associated with the formation of PDMAEMA on the mesopore surface (Figure 1). This observation indicates that the SBDC initiating groups are indeed present and available on the surface of the mesoporous framework. The free diffusion of monomer and solvent is further corroborated by incubation experiments (see Supplementary Materials, Figure S11). This is further supported by a decrease in the static contact angle of the 5SBDCSi film from ~45° to 27° (Figure 2b) upon performing a CO_2 plasma treatment [19,29].

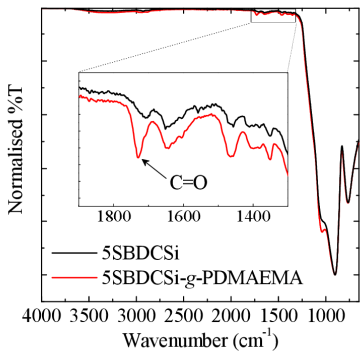

Figure 1. IR spectrum of a 5SBDCSi film on a glass substrate after performing a SI-PIMP of DMAEMA for 4 h in the presence of a SI (red trace) in comparison to a 5SBDCSi film on a glass substrate (black trace). The free polymer was characterised by ^1H NMR (58% monomer conversion, $DP_{n,th}$ 15, $M_{n,th}$ 2520 g·mol^{-1}) and SEC ($M_{n,SEC}$ 3420 g·mol^{-1}, $M_{w,SEC}$ 5575 g·mol^{-1}, $Đ$ = 1.629). Reaction conditions: [DMAEMA]:[BDC] = 25:1, DMAEMA:DMF = 1:8 (*v*/*v*), 4 h, 320–400 nm.

3.1.2. Monomer Concentration

One strategy to enhance the amount of incorporated polymer is the pre-concentration of reagents within the pores prior to polymerisation by increasing the initial solution monomer concentration from 0.74 M. After extracting the residual monomer, low molecular weight polymer, and solvent

in tetrahydrofuran (THF), the prepared materials were characterised by static contact angle (CA) measurements and infrared (IR) spectroscopy (Figure 2).

PDMAEMA was successfully grafted to the SBDC-fixed silica mesopores upon UV exposure with the appearance of a clear C=O band at approximately 1730 cm^{-1} in all IR spectra (Figure 2a). The absence of monomer and polymer peaks following incubation without irradiation confirms the solvent extraction conditions are sufficient, and verifies the polymerisation does not proceed in the absence of UV light.

There is no correlation between monomer concentration and polymer content by IR; however, CA measurements suggest that higher monomer concentrations lead to higher amounts of grafted PDMAEMA within the mesopores (Figure 2b). Faster polymerisation kinetics are expected under confinement [20,42]; the increased rate of polymerisation under confinement results in the observed higher amount of grafted polymer after the same polymerisation time when higher monomer concentrations are used. The disparity between the measured CA at a solution monomer concentration of 1.48 M compared to lower monomer concentrations, indicated in yellow, suggests irreversible termination is further exacerbated under concentrated conditions due to higher local radical concentrations. Whilst higher radical concentrations lead to premature termination within the pores, iniferter groups present on the exterior surface continue to grow over prolonged polymerisation times as evidenced by higher CAs (red circles), in agreement with our previous studies [24].

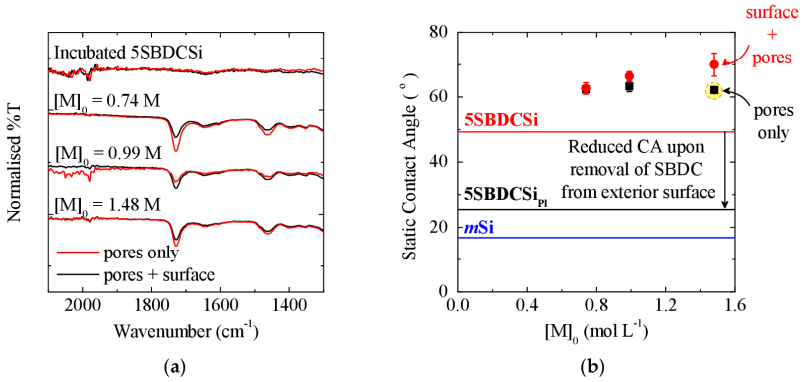

Figure 2. (**a**) IR; and (**b**) static CA measurements of mesoporous silica (*m*Si) co-condensed with 5 mol % SBDC with (5SBDCSi$_{PI}$) and without (5SBDCSi) a CO_2 plasma treatment prior to irradiation with UV light for 4 h shows their successful functionalisation and potential to tune the polymer content by varying the initial monomer concentration, $[M]_0$, from 0.74 to 0.99 and 1.48 M.

3.1.3. Exterior Surface

While the exterior surface area is relatively small compared to the internal mesoporous structure, it can impact reagent diffusion to active sites within the pores as the polymer grows, resulting in the evolution of molecular weight gradients along the pore channels [19,20,35,42].

The SIP was therefore performed concurrently with and without a CO_2 plasma pre-treatment to elucidate the impact of growing chains on the exterior surface on the polymer formed within the mesopores. The IR spectra are shown in Figure 3a. As expected, the amount of PDMAEMA formed is higher when the SBDC groups are present and undergo polymerisation from the exterior surface (——) than when confined exclusively within the mesopores (- - - -).

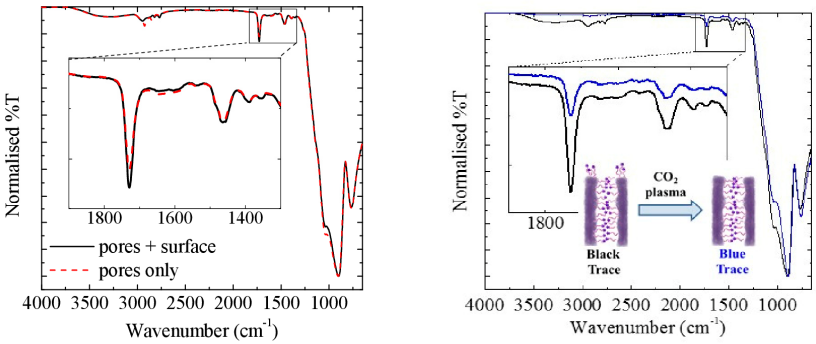

Figure 3. The presence of polymerisable groups and subsequent formation of a polymer on the exterior surface can hinder the formation of polymer within the mesopores: (**a**) IR spectra of 5SBDCSi after performing a SIP for 60 min where the SIP is confined exclusively to the pores (- - - -), and the pores and exterior surface (——); (**b**) IR spectra before (——) and after (——) performing an additional CO_2 plasma treatment to remove the polymer formed on the exterior surface after polymerisation. Reaction conditions: DMAEMA:DMF = 1:8 (*v*/*v*), 1 h, 320–400 nm.

An additional CO_2 plasma treatment was then applied to the polymer-functionalised mesoporous films to remove the polymer grafted from the exterior surface. A dramatic reduction in the C=O stretching band at ~1730 cm^{-1} (Figure 3b) clearly demonstrates that the functionalisation of the exterior surface dominates over the interior surface.

Furthermore, the amount of PDMAEMA incorporated within the mesopores is drastically lower when polymer grows simultaneously from the exterior surface and interior pore walls. This is clearly seen by comparing the insets in Figure 3a,b. When the polymerisation can proceed simultaneously inside the pores and from the exterior surface, i.e., no CO_2 plasma pre-treatment prior to performing the SIP, the formation of polymer on the exterior surface severely hampers the SIP within the pores in the current system through monomer consumption and reduced diffusion of reagents. Hence, to achieve higher and more uniform polymer functionalisation, the polymerisation must be confined within the pores.

3.1.4. Sacrificial Iniferters

Sacrificial initiators (SIs) are commonly used to control the surface-initiated polymerisation (SIP) from particles and planar substrates, particularly in SI-ATRP [19,43–45]. The free polymer is easily collected and characterised in place of the grafted polymer, and generally provides a good representation of the grafted chains. This assumption often circumvents the need for laborious and potentially hazardous degrafting of the surface-fixed chains [18,45,46].

Furthermore, as the free initiator is in excess of the surface-fixed initiators, the monomer to free initiator ratio dictates the polymerisation kinetics, and therefore the chain length formed on the surface. This allows the material properties to be precisely tuned, making the use of SIs an attractive tool in the preparation of organic-inorganic hybrid materials with precisely targeted properties for a specific application. Currently, there are no exhaustive studies on the effect of sacrificial initiators under confinement. Studies which have incorporated sacrificial initiators under confinement have been limited to ATRP systems [19,20]. In these systems, the SI is required to ensure a sufficient quantity of deactivator is present to effectively control the polymerisation from the surface [18–21,44,46].

In this system, the presence of a sacrificial iniferter, BDC, consistently results in a drastically lower polymer content within the mesopores. A representative IR spectrum is shown in Figure 4b,

which is further supported by CA measurements (Table 1 and Tables S2 and S3). The effect of the added SI is more apparent when the SIP is confined within the mesopores, with a CA over 30° higher when performed in the absence of a SI of 86°. This observation further suggests that the formation of polymer on the exterior surface hinders reagent diffusion from solution into the mesopores, and that the polymerisation is accelerated under confinement. Benetti et al. [20] examined the confinement of SI-ATRP of methacrylates by adjusting the distance between a grafting surface and inert plane. They observed nearly a 4-fold increase in the brush molar mass when the SI-ATRP was performed under highly confined environments. The faster grafting kinetics under increasing confinement was attributed to the progressive hindering of the Cu(II) deactivator from the propagating chain ends. This effect was considerably more apparent in viscous media such as bulk polymerisations or in the presence of a SI, and contrary to non-confined SIPs. They also exploited this behaviour to prepared polymer gradients over a planar substrate by spatially tuning the vertical distance between the grafting and confining surface. However, this system varied between 400 nm and 10 μm.

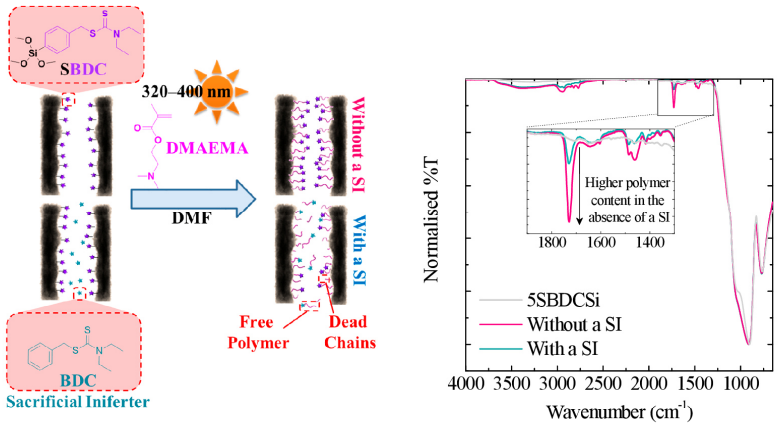

Figure 4. (**a**) Schematic diagram depicting the potential increased termination under confinement in the presence of a SI, BDC, leading to a reduced polymer amount as shown by (**b**) IR spectroscopy. Reaction conditions: DMAEMA:DMF = 1:8 (*v*/*v*), 4 h, 320–400 nm, and a [DMAEMA]:[BDC] molar ratio of 25:1 was used when performed in the presence of a SI (BDC).

Table 1. Static CA measurements of the prepared 5SBDCSi substrates grafted with PDMAEMA [1].

Polymer Location	Static Contact Angle (°)		
	With BDC [3]	Without BDC	Δ
Pores only [2]	53 ± 1	86 ± 1	32
Pores + Exterior Surface	65 ± 2	79 ± 4	14

[1] Reaction conditions: DMAEMA:DMF = 1:8 (*v*/*v*), 4 h, 320–400 nm; a [DMAEMA]:[BDC] molar ratio of 25:1 was used when performed in the presence of a SI. [2] The substrate was pre-treated with a CO_2 plasma to remove the SBDC initiating sites from the exterior surface before performing the SIP. [3] The free polymer was characterised by NMR (62% monomer conversion, $DP_{n,th}$ 15.6, $M_{n,th}$ 2690 g mol^{-1}) and SEC ($M_{n,SEC}$ 2870 g mol^{-1}, $M_{w,SEC}$ 4790, $Đ$ 1.67).

It is well-documented that high SI concentrations lead to significantly lower molecular weight chains on the surface due to monomer consumption through the formation of free polymer in solution [47]. However, this is unlikely to play such an important role under the high dilutions used in this system. And contrary to ATRP and RAFT, each iniferter can initiate upon exposure to UV light leading to high local radical concentrations upon illumination. Consequently, the inclusion

of a free photoiniferter creates a higher radical concentration within the mesopores; this may lead to increased irreversible termination in addition to higher monomer consumption. This scenario is depicted in Figure 4a.

To elucidate the origin of the lower polymer content in the presence of BDC, successive SIPs were carried out to compare the livingness of the surface polymer formed in the presence and absence of BDC. The polymerisations were carried out in a similar fashion as previously described. Briefly, a mixture of DMAEMA (1 mL) in DMF (8 mL) was transferred to a flask containing two 5SBDCSi films under nitrogen protection before being irradiated with UV light. After 30 min, the polymerisation was quenched by exposure to air and one film was removed before the flask was sealed, deoxygenated, and then irradiated for a further 30 min. The films were then extracted with THF (3 × 30 min) to remove residual monomer, free polymer, and solvent. For comparison, this was also conducted in the presence of a SI, using a [DMAEMA]:[BDC] molar ratio of 25:1. The IR and CA results are summarised in Figure 5 and Table 2, respectively.

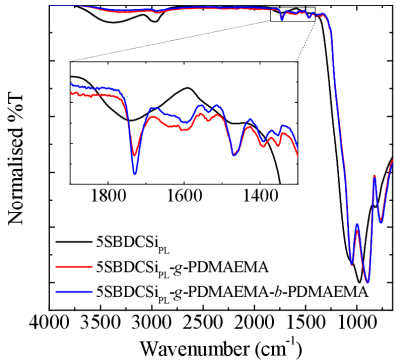

Figure 5. Normalised IR spectra of a CO_2 plasma-treated 5SBDCSi film (black trace) in comparison to 5SBDCSi after performing a SIP in the presence of a SI for 30 min (red trace), followed by chain extension for a further 30 min (blue trace).

The increased intensity of the C=O stretching band at ~1730 cm^{-1} upon chain extension shown in Figure 5, in combination with the increase in static CA from 43° to 48° upon performing a second polymerisation in the presence of a SI, indicates that the chains possess living character and can re-initiate to form block co-polymers. Although the chain-end fidelity remains unknown from these investigations.

The rapid polymerisation rate in the absence of a SI, as evidenced from the high intensity C=O band (Figure 4b) and contact angles exceeding 60° that do not increase further upon performing a second polymerisation (Table 2), indicates the surface-fixed chains undergo irreversible termination. The low chain-end fidelity when performed in the absence of a SI likely arises from the rapid and uncontrolled polymerisation under confinement. These chains then terminate irreversibly in the absence of a sufficient quantity of stable radicals that a SI would provide to reversibly terminate growing chains upon exposure to air.

In this way, the presence of a SI may be beneficial in capturing growing radicals reversibly similarly to the reversible deactivator in ATRP. Hence, sacrificial iniferters offer the potential to mediate a controlled SIP with tuneable graft molecular weight under high dilution, and further permit the formation of block copolymers. The efficacy of PIMP to prepare block copolymers under confinement in the absence of a SI is further explored in Section 3.3.

Table 2. Average static CA of a CO_2 plasma-treated 5SBDCSi film before and after performing a SIP for 30 min, and then after a chain-extension for a further 30 min with and without a SI.

Total Polymerisation Time (min)	Static Contact Angle (°)	
	With a SI	Without a SI
0	27 ± 0	27 ± 0
30	43 ± 1	63 ± 3
60	48 ± 3	62 ± 3

3.1.5. Polymerisation Time and SIP Kinetics

To improve our understanding of SI-PIMP kinetics under confinement in the absence of a sacrificial iniferter, 5SBDCSi films were pre-treated with a CO_2 plasma to confine the polymerisation to the interior walls of the mesopores. This ensures the observed behaviour arises from the mesopore-bound polymer. Parallel polymerisations were then carried out for varying timescales between 5 and 240 min before being exposed to oxygen to quench the polymerisation and extracted in THF (3 × 10 min). The IR, CA, and ellipsometry results are summarised in Figure 6.

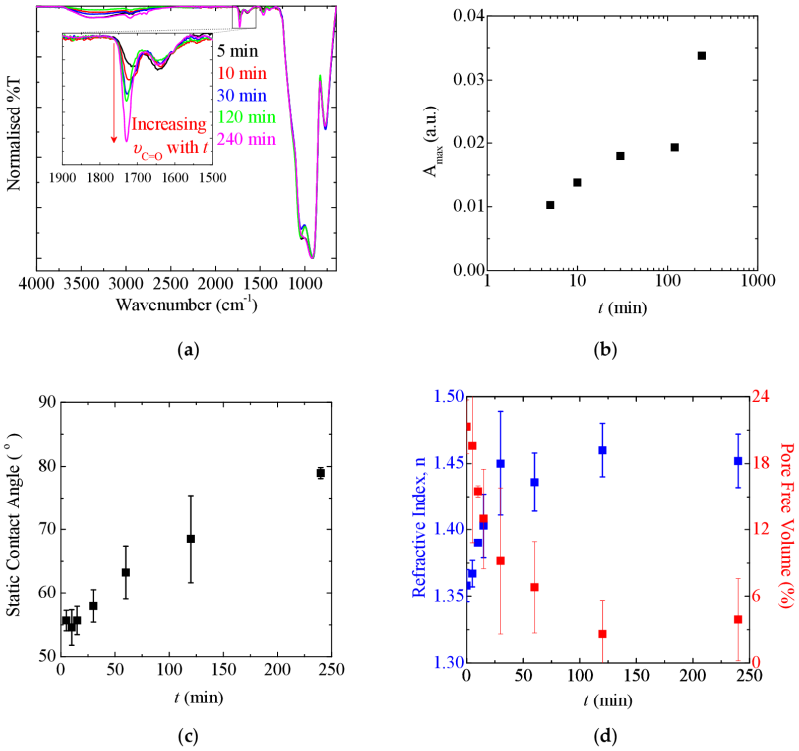

Figure 6. Polymerisation kinetics under confinement: (**a**) IR spectra; (**b**) corresponding C=O stretching absorbance associated with grafted PDMAEMA; (**c**) static CA measurements; and (**d**) refractive index (■) and corresponding free volume (■) from ellipsometry. Reaction conditions: DMAEMA:DMF = 1:8 (*v*/*v*), 0–240 min, SIP confined to pores by pre-treating the 5SBDCSi films with a CO_2 plasma.

As shown in Figure 6a–c, the carbonyl stretching band and CA continue to increase over the irradiation time examined. This is a good indication that the polymerisation continues within the pores over the timescale explored in a controlled fashion. This is contrary to a previous system we reported where the SIP of CBMA within the pores was observed to cease after a relatively short time compared to the exterior surface, where the polymer grafts continue to grow for prolonged periods [24]. The premature demise of the SIP within the pores likely arises from the higher monomer concentration (see Section 3.1.2), surface curvature, and the initiator grafting density used. These factors lead to a higher local radical concentration within the mesopores. Electrostatic exclusion of the positively charged monomer from the polymer-functionalised mesopores may also be a limiting factor in that case. Moreover, using our optimised polymerisation conditions, it is possible to achieve high polymer fillings up to geometrical pore blocking within 60 min (Figure 6d), with a high degree of control over the polymer content (Figure 6a–c) regardless of whether a co-condensation or post-grafting strategy of SBDC is employed. The film stability under these conditions was also assessed to ensure pore blocking is indeed a consequence of grafted polymer (see Supplementary Materials, Figure S13).

When the current system proceeds without interference, i.e., without exposure to air (Section 3.1.4, Table 1), significantly higher contact angles nearing 80° are achievable after 240 min. In the absence of an added sacrificial initiator, the poor re-initiation observed upon chain extension supports our hypothesis that a high radical concentration is present that terminates irreversibly upon exposure to air, contrary to other controlled/"living" radical polymerisation techniques. In the case where a SI is present, the growing free polymers originating from the SI may further act as radical scavengers to produce dead free chains to allow further growth from initiating sites attached to the surface. The SI may also provide a sufficient concentration of stable radicals to reversibly deactivate the surface-fixed chains. This allows the surface polymer to continue to grow upon subsequent irradiation and exposure to a monomer.

Having demonstrated that the amount of polymer incorporated in a mesoporous silica film can be easily tuned by adjusting the polymerisation time and monomer concentration, we investigated the effect of polymer content on the ionic permselectivity behaviour.

3.2. Tuneable Ionic Permselectivity

The electrochemical properties of the organic–inorganic hybrid materials prepared via SI-PIMP were investigated by cyclic voltammetry (CV) using positive and negative probe molecules under acidic and basic conditions. The impact of the incorporated polymer is highlighted clearly by the measured peak currents, which are shown graphically with increasing polymerisation time in Figure 7. The raw CV traces are available in the Supplementary Materials for reference (Figure S12, Table S4).

The rapid reduction in peak current by over 99% under basic conditions towards positive probe molecules within 30 min correlates to a pore filling of ~70%, and supports rapid polymerisation and geometrical pore blocking, with gated transport towards both positive and negative species under basic conditions (Figure 7a). After approximately 25 min of polymerisation, there is a slight increase in the ionic pore accessibility towards negative charges. This may arise from the growing PDMAEMA chains shielding the negatively charged silica walls.

The significantly higher pore accessibility towards negatively-charged species under acidic conditions allows gated transport with amplitude control. The PDMAEMA-grafted mesoporous silica films are (i) permselective to anions under acidic conditions ($pH < pK_{a,PDMAEMA}$); (ii) permselective to cations under basic conditions ($pH > pK_{a,PDMAEMA}$); and (iii) gated towards cations at high polymer content regardless of pH.

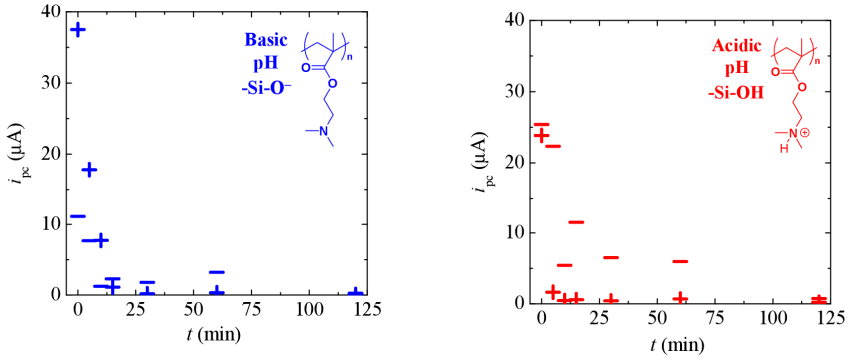

Figure 7. Ionic permselectivity with increasing polymerisation time under (**a**) basic and (**b**) acidic conditions for positive (+) and negative (–) probe molecules. Cathodic peak currents were recorded at a scan rate of 100 mV s^{-1}. Reaction conditions: DMAEMA:DMF = 1:8 (v/v), 0–240 min, 320–400 nm, SIP confined to pores by pre-treating the 5SBDCSi films with a CO_2 plasma.

There is a clear pore filling-pore wall charge effect that determines the observed permselectivity behaviour. The permselectivity correlates well with the pore filling calculated from ellipsometry measurements, which decreases rapidly with increased polymerisation time (Figure 6d, Table S4). The reduced wetting observed (Figure 6c) also impacts the permselectivity of aqueous solutions, and the contact angle increases approximately linearly with polymerisation time. Such behaviour is consistent with previous studies by Chen et al., [22] where the ionic permselectivity was investigated in mesoporous silica films grafted with PDMAEMA using SI-RAFT. They observed that, once the degree of polymerisation exceeded 75 monomer units, the conductivity decreased dramatically. This behaviour may be exacerbated by narrow necks relative to the pore diameter, and the significantly lower surface area of these co-condensed films when compared to pure mesoporous silica structured with F127 (Supplementary Materials, Table S1). It is worth noting that the polymer chain length is unknown. As these polymerisations were performed in the absence of a SI—which would theoretically limit the degree of polymerisation to 25 monomer units from an ideal surface, i.e., spherical or planar substrates—the polymerisation proceeds significantly faster under confinement compared to solution, and therefore the surface-bound polymer may in fact reach these high chain lengths to result in the observed pore blocking. To preserve the permselectivity of these films, it is important to avoid pore blocking, and incorporate a low polymer amount. Other approaches to reduce geometrical pore blocking resulting from termination and high polymerisation rates is slowing the polymerisation by further dilution and reducing the light intensity used to initiate the polymerisation [28]. However, studies at lower intensity and extended polymerisation times result in iniferter degradation [28].

We have shown using DMAEMA as a model and dual-responsive monomer that it is possible to control the amount of polymer grafted from mesoporous silica films via SI-PIMP. This allows us to fine-tune the ionic permselectivity behaviour of these organic-inorganic hybrid materials by controlling the charge density and/or wetting behaviour. To design materials with targeted properties for a specific application, the system should be easily adapted for other monomers, and even permit the formation of block copolymers (Scheme 3).

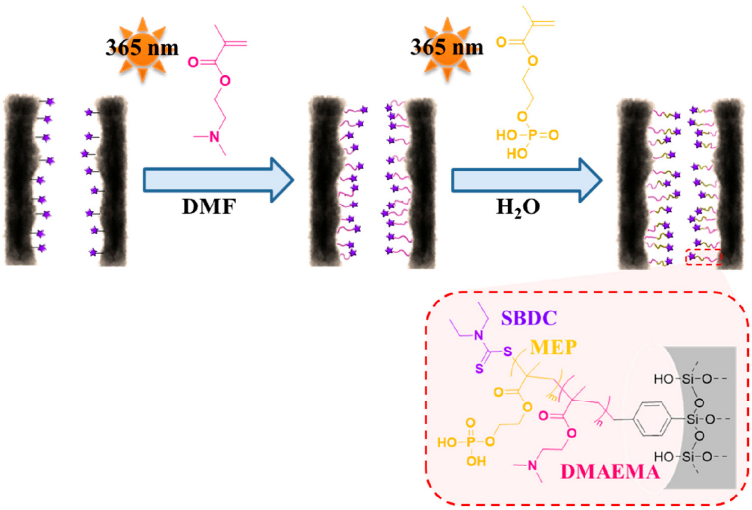

Scheme 3. Schematic illustration of the re-initiation of PDMAEMA grafted from SBDC-functionalised mesoporous silica thin films to form block copolymers under confinement by exposure to UV light and appropriate monomers.

3.3. Re-Initiation and the Potential to form Block Copolymers under Confinement

It is essential that we can control the polymer that forms from the surface in terms of molecular weight, dispersity, functionality, and architecture to design materials with specific and targeted properties. We have shown that it is possible to control the SIP under confinement by adjusting the monomer concentration, polymerisation time, and by the incorporation of a sacrificial iniferter. The ability to form block copolymers enables us to further tune the properties and behaviour of the hybrid materials. Due to higher levels of termination under confinement, particularly relevant in 8 nm pores, this is a considerable challenge to overcome. The incorporation of a SI also further complicates the polymerisation procedure, and requires more thorough washing to remove the free polymer from the hybrid material. Limiting the polymerisation time of the first block to 5 min under high dilution ensures high retention of active chain ends that can then be re-initiated upon exposure to a second monomer, 2-(methacryloyloxy)ethyl phosphate (MEP), under UV irradiation in the absence of a SI as shown in Figure 8. Under the applied conditions, re-initiation and probable chain extension is possible within both 8 and 16 nm mesopores [48], reaching a high pore filling irrespective of pore size. Re-initiation of the first block is the most probable scenario since the initiating sites located at the surface are less accessible due to sterics, particularly at the high pore filling after the formation of the first block. Further details and raw data are provided in the Supplementary Materials (Section 4, Figure S14, and Tables S5 and S6).

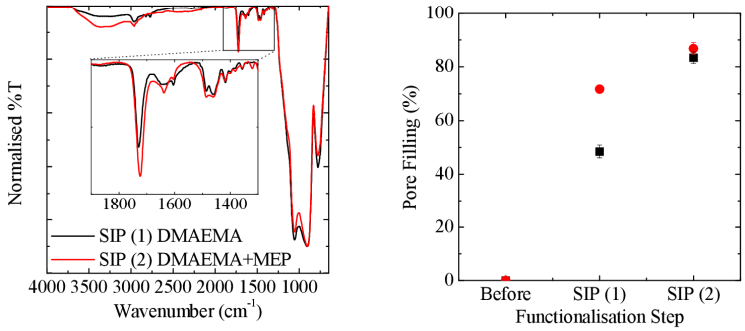

Figure 8. (**a**) IR spectra of mesoporous silica (16 nm pores) after performing a SIP with DMAEMA (SIP (1), black trace) and subsequent chain-extension with MEP (SIP (2), red trace); (**b**) corresponding volume pore filling of mesoporous silica with 8 nm (black squares) and 16 nm (red circles) pores post-grafted with SBDC before and after performing a SIP with DMAEMA (SIP (1)) and chain-extension with MEP (SIP (2)). The non-functionalised 8 and 16 nm mesoporous silica films are characterised by a porosity of 40 and 57%, respectively. Reaction conditions for SIP (1): DMAEMA:DMF = 1:8 (*v*/*v*), *t* = 5 min, λ = 365 nm. Reaction conditions for SIP (2): [MEP] = 0.125 M, solvent = water, *t* = 15 min, λ = 365 nm. The pore filling was estimated assuming the refractive index of the polymer is 1.517 (PDMAEMA) [49].

4. Conclusions

The synthetic ease of preparing organic-inorganic hybrid materials via SI-PIMP from a mesoporous silica support to pore blocking in pores less than 10 nm in diameter was demonstrated. The successful incorporation of an iniferter moiety, SBDC, through co-condensation provides a simple one-pot method to prepare functional mesoporous materials capable of further functionalisation by SIP simply by exposure to appropriate monomers and UV light. Moreover, co-condensation offers the potential to locally functionalise mesoporous materials, which is of high-importance in achieving fine control over ionic permselectivity with potential applications in self-sustained sensing and separation devices, including lab-on-chip devices. We will elaborate on this aspect in future reports.

We further demonstrated that the SIP from the inner surface is diffusion-limited, with significantly less polymer incorporated when polymer is able to grow from both the exterior and interior surface. This makes PIMP more suited for application under confinement when compared to ATRP since fewer reaction components are required to access the initiating sites, allowing the polymer content to be controlled in pores below 10 nm; PIMP also proceeds in the absence of any transition metal catalyst that ultimately pollutes the final material.

By the incorporation of a dual responsive polymer, PDMAEMA, we illustrated that the permselectivity towards both positively and negatively-charged species can be selectively controlled and fine-tuned by varying the polymer content and solution pH. We further showed that the formation of block copolymers under confinement is possible, a feat which has not yet been reported. The use of a sacrificial iniferter under high dilution was also investigated; sacrificial iniferters offer the possibility to control the molecular weight of the polymer grafted from the exterior surface, and potentially the amount of polymer incorporated within the pores in a controlled fashion by providing a sufficient concentration of stable radicals to deactivate surface-fixed polymer after prolonged polymerisation times. The amount of polymer incorporated within the pores can also be tuned by varying the initial monomer concentration, and polymerisation time.

Supplementary Materials: Supplementary Materials is available online at www.mdpi.com/2073-4360/9/10/539/s1.

Acknowledgments: The authors first wish to thank Felix H. Schacher for inviting us to publish our work in this special issue of *Polymers* entitled "Polymers and Block Copolymers at Interfaces and Surfaces", which could not have been achieved without the financial support provided by the Boehringer Ingelheim Stiftung through the Exploration Grant, as well as the technical facilities at the Technische Universität Darmstadt. This includes the Transmission Electron Microscopy and Scanning Electron Microscopy facilities, technical support from the Materials Science Department, the NMR Department, and Heike Herbert for SEC sample preparation and analysis. Preliminary PIMP work was carried out by Kevin Breitwieser, and Katharina Schmidt performed set experiments and repeats involving PIMP as part of their student projects under the supervision of Jessica C. Tom. We also thank Nicole Herzog for performing the final extraction tests included in the SI. Robert Brilmayer further acknowledges funding from the Hessen State Ministry of Higher Education, Research and the Arts, Germany, in the frame of the LOEWE project iNAPO.

Author Contributions: Jessica C. Tom was the primary investigator responsible for designing and performing the experiments; and Robert Brilmayer further investigated and optimised the conditions for re-initiation under confinement; Johannes Schmidt performed the BET measurements, including data analysis and calculation of the specific surface area of the prepared mesoporous films; Jessica C. Tom collated and analysed the data to write the manuscript, with corrections provided by all co-authors. Annette Andrieu-Brunsen provided the initial project concept with continued input throughout the course of the project.

Conflicts of Interest: The authors declare no conflict of interest. The founding sponsors had no role in the design of the study; in the collection, analyses, or interpretation of data; in the writing of the manuscript, and in the decision to publish the results.

References

1. Tagliazucchi, M.; Szleifer, I. Transport mechanisms in nanopores and nanochannels: Can we mimic nature? *Mater. Today* **2015**, *18*, 131–142. [CrossRef]
2. Perez-Mitta, G.; Albesa, A.G.; Trautmann, C.; Toimil-Molares, M.E.; Azzaroni, O. Bioinspired integrated nanosystems based on solid-state nanopores: "Iontronic" transduction of biological, chemical and physical stimuli. *Chem. Sci.* **2017**, *8*, 890–913. [CrossRef] [PubMed]
3. Liu, Y.; Liu, X.; Ye, G.; Song, Y.; Liu, F.; Huo, X.; Chen, J. Well-defined functional mesoporous silica/polymer hybrids prepared by an ICAR ATRP technique integrated with bio-inspired polydopamine chemistry for lithium isotope separation. *Dalton Trans.* **2017**, *46*, 6117–6127. [CrossRef] [PubMed]
4. Walcarius, A. Mesoporous materials and electrochemistry. *Chem. Soc. Rev.* **2013**, *42*, 4098–4140. [CrossRef] [PubMed]
5. Sun, M.-H.; Huang, S.-Z.; Chen, L.-H.; Li, Y.; Yang, X.-Y.; Yuan, Z.-Y.; Su, B.-L. Applications of hierarchically structured porous materials from energy storage and conversion, catalysis, photocatalysis, adsorption, separation, and sensing to biomedicine. *Chem. Soc. Rev.* **2016**, *45*, 3479–3563. [CrossRef] [PubMed]
6. Pal, N.; Bhaumik, A. Soft templating strategies for the synthesis of mesoporous materials: Inorganic, organic–inorganic hybrid and purely organic solids. *Adv. Colloid Interface Sci.* **2013**, *189–190*, 21–41. [CrossRef] [PubMed]
7. Sanchez, C.; Boissière, C.; Grosso, D.; Laberty, C.; Nicole, L. Design, synthesis, and properties of inorganic and hybrid thin films having periodically organized nanoporosity. *Chem. Mater.* **2008**, *20*, 682–737. [CrossRef]
8. Soler-Illia, G.J.A.A.; Azzaroni, O. Multifunctional hybrids by combining ordered mesoporous materials and macromolecular building blocks. *Chem. Soc. Rev.* **2011**, *40*, 1107–1150. [CrossRef] [PubMed]
9. Olivier, A.; Meyer, F.; Raquez, J.-M.; Damman, P.; Dubois, P. Surface-initiated controlled polymerization as a convenient method for designing functional polymer brushes: From self-assembled monolayers to patterned surfaces. *Prog. Polym. Sci.* **2012**, *37*, 157–181. [CrossRef]
10. Chen, M.; Zhou, H.; Zhou, L.; Zhang, F. Confined polymerization: ARGET ATRP of MMA in the nanopores of modified SBA-15. *Polymer* **2017**, *114*, 180–188. [CrossRef]
11. Li, Y.; Fu, Z.-Y.; Su, B.-L. Hierarchically structured porous materials for energy conversion and storage. *Adv. Funct. Mater.* **2012**, *22*, 4634–4667. [CrossRef]
12. Fu, K.; Bohn, P.W. Nanochannel arrays for molecular sieving and electrochemical analysis by nanosphere lithography templated graphoepitaxy of block copolymers. *ACS Appl. Mater. Interfaces* **2017**, *9*, 24908–24916. [CrossRef] [PubMed]

13. Yan, F.; Lin, X.; Su, B. Vertically ordered silica mesochannel films: Electrochemistry and analytical applications. *Analyst* **2016**, *141*, 3482–3495. [CrossRef] [PubMed]
14. Vilà, N.; André, E.; Ciganda, R.; Ruiz, J.; Astruc, D.; Walcarius, A. Molecular sieving with vertically aligned mesoporous silica films and electronic wiring through isolating nanochannels. *Chem. Mater.* **2016**, *28*, 2511–2514. [CrossRef]
15. Yang, M.-Y.; Tan, L.; Wu, H.-X.; Liu, C.-J.; Zhuo, R.-X. Dual-stimuli-responsive polymer-coated mesoporous silica nanoparticles used for controlled drug delivery. *J. Appl. Polym. Sci.* **2015**, *132*. [CrossRef]
16. Xu, P.; Chen, C.; Li, X. Mesoporous-silica nanofluidic channels for quick enrichment/extraction of trace pesticide molecules. *Sci. Rep.* **2015**, *5*, 17171. [CrossRef] [PubMed]
17. Kruk, M. Surface-initiated controlled radical polymerization in ordered mesoporous silicas. *Isr. J. Chem.* **2012**, *52*, 246–255. [CrossRef]
18. Zoppe, J.O.; Ataman, N.C.; Mocny, P.; Wang, J.; Moraes, J.; Klok, H.-A. Surface-initiated controlled radical polymerization: State-of-the-art, opportunities, and challenges in surface and interface engineering with polymer brushes. *Chem. Rev.* **2017**, *117*, 1105–1318. [CrossRef] [PubMed]
19. Chu, C.-W.; Higaki, Y.; Cheng, C.-H.; Cheng, M.-H.; Chang, C.-W.; Chen, J.-T.; Takahara, A. Zwitterionic polymer brush grafting on anodic aluminum oxide membranes by surface-initiated atom transfer radical polymerization. *Polym. Chem.* **2017**, *8*, 2309–2316. [CrossRef]
20. Benetti, E.M.; Kang, C.; Mandal, J.; Divandari, M.; Spencer, N.D. Modulation of surface-initiated ATRP by confinement: Mechanism and applications. *Macromolecules* **2017**, *50*, 5711–5718. [CrossRef]
21. Kruk, M.; Dufour, B.; Celer, E.B.; Kowalewski, T.; Jaroniec, M.; Matyjaszewski, K. Grafting monodisperse polymer chains from concave surfaces of ordered mesoporous silicas. *Macromolecules* **2008**, *41*, 8584–8591. [CrossRef]
22. Chen, F.; Jiang, X.; Kuang, T.; Chang, L.; Fu, D.; Yang, J.; Fan, P.; Zhong, M. Polyelectrolyte/mesoporous silica hybrid materials for the high performance multiple-detection of pH value and temperature. *Polym. Chem.* **2015**, *6*, 3529–3536. [CrossRef]
23. Pan, X.; Tasdelen, M.A.; Laun, J.; Junkers, T.; Yagci, Y.; Matyjaszewski, K. Photomediated controlled radical polymerization. *Prog. Polym. Sci.* **2016**, *62*, 73–125. [CrossRef]
24. Silies, L.; Didzoleit, H.; Hess, C.; Stühn, B.; Andrieu-Brunsen, A. Mesoporous thin films, zwitterionic monomers, and iniferter-initiated polymerization: Polymerization in a confined space. *Chem. Mater.* **2015**, *27*, 1971–1981. [CrossRef]
25. Huang, L.; Dolai, S.; Raja, K.; Kruk, M. "Click" grafting of high loading of polymers and monosaccharides on surface of ordered mesoporous silica. *Langmuir* **2010**, *26*, 2688–2693. [CrossRef] [PubMed]
26. Liu, Z.; Wang, W.; Xie, R.; Ju, X.-J.; Chu, L.-Y. Stimuli-responsive smart gating membranes. *Chem. Soc. Rev.* **2016**, *45*, 460–475. [CrossRef] [PubMed]
27. Gorman, C.B.; Petrie, R.J.; Genzer, J. Effect of substrate geometry on polymer molecular weight and polydispersity during surface-initiated polymerization. *Macromolecules* **2008**, *41*, 4856–4865. [CrossRef]
28. Chen, M.; Zhong, M.; Johnson, J.A. Light-controlled radical polymerization: Mechanisms, methods, and applications. *Chem. Rev.* **2016**, *116*, 10167–10211. [CrossRef] [PubMed]
29. De Boer, B.; Simon, H.K.; Werts, M.P.L.; van der Vegte, E.W.; Hadziioannou, G. "Living" free radical photopolymerization initiated from surface-grafted iniferter monolayers. *Macromolecules* **2000**, *33*, 349–356. [CrossRef]
30. Krause, J.E.; Brault, N.D.; Li, Y.; Xue, H.; Zhou, Y.; Jiang, S. Photoiniferter-mediated polymerization of zwitterionic carboxybetaine monomers for low-fouling and functionalizable surface coatings. *Macromolecules* **2011**, *44*, 9213–9220. [CrossRef]
31. Karesoja, M.; McKee, J.; Karjalainen, E.; Hietala, S.; Bergman, L.; Linden, M.; Tenhu, H. Mesoporous silica particles grafted with poly(ethyleneoxide-block-n-vinylcaprolactam). *J. Polym. Sci. Part A Polym. Chem.* **2013**, *51*, 5012–5020. [CrossRef]
32. Boissiere, C.; Grosso, D.; Lepoutre, S.; Nicole, L.; Bruneau, A.B.; Sanchez, C. Porosity and mechanical properties of mesoporous thin films assessed by environmental ellipsometric porosimetry. *Langmuir* **2005**, *21*, 12362–12371. [CrossRef] [PubMed]
33. Brunsen, A.; Calvo, A.; Williams, F.J.; Soler-Illia, G.J.A.A.; Azzaroni, O. Manipulation of molecular transport into mesoporous silica thin films by the infiltration of polyelectrolytes. *Langmuir* **2011**, *27*, 4328–4333. [CrossRef] [PubMed]

34. Babu, D.J.; Yadav, S.; Heinlein, T.; Cherkashinin, G.; Schneider, J.J. Carbon dioxide plasma as a versatile medium for purification and functionalization of vertically aligned carbon nanotubes. *J. Phys. Chem. C* **2014**, *118*, 12028–12034. [CrossRef]
35. Turgman-Cohen, S.; Genzer, J. Computer simulation of controlled radical polymerization: Effect of chain confinement due to initiator grafting density and solvent quality in "grafting from" method. *Macromolecules* **2010**, *43*, 9567–9577. [CrossRef]
36. Suteewong, T.; Sai, H.; Bradbury, M.; Estroff, L.A.; Gruner, S.M.; Wiesner, U. Synthesis and formation mechanism of aminated mesoporous silica nanoparticles. *Chem. Mater.* **2012**, *24*, 3895–3905. [CrossRef]
37. Matheron, M.; Bourgeois, A.; Brunet-Bruneau, A.; Albouy, P.-A.; Biteau, J.; Gacoin, T.; Boilot, J.-P. Highly ordered ctab-templated organosilicate films. *J. Mater. Chem.* **2005**, *15*, 4741–4745. [CrossRef]
38. Matheron, M.; Gacoin, T.; Boilot, J.-P. Stabilization of well-organized transient micellar phases in CTAB-templated silica and organosilica thin films. *Soft Matter* **2007**, *3*, 223–229. [CrossRef]
39. Cagnol, F.; Grosso, D.; Sanchez, C. A general one-pot process leading to highly functionalised ordered mesoporous silica films. *Chem. Commun.* **2004**, 1742–1743. [CrossRef] [PubMed]
40. Tsujii, Y.; Ejaz, M.; Sato, K.; Goto, A.; Fukuda, T. Mechanism and kinetics of raft-mediated graft polymerization of styrene on a solid surface. 1. Experimental evidence of surface radical migration. *Macromolecules* **2001**, *34*, 8872–8878. [CrossRef]
41. Benedikt, S.; Moszner, N.; Liska, R. Benzoyl phenyltelluride as highly reactive visible-light TERP-reagent for controlled radical polymerization. *Macromolecules* **2014**, *47*, 5526–5531. [CrossRef]
42. Zhang, T.; Du, Y.; Muller, F.; Amin, I.; Jordan, R. Surface-initiated Cu(0) mediated controlled radical polymerization (SI-CuCRP) using a copper plate. *Polym. Chem.* **2015**, *6*, 2726–2733. [CrossRef]
43. Barbey, R.; Lavanant, L.; Paripovic, D.; Schuwer, N.; Sugnaux, C.; Tugulu, S.; Klok, H.A. Polymer brushes via surface-initiated controlled radical polymerization: Synthesis, characterization, properties, and applications. *Chem. Rev.* **2009**, *109*, 5437–5527. [CrossRef] [PubMed]
44. Von Werne, T.; Patten, T.E. Atom transfer radical polymerization from nanoparticles: A tool for the preparation of well-defined hybrid nanostructures and for understanding the chemistry of controlled/"living" radical polymerizations from surfaces. *J. Am. Chem. Soc.* **2001**, *123*, 7497–7505. [CrossRef] [PubMed]
45. Ohno, K.; Akashi, T.; Huang, Y.; Tsujii, Y. Surface-initiated living radical polymerization from narrowly size-distributed silica nanoparticles of diameters less than 100 nm. *Macromolecules* **2010**, *43*, 8805–8812. [CrossRef]
46. Ohno, K.; Morinaga, T.; Koh, K.; Tsujii, Y.; Fukuda, T. Synthesis of monodisperse silica particles coated with well-defined, high-density polymer brushes by surface-initiated atom transfer radical polymerization. *Macromolecules* **2005**, *38*, 2137–2142. [CrossRef]
47. Jeyaprakash, J.D.; Samuel, S.; Dhamodharan, R.; Rühe, J. Polymer brushes via ATRP: Role of activator and deactivator in the surface-initiated ATRP of styrene on planar substrates. *Macromol. Rapid Commun.* **2002**, *23*, 277–281. [CrossRef]
48. Dunphy, D.R.; Sheth, P.H.; Garcia, F.L.; Brinker, C.J. Enlarged pore size in mesoporous silica films templated by pluronic F127: Use of poloxamer mixtures and increased template/SiO_2 ratios in materials synthesized by evaporation-induced self-assembly. *Chem. Mater.* **2015**, *27*, 75–84. [CrossRef]
49. Gupta, S.; Agrawal, M.; Conrad, M.; Hutter, N.A.; Olk, P.; Simon, F.; Eng, L.M.; Stamm, M.; Jordan, R. Poly(2-(dimethylamino)ethyl methacrylate) brushes with incorporated nanoparticles as a SERS active sensing layer. *Adv. Funct. Mater.* **2010**, *20*, 1756–1761. [CrossRef]

NANO · MICRO small
www.small-journal.com

Influence of Chain Architecture on Nanopore Accessibility in Polyelectrolyte Block-Co-Oligomer Functionalized Mesopores

*Robert Brilmayer, Christian Hess, and Annette Andrieu-Brunsen**

Functionalized ordered mesoporous silica materials are commonly investigated for applications such as drug release, sensing, and separation processes. Although, various homopolymer functionalized responsive mesopores are reported, little focus has been put on copolymers in mesopores. Mesoporous silica films are functionalized with responsive and orthogonally charged block-co-oligomers. Responsive 2-dimethylamino)ethyl methacrylate)-block-2-(methacryloyloxy)ethyl phosphate (DMAEMA-*b*-MEP) block-co-oligomers are introduced into mesoporous films using controlled photoiniferter initiated polymerization. This approach allows a very flexible charge composition design. The obtained block-co-oligomer functionalized mesopores show a complex gating behavior indicating a strong interplay between the different blocks emphasizing the strong influence of charge distribution inside mesopores on ionic pore accessibility. For example, in contrast to mesopores functionalized with zwitterionic polymers, DMAEMA-*b*-MEP block-co-oligomer functionalized mesopores, containing two oppositely charged blocks, do not show bipolar ion exclusion, demonstrating the influence of the chain architecture on mesopore accessibility. Furthermore, ligand binding–based selective gating is strongly influenced by this chain architecture as demonstrated by an expansion of pore accessibility states for block-co-oligomer functionalized mesopores as compared to the individual polyelectrolyte functionalization for calcium induced gating.

Inspired by nature and its excellent control over ion transport and ion selectivity, e.g., exemplified by potassium ion channels, as well as inspired by the increasing demand of improved sensor technology in the context of future water management concepts, transport control in technological nanopores becomes increasingly relevant.[1] A wide range of synthetic nanopores has been reported, varying from ion track etched single and multipores in polymer foils, porous polymers as well as inorganic materials such as porous metal oxides or silica based materials.[2] Out of those materials mesoporous silica has been used in various applications due to its high specific surface area, stability, tunable pore characteristics, and adjustable surface chemistry.[3]

The combination of synthetic nanopores with responsive polymers has led to the formation of "smart" nanomaterials as a fascinating research field, achieving increasing interest over the last decade.[4] Responsive hybrid materials can be found in several applications such as separation processes, drug delivery or as chemical sensor.[5] In this context responsive polymers have been used to prepare gates and membranes with adjustable pore accessibility.[6] Polymer functionalization bares the advantage to control pore filling and with this multiplying charges by adjusting chain length and chain density.[7] Various polymerization techniques such as atom transfer radical polymerization (ATRP), reversible addition-fragmentation chain transfer (RAFT), and surface initiated photoiniferter polymerization (SI-PIP) have been studied to graft responsive polymers into nanoscale pores and to vary polymer amount in mesopores.[7a,b,8] In response to stimulation by light, ion concentration, temperature or pH, the surface and pore wall grafted polymers can change their charge, aggregation, and expansion.[4b,c,9] Thereby, pH responsive polymers have been the most extensively studied.[2b,4c,10] This is mainly due to the fact that pH is one of the most important biochemical factors in life processes and can be easily controlled experimentally through acid/base regulation. A wide range of pH responsive polymers that carry a single charge per monomer such as poly(vinylpyridine) (PVP), poly(2-(Dimethylamino)ethyl methacrylate) (PDMAEMA), poly(acrylic acid) (PAA) are reported. In addition multicharged monomers such as (2-(methacryloyloxy) ethyl phosphate) (MEP) or zwitterionic monomers such as carboxybetaine methyl acrylate (CBMA) have been polymerized in nanoporous materials.[2b,4d,6c,d,7a,10a] Additionally, their gating properties and applications have been well investigated.[4e,9,11] Very recent developments going beyond gating focus on asymmetric material structure design being exemplified for example

R. Brilmayer, Prof. A. Andrieu-Brunsen
Ernst-Berl-Institut für Technische und Makromolekulare Chemie
Technische Universität Darmstadt
Alarich-Weiss-Str. 12, 64287 Darmstadt, Germany
E-mail: andrieu-brunsen@smartmem.tu-darmstadt.de
Prof. C. Hess
Eduard-Zintl-Institut für Anorganische und Physikalische Chemie
Technische Universität Darmstadt
Alarich-Weiss-Str. 8, 64287 Darmstadt, Germany
The ORCID identification number(s) for the author(s) of this article can be found under https://doi.org/10.1002/smll.201902710.

DOI: 10.1002/smll.201902710

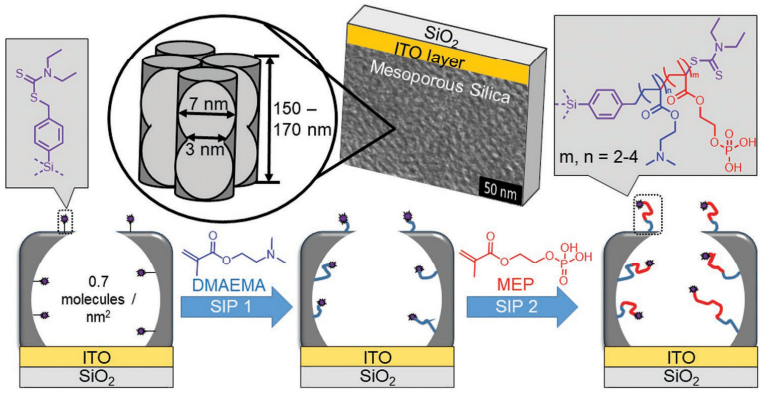

Figure 1. a) Scheme representing block-co-oligomer functionalization of mesoporous silica thin film which are investigated regarding their ionic permselectivity. The mesoporous silica film, displayed in the form of a TEM image, is directly supported on the ITO-coated glass substrate. b) The photoiniferter SBDC is grafted on the outer surface as well as inside the mesopores of the mesoporous silica film. Block-co-oligomer synthesis is performed in two consecutive steps: The first block is synthesized by surface initiated polymerization (SIP) 1 using DMAEMA as monomer. Subsequently, the second block oligomer formation is performed by SIP using MEP as monomer. Chain length of each block (m, n) is determined to be 2–4 repetition units based on X-ray photoelectron spectroscopy and TGA.

by so called Janus membranes enabling side selective or direction dependent oil–water separation or being investigated in the context of ionic energy conversion and the complex interplay of wetting and charge on ionic permselectivity.[5b,12]

Although controlled polymerizations are applied, to our knowledge, responsive polymer functionalized nanoscale pores are limited to homopolymers. On the other hand, it has recently been highlighted by a theoretical work from Szleifer and coworkers that the use of di-block copolymers and statistical block-co-polymers with precise charge composition could be of great use for designing advanced functions and to reach the full potential of smart nanomaterials.[13] Experimentally designing such precisely functionalized nanopores with respect to pore filling and chain architecture control is a challenge. The preparation of DMAEMA-*b*-PMEP diblock containing silica mesopores has previously been demonstrated by our group through reinitiation of Si-PIP polymerization.[7a] A combination of DMAEMA and MEP is expected to be exceptionally interesting for future applications and ion transport investigations because each homopolymer is already known to be multiresponsive, both carry orthogonal charges. PMEP shows two pKa values and thus each monomer can be negatively charged twice and serves as chelating agent for two valent ions such as Ca^{2+}.[6c] DMAEMA on the other hand is known to be temperature- and pH-responsive being able to carry a positive charge per monomer.[14] Combining both into one chain located in a mesopore is expected to result into a functional mesopore, allowing complex transport design in dependence of pore filling, chain architecture and external conditions. Based on these considerations, we herein address the question of oligomer chain architecture influence on the responsive mesopore ionic permselectivity characteristic and report multistimuli responsive and confinement controlled gating properties of PDMAEMA-*b*-PMEP functionalized mesoporous silica thin films varying both simultaneously: the environmental pH and calcium ion presence for highly PDMAEMA-PMEP block oligomer filled mesopores.

Due to their excellent stability and variable structure we choose sol–gel evaporation assembly (EISA) based mesoporous silica thin films as nanoscale porous material. As determined by ellipsometry (Table S1, Supporting Information) and electron microscopy (**Figure 1**), and in accordance with previously reported as-prepared mesoporous silica thin films, the applied mesoporous films have a thickness of ≈200 nm, elliptical mesopores with pore diameters of 6–7 nm and neck diameters of 3 nm, as well as a porosity of ≈45 vol% resulting in ≈440 $m^2\ g^{-1}$ specific surface area.[7a,b]

For the formation of a multiresponsive hybrid material and to investigate the influence of chain architecture and complex charge situation on nanopore permselectivity the photoiniferter (*N*,*N*-(diethylamino)dithiocarbamoyl-benzyl(trimethoxy)silane (SBDC) is postgrafted to the mesopores as shown in Figure 1. The SBDC grafting density has been determined by TGA (thermogravimetric analysis) measurements (Figure S1, Supporting Information) to be 0.7 molecules nm^{-2}. The subsequent SBDC-based surface-initiated polymerizations of 2-(dimethylamino)ethyl methacrylate (DMAEMA) and MEP are performed as previously reported.[7a] Homogeneous distribution of PMEP and Iniferter was proven using cryo-EM (cryogenic electron microscopy) in combination with EDX (energy dispersive X-ray spectroscopy) mapping (data not shown). Through XPS (X-ray photoelectron spectroscopy) measurements of a PDMAEMA-PMEP block-co-oligomer modified film and TGA measurements of PMEP grafted mesoporous silica films the length of each block is determined to be 2–4 repetition units (Figures S5 and S8, Supporting Information). This block-co-oligomer chain ratio of 1:1 is important because it allows to generate an identical number of positive and negative charges within the oligomer chain while charging the individual blocks especially up to a pH value of 7.5 referring to monomer solution pKa values. At pH values higher than 7.5, based on the solution

pKa value, each MEP monomer is expected to generate two negative charges which should turn the overall pore charge to be negative. This result of comparable DMAEMA and MEP oligomer block length is further supported by CV (cyclic voltammetry) measurements. As shown in **Figure 2**d) the peak current density (j_p) for the anionic probe molecule $[Fe(CN)_6]^{3-/4-}$ at acidic pH and the cationic probe molecule $[Ru(NH_3)_6]^{2+/3+}$ at basic pH, and thus the j_p under electrostatic attraction, are comparable.

To first validate the ionic permselectivity and gating properties of the PDMAEMA-*b*-PMEP block-co-oligomer

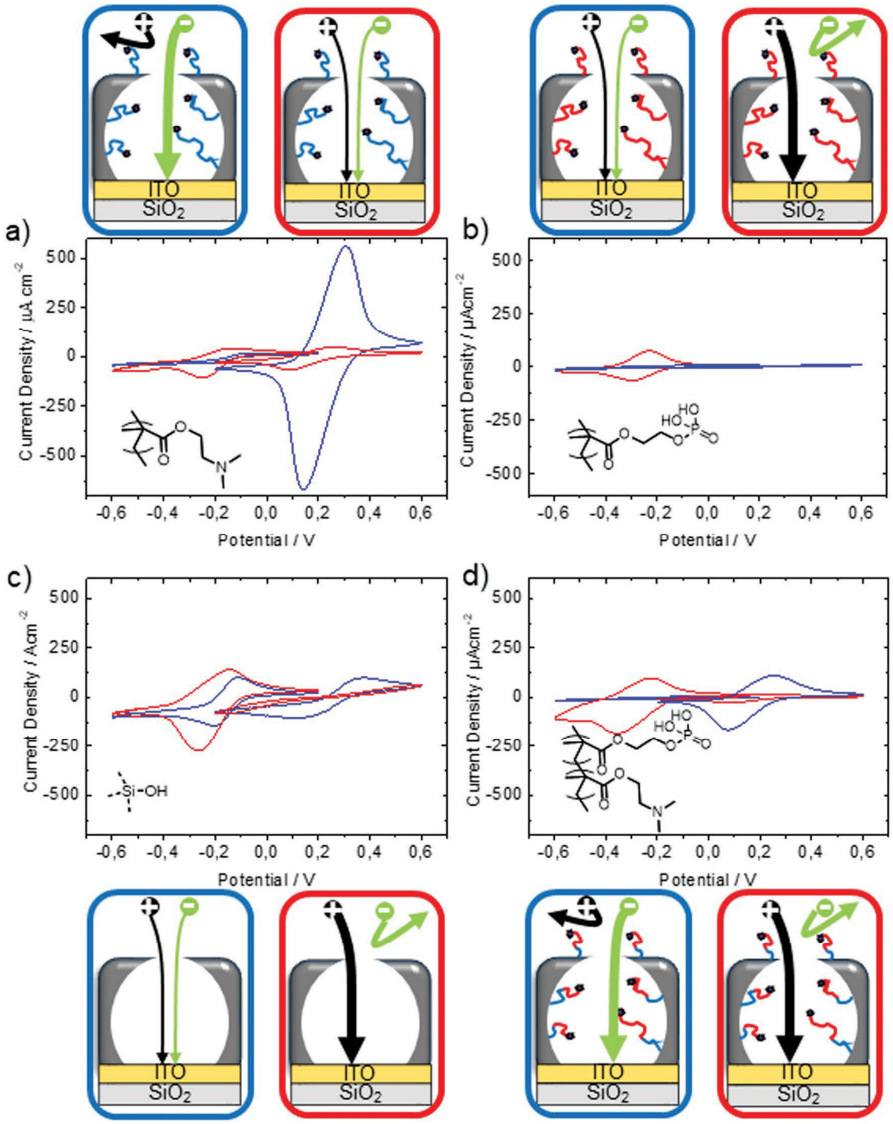

Figure 2. Ionic permselectivity as detected by cyclic voltammetry at an ITO electrode below the mesoporous film for a) PDMAEMA (pore filling 50 vol%), b) PMEP (pore filling 80 vol%), c) unmodified, d) PDMAEMA-*b*-PMEP block-co-oligomer (pore filling 95 vol%) modified mesoporous silica thin films. Cyclic voltamogramms are recorded at a scan rate of 100 mV s^{-1} in a 0.1 M KCl-solution and a 150 × 10^{-3} M PBS solution in the case of d) at pH 8–9 (red) and pH 2–3 (blue) using $[Fe(CN)_6]^{3-/4-}$ as anionic (–0.2 to 0.6 V) and $[Ru(NH_3)_6]^{2+/3+}$ as cationic probe molecule (–0.6 to 0.2 V).

modified mesoporous silica film, CV measurements are performed (Figure 2). The obtained results are compared with PDMAEMA and PMEP homopolymer-functionalized nanopores (Figure 2a,b) at an acidic (Figure 2 blue) and basic pH value (Figure 2 red). As reference (Figure 2c) the gating behavior of an unmodified mesoporous silica film is shown. The positively charged probe molecule $[Ru(NH_3)_6]^{2+/3+}$ enters the unmodified silica mesopores at acidic (Figure 2c, blue lines) and is slightly preconcentrated at basic (Figure 2c, red lines) pH values. The anionic probe molecule $[Fe(CN)_6]^{3-/4-}$ is excluded at basic pH as expected due to electrostatic repulsion resulting from the deprotonated mesopore wall silanol groups together with the pore diameters within the Debye Screening length. After modification with homo oligomers (Figure 2a for PDMAEMA and Figure 2b for PMEP) mesoporous silica films show inaccessible pores for the probe molecule being identically charged to the pore wall-grafted monomers which is in accordance to corresponding literature studies.[6c,15] For the homo-oligomer modification we choose the same polymerization conditions as for the corresponding blocks of the PDMAEMA-*b*-PMEP block-co-oligomer. Those conditions lead to a pore filling of ≈50 vol% in case of the PDMAEMA modification and ≈80 vol% for the PMEP modification (Table S1, Supporting Information) in initially empty mesopores.[7a] As prepared PDMAEMA-modified mesopores entirely exclude $[Ru(NH_3)_6]^{2+/3+}$ molecules at acidic pH (Figure 2a) and hinder transport (reduced j_p as compared to unfunctionalized mesopores) at basic pH. This effect is even more prominent for PMEP-modified mesopores entirely excluding $[Fe(CN)_6]^{3-/4-}$ molecules (Figure 2b) independently of pH as well as $[Ru(NH_3)_6]^{2+/3+}$ molecules at acidic pH and thus at conditions at which the oligomer is not charged. Reduced j_p values for uncharged pores compared to the mesoporous silica reference can be mainly ascribed to the pore filling with polymer, inducing steric hindrance. A strong influence of the pore filling on the ionic mesopore accessibility can as well be deduced from the j_p obtained under electrostatic attraction between oligomer-functionalized pore and probe molecule: Compared to the mesopore accessibility of $[Ru(NH_3)_6]^{2+/3+}$ into the unmodified mesoporous silica (Figure 2c) film the maximum current density of $[Fe(CN)_6]^{3-/4-}$ in PDMAEMA-modified mesoporous films (Figure 2a) show a significant preconcentration as indicated by the doubled maximum current density. On the other hand, the peak current density of $[Ru(NH_3)_6]^{2+/3+}$ at pH 9 significantly decreases for the PMEP modified mesopores with high pore filling degrees of 80 vol% (Figure 2b) despite the electrostatic attraction between PMEP and $[Ru(NH_3)_6]^{2+/3+}$. These results clearly show the importance of controlling the polymerization and thus the pore filling to tune transport properties either toward higher ion concentration inside the mesopores or toward ion selectivity.

Based on these reference experiments ionic permselectivity of the block-co-oligomer functionalized mesopores with a pore filling degree of 95 vol% has been conducted (Figure 2d).[7a] Thereby our interest was triggered by the behavior of zwitterionically functionalized mesopores showing a bipolar nanopore behavior excluding ions independently of their charge.[10a,16] Designing the PDMAEMA-*b*-PMEP block-co-oligomer functionalization allows to introduce an identical number of opposite charges into one pore and into each polymer/oligomer chain but with a different chain architecture as compared to zwitterionic PCBMA, inducing a different nanoscale order. At an acidic pH the PDMAEMA-*b*-PMEP modified mesoporous silica film (Figure 2d) completely excludes the $[Ru(NH_3)_6]^{2+/3+}$ meanwhile the detected j_p of $[Fe(CN)_6]^{3-/4-}$ ions is comparable to unmodified silica films but does not show a preconcentration as strong as for the PDMAEMA modified mesoporous films. In contrast to this, at a basic pH the PDMAEMA-*b*-PMEP functionalized mesopores show a complete exclusion of $[Fe(CN)_6]^{3-/4-}$ ions while the maximum peak current density for the $[Ru(NH_3)_6]^{2+/3+}$ triples with a current peak density of 180 μA cm^{-2} compared to 53 μA cm^{-2} for the MEP homooligomer modified mesoporous film. From this observation we draw the following two conclusions: The first PDMAEMA block is as visible to ions as the second PMEP block, indicating that the position of the blocks does not significantly determine or hinder ionic permselectivity of such highly filled mesopores and thus the polymer synthesis can be planned purely on synthetic needs at least for the shown degrees of pore filling. Secondly, the maximum current density and thus the probe molecule concentration in the mesopores for block-co-oligomer filled pores are higher than for highly filled PMEP-homo-oligomer functionalized pores indicating that electrostatic attraction dominates and that an interaction between the different repetitions units is probable.

To fully exclude bipolar pore formation, which is not observed for acidic and basic pH (Figure 2d), ionic pore accessibility has been investigated upon gradually changing the solution pH. **Figure 3** shows the maximum peak current densities of the cationic ($[Ru(NH_3)_6]^{2+/3+}$, black spheres) and the anionic ($[Fe(CN)_6]^{3-/4-}$, green spheres) probe molecule at pH values between 2 and 12. From these data it is possible to distinguish three different ion selectivity regimes as illustrated in Figure 3 by the red to blue background color. At acidic pH values below the solution pKa_1 of MEP ($pKa_1 = 4.5$), the pore is purely anion selective (red background color regime in Figure 3b) with a nondetectable peak current density for the cationic probe molecule $[Ru(NH_3)_6]^{2+/3+}$. At these acidic pH values the pore is positively charged due to the PDMAEMA block. Starting at a solution pH of around 4 the maximum peak current density of the anionic probe molecule $[Fe(CN)_6]^{3-/4-}$ decreases by 35% from 242 to 160 μA cm^{-2} and stays constant until a pH of 8. Under the same conditions the maximum peak current density of the cationic probe molecule increases until it reaches the same peak current density as detected for the anionic probe molecule at pH 7.5–8. This second, neutral region between pH 4 and 8 has been identified to be between the pKa of DMAEMA (8.4) and the pKa_1 of MEP ($pKa_1 = 4.5$), resulting in both blocks being charged. This regime, indicated in violet color in Figure 3, is characterized by an increasing number of charged MEP repetition units of the block oligomer while the DMAEMA monomers are expected to stay positively charged. The existence of both charges can be expected since otherwise the detected maximum peak current density would be much smaller as visible in Figure 2a) and b) due to the mesopores being filled with polymer. The 3rd transport regime starts close to the solution pKa of DMAEMA at pH 8. The detected maximum peak current density for the anionic probe molecule in this basic pH range finally drops rapidly from 170 to almost

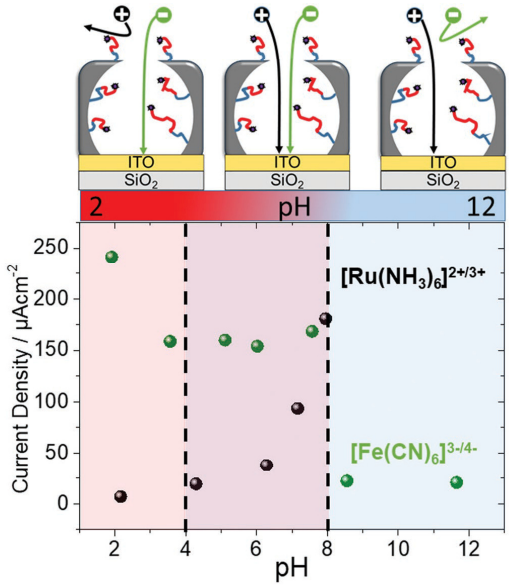

Figure 3. Pore scheme of a PDMAEMA-*b*-PMEP block-co-oligomer modified mesopore and its ionic permselectivity behavior with varying solution pH value. The measured ionic permselectivity can be gradually adjusted from anion selective at acidic pH (red area) over an open state between approximately pH 4–8 to a cation selective nanopore at basic pH (blue area). This observation is based on the pH-dependent current peak densities of $[Fe(CN)_6]^{3-/4-}$ (green spheres) and $[Ru(NH_3)_6]^{2+/3+}$ (black spheres) recorded at an ITO electrode below the mesoporous film at a scan rate of 100 mV s^{-1} in a 150×10^{-3} M PBS solution at solution pH values between 2 and 12.

20 µA cm^{-2} resulting into a cation selective pore (Figure 3 blue coded regime). Interestingly, these PDMAEMA-*b*-PMEP block oligomer with both monomers charged or partially charged obviously behave differently than mesopores functionalized with zwitterionic oligomers which exclude both, anions as well as cations, being described as bipolar pores.[16,17] This bipolar behavior is not observed for the described PDMAEMA-*b*-PMEP block-co-oligomer functionalized mesopores although, positive and negative charges are simultaneously present in each polymer chain within a mesopore, too. Thus, the polymer/oligomer chain architecture, anion and cation confined into each monomer for zwitterionic polymers versus separation of anions and cations into a block like sequence seems to crucially affect the resulting ionic mesopore accessibility. This behavior might be partially due to interactions between the blocks of different oligomer chains, which surely get in contact in such a confined environment as an 8 nm pore. The measurements described were performed at an ionic strength of 150×10^{-3} M which corresponds to a Debye Screening length of ≈0.9 nm. Since the Debye Screening length can play a crucial role on pore accessibility and thus on ion selectivity, additional measurements at an ionic strength of 30×10^{-3} M were performed (Figure S2c,d, Supporting Information). These measurements showed no significant difference with respect to charge selectivity of the modified mesoporous silica films under the applied measurement conditions as well supporting high pore filling degrees. In addition to its double pH responsiveness, PMEP bares the potential to investigate ligand binding and selective gating because it chelates divalent cations such as Ca^{2+}. Both aspects strongly influence transport related applications such as (bio)separation and sensing in which a variety of ions is present and selective interaction is required. In a previous work we demonstrated two-valent ion induced gating of PMEP functionalized mesopores at basic pH resulting in similar ionic pore accessibility characteristics as for acidic pH conditions.[6c] Here, we are systematically addressing significantly higher pore filling degrees (23 vol% vs up to >80 vol%) as well as the chain architecture. By comparing purely PMEP functionalized pores to PDMAEMA-*b*-PMEP block-co-oligomer functionalized mesopores. As a first result the high pore-filling degress of ≈80 vol% for PMEP functionalized mesopores block the pore for $[Fe(CN)_6]^{3-/4-}$ probe molecules as already shown in Figure 2. The presence of calcium ions does not affect this behavior (Figure S2b, Supporting Information). Nevertheless, the pore accessibility for electrostatically attracted $[Ru(NH_3)_6]^{2+/3+}$ probe molecules behaves as expected (**Figure 4**a black vs green). The maximum peak current density significantly decreases upon addition of calcium from initially 60 to 20 µA cm^{-2} due to the blocking of PMEP charges and thus decreasing electrostatic attraction. Additionally the redox peak potential shifts which seems to indicate electrostatic attraction (Figure S2c, Supporting Information). This leads also to a decrease in the pH responsiveness of the system. Upon the addition of Ca^{2+}-ions (2×10^{-3} M) to the solution the cyclic voltammograms do not vary significantly when measured at a solution pH of 2 and 11 (Figure S2a, Supporting Information). In addition, the chelation between the MEP and calcium ions is clearly transport limited and equilibrium is reached after ≈30 min (Figure 4a different colors) as well supporting the influence of high pore filling degrees. Upon addition of Ca^{2+}-ions to PDMAEMA-*b*-PMEP block-co-oligomer functionalized mesopores (Figure 4b) the effect of chain architecture on ionic pore accessibility again becomes very clear. In contrast to purely PMEP functionalized mesopores no effect of calcium ions on ionic pore accessibility (j_p) is observed for PDMAEMA-*b*-PMEP functionalized mesoporous films at basic pH (Figure 4b). Whereas calcium ions strongly affect ionic pore accessibility at pH values between 2 and 7.5 corresponding to the anion selective and neutral pH regime in Figure 3. This strongly indicates an interaction between calcium ions and PMEP still at acidic pH which implicates, in contrast to the expectation based on solution pKa values, that PMEP still is not fully neutralized within this pH range. This is additionally supported by the j_p, indicating a significant preconcentration for $[Fe(CN)_6]^{3-/4-}$ probe molecules in this pH-range (Figure 4b). Comparing the maximum peak current density of PDMAEMA-*b*-PMEP block-co-oligomer functionalized mesopores in the absence of calcium (Figure 4b spheres, Figure 2d) this is much lower as for purely PDMAEMA functionalized pores under identical conditions (acidic pH, Figure 2a red). Upon addition of calcium ions to PDMAEMA-*b*-PMEP block-co-oligomer functionalized mesopores with a pore filling degree of ≈95 vol% (Figure 4b, red star, pH 2) the pore accessibility and thus the measured

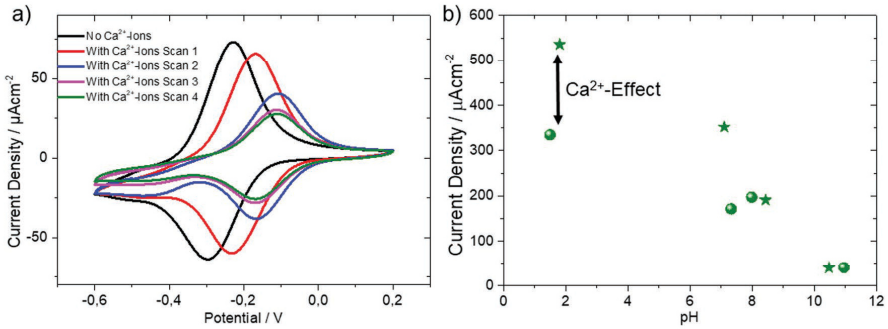

Figure 4. a) Cyclic voltamogramms of a PMEP modified mesoporous silica film before (black line) and after addition of Ca^{2+}-ions into the bulk solution in dependence of time after addition (red 0 min, blue 7 min, pink 14 min, and green 21 min). Measurements are recorded using $[Ru(NH_3)_6]^{2+/3+}$ as probe molecule at a scanrate of 100 mV s^{-1} in a 150 × 10^{-3} M PBS solution at a solution pH of 11. b) Current peak densities of a PDMAEMA-*b*-PMEP modified mesoporous silica film using $[Fe(CN)_6]^{3-/4-}$ as probe molecule and recorded at a scan rate of 100 mV s^{-1} in a 1× PBS solution (150 × 10^{-3} M) at pH values between 2 and 12 in the presence (stars) and absence (spheres) of 2 × 10^{-3} M $CaCl_2$.

maximum peak current density increases by 200 µA cm^{-2} corresponding to a factor of 1.6–2 and reaches values of ≈535 µA cm^{-2} comparable to purely PDMAEMA functionalized mesopores with a pore filling degree of ≈80 vol%. This fully inversed transport behavior of the block-co-oligomer functionalized mesopores compared to homooligomer functionalized mesopores demonstrates the strong influence of the charge composition and chain architecture. This is an essential aspect in approaching nature's pore design and transport control precision and with this implementing and pushing nanopore transport dependent technologies. Our results are a first experimental step toward this direction allowing multifunctionality combined with precise design in pore filling and chain architecture, although still being less precise as theoretical studies implicate with respect to monomer positioning along a polymer chain.[13]

Precise design of nanopore functionalization, and not only the choice of functional polymers, strongly determines their ionic accessibility and transport performance. Pore filling limits transport especially if no electrostatic attraction exists. Nevertheless, this effect can be overcompensated by precise chain architecture and charge composition design. Based on functionalization of mesopores with block-co-oligomer polyelectrolytes, composed of pH-responsive and orthogonally charged blocks, a complex transport behavior differing from the homo-oligomer functionalized mesopores has been implemented. This functionalization has been achieved by reinitiation of controlled iniferter-initiated polymerization. PDMAEMA-*b*-PMEP functionalized mesopores with high pore filling degrees of up to 95 vol% have been gradually tuned from anion to cation selective depending on solution pH. Thereby no bipolar pore behavior, as reported for zwitterionic polymer modified mesopores, is observed in pH-regimes in which both blocks should be orthogonally charged. This demonstrates the importance of oligomer chain architecture design for ionic mesopore permselectivity. Finally, ligand binding and selective gating is strongly influenced by this chain architecture. We demonstrate that the pore opening and closing behavior can be expanded by using block-co-oligomer polyelectrolytes PDMAEMA-*b*-PMEP as compared to the individual polyelectrolytes PDMAEMA and PMEP. All together this functionalization and the observed complex transport control offers a toolbox to fine tune mesopore transport based on pore filling degrees and block-co-oligomer ratios allowing to approach nature's design precision. Especially if the precision of chain design will be further improved, e.g., by using peptide synthesis and precise combinations and placement of chargeable or ligand binding functional units. This fine tuning is expected to advance technologies depending on pore accessibility and transport control such as sensors or (bio)separation and water management.

Experimental Section

Surface-Initiated Polymerization (SIP) of DMAEMA-b-MEP: Following the literature procedure by Tom et al. the block-co-oligomer functionalization was done in two consecutive steps.[7a] As a first step surface-initiated polymerization (SIP) (1), DMAEMA (2.0 mL, 11.8 mmol) were dissolved in dry DMF (16 mL). To this solution, a SBDC functionalized mesoporous silica film deposited on an ITO coated glass substrate was added before the mixture was sealed with a rubber septum and deoxygenated by nitrogen bubbling for 5 min before irradiation using a Bio-Link BLX by Vilber Lourmat (t = 5 min, λ = 365 nm, P = 40 W). The substrates were subsequently extracted through multiple washing steps with DMF and distilled H_2O. For the subsequent second SIP, SIP (2), MEP (0.55 g) was dissolved in distilled H_2O (20 mL). The substrate was added to this solution before the mixture was sealed using a rubber septum and deoxygenated for 15 min before irradiation using a Bio-Link BLX by Vilber Lourmat (t = 15 min, λ = 365 nm, P = 40 W). Finally, the substrates were extracted in distilled water overnight.

Supporting Information

Supporting Information is available from the Wiley Online Library or from the author.

Acknowledgements

The authors acknowledge funding from the Hessen State Ministry of Higher Education, Research and the Arts, Germany, in the frame of the

LOEWE project iNAPO. The authors thank Nicole Herzog for her help with XPS and TEM sample preparation and Karl Kopp for performing XPS measurements. The authors also thank Ulrike Kunz and Prof. Kleebe from the department of Materials Science of the Technische Universität Darmstadt for their support with TEM measurements and Prof. Markus Biesalski for access to interface characterization facilities.

Conflict of Interest

The authors declare no conflict of interest.

Keywords

confinement effects, ionic permselectivity, mesoporous silica, multiresponsive gating, polyelectrolyte block copolymers

Received: May 25, 2019
Revised: August 12, 2019
Published online: August 25, 2019

[1] a) D. M. Mitrano, E. Rimmele, A. Wichser, R. Erni, M. Height, B. Nowack, *ACS Nano* **2014**, *8*, 7208; b) D. A. Doyle, J. M. Cabral, R. A. Pfuetzner, A. Kuo, J. M. Gulbis, S. L. Cohen, B. T. Chait, R. MacKinnon, *Science* **1998**, *280*, 69.

[2] a) A. Walcarius, *Chem. Soc. Rev.* **2013**, *42*, 4098; b) B. Yameen, M. Ali, R. Neumann, W. Ensinger, W. Knoll, O. Azzaroni, *Chem. Commun.* **2010**, *46*, 1908; c) J. Weber, L. Bergstrom, *Langmuir* **2010**, *26*, 10158.

[3] a) G. J. Soler-Illia, O. Azzaroni, *Chem. Soc. Rev.* **2011**, *40*, 1107; b) L. Nicole, C. Boissière, D. Grosso, A. Quach, C. Sanchez, *J. Mater. Chem.* **2005**, *15*, 3598; c) C. J. Brinker, Y. Lu, A. Sellinger, H. Fan, *Adv. Mater.* **1999**, *11*, 579; d) D. R. Dunphy, P. H. Sheth, F. L. Garcia, C. J. Brinker, *Chem. Mater.* **2015**, *27*, 75.

[4] a) H. Zhang, Y. Tian, L. Jiang, *Nano Today* **2016**, *11*, 61; b) F. Xia, L. Jiang, *Adv. Mater.* **2008**, *20*, 2842; c) X. Hou, W. Guo, L. Jiang, *Chem. Soc. Rev.* **2011**, *40*, 2385; d) M. Tagliazucchi, O. Azzaroni, I. Szleifer, *J. Am. Chem. Soc.* **2010**, *132*, 12404; e) M. Ulbricht, *Polymer* **2006**, *47*, 2217.

[5] a) M. H. Sun, S. Z. Huang, L. H. Chen, Y. Li, X. Y. Yang, Z. Y. Yuan, B. L. Su, *Chem. Soc. Rev.* **2016**, *45*, 3479; b) Z. Zhang, X. Sui, P. Li, G. Xie, X. Y. Kong, K. Xiao, L. Gao, L. Wen, L. Jiang, *J. Am. Chem. Soc.* **2017**, *139*, 8905.

[6] a) G. Perez-Mitta, W. A. Marmisolle, A. G. Albesa, M. E. Toimil-Molares, C. Trautmann, O. Azzaroni, *Small* **2017**, *14*, 1702131; b) F. M. Gilles, M. Tagliazucchi, O. Azzaroni, I. Szleifer, *J. Phys. Chem. C* **2016**, *120*, 4789; c) A. Brunsen, C. Diaz, L. I. Pietrasanta, B. Yameen, M. Ceolin, G. J. Soler-Illia, O. Azzaroni, *Langmuir* **2012**, *28*, 3583; d) H. Zhang, X. Hou, L. Zeng, F. Yang, L. Li, D. Yan, Y. Tian, L. Jiang, *J. Am. Chem. Soc.* **2013**, *135*, 16102.

[7] a) J. Tom, R. Brilmayer, J. Schmidt, A. Andrieu-Brunsen, *Polymers* **2017**, *9*, 539; b) L. Silies, H. Didzoleit, C. Hess, B. Stühn, A. Andrieu-Brunsen, *Chem. Mater.* **2015**, *27*, 1971; c) M. Kruk, *Isr. J. Chem.* **2012**, *52*, 246.

[8] a) J. O. Zoppe, N. C. Ataman, P. Mocny, J. Wang, J. Moraes, H. A. Klok, *Chem. Rev.* **2017**, *117*, 1105; b) E. M. Benetti, C. Kang, J. Mandal, M. Divandari, N. D. Spencer, *Macromolecules* **2017**, *50*, 5711; c) H. K. S. B. de Boer, M. P. L. Werts, E. W. van der Vegte, G. Hadziioannou, *Macromolecules* **2000**, *33*, 349; d) J. Jiang, X. Xiao, P. Zhao, H. Tian, *J. Polym. Sci., Part A: Polym. Chem.* **2010**, *48*, 1551; e) J. Elbert, M. Gallei, C. Rüttiger, A. Brunsen, H. Didzoleit, B. Stühn, M. Rehahn, *Organometallics* **2013**, *32*, 5873; f) T. Otsu, A. Kuriyama, *J. Macromol. Sci.,– Chem.* **1984**, *21*, 961; g) K. Matyjaszewski, *Macromolecules* **2012**, *45*, 4015; h) L. Cao, M. Kruk, *Polym. Chem.* **2010**, *1*, 97; i) C. Barner-Kowollik, T. P. Davis, J. P. A. Heuts, M. H. Stenzel, P. Vana, M. Whittaker, *J. Polym. Sci., Part A: Polym. Chem.* **2003**, *41*, 365.

[9] S. P. Adiga, D. W. Brenner, *J. Funct. Biomater.* **2012**, *3*, 239.

[10] a) B. Yameen, M. Ali, R. Neumann, W. Ensinger, W. Knoll, O. Azzaroni, *J. Am. Chem. Soc.* **2009**, *131*, 2070; b) G. Chen, S. Das, *J. Appl. Phys.* **2015**, *117*, 185304.

[11] D. F. Stamatialis, B. J. Papenburg, M. Gironés, S. Saiful, S. N. M. Bettahalli, S. Schmitmeier, M. Wessling, *J. Membr. Sci.* **2008**, *308*, 1.

[12] a) A. Brunsen, J. Cui, M. Ceolin, A. del Campo, G. J. Soler-Illia, O. Azzaroni, *Chem. Commun.* **2012**, *48*, 1422; b) Z. Wang, X. Yang, Z. Cheng, Y. Liu, L. Shao, L. Jiang, *Mater. Horiz.* **2017**, *4*, 701; c) Y. Feng, W. Zhu, W. Guo, L. Jiang, *Adv. Mater.* **2017**, *29*, 1702773; d) H. Cheng, Y. Zhou, Y. Feng, W. Geng, Q. Liu, W. Guo, L. Jiang, *Adv. Mater.* **2017**, *29*, 1700177; e) G. Xie, L. Wen, L. Jiang, *Nano Res.* **2016**, *9*, 59.

[13] K. Huang, I. Szleifer, *J. Am. Chem. Soc.* **2017**, *139*, 6422.

[14] a) C. S. Hang, J. M. Shik, Y. S. Hong, L. H. Bang, *J. Polym. Sci., Part B: Polym. Phys.* **1997**, *35*, 595; b) H. Lee, S. H. Son, R. Sharma, Y. Y. Won, *J. Phys. Chem. B* **2011**, *115*, 844.

[15] N. Herzog, J. Kind, C. Hess, A. Andrieu-Brunsen, *Chem. Commun.* **2015**, *51*, 11697.

[16] L. Silies, A. Andrieu-Brunsen, *Langmuir* **2017**, *34*, 807.

[17] A. Calvo, B. Yameen, F. J. Williams, G. J. A. A. Soler-Illia, O. Azzaroni, *J. Am. Chem. Soc.* **2009**, *131*, 10866.

4.4. Synthese und Verwendung von Farbstoffen zur pH-Detektion in Silicamesoporen

In diesem Teil der Arbeit soll die Herstellung und Verwendung von farbstofffunktionalisierten mesoporösen Silicamaterialien zur in-situ pH-Detektion im Vordergrund stehen.

Die Kombination aus Farbstoffmolekülen als molekulare pH-Sensoren und mesoporösen Silicadünnfilmen oder –partikeln ist ein etablierter Prozess, um nanoskalige Sensorikmaterialien für etwa Schwermetallionen oder auch den pH-Wert herzustellen. Allerdings steht in der Regel nicht der pH-Wert in diesen Poren selbst im Fokus. Aus der eher biologischen Forschung ist zudem bekannt, dass z. B. Krebszellen Veränderungen im pH-Wert aufweisen. Um dieses Phänomen genauer zu untersuchen, wurden Farbstoffe als molekulare pH-Sensoren eingesetzt. Das bekannteste Beispiel ist vermutlich das seit 30 Jahren etablierte Carboxy-SNARF.[204] Auch für die pH-Detektion in Nanoporen ist SNARF-1 genutzt worden.[161] In einer Studie von *Mori et al.* wurde z. B. durch Eintauchen in eine Farbstofflösung mit SNARF-1 dieses an Nanoporen adsorbiert, jedoch nicht kovalent an die Nanopartikel angebunden. Des Weiteren waren aufwändige Messungen mit einem Konfokalmikroskop nötig, um pH-Werte auslesen zu können. Ein weiteres Beispiel für pH-Detektion auf der Nanoskala aus Arbeiten unserer Gruppe ist die Verwendung von Fluorescein und Rhodamin B FRET-Farbstoffpaaren. Im Rahmen einer von mir mitbetreuten Masterarbeit konnte Mathias Stanzel auf Basis dieses FRET-Paares Silicamaterialien mit einem einstellbaren Detektionsbereich herstellen.[44] Dieses Sensorsystem erlaubt durch die Natur von FRET allerdings keinen Vergleich zu Messungen in Bulklösungen, da für erfolgreiches FRET die räumliche Distanz zwischen Donor und Akzeptor stimmen muss, ein Aspekt, der in Bulklösung nicht kontrolliert werden kann. Ratiometrische Farbstoffe zeigen hier einen klaren Vorteil für das Konzept der pK_s-Wert-Detektion in Nanoporen.

Interessanterweise gibt es bisher keine Arbeiten, die pH-auslesende Farbstoffe mit einem für die Silicasilanolgruppen relevanten Detektionsbereich in Silicamaterialien kombinieren, um deren pH-responsives Schaltverhalten zu untersuchen. Die für Anwendungen in Zellen / biologischen Fragestellungen entwickelten Farbstoffe sind auf den in diesen Fragestellungen relevanten pH-Bereich um ca. pH 7 optimiert. Dies trifft auch für SNARF zu. In dieser Arbeit konnte ein ratiometrischer Farbstoff auf Basis des von *Zheng et al.* entwickelten MPT-Farbstoffes hergestellt, charakterisiert, kovalent an Silicamesoporen angebunden und erfolgreich für pH-Messungen verwendet werden. Die Charakterisierung des Farbstoffs und die Anbindung erfolgte dabei in Kooperation mit Martin Brodrecht und Bharti Kumari (AG Buntkowsky, TU Darmstadt) und Christoph Kaiser (AG Wachtveitl, Goethe-Universität Frankfurt am Main). Eine Übersicht der für dieses Kapitel relevanten Farbstoffe ist in Abbildung 4-1 dargestellt:

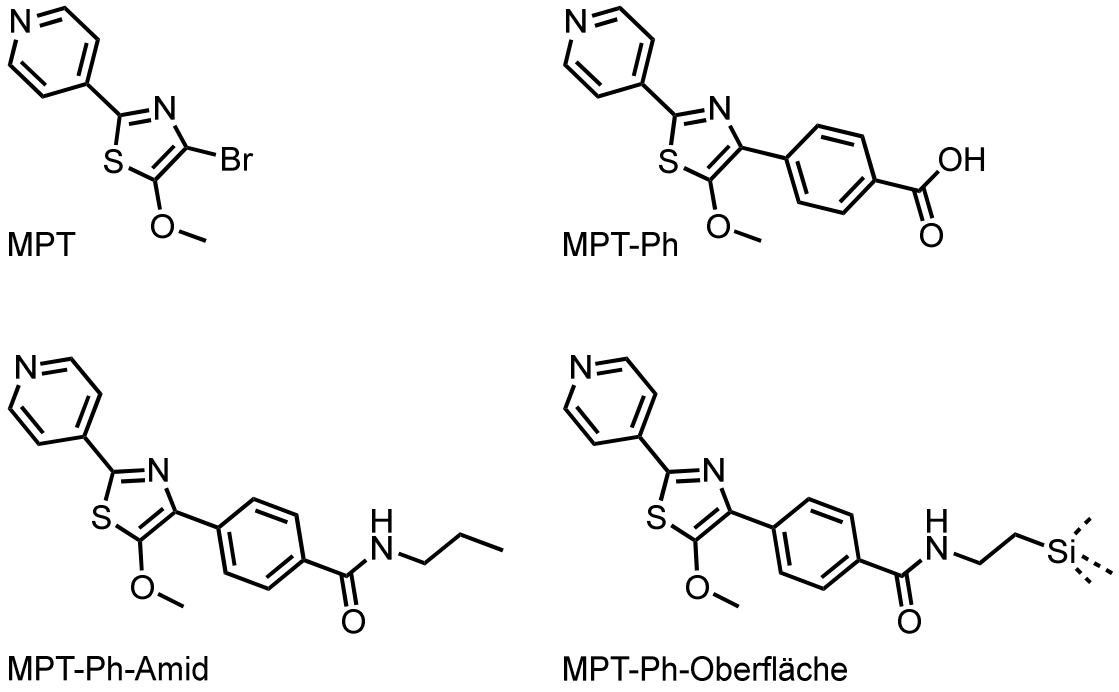

Abbildung 4-1 Darstellung der in diesem Abschnitt synthetisierten Farbstoffe MPT, MPT-Ph, MPT-Ph-Amid und MPT-Ph-Oberfläche

Im ersten Schritt wurde der durch Arbeiten von *Zheng et al.*[205] bekannte MPT-Farbstoff um einen Carboxyphenylrest erweitert, wodurch eine Ankergruppe zur Anbindung an Aminosilica eingebracht werden konnte und das Absorptions- und Emissionsspektrum des Farbstoffes weiter in den sichtbaren Wellenlängenbereich verschoben wurde. Dies ist vorteilhaft für eine optische Verfolgung von pH-Änderungen mit dem Auge. Zudem vereinfacht eine Verschiebung des Absorptionsmaximums ins sichtbare Licht die Verwendung des Farbstoffes mit laserbasierten Mikroskopen, da diese meist mit Lasern von Wellenlängen <400 nm eingesetzt werden. Die optischen Eigenschaften des MPT-Ph sowie der protonierten Form MPT-Ph-H^+ wurden von Christoph Kaiser (AG Wachtveitl, Universität Frankfurt/Main) untersucht.

Im zweiten Schritt wurde der hergestellte MPT-Ph-Farbstoff in Zusammenarbeit mit Martin Brodrecht (AG Buntkowsky, TU-Darmstadt) erfolgreich an von mir hergestellte aminofunktionalisierte mesoporöse Silicadünnfilme und an von Martin Brodrecht hergestellte mesoporöse SBA-15 Nanopartikel angebunden. Die SBA-15 Nanopartikel dienten hierbei als Referenzmaterial, durch deren Verwendung in BET- und Festkörper-NMR-Experimenten die erfolgreiche Anbindung von Martin Brodrecht nachgewiesen werden konnte. Durch Anwendung von Festkörper-NMR-DNP-Experimenten konnte Bharti Kumari (AG Buntkowsky, TU-Darmstadt) die Protonierung des Pyridyl-Stickstoffatoms des MPT-Ph in saurer Umgebung nachweisen.

MPT-Ph und MPT-Ph-Amide wurden im letzten Schritt in Bulklösung und in mesoporösen Silicafilmen bei unterschiedlichen pH-Werten per UV-Vis untersucht, untereinander verglichen und deren pK_s-Werte bestimmt. Hierbei konnte ein starker Einfluss der nanoskaligen Umgebung auf das Schaltverhalten des Farbstoffes nachgewiesen werden. Der pK_s-Wert wurde verglichen mit

MPT-Ph und MPT-Ph-Amid um etwa eine pH-Einheit hin zu saureren pH-Werten verschoben. Desweiteren konnte auch gezeigt werden, dass sich die Ionenstärke der Messlösung, welche die di-elektrische Doppelschicht in Mesoporen beeinflusst, auch die Schaltung des Farbstoffes beeinflusst. Bei einer größeren di-elektrischen Doppelschicht (geringere Ionenstärke) wurde die Verschiebung des MPT-Ph-pK_s-Wertes größer.

Mein Beitrag zu diesem Kapitel bestand in der Entwicklung und Synthese des MPT-Ph-Farbstoffes, dessen kovalente Anbindung an mesoporöse Silicadünnfilme, sowie die pH-abhängigen UV-Vis-Messungen von MPT-Ph, MPT-Ph-Amide und MPT-Ph-Oberfläche.

Die Ergebnisse der Masterarbeit von Mathias Stanzel, an denen ich mitgewirkt habe, sind bei Microporous and Mesoporous Materials veröffentlicht:
M. Stanzel, R. Brilmayer, M. Langhans, T. Meckel, A. Andrieu-Brunsen, **FRET-based pH-sensing in mesoporous thin films with tunable detection range**, *Microporous and Mesoporous Materials*, **2019**, 282, 29-37.
Publiziert von Elsevier – © 2019 – mit Genehmigung verwendet;
DOI: 10.1016/j.micromeso.2019.03.009

Die *Supporting Information* ist nicht abgedruckt, aber in der elektronischen Version dieses Artikels (DOI: 10.1016/j.micromeso.2019.03.009) verfügbar.

Die restlichen Ergebnisse dieses Abschnittes wurden noch nicht veröffentlicht:

Robert Brilmayer*, Martin Brodrecht*, Christoph Kaiser, Hergen Breitzke, Bharti Kumari, Josef Wachtveitl, Gerd Buntkowsky, Annette Andrieu-Brunsen, **A new dye for ratiometric pH detection inside silica mesopores**
*These authors contributed equally to this work

The interplay of nanoconfinement and pH: a new dye for in-situ ratiometric pH detection inside silica mesopores

Robert Brilmayer[1+], Martin Brodrecht[2+], Christoph Kaiser[3], Hergen Breitzke[2], Bharti Kumari[2], Josef Wachtveitl[3], Gerd Buntkowsky[2], Annette Andrieu-Brunsen[1*]*

Robert Brilmayer[+], Dr. Martin Brodrecht[+], Dr. Hergen Breitzke, Dr. Bharti Kumari, Prof. Dr. Josef Wachtveitl, Prof. Dr. Gerd Buntkowsky, Prof. Dr. Annette Andrieu-Brunsen*

Robert Brilmayer[+], Prof. Dr. Annette Andrieu-Brunsen*
Ernst-Berl-Institut für Technische und Makromolekulare Chemie
Technische Universität Darmstadt
Alarich-Weiss-Str. 12, 64287 Darmstadt, Germany

Dr. Martin Brodrecht[+], Dr. Hergen Breitzke, Dr. Bharti Kumari, Prof. Dr. Gerd Buntkowsky*
Eduard-Zintl-Institut für Anorganische und Physikalische Chemie
Technische Universität Darmstadt
Alarich-Weiss-Str. 8, 64287 Darmstadt, Germany

Christoph Kaiser, Prof. Dr. Josef Wachtveitl
Institute for Physical and Theoretical Chemistry
Goethe University
Max von Laue-Straße 7, 60438 Frankfurt/Main, Germany.

[+]Both authors contributed equally

Correspondence:
*andrieu-brunsen@smartmem.tu-darmstadt.de; *gerd.buntkowsky@chemie.tu-darmstadt.de

Keywords: fluorescence dye, ratiometric, silica, mesopore, solid-state NMR

Abstract: A novel thiazol based ratiometric dye for the detection of local pH-values is synthesized and its properties are characterized by a combination of optical spectroscopy, solid-state NMR and DNP enhanced solid-state NMR. This novel dye covers a completely different sensitivity range with its acidic pKa value of 3.5 as compared to other established dyes for ratiometric pH detection. The dye has been grafted to the surfaces of mesoporous silica materials, which enabled for the first time a direct in-situ

readout of the local pH values in silica mesopores by simple UV-vis measurements. The obtained results, which are in good agreement with previous indirect techniques, indicate a background electrolyte dependent pKa-shift of at least one pH unit under nano confinement as compared to bulk solution.

1. Introduction

Since their discovery in 1992 template based mesoporous silica materials (MSM) have attracted a growing interest in various research fields.[1] Nowadays MSM are commonly used in applications such as sensing[2-4], separation processes[5-6] or energy conversion[7]. MSM offer interesting properties such as a high specific surface area in addition to their high chemical and physical stability.[8] In addition to those attributes the surface silanol groups can be used to introduce organic functions in the inorganic framework.[9-10] This has particularly been relevant for mesoporous silica thin films as well as for mesoporous silica nanoparticles.[11] The functionalization with responsive organic moieties has led to the formation of the research field smart materials, which has been of significant relevance in the past 15 years.[9, 12-19] In these smart or responsive materials but as well in the application areas of smart materials such as drug delivery or sensing the environmental, pH plays a crucial role and its influence has thus been studied extensively. In this context differences between the pH value in solution and in nano confinement, for example within silica mesopores, have been reported based on theoretical studies and indirect experimental observation.[20-24] To this date experimental studies have been limited to indirect read out functions such as ion flow through nano channels or mesopore permselectivity to determine the charge of molecules inside nano scale environments.[25-26] [27-30] Although the pH detection in MSM has gained more importance over the last years the direct readout of the apparent pH value inside nanopores has not yet been fully explored.[23, 31-32] The most prominent recent advances can be ascribed to theoretical studies by the *Szleifer* group, who demonstrated the pKa shift of polyelectrolytes in nano channels. Until now the experimental determination and prediction of pH values in nanopores remains a challenge, but represents a crucial confinement parameter to understand in detail transport or release processes from or in mesoporous materials.[13]

One promising approach to investigate the pH value on a nano scale has been the use of dyes.

In the context of dyes as pH reporter molecules, a special focus was set to detect pH changes in cells over the last few years. In this research field various studies explored pH changes in cancer cells as compared to healthy cells, offering a new cancer detection method with huge potential.[33-38] Due to the nature of living cells those studies focused on very narrow pH detection range (pH 6.5-7.6). However, to cover the entire relevant range of functionalized nanopores and their applications dyes with sensitivity ranges between pH 1-5 are also needed. Potential dye sensors that have been explored together with mesoporous silica materials are on the one hand FRET (*Förster Resonance Energy Transfer*) dye pairs consisting of a pH-sensitive reporter and a pH-insensitive dye for concentration calibration. Due to the distinct nature of FRET a constant distance between the donor and the acceptor molecule has to be retained to allow reproducible FRET transfer and with this pH-detection. Since this is a parameter that cannot be easily controlled in bulk solution and cannot be sufficiently precisely characterized on surfaces or in mesopores, the use of FRET-dye pairs is not very suitable to draw comparisons between measurements in nano confinement and bulk solution,[23] Ratiometric dyes, which have a distinct absorption and/or emission maxima for their protonated and deprotonated state, are suitable to overcome the issues of FRET pH reporters for their use in nanopores. Additionally the spectral maxima of ratiometric dyes are concentration independent, what further facilitates comparisons between different measurements.[39-44] Out of the ratiometric dyes many, commonly in cells applied dyes such as the SNARF dye family, have a sensitivity region that does not overlap with the pKa value of silanol groups in mesoporous silica. One dye family that meets all the requirements mentioned above are thiazol based dyes such as the 5-methoxy-pyridylthialzole (MPT) dye introduced by *Zheng et al.*.[45] These dyes are of special interest in combination with silica materials since their pKa value is in the responsive range of silanol groups.[29-30, 45-47]

To address the pH region between 1.5 and 5.0 in nanoscale pores in this study we synthesize and investigate the potential of a new MPT based ratiometric pH reporter dye in conjunction with MSM. Besides the characterization and determination of the optical properties, the successful attachment of the dye on the silica framework has been confirmed by solid state NMR, thermogravimetric analysis (TGA), elemental analysis (EA) and Brunauer–Emmett–Teller based nitrogen adsorption–desorption (BET) measurements. Lastly, MPT-Ph has been successfully used to

determine pH shifts between bulk solutions and silica mesopores with a diameter smaller than 20 nm. Thereby, pH-shifts of more than one pH unit were observed.

2. Results and Discussion

2.1 Synthesis and optical properties of MPT-Ph

MPT-Ph (4-(5-methoxy-2-(pyridin-4-yl)thiazol-4-yl)benzoic acid) **2** and MPT-Amide (4-(5-methoxy-2-(pyridin-4-yl)thiazol-4-yl)-N-propylbenzamide) **3** were synthesized as outlined in **Scheme 1a**.

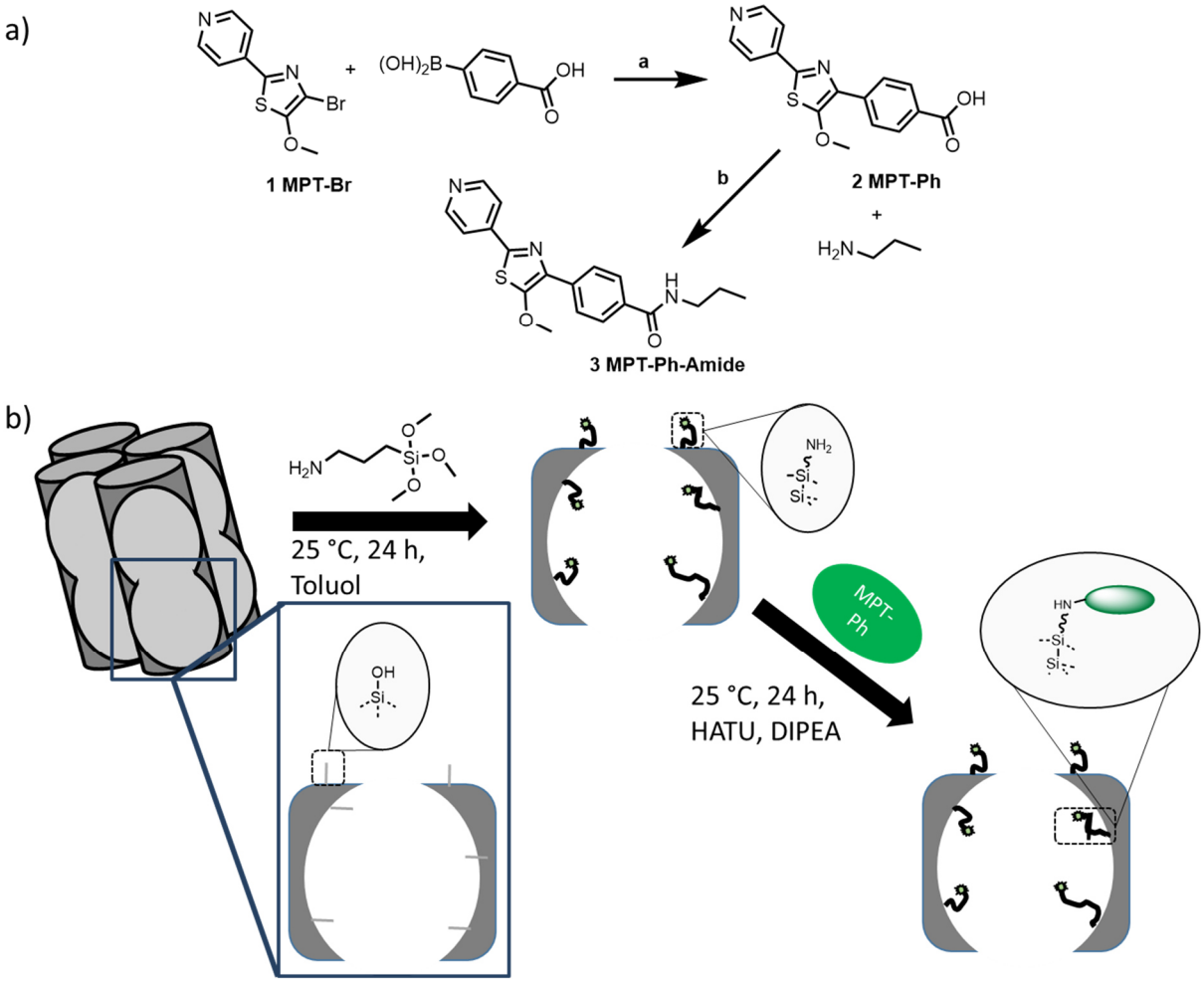

Scheme 1. a)Synthesis of MPT-Ph (4-(5-methoxy-2-(pyridin-4-yl)thiazol-4-yl)benzoic acid) **2** and MPT-Amide (4-(5-methoxy-2-(pyridin-4-yl)thiazol-4-yl)-N-propylbenzamide) **3**: a) X-Phos Pd G2 (Chloro(2-dicyclohexylphosphino-2′,4′,6′-triisopropyl-1,1′-biphenyl)[2-(2′-amino-1,1′-biphenyl)]palladium(II)), Dioxan/H_2O, K_2CO_3, reflux 24 h under inert atmosphere, 70 %; b) HATU (O–N, N, N′, N′-tetramethyluronium-hexafluorphosphat), DIPEA (diisopropylethylamine), DMF (N, N-dimethylformamide), 48 h under inert atmosphere, 71 %; b) Schematic illustration of silica modification. In the first step APTMS (aminopropyl trimethoxy silane) is attached to the unfunctionalized silica pores. In a second step the MPT-Ph is coupled to the amino function through an amide bond formation.

MPT-Br (4-Bromo-5-methoxy-2-(pyridin-4-yl)thiazole) **1** was synthesized in three steps according to a method established for MPT based dyes by *Zheng et al.*.[45-46] C-C bond formation was achieved by a *Suzuki* coupling reaction to form MPT-Ph **2** followed by an amination to yield MPT-Ph-Amide **3**. The compounds **2** and **3** were characterized by 1D- and 2D-NMR as well as ESI-MS (Fig S1-S8).

The MPT compound **1** is an acidochromic chromophore since its absorbance and emission shift bathochromicly upon acidification and thus protonation on the pyridine moiety. How the introduction of the phenyl group (MPT-Ph **2**) exerts on the photophysical properties of the MPT-Br **1** is depicted in Fig. 1B. For the protonated (Fig. 1b, green) and deprotonated MPT-Ph species (Fig. 1b, blue) the absorption and fluorescence are shifted bathochromicly by around 50 nm as compared to MPT-Br **1.** This is ascribed to the significant enlargement of the electronic □-system of the MPT-Ph **2**. Regarding MPT-Ph, protonation of the N-basic site entails a redshift of the emission band from approximately 450 nm to 510 nm. The introduction of the positive charge results in a more pronounced charge displacement and a lowered transition energy of the MPT-Ph (Fig. 1C).

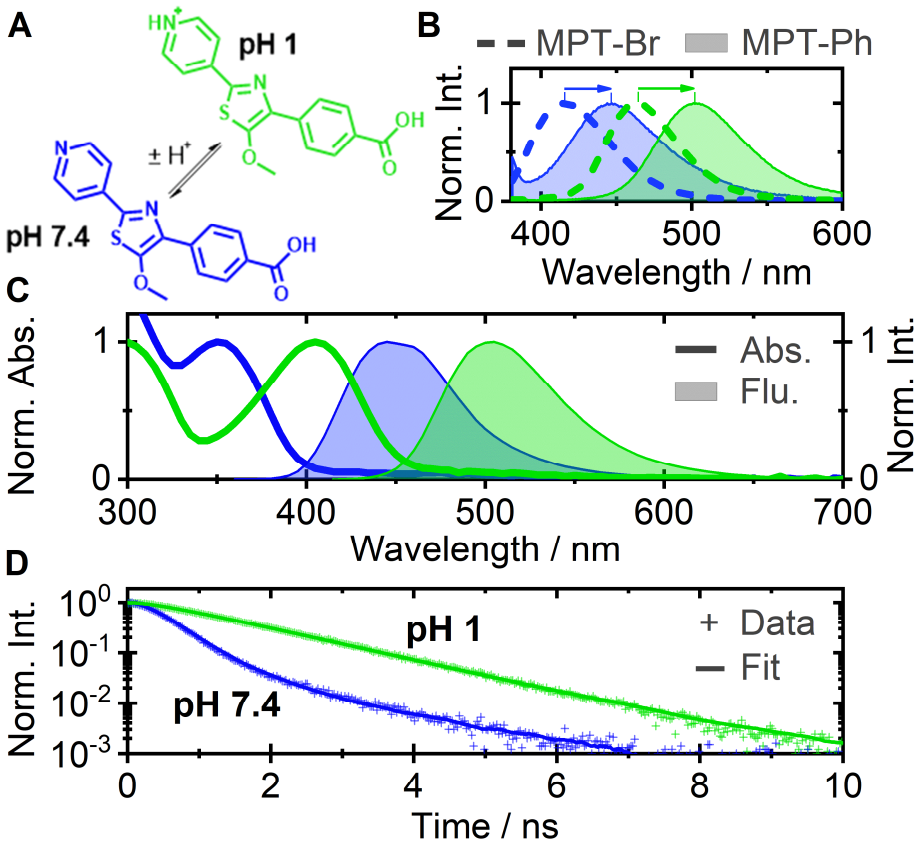

Figure 1. The protonated form of the MPT-Ph **2** dye and its spectra at pH 1 are shown in green and the deprotonated form at pH 7.4 in blue. A) Protonation reaction of MPT-Ph. B) Emission spectra of the deprotonated and protonated form of MPT-Br (dashed lines) and redshifted spectra of MPT-Ph (solid lines / green area). C) Absorbance (solid lines) and emission spectra (filled areas) of MPT-Ph. D) Fluorescence decays (plus signs) and exponential fits (solid lines) of both forms of the MPT-Ph dye.

The molar extinction coefficients of both forms MPT-Ph and MPT-Ph-H^+ were determined by measurement of the concentration dependent absorbance values at the maxima of their S1 bands. Following Lambert-Beer`s law, the protonated and deprotonated form exhibit extinction coefficients of (8070 ± 60) and (7440 ± 30) M^{-1} cm^{-1}, respectively (Figure S8). With use of an integrating sphere, fluorescence quantum yields of 7 % for the deprotonated and 23 % for the protonated form were calculated. The maximum emission signal can be obtained through excitation at the maximum of the S1 absorption bands for

both species (Figure S10, 3D contour plots). The excitation spectrum which is in fact a vertical cut through the contour plots at the maximum emission wavelength, resembles the absorption spectrum. In the excitation wavelength dependent contour plots, only the emission signals of the particular species are observed. Upon excitation of the deprotonated species at pH 7.4, no emission of the protonated form is detected, which indicates that the pyridine group does not act as a strong photobase and acquires a proton from the solvent, like related nitrogen-containing compounds reported in literature.[48-49] Interestingly, the fluorescence decays of MPT-Ph, recorded by means of time-correlated single photon counting (TCSPC), are significantly accelerated compared to other MPT derivatives.[45] The decay curve of the protonated form MPT-Ph-H^+ could be fitted monoexponentially, which revealed a lifetime of 1.4 ns (Fig. 1D). For the deprotonated MPT-Ph a sum of two exponential functions was required, where a 1.7 % contribution of the 1.4 ns lifetime could be assigned to residual amounts of the protonated species at pH 7.4. The major contribution of 98.3 % of a 0.3 ns lifetime accounts for deprotonated form.

2.3 MPT-Ph as pH-reporter in silica mesopores

Two different mesoporous silica materials with comparable porous structure were used as framework to incorporate the MPT-Ph dye. Mesoporous silica thin films with pore diameters of 8 and 16 nm and film thicknesses of 200-1000 nm were prepared using sol-gel chemistry and evaporation induced self-assembly as previously reported.[26, 50-51] Additionally, amino-functionalized mesoporous silica SBA-15 (Santa Barbara Amorphous 15) particles were prepared by a previously reported strategy.[52] The amino groups were introduced by a co-condensation approach using tetraethyl orthosilicate (TEOS) and (3-aminopropyl)triethoxysilane (APTES). BET characterization of the SBA-15 materials is presented in detail in the supporting information (Figure S11-S14 and Tabel S1-S4).

To explore the influence of spatial confinement on the pH value inside of silica mesopores the MPT-Ph pH reporter must be introduced into the silica framework, while being accessible for the measurement solution as illustrated for a post grafting approach in **Scheme 1b**. For this purpose, a covalent attachment of the dye is necessary to avoid leaching and thus a possible mixture of the dye in mesopores and dye in bulk solution.

The MPT-Ph dye carries a free carboxyl group which is not involved in the pH detection and can thus be used as anchor group. Amino groups are suitable reaction partners resulting in amide bond formation under very mild reaction conditions. For this reason, the prepared mesoporous silica thin films were first functionalized with APTMS (aminopropyl trimethoxy silane) via a post grafting approach while the amino functions in the SBA-15 material were introduced through co-condensation. In both cases the dye attachment through amide formation was performed using HATU as coupling reagent under identical reaction conditions.

Comparing thermogravimetric analysis (TGA) of the SBA-15 material before and after dye coupling (Figure S11) the weight fraction of the dye can be obtained (Table S1) leading to a dye loading of 0.33± 0.02 mmol/g. By applying elemental analysis (EA) weight and molar fractions of the elements nitrogen, carbon and hydrogen can be obtained (Table S2 and Table S3). Based on the result for nitrogen a dye loading of 0.54 ± 0.05 mmol/g can be calculated. The same applies for carbon leading to dye loading of 0.55 ± 0.02 mmol/g respectively.

Values for pore volume and specific surface area (Table S4) of the functionalized SBA-15 materials can be obtained by the Brunauer–Emmett–Teller (BET) analysis of the nitrogen adsorption-desorption isotherms (Figure S12). To investigate changes to the pore diameter due to dye functionalization, Barrett-Joyner-Halenda (BJH) (Figure S13) and density functional theory (NLDFT) (Figure S14) methods are applied. While BJH analysis suggests a decrease in pore diameter from 5.6 ± 0.2 nm to 4.9 ± 0.3 nm, NLDFT analysis states a decrease from 7.9 ± 0.2 nm to 6.6 ± 0.3 nm.

Combining the specific surface area of the dye functionalized SBA-15 material (271 ± 7 m^2/g) and the results of the molar dye grafting densities by TGA and EA analysis a surface grafting densities of the dye can be calculated leading to the results shown in Table 1.

Table 1. Calculated surface grafting densities of the MPT-Ph dye functionalized SBA-15 material obtained by the combination of the specific surface area obtained by nitrogen adsorption-desorption and molar dye grafting densities obtained by TGA and EA.

	TGA	EA (nitrogen)	EA (carbon)
Surface grafting density	0.73 ± 0.06	1.20± 0.14	1.22 ± 0.08

Both methods suggest a high degree of surface functionalization at the surface of the functionalized SBA-15 material.

To investigate the coupling efficiency and to proof the covalent binding of the MPT-Ph dye solid state NMR techniques were used. Since solid-state NMR requires a rather large amount of sample and a high degree of functionalization these investigations were carried out with the functionalized SBA-15 nanoparticles.

To monitor the success of the MPT-Ph dye modification ^{13}C CP MAS solid state NMR spectra were recorded before (**Figure 2a)** and after dye coupling (**Figure 2c)**. A spectrum of the MPT-Ph dye was also included to facilitate the peak assignment (**Figure 2b)**.

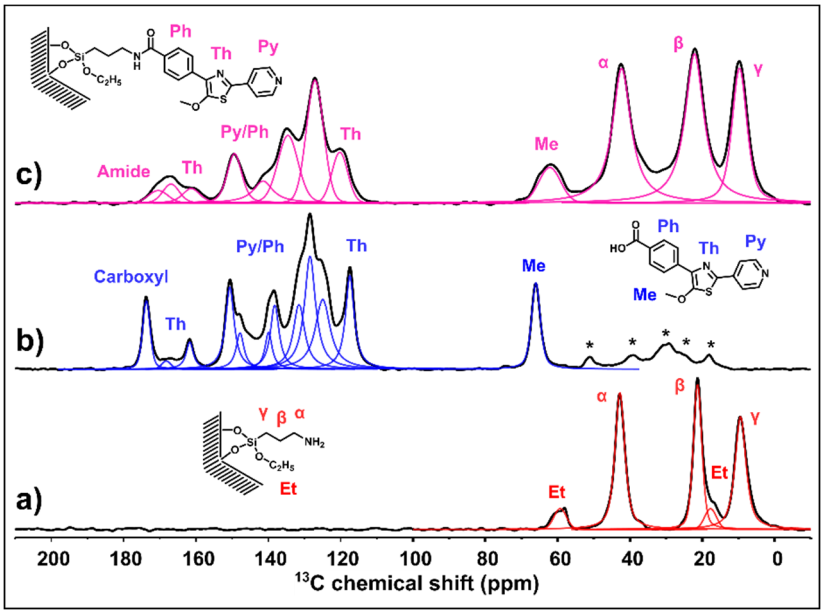

Figure 2. Comparison of the ^{13}C CP MAS spectra of the functionalized SBA-15 at 6 kHz (10 kHz for (b) and (c)) spinning. From bottom to the top spectra of the APTES functionalized SBA-15 (a), pure MPT-Ph dye (b) and MPT-Ph dye functionalized SBA-15 species (c).

Looking at the ^{13}C CP MAS spectrum of the APTES functionalized SBA-15 (**Figure 2a)** the signals at 9 ppm, 21 ppm and 43 ppm are assigned to the α, β and γ carbon atoms of the APTES-linker. The small additional features at 18 ppm and 59 ppm are assigned to not fully hydrolyzed ethoxy-groups of either APTES or TEOS.

The spectrum of the pure MPT-Ph dye (**Figure 2b)** shows a signal at 66 ppm, which is characteristic for the carbon atom for the methoxy group (Me). The resonances between 127 ppm and 144 ppm can be assigned to the aromatic carbon atoms of the phenyl (Ph) and pyridine (Py) ring. Additionally, the peaks at 117 ppm, 161 ppm and 168 ppm can be assigned to carbon atoms of the thiazole (Th) heterocycle. Finally, a peak at 173 ppm is assigned to the carbonyl carbon atom of the carboxyl group.

After coupling MPT-Ph to the silica mesopores (**Figure 2c)** the resonances of the α, β and γ carbon atoms of the APTES-linker at 10 ppm, 22 ppm and 42 ppm are still observed, which suggests that the linker is still attached to the surface. The signal at 62 ppm can be assigned to the methoxy carbon atom of the MPT-Ph dye. The resonances between 120 ppm and 149 ppm of the aromatic carbon atoms of the phenyl (Ph) are preserved. The signals at 117 ppm and between 161 ppm and 170 ppm previously assigned to the carbon atoms of the thiazole heterocycle are also still obtained. Most importantly, the resonance at 170 ppm can be assigned to the carbon atom of the newly formed amide bond between the APTES-linker and the dye. The chemical shift change of the carbonyl carbon from 173 ppm to 170 ppm indicates the conversion of the carboxylic carbon to an amide carbon.

To investigate the binding situation between the surface bound NH_2 group and the COOH group of the dye DNP-enhanced ^{15}N solid-state NMR was applied, which is able to detect the ^{15}N nuclei of an amide bond in natural abundance and thus avoids costly ^{15}N isotope labeling.[53-54]

The DNP-enhanced ^{15}N CP MAS NMR spectrum of the MPT-Ph dye functionalized SBA-15 species (**Figure 3a)** shows a signal at -6 ppm. This signal is assigned either to the protonated (NH_3^+) or non-protonated (NH_2) form of the nitrogen atom of the APTES-linker. The presence of this signal indicates unreacted amine groups on the surface. In addition, a second signal at 81 ppm is observed, which is assigned to the nitrogen atom of the amid group between the APTES-linker and the surface coupled dye. This clearly demonstrates the covalent binding of the MPT-Ph to the mesoporous silica surface. Furthermore, the small signal at 165 ppm is characteristic for Pyridinium cation (Py^+-H). The residual signals at 251 ppm and 268 ppm can be assigned to non-protonated nitrogen atom of the pyridine (Py) and the nitrogen atom of the thiazole heterocycle (Th).[55]

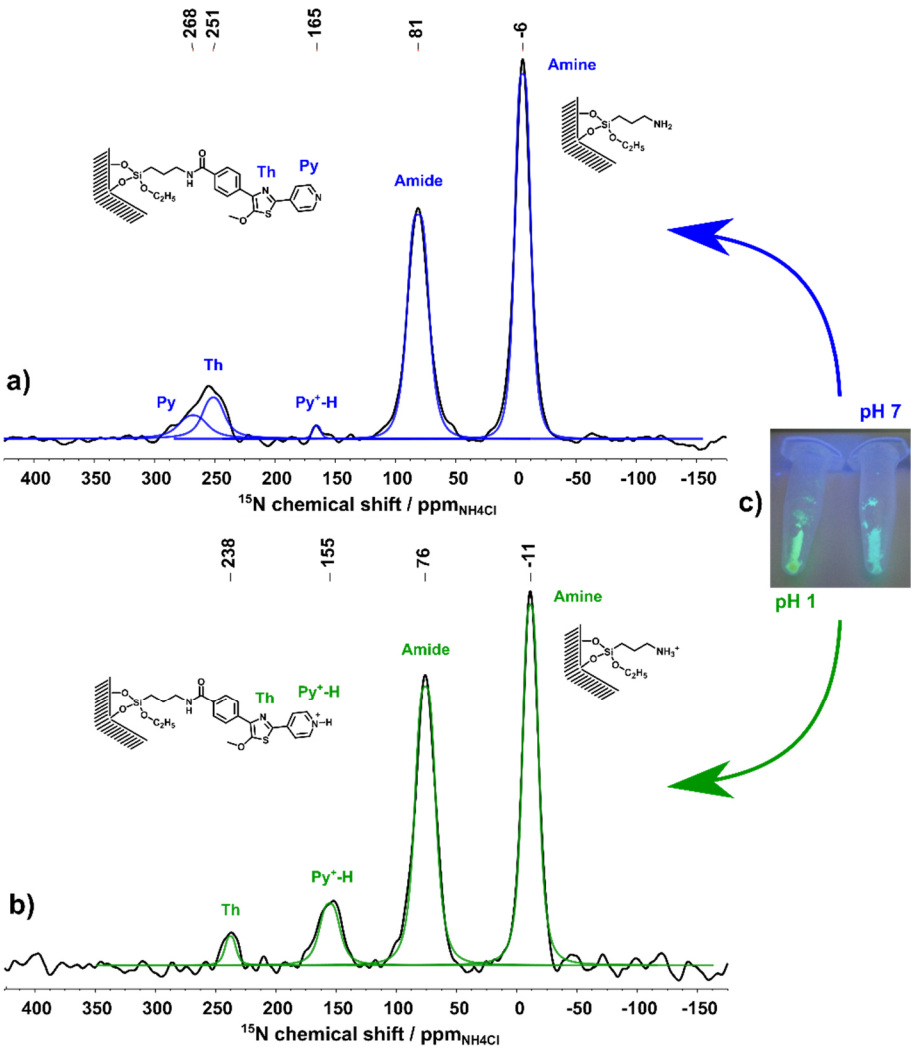

Figure 3. Comparison of DNP enhanced ^{15}N CP MAS spectra of the functionalized SBA-15 at 8 kHz spinning nominally at 110 K. Spectra of MPT-Ph dye functionalized SBA-15 silica at pH 7 (a) and pH

1 (b). Comparison (c) of dried MPT-Ph dye functionalized SBA-15 silica under UV light irradiation (352 nm) used for the NMR measurements.

To investigate the pH responsiveness of the dye bound to surface of the pore system the pH value of the DNP matrix was adjusted to pH 1 by the addition of DCl. The pH change results in a color change from blue (pH 7) to green (pH 1) under UV light irradiation (352 nm). This color is maintained even after removing the excess liquid (**Figure 3c)**, which proofs pH response of the surface bound dye.

Additionally, a DNP-enhanced ^{15}N CP MAS NMR spectrum of the acidic sample was recorded to investigate chemical changes of the dye induced by the pH change (**Figure 3b)**. Comparing the spectrum recorded before (**Figure 3a)** and after pH adjustment the signal at -11 ppm is preserved. At this pH this signal is assigned to the protonated (NH_3^+) form of the nitrogen atom of the APTES-linker. The resonance of the amide nitrogen is still observed at 76 ppm, which clearly states the stability of the covalent MPT-Ph binding to the silica surface even at pH 1. Also, the signal of the protonated pyridine nitrogen (Py^+-H) is preserved at pH 1 and seems to be increased in intensity compared to pH 7.

In the region of higher chemical shift only the signal at 238 ppm remains which is assigned to the nitrogen atom of the thiazole heterocycle (Th). The signal of the non-protonated nitrogen atom of the pyridine (Py) is not observed anymore. Since the pH switching mechanism of the dye suggests a protonation of the pyridine nitrogen this is in good agreement with this observation, since the signal intensity of the protonated pyridine nitrogen (Py^+-H) also increased.

2.5 Optical characterization of MPT-Ph functionalized silica thin films

From UV-vis measurements and determined by the *Lambert-Beer-law* (**Equation 1**) using twice the film thickness and the determined ε of 8070 mol l^{-1} cm^{-1} it is clear that the 16 nm large pores can incorporate higher dye concentrations (0.24 mol l^{-1}) as compared to the 8 nm pores (0.12 mol l^{-1}) (**Figure 4 a** red line with purple line).

(1) $$A = \varepsilon \cdot c \cdot d$$

In accordance with Lambert-Beer's law, the amount of dye per substrate surface and thus the maximum absorbance can be adjusted by variation of the mesoporous silica film thickness. This leads to the film thickness and pore size being critical parameters to adjust the dye amount in the mesoporous thin films, to reach a clearly and well visible coloration of the mesoporous silica film (**Figure 4b**). The UV-Vis measurements prove a homogeneous dye functionalization along the mesoporous silica film thickness as the absorbance approximately doubles for twice as thick mesoporous thin films (Figure 4a blue line vs purple line).

To investigate the infiltration of the measurement solution and diffusion into the mesoporous thin films on a relevant time scale for the experiments performed in this study, UV-vis measurements were performed directly after immersing a MPT-Ph functionalized and dry film into a test solution. The film was kept in the measurement solution for 60 minutes while measuring one UV-vis spectrum per minute. This test showed no difference between the measurement at t = 0 minutes and t = 60 minutes (Figure S15) indicating that the acid-base equilibrium of the incorporated MPT-Ph dye is obtained during sample preparation and no leaching of dye is observed. This also shows that the diffusion of solution through the film is not hindered and that the system can react fast towards a change in the solution pH. In addition, the UV-Vis measurements show that the mesoporous silica film and the dye functionalization are stable towards the measurement solution for at least 60 minutes, while measurements are conducted in less than a minute.

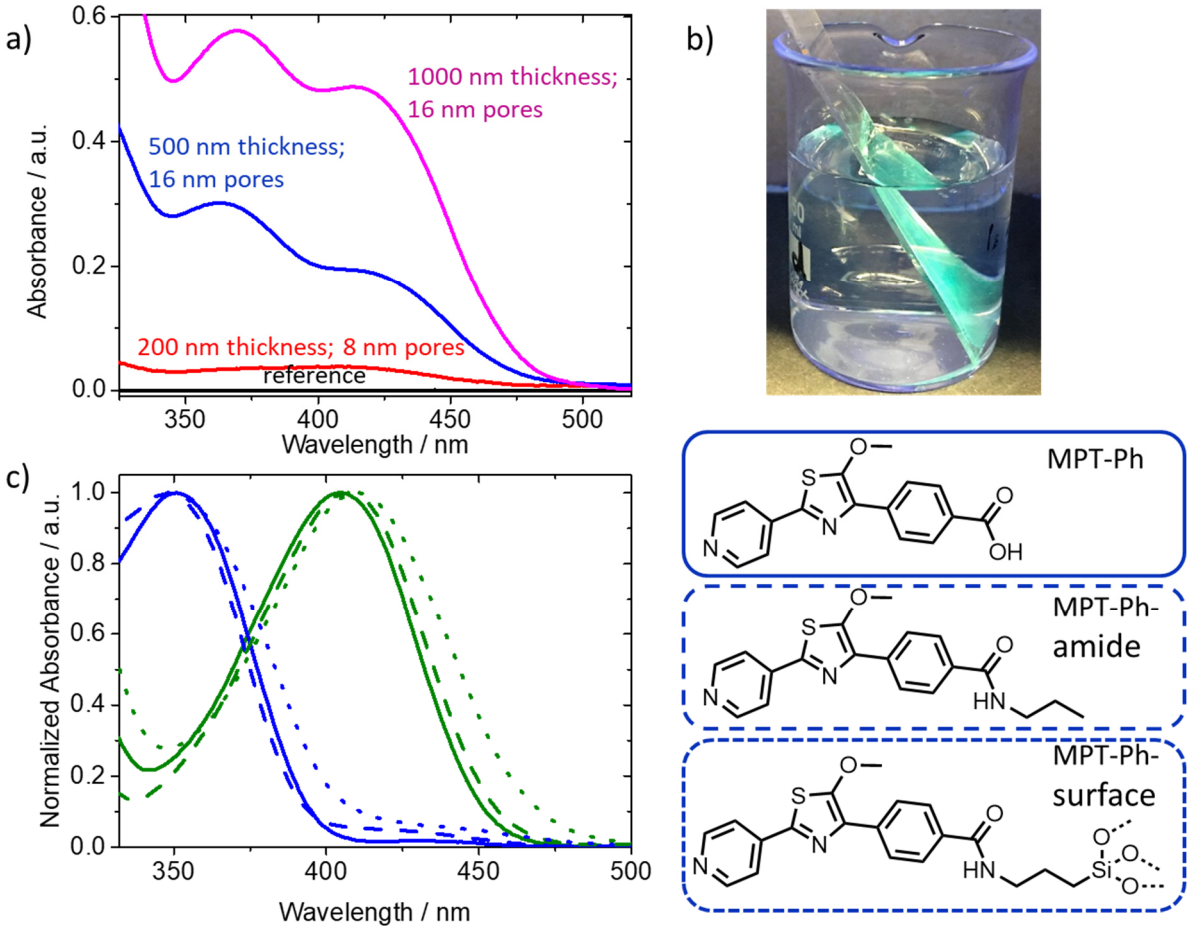

Figure 4. a) UV-vis spectra of MPT-Ph functionalized mesoporous silica films with film thicknesses of 200 nm (red line), 500 nm (blue line) and 1000 nm (pink line). The black line is an unfunctionalized mesoporous silica film. Measurements were recorded at a solution pH of ~3; b) Picture of a MPT-Ph functionalized mesoporous silica thin film under UV-light irradiation (365 nm); c) UV-vis spectra and the corresponding chemical structures of MPT-Ph (solid lines), MPT-Ph-Amide (dashed lines) and MPT-Ph-Surface (dotted lines) of the protonated form at pH 1.5 (green) and the deprotonated form at pH 7.5 (blue).

To prove that the combination of MPT-Ph and mesoporous silica is suitable for pH investigation in thin mesoporous films the pH responsiveness of the dye was confirmed after surface anchoring. As shown in **Figure 4c** the MPT-Ph-amide and the MPT-Ph-surface show both the same pH responsive behavior as the MPT-Ph. While the MPT-Ph-amide (Figure 4c dashed lines) was used as a chemical analogon to the surface anchored MPT-Ph (Figure 4c solid lines) a slight influence of the surface is

noticeable. The absorption maxima of the surface anchored dye (Figure 4c doted lines) are slightly red shifted compared to both dyes measured in bulk solution.

2.5 pH measurements bulk vs confinement

For the pH detection using MPT-Ph as pH reporter, measurement solutions with a predetermined pH values between 8.4 and 1.7 were prepared. Their pH values were stabilized using PBS buffer solution (150 mM). Subsequently, UV-vis spectra were recorded. With decreasing pH-value the absorption maximum at ~350 nm decreases while the absorption maximum at 411 nm increases (**Figure 5** a). To determine the pKa value of the MPT-Ph the quotient of $\frac{[MPT-Ph-H^+]}{[MPT-Ph]}$ can be plotted against the measured solution pH value. A mathematical sigmoidal fit has been used to determine the pKa value of 3.3 (Figure 4 b).

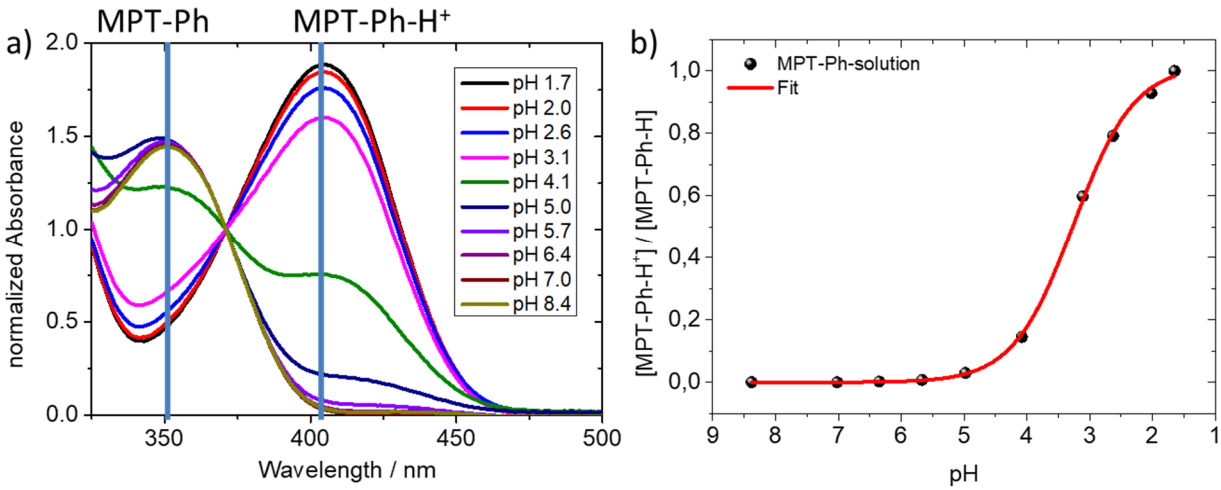

Figure 5. a) UV-vis spectra of MPT-Ph at pH values between 8.4 and 1.7; b) corresponding plot to measurements from a), showing the quotient MPT-Ph-H^+/MPT-Ph plotted against the solution pH value (black spheres). Red line shows a mathematical sigmoidal fit to determine the pKa value of MPT Ph (pKa=3.3)

The same procedure was further used to determine the pKa value for MPT-Ph-amide as well as for the surface bound MPT-Ph-surface derivate (**Figure 6a**). The results show that the difference between the residual carboxyl group of the MPT-Ph dye (pKa 3.3) and the residiual amide function of the MPT-Ph-amide dye (pKa 3.5) towards the resulting pKa value is very small. On the other

hand, the MPT-Ph-surface when entrapped in the nanoconfinement of silica mesopores shows a pKa value of 2.1. This pK_a shift of more than one pH unit as compared to its pK_a value in solution (**Figure 6a**) resembles a ten times more acidic environment in mesopores as compared to the measurements in bulk solution.

These findings using MPT-Ph as a new pH-reporter dye molecule sensitive to the required pH region (pH 1-5) in which mesoporous silica responds are in accordance with previous findings from our group investigating the pKa value of short oligomer chains in silica mesopores as well as with theoretical simulations for short polymer chains in ion channels.[20, 26]

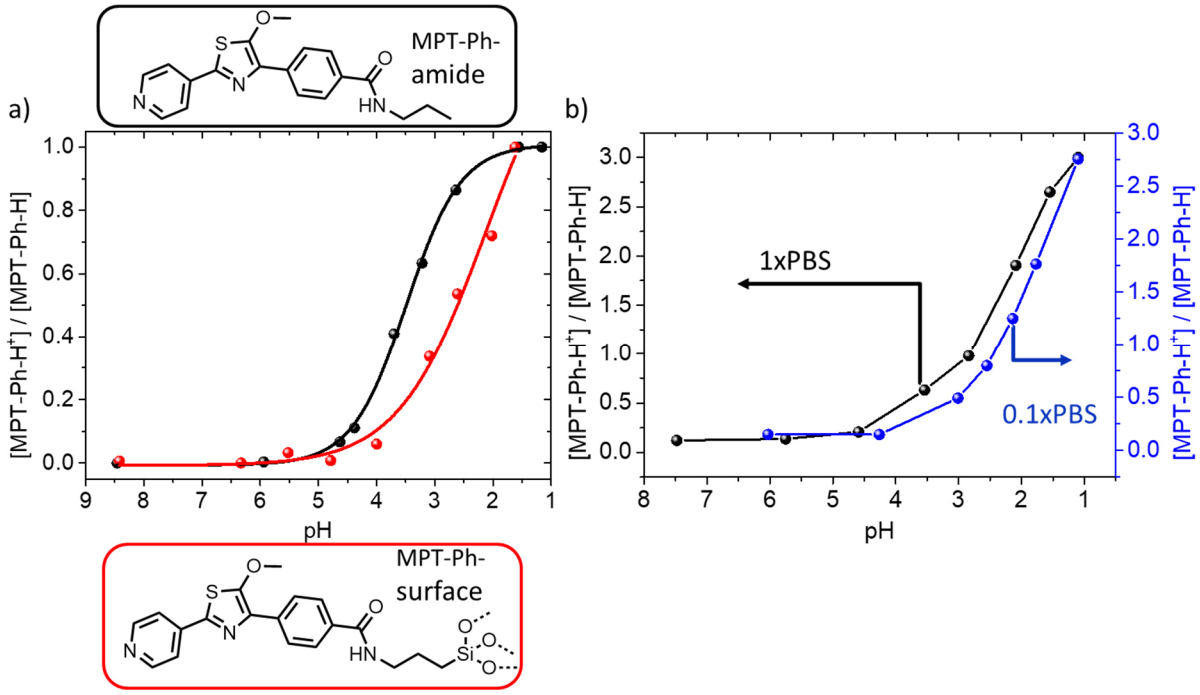

Figure 6. a) Quotient of MPT-Ph-Amide-H^+/MPT-Ph-Amide (black spheres) and MPT-Ph-Surface-H^+/MPT-Ph-Surface (red spheres) plotted against the solution pH value. Black and red lines show the corresponding mathematical sigmoidal fit to determine the pKa value of MPT-Ph-Amide (pKa=3.5) and MPT-Ph-Surface (pKa=2.1)

Additionally, the titration experiments with the surface attached MPT-Ph derivate were carried out at an ionic strength of 150 and 15 mM PBS buffer. The obtained results clearly show that at a lower salt concentration of 0.1xPBS (15 mM) as compared to the 1xPBS (150 mM) and thus an increased Debye-screening length from approximately 0.7 nm to 2.5 nm, the protonation process is even further shifted towards more extreme (here acidic) conditions (Figure 6b and Figure S16).

3. Conclusion

A new thiazol based ratiometric pH reporting dye has been synthesized and fully characterized regarding its optical properties. This MPT-Ph dye covers a completely different sensitivity range with its acidic pKa value of 3.5 as compared to other established dyes for ratiometric pH detection such as SNARF. As demonstrated in this study this more acidic pH range is especially interesting to follow confinement effects in nanoscale pores on pH as for example in mesoporous silica.in which the pH value plays a crucial role for various applications from separation processes to drug delivery. MPT-Ph can be easily grafted to the silica surface and mesopore wall. This study proves the covalent bond between dye and surface by solid state NMR studies. Advanced solid state NMR DNP methods further prove the protonation of the nitrogen atom of the MPT-Ph molecule at acidic pH within silica mesopores.

The developed ratiometric MPT-Ph dye has been successfully employed to measure pH variations between bulk solutions and nanoscale silica pores and enabled in-situ readout of the "pH value" in silica mesopores by simple UV-vis measurements. The obtained results indicate a background electrolyte dependent pKa-shift of at least one pH unit under nano confinement as compared to bulk solution. This study is the first to employ a direct read out approach using a covalently coupled reporter molecule to determine the "pH value" inside of silica mesopores and to compare it with data from bulk solution to finally determine the confinement effect on the pH value in silica mesopores. The obtained results are in good agreement with previous experimental findings using indirect read out as well as with theoretical simulations.

4. Experimental Section

Preparation of 1x PBS buffer solution: In 1000 ml distilled water 8.00 g (136.9 mmol) NaCl, 0.20 g (2.7 mmol) KCl, 1.42 g Na2HPO$_4$ (10.0 mmol) 0.27 g (2.0 mmol) KH_2PO_4 were dissolved and the solution was stirred for 24 hours before being used for UV-vis measurements.

Preparation of Mesoporous Silica Thin Films: The mesoporous silica films were prepared via sol–gel chemistry using tetraethoxysilane (TEOS) as an inorganic precursor. The sol contained an amphiphilic triblock copolymer, Pluronic® F127 (BioReagent, Sigma-Aldrich, 13,800 g mol^{-1}) in different ratios, which undergoes micellization upon solvent evaporation resulting in the formation of a porous inorganic network. A typical synthesis of films with 8 nm (or 16 nm) pores used 1.37 g (2.61 g) of Pluronic® F127, which was dissolved in 33.8 mL (24.0 mL) of absolute ethanol and 5.22 mL of H2O, 0.33 mL of 37% HCl (6.4 mL of 0.05 M HCl). After which, 6.55 mL (4.88 mL) of TEOS was added to the mixture, and the solution was then stirred overnight under ambient conditions before being used to prepare films through evaporation-induced self-assembly (EISA). Dip-coating was performed in a climate-controlled chamber at a temperature of 23 °C and a relative humidity of 50 %, at a withdrawal speed of 2 mm s^{-1}. After aging the films for 1 h at 50 % relative humidity and at 23 °C they were subjected to the following thermal treatment: Two 1 h steps at 60 and 130 °C followed by heating to 350 °C with a heating rate of 1 °C/min. Finally, the films were stabilized at 350 °C for 2 h before cooling to room temperature.

Preparation of amino-functionalized SBA-15:

Based on our protocol reported earlier,[52] in a typical procedure, 7.10 g (0.017 eq) Pluronic P123 was dissolved in 191.2 ml (165.0 eq) of deionized water and 36.0 ml (6.0 eq) of 37w% HCl was added which results in a HCl concentration of 1.9 mol/L. The solution was heated to 40°C and 12.0 g (0.8 eq) of tetraethyl orthosilicate (TEOS) was added slowly while stirring. Stirring was continued for 1 h which results in a white precipitate. After this prehydrolysis step, 3.19 g (0.2 eq) of (3-aminopropyl)triethoxysilane (APTES) was added. The suspension was stirred for 24 h at 40°C and then transferred into a polypropylene (PP) bottle. The bottle was stored under static conditions at 100°C for 48 h. The white precipitate was filtered off and washed two times with deionized water, ethanol and acetone. The product was dried in an oven at 90 °C over night. The leftover template was removed by Soxhlet extraction with ethanol for 48 h. The product was dried under high vacuum yielding 3.19 g of the functionalized SBA-15.

Synthesis of MPT-Ph:

489 mg of MPT-Br, 401 mg of 4-carboxyphenylboronic acid and 518 mg of K_2CO_3 were dissolved in a mixture of 40 ml dioxan and 10 ml H_2O and deoxygenated for 15 minutes by nitrogen bubbling. Then the X-Phos Pd-G2 precatalyst was added (90 mg) and the reaction mixture was heated to 80 C for 16 hours. The MPT-Ph was isolated by column chromatography using methanol and ethyl acetate as eluent. 400 mg (71 %)

1H NMR (700 MHz, DMSO-d6) δ 8.67 (d, J = 5.7 Hz, 2H), 8.25 (d, J = 6.0 Hz, 2H), 7.96 (d, J = 8.2 Hz, 2H), 7.81 (d, J = 8.2 Hz, 2H), 4.06 (s, 3H); HRMS (ESI) *m/z*: $[M + H]^+$ calcd for $C_{16}H_{12}N_2O_3S$, 313.06; found, 313.07.

Synthesis of MPT-Ph-amide:

50 mg of MPT-Ph were dissolved in 15 ml Dimethyl formamide (DMF). Subsequently 45 µl diisoprpylethylamine (DIPEA) and 61 mg HATU was added and the solution was stirred for 15 minutes. Then 5.7 mg propylamine was added and the reaction mixture was stirred for 24 hours at room temperature. The MPT-Ph-Amide was isolated by column chromatography using methanol and ethyl acetate as eluent as well as HPLC. 40 mg (71 %).

1H NMR (700 MHz, Methanol-d4) δ 8.78 – 8.75 (m, 2H), 8.38 – 8.35 (m, 2H), 8.22 – 8.18 (m, 2H), 7.92 – 7.88 (m, 2H), 4.29 (s, 3H), 3.37 (t, J = 7.2 Hz, 2H), 1.67 (h, J = 7.4 Hz, 2H), 1.00 (t, J = 7.4 Hz, 3H); 13C NMR (176 MHz, MeOD) δ 169.48, 165.90, 148.77, 146.06, 144.55, 137.66, 136.80, 134.49, 128.24, 127.63, 122.16, 65.46, 49.26, 49.10, 48.97, 48.85, 48.73, 48.61, 48.49, 48.37, 42.56, 23.49, 11.51; HRMS (ESI) *m/z*: $[M + H]^+$ calcd for $C_{19}H_{19}N_3O_3S$, 354.13; found, 354.13.

Aminopropyltrimethoxysilane (APTMS) grafting on mesoporous silica thin films:

A 0.05 wt% solution of APTMS in dry Toluene (51,1 µl in 140 ml of dry Toluene) was prepared and used to overlay the glass substrates in a schlenkflask. Afterwards the samples

in the Schlenkflasks were kept at room temperature over night. Afterwards the samples were rinsed and extracted with ethanol.

Coupling of MPT-Ph to amino functionalized mesoporous silica films:

Under schlenk conditions 10 mg of MPT-Ph was dissolved in dry Dimethyl formamide (DMF). Subsequently 10.9 µl diisoprpylethylamine (DIPEA) and 24.3 mg HATU was added and the solution was stirred for 15 minutes. Then the amino functionalized mesoporous silica film was immersed in the solution for 24 hours. Afterwards the film was rinsed with DMF and methanol before being dried.

Coupling of MPT-Ph to amino functionalized mesoporous silica (SBA-15):

MPT-Ph was coupled by activating its COOH group with 1-[bis(dimethylamino)methylene]-1H-1,2,3-triazolo[4,5-b]pyridinium 3-oxide hexafluorophosphate (HATU) and N-ethyl-N-(propan-2-yl)propan-2-amine (DIEA). 121 mg (1.0 eq) of *MPT-Ph* and 145 mg (0.98 eq) of HATU were dissolved in 8 ml of dry DMF. The solution was activated by adding 100 mg (2.0 eq) of DIEA and by shaking it for 2 min. 400 mg of dried amino-functionalized SBA-15 was added to the activated amino acid solution. The suspension has been shaken at 1000 rpm at RT for 16 h. The solid was filtered off and washed two times with each DMF, distilled water and acetone. The functionalized SBA-15 was dried under reduced pressure at room temperature, which resulted in 475 mg colorless solid.

NMR measurements: ^{1}H-, ^{13}C-, and 2D-NMR experiments were conducted on a Bruker AV-III 600, or Bruker AV-III HD 700 NMR-spectrometer. To shift the water signal and protonate the MPT-Ph and MPT-Ph-Amide DCl (37%) was added to some samples.

Solid state NMR measurements:

^{13}CP-MAS and ^{29}Si CP-MAS solid state NMR measurements were carried out at room temperature on a Bruker AVANCE II+ 400 spectrometer corresponding to a frequency of 400.13 MHz for ^{1}H, 100.62 MHz for ^{13}C, and 79.48 MHz for ^{29}Si employing a Bruker 4 mm double resonance probe. Spectra were recorded with a contact time of 1.5 ms for ^{13}C and 6.5 ms for ^{29}Si employing a recycle delay of 2 s. Protons were decoupled during data acquisition employing the tppm15 decoupling sequence.[56] Referencing was performed with respect to tetramethylsilane (TMS) (0 ppm) employing adamantane (-38.5 ppm) and kaolin (-92.5 ppm) as external standards for ^{13}C and ^{29}Si, respectively.

Dynamic nuclear polarization (DNP) enhanced NMR measurements:

Samples for DNP experiments were prepared by impregnating ca. 15 mg of the sample with 15 µl of a 15 mM AMUPol in glycerol-d_8/D_2O/H_2O (60:30:10 v/v/v) solution. Samples were packed into 3.2 mm sapphire rotors and sealed with a teflon plug and ZrO_2 driving cap. For pH adjustment of the matrix 38% DCl was used.

All DNP experiments were performed on a Bruker Avance III 400 DNP spectrometer equipped with an Ascend 400 DNP magnet system and a low temperature ^{1}H/X/Y probe. DNP enhanced spectra were measured with microwave irradiation (MW on). All DNP enhanced spectra were recorded at a field of 9.4 T corresponding to frequencies of 400.25 MHz for ^{1}H, 100.58 MHz for ^{13}C and 40.53 MHz for ^{15}N, respectively, at nominally 110 K and at a rate of 8 kHz spinning. The recycle delay was taken as 1.3 T_1 (^{1}H) according to ref.,[57] where T_1 (^{1}H) is the built-up time for ^{1}H obtained from a saturation recovery experiment recorded with microwave irradiation. During data acquisition tppm20[56] heteronuclear decoupling was applied for the ^{15}N CP MAS spectra. The ^{15}N CP MAS spectra were recorded with contact times of 2 ms and referenced with NH_4Cl as an external standard (chemical shift 0 ppm).

UV-Vis measurements:

UV-Vis measurements were performed using an Agilent Cary 60 UV-Vis or an AnalytikJena Specord S600 spectrophotometer using PMMA cuvettes. The concentrations of sample solutions were kept below 50 mM and the dye functionalized mesoporous silica films were fixated straight in the cuvette diagonally to the light beam.

Fluorescence measurements:

The steady-state (time-integrated) fluorescence spectra were recorded with a Jasco FP-8500 spectrofluorometer in 4x10 mm UV grade quartz cuvettes. The spectra were corrected for their offset, the detector sensitivity of the device, the wavelength-dependent excitation light intensity and for reabsorption contributions. For the determination of the fluorescence quantum yields, the FP-8500 spectrofluorometer was equipped with a 100 mm integrating sphere also from Jasco (ILF-835) and the calculations were carried out with the Origin 2019 data analysis software.

The time-correlated single photon counting (TCSPC) measurements were performed at a self-assembled setup with a PicoQuant photomultiplier tube (PMT) PMA-C 182-M for single-photodetection. Data were acquired with a TimeHarp 260 PICO single PCIe card and data analysis and multiexponential fitting was executed with the FluoFit Pro 4.6 software from PicoQuant. The samples were also prepared in 4x10 mm quartz glass cuvettes and the excitation of the samples was carried out with pulsed light-emitting diodes (LEDs), enabling a maximum time resolution of roughly 200 ps. The instrumental response function (IRF) was recorded with a TiO2 suspension as a scattering sample. For the detection of the sample fluorescence decay curves, colored glass filters (Schott AG) were used in order to suppress excitation stray light.

Acknowledgements

The authors acknowledge funding in the frame of the LOEWE project iNAPO by the Hessen State Ministry of Higher Education, Research and the Arts. Also financial support by the Deutsche Forschungsgemeinschaft in the framework through grants Bu-911/18-1/2 as well as for SFB 902 "RNA-based Regulation" is gratefully acknowledged. The authors especially thank Dr. Sharon Jeziorowski and Dr. Jonas Kind in the working group of Prof. Dr. Christina Thiele for NMR measurements. Additionally, the authors thank Prof. Markus Biesalski for access to interface characterization facilities. Marlen Saalbach is acknowledged UV-vis measurements.

Received: ((will be filled in by the editorial staff))
Revised: ((will be filled in by the editorial staff))
Published online: ((will be filled in by the editorial staff))

References

1. Kresge, C. T.; Leonowicz, M. E.; Roth, W. J.; Vartuli, J. C.; Beck, J. S., Ordered mesoporous molecular sieves synthesized by a liquid-crystal template mechanism. *Nature* **1992,** *359* (6397), 710-712.

2. Nasir, T.; Herzog, G.; Hebrant, M.; Despas, C.; Liu, L.; Walcarius, A., Mesoporous Silica Thin Films for Improved Electrochemical Detection of Paraquat. *ACS Sens* **2018,** *3* (2), 484-493.

3. Walcarius, A.; Sibottier, E.; Etienne, M.; Ghanbaja, J., Electrochemically assisted self-assembly of mesoporous silica thin films. *Nat. Mater.* **2007,** *6* (8), 602-8.

4. Wang, K.; He, J., One-Pot Fabrication of Antireflective/Antibacterial Dual-Function Ag NP-Containing Mesoporous Silica Thin Films. *ACS Appl. Mater. Interfaces.* **2018,** *10* (13), 11189-11196.

5. Alothman, Z., A Review: Fundamental Aspects of Silicate Mesoporous Materials. *Materials* **2012,** *5* (12), 2874-2902.

6. Kruk, M., Surface-Initiated Controlled Radical Polymerization in Ordered Mesoporous Silicas. *Israel Journal of Chemistry* **2012,** *52*, 246-255.

7. van der Heyden, F. H.; Bonthuis, D. J.; Stein, D.; Meyer, C.; Dekker, C., Electrokinetic energy conversion efficiency in nanofluidic channels. *Nano Lett* **2006,** *6* (10), 2232-7.

8. Hoffmann, F.; Cornelius, M.; Morell, J.; Froba, M., Silica-based mesoporous organic-inorganic hybrid materials. *Angew. Chem. Int. Ed. Engl.* **2006,** *45* (20), 3216-51.

9. Narayan, R.; Nayak, U. Y.; Raichur, A. M.; Garg, S., Mesoporous Silica Nanoparticles: A Comprehensive Review on Synthesis and Recent Advances. *Pharmaceutics* **2018,** *10* (3).

10. Hoffmann, F.; Cornelius, M.; Morell, J.; Fröba, M., Mesoporöse organisch-anorganische Hybridmaterialien auf Silicabasis. *Angewandte Chemie* **2006,** *118* (20), 3290-3328.

11. Tagliazucchi, M.; Azzaroni, O.; Szleifer, I., Responsive Polymers End-Tethered in Solid-State Nanochannels: When Nanoconfinement Really Matters. *J. Am. Chem. Soc.* **2010,** *132*, 12404–12411.

12. Brunsen, A.; Cui, J.; Ceolin, M.; del Campo, A.; Soler-Illia, G. J.; Azzaroni, O., Light-activated gating and permselectivity in interfacial architectures combining "caged" polymer brushes and mesoporous thin films. *Chem. Commun. (Camb)* **2012,** *48* (10), 1422-4.

13. Huang, K.; Szleifer, I., Design of Multifunctional Nanogate in Response to Multiple External Stimuli Using Amphiphilic Diblock Copolymer. *J. Am. Chem. Soc.* **2017,** *139* (18), 6422-6430.

14. Hou, X.; Guo, W.; Jiang, L., Biomimetic smart nanopores and nanochannels. *Chem. Soc. Rev.* **2011,** *40* (5), 2385-401.

15. Huang, X.; Appelhans, D.; Formanek, P.; Simon, F.; Voit, B., Tailored synthesis of intelligent polymer nanocapsules: an investigation of controlled permeability and pH-dependent degradability. *ACS Nano* **2012,** *6* (11), 9718-26.

16. Perez-Mitta, G.; Albesa, A. G.; Knoll, W.; Trautmann, C.; Toimil-Molares, M. E.; Azzaroni, O., Host-guest supramolecular chemistry in solid-state nanopores: potassium-driven modulation of ionic transport in nanofluidic diodes. *Nanoscale* **2015,** *7* (38), 15594-8.

17. Qiang Fu, G. V. R. R., Linnea K. Ista, Yang Wu, Brett P. Andrzejewski, Larry A. Sklar, Timothy L. Ward, and Gabriel P. Lopez, Control of Molecular Transport Through Stimuli-Responsive Ordered Mesoporous materials. *Adv. Mat.* **2003,** *15* (15), 1262-1266.

18. Wen, J.; Yang, K.; Liu, F.; Li, H.; Xu, Y.; Sun, S., Diverse gatekeepers for mesoporous silica nanoparticle based drug delivery systems. *Chem. Soc. Rev.* **2017,** *46* (19), 6024-6045.

19. Yu, F.; Tang, X.; Pei, M., Facile synthesis of PDMAEMA-coated hollow mesoporous silica nanoparticles and their pH-responsive controlled release. *Microporous and Mesoporous Materials* **2013,** *173*, 64-69.

20. Gilles, F. M.; Tagliazucchi, M.; Azzaroni, O.; Szleifer, I., Ionic Conductance of Polyelectrolyte-Modified Nanochannels: Nanoconfinement Effects on the Coupled Protonation Equilibria of Polyprotic Brushes. *J. Phys. Chem. C* **2016,** *120* (9), 4789-4798.

21. Gong, P.; Wu, T.; Genzer, J.; Szleifer, I., Behavior of Surface-Anchored Poly(acrylic acid) Brushes with Grafting Density Gradients on Solid Substrates: 2. Theory. *Macromolecules* **2007,** *40* (24), 8765-8773.

22. Schepelina, O.; Zharov, I., Poly(2-(dimethylamino)ethyl methacrylate)-modified nanoporous Colloidal films with pH and ion response. *Langmuir* **2008,** *24* (24), 14188-94.

23. Stanzel, M.; Brilmayer, R.; Langhans, M.; Meckel, T.; Andrieu-Brunsen, A., Systematic study on FRET-pair functionalization of mesoporous thin films for correlation of pH-sensing and ionic mesopore accessibility. *Microporous and Mesoporous Materials* **2019,** *282*, 29-37.

24. Yamaguchi, A.; Namekawa, M.; Kamijo, T.; Itoh, T.; Teramae, N., Acid-base equilibria inside amine-functionalized mesoporous silica. *Anal. Chem.* **2011,** *83* (8), 2939-46.

25. Tagliazucchi, M.; Azzaroni, O.; Szleifer, I., Responsive Polymers End-Tethered in Solid-State Nanochannels: When Nanoconfinement Really Matters. *J. Am. Chem. Soc.* **2010,** *132* (35), 12404-12411.

26. Brilmayer, R.; Kübelbeck, S.; Khalil, A.; Brodrecht, M.; Kunz, U.; Kleebe, H. J.; Buntkowsky, G.; Baier, G.; Andrieu-Brunsen, A., Influence of Nanoconfinement on the pKa of Polyelectrolyte Functionalized Silica Mesopores. *Adv. Mat. Interf.* **2020**.

27. Richter, C.; Schneider, C.; Quick, M. T.; Volz, P.; Mahrwald, R.; Hughes, J.; Dick, B.; Alexiev, U.; Ernsting, N. P., Dual-fluorescence pH probe for bio-labelling. *Phys. Chem. Chem. Phys.* **2015,** *17* (45), 30590-7.

28. Thörn, C.; Carlsson, N.; Gustafsson, H.; Holmberg, K.; Åkerman, B.; Olsson, L., A method to measure pH inside mesoporous particles using protein-bound SNARF1 fluorescent probe. *Microporous and Mesoporous Materials* **2013,** *165*, 240-246.

29. Sulpizi, M.; Gaigeot, M. P.; Sprik, M., The Silica-Water Interface: How the Silanols Determine the Surface Acidity and Modulate the Water Properties. *J. Chem. Theory. Comput.* **2012,** *8* (3), 1037-47.

30. Rosenholm, J. M.; Czuryszkiewicz, T.; Kleitz, F.; Rosenholm, J. B.; Lindén, M., On the Nature of the Brønsted Acidic Groups on Native and Functionalized Mesoporous Siliceous SBA-15 as Studied by Benzylamine Adsorption from Solution. *Langmuir* **2007,** *23* (8), 4315-4323.

31. Lei, J.; Wang, L.; Zhang, J., Ratiometric pH sensor based on mesoporous silica nanoparticles and Forster resonance energy transfer. *Chem. Commun. (Camb)* **2010,** *46* (44), 8445-7.

32. Zheng, M.-H.; Jin, J.-Y.; Sun, W.; Yan, C.-H., A new series of fluorescent 5-methoxy-2-pyridylthiazoles with a pH-sensitive dual-emission. *New Journal of Chemistry* **2006,** *30* (8).

33. Moerner, S. B. a. W. E., Fluorescence Behavior of Single-Molecule pH-Sensors. *Single Mol. 1* **2000,** (1), 17-23.

34. Wan, S.; Zheng, Y.; Shen, J.; Yang, W.; Yin, M., "On-off-on" switchable sensor: a fluorescent spiropyran responds to extreme pH conditions and its bioimaging applications. *ACS Appl. Mater. Interfaces.* **2014,** *6* (22), 19515-9.

35. Martínez-Máñez, R.; Sancenón, F.; Biyikal, M.; Hecht, M.; Rurack, K., Mimicking tricks from nature with sensory organic–inorganic hybrid materials. *J. Mater. Chem.* **2011,** *21* (34).

36. Han, J.; Loudet, A.; Barhoumi, R.; Burghardt, R. C.; Burgess, K., A ratiometric pH reporter for imaging protein-dye conjugates in living cells. *J. Am. Chem. Soc.* **2009,** *131* (5), 1642-3.

37. Lee, H. L.; Lord, S. J.; Iwanaga, S.; Zhan, K.; Xie, H.; Williams, J. C.; Wang, H.; Bowman, G. R.; Goley, E. D.; Shapiro, L.; Twieg, R. J.; Rao, J.; Moerner, W. E., Superresolution imaging of targeted proteins in fixed and living cells using photoactivatable organic fluorophores. *J. Am. Chem. Soc.* **2010,** *132* (43), 15099-101.

38. Ji, J.; Rosenzweig, N.; Griffin, C.; Rosenzweig, Z., Synthesis and application of submicrometer fluorescence sensing particles for lysosomal pH measurements in murine macrophages. *Anal. Chem.* **2000,** *72* (15), 3497-503.

39. Ajayaghosh, A.; Carol, P.; Sreejith, S., A ratiometric fluorescence probe for selective visual sensing of Zn2+. *J. Am. Chem. Soc.* **2005,** *127* (43), 14962-3.

40. Li, L. I.; Yun, S.; Yuan-Hui, Z.; Lan, M. U.; Xi, Z.; Redshaw, C.; Gang, W. E. I., A single chemosensor for multiple analytes: Fluorogenic and ratiometric absorbance detection of Zn2+, Mg2+ and F−, and its cell imaging. *Sensors and Actuators B: Chemical* **2016,** *226*, 279-288.

41. Li, S.; Zhang, D.; Xie, X.; Ma, S.; Liu, Y.; Xu, Z.; Gao, Y.; Ye, Y., A novel solvent-dependently bifunctional NIR absorptive and fluorescent ratiometric probe for detecting Fe3+/Cu2+ and its application in bioimaging. *Sensors and Actuators B: Chemical* **2016,** *224*, 661-667.

42. Maity, D.; Govindaraju, T., A differentially selective sensor with fluorescence turn-on response to Zn2+ and dual-mode ratiometric response to Al3+ in aqueous media. *Chem. Commun. (Camb)* **2012,** *48* (7), 1039-41.

43. Qu, L.; Yin, C.; Huo, F.; Chao, J.; Zhang, Y.; Cheng, F., A pyridoxal-based dual chemosensor for visual detection of copper ion and ratiometric fluorescent detection of zinc ion. *Sensors and Actuators B: Chemical* **2014,** *191*, 158-164.

44. Wang, L.; Yan, J.; Qin, W.; Liu, W.; Wang, R., A new rhodamine-based single molecule multianalyte (Cu2+, Hg2+) sensor and its application in the biological system. *Dyes and Pigments* **2012,** *92* (3), 1083-1090.

45. Zheng, M.-H.; Jin, J.-Y.; Sun, W.; Yan, C.-H., A new series of fluorescent 5-methoxy-2-pyridylthiazoles with a pH-sensitive dual-emission. *New Journal of Chemistry* **2006,** *30* (8), 1192.

46. Li, L.-L.; Sun, H.; Fang, C.-J.; Xu, J.; Jin, J.-Y.; Yan, C.-H., Optical sensors based on functionalized mesoporous silica SBA-15 for the detection of multianalytes (H+ and Cu2+) in water. *J. of Mater. Chem.* **2007,** *17* (42), 4492.

47. Shenderovich, I. G.; Buntkowsky, G.; Schreiber, A.; Gedat, E.; Sharif, S.; Albrecht, J.; Golubev, N. S.; Findenegg, G. H.; Limbach, H.-H., Pyridine-15NA Mobile NMR Sensor for Surface Acidity and Surface Defects of Mesoporous Silica. *J. Phys. Chem. B* **2003,** *107* (43), 11924-11939.

48. Driscoll, E. W.; Hunt, J. R.; Dawlaty, J. M., Proton Capture Dynamics in Quinoline Photobases: Substituent Effect and Involvement of Triplet States. *J. Phys. Chem. A* **2017,** *121* (38), 7099-7107.

49. Brenlla, A.; Veiga, M.; Perez Lustres, J. L.; Rios Rodriguez, M. C.; Rodriguez-Prieto, F.; Mosquera, M., Photoinduced proton and charge transfer in 2-(2'-hydroxyphenyl)imidazo[4,5-b]pyridine. *J. Phys. Chem. B* **2013,** *117* (3), 884-96.

50. Herzog, N.; Brilmayer, R.; Stanzel, M.; Kalyta, A.; Spiehl, D.; Dörsam, E.; Hess, C.; Andrieu-Brunsen, A., Gravure printing for mesoporous film preparation. *RSC Advances* **2019,** *9* (41), 23570-23578.

51. Brilmayer, R.; Hess, C.; Andrieu-Brunsen, A., Influence of Chain Architecture on Nanopore Accessibility in Polyelectrolyte Block-Co-Oligomer Functionalized Mesopores. *Small* **2019**, e1902710.

52. Brodrecht, M.; Breitzke, H.; Gutmann, T.; Buntkowsky, G., Biofunctionalization of Nano Channels by Direct In-Pore Solid-Phase Peptide Synthesis. *Chemistry* **2018,** *24* (67), 17814-17822.

53. Brodrecht, M.; Kumari, B.; Thankamony, A.; Breitzke, H.; Gutmann, T.; Buntkowsky, G., Structural Insights into Peptides Bound to the Surface of Silica Nanopores. *Chemistry* **2019,** *25* (20), 5214-5221.

54. Werner, M.; Heil, A.; Rothermel, N.; Breitzke, H.; Groszewicz, Pedro B.; Thankamony, Aany S.; Gutmann, T.; Buntkowsky, G., Synthesis and solid state NMR characterization of novel peptide/silica hybrid materials. *Solid State Nuclear Magnetic Resonance* **2015,** *72*, 73-78.

55. Shenderovich, I. G.; Buntkowsky, G.; Schreiber, A.; Gedat, E.; Sharif, S.; Albrecht, J.; Golubev, N. S.; Findenegg, G. H.; Limbach, H.-H., Pyridine-15N A Mobile NMR Sensor for Surface Acidity and Surface Defects of Mesoporous Silica. *J. Phys. Chem. B* **2003,** *107* (43), 11924-11939.

56. Scholz, I.; Hodgkinson, P.; Meier, B. H.; Ernst, M., Understanding two-pulse phase-modulated decoupling in solid-state NMR. *J. Chem. Phys.* **2009,** *130* (11), 114510.

57. Lange, S.; Linden, A. H.; Akbey, U.; Franks, W. T.; Loening, N. M.; van Rossum, B. J.; Oschkinat, H., The effect of biradical concentration on the performance of DNP-MAS-NMR. *J. Magn. Reson.* **2012,** *216*, 209-12.

Supporting Information

A new dye for ratiometric pH detection inside silica mesopores

Robert Brilmayer, Martin Brodrecht, Christoph Kaiser, Hergen Breitzke, Bharti Kumari, Josef Wachtveitl, Gerd Buntkowsky, Annette Andrieu-Brunsen

Characterization Data for MPT-Ph (Compound 2)

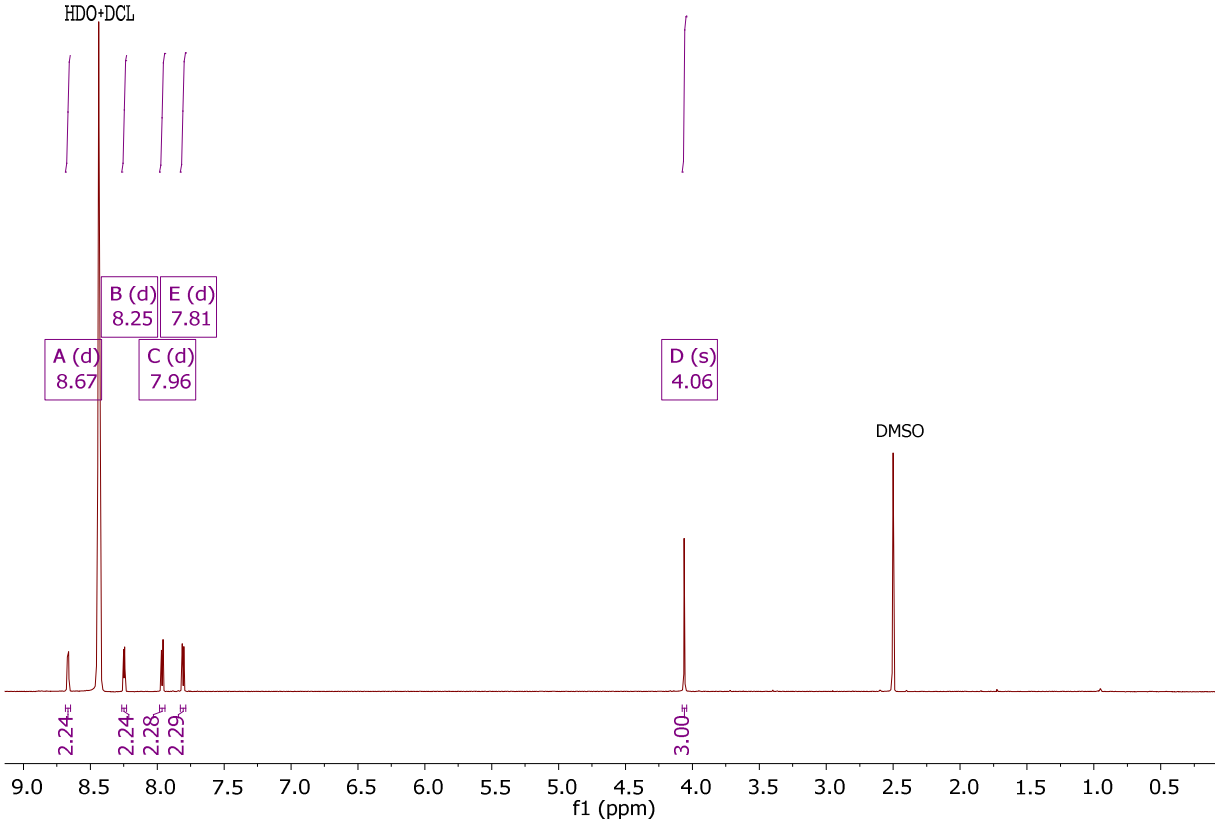

Figure S1. 1H-NMR of compound 2 MPT-Ph. 1H NMR (700 MHz, DMSO-d6) δ 8.67 (d, J = 5.7 Hz, 2H), 8.25 (d, J = 6.0 Hz, 2H), 7.96 (d, J = 8.2 Hz, 2H), 7.81 (d, J = 8.2 Hz, 2H), 4.06 (s, 3H).

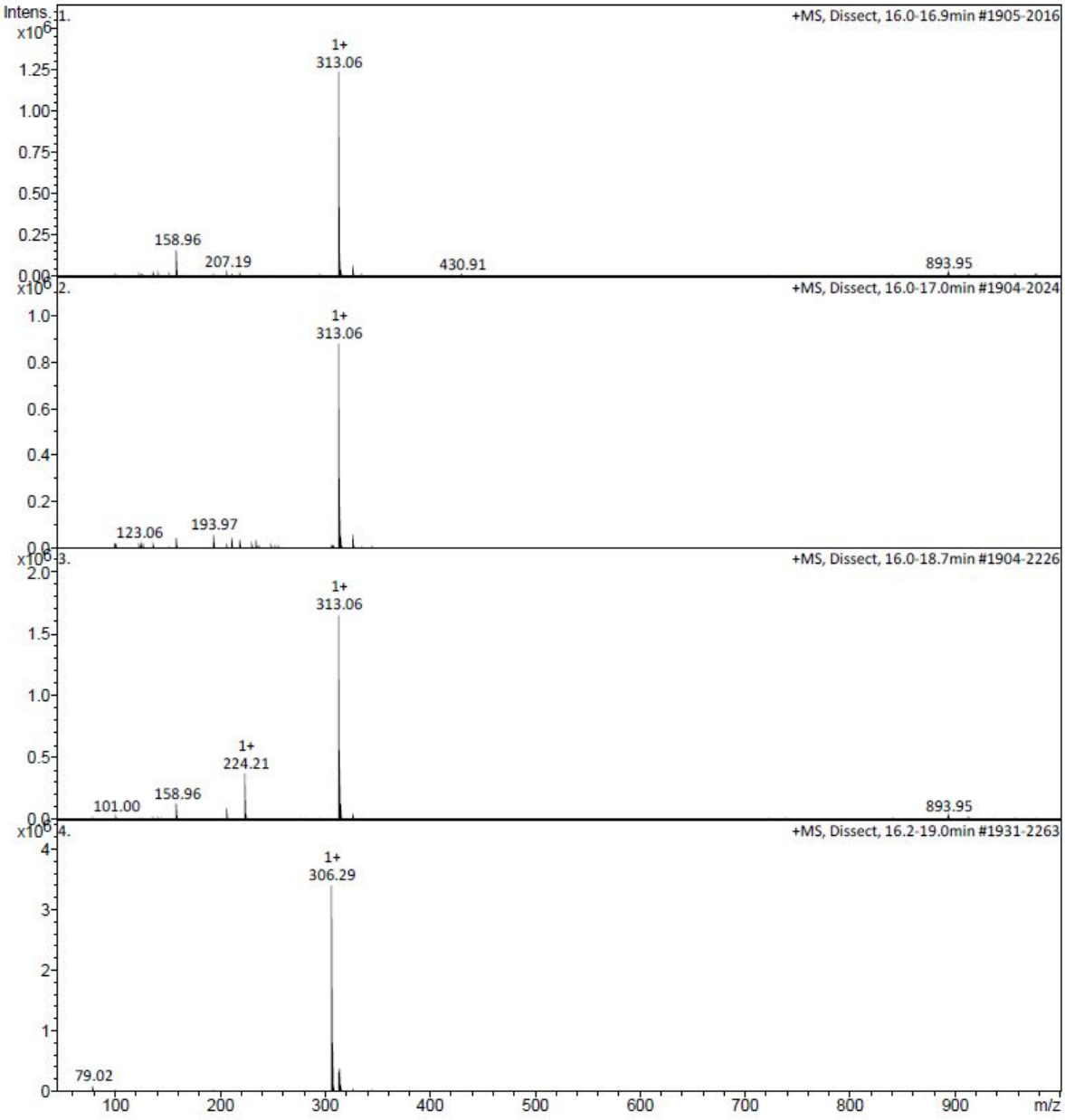

Figure S2. ESI-MS spectrum of compound 2 MPT-Ph.

Characterization Data for MPT-Ph-amide (Compound 3)

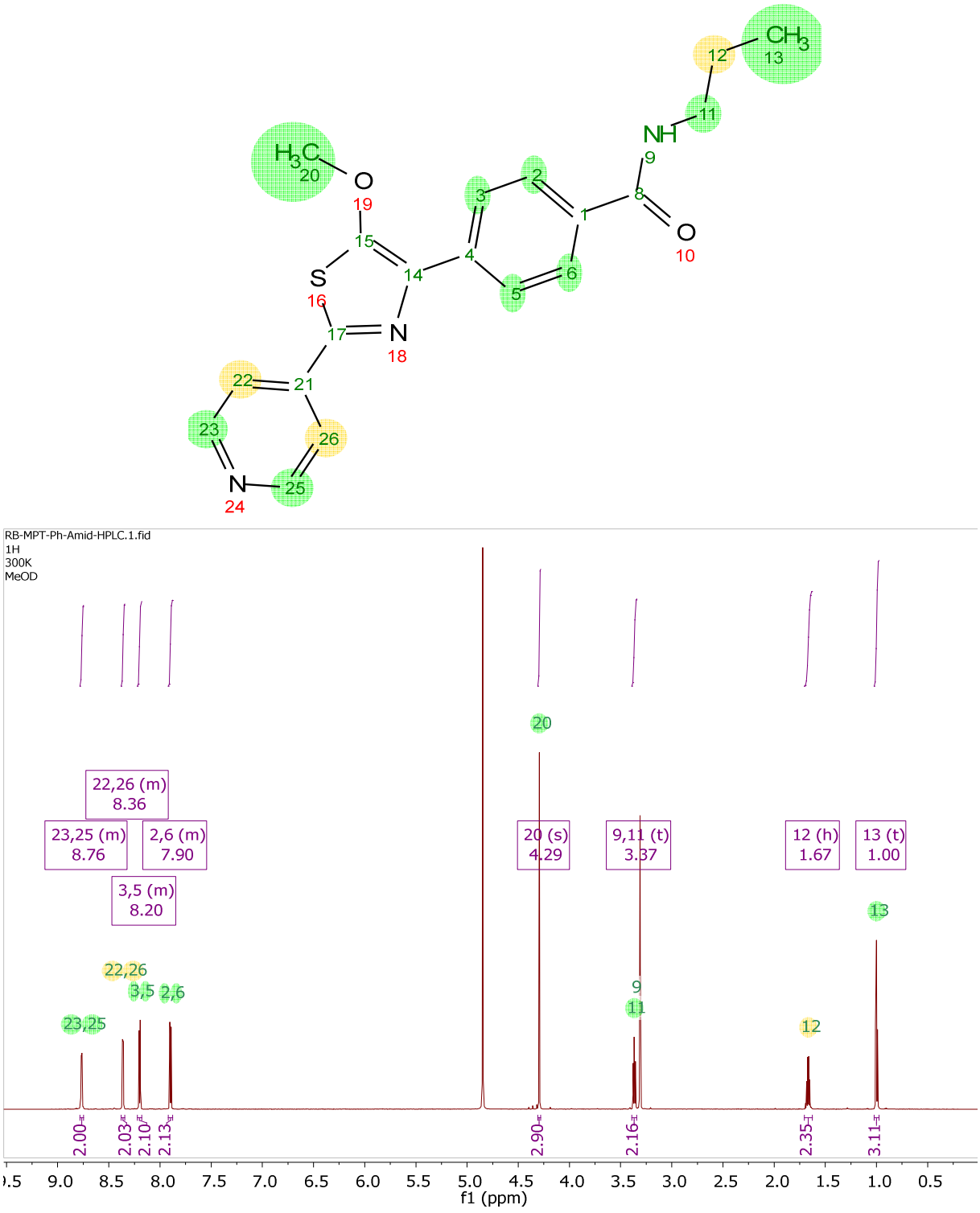

Figure S3. Chemical structure (top) and 1H-NMR (bottom) of compound 3 MPT-Ph-amide.

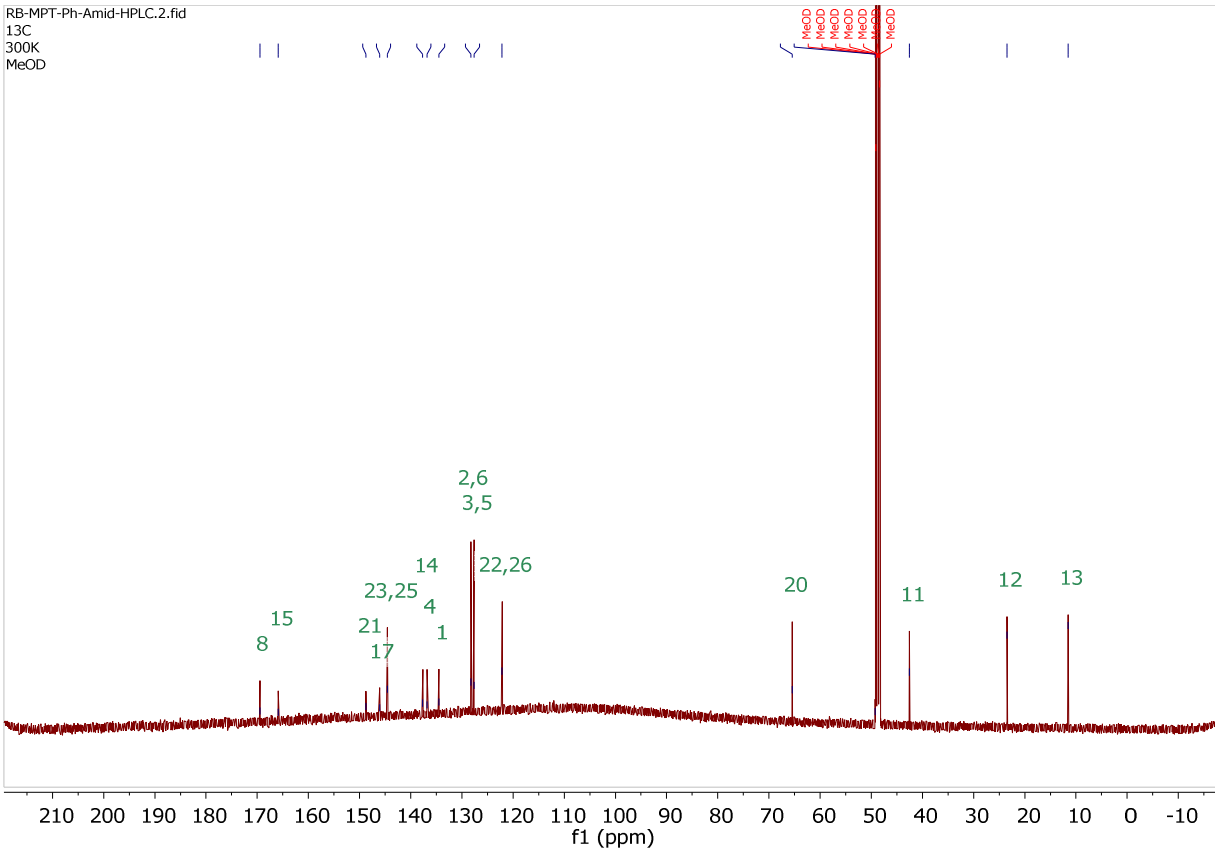

Figure S4. 13C-NMR spectrum of compound 3 MPT-Ph-amide.

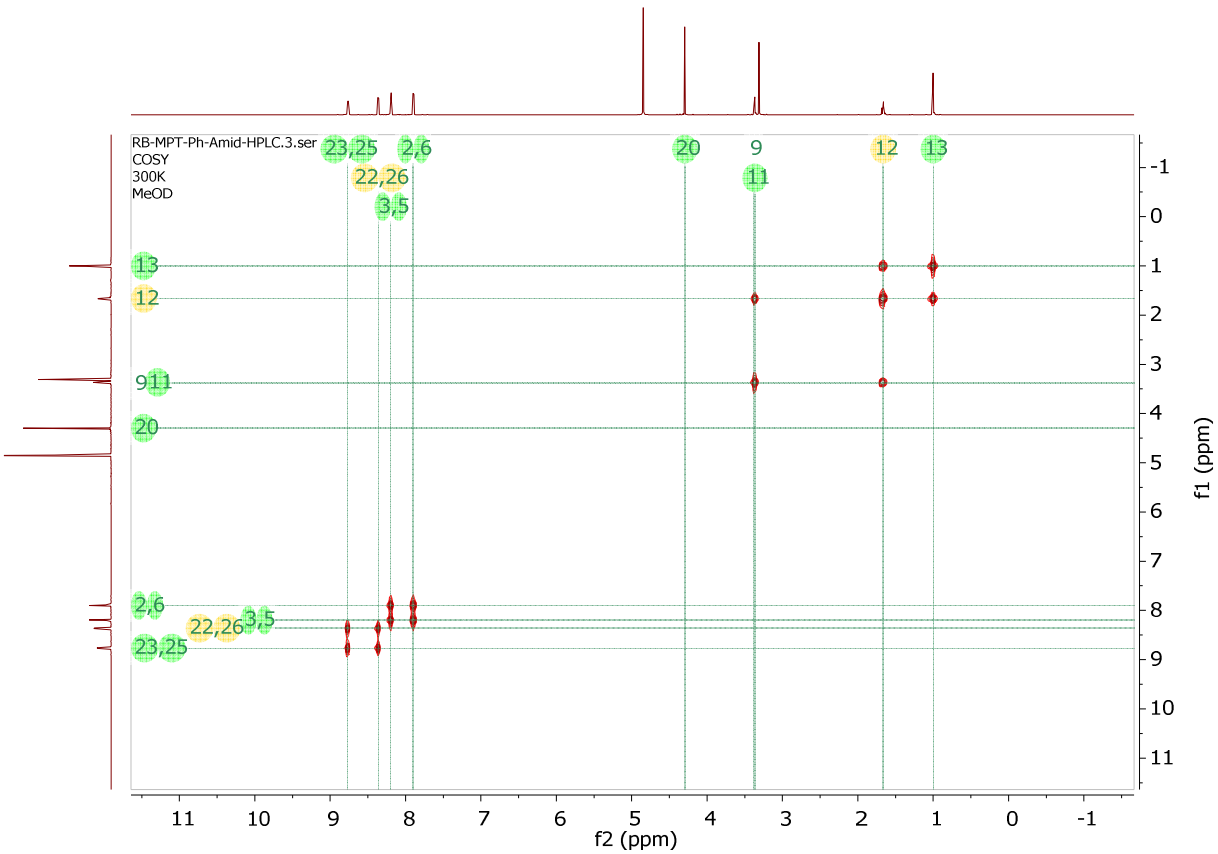

Figure S5. 1H-COSY-NMR spectrum of compound 3 MPT-Ph-amide.

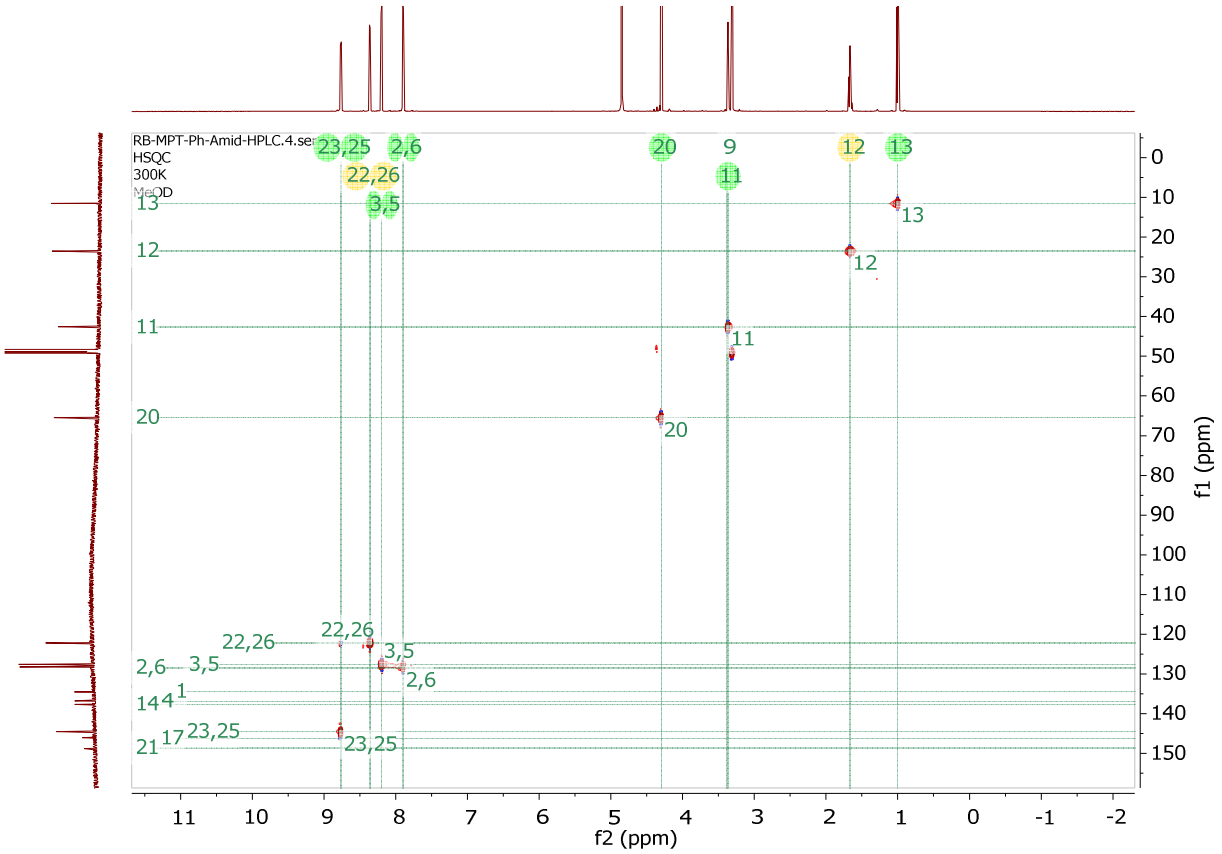

Figure S6. 1H-13C-HSQC-NMR spectrum of compound 3 MPT-Ph-amide.

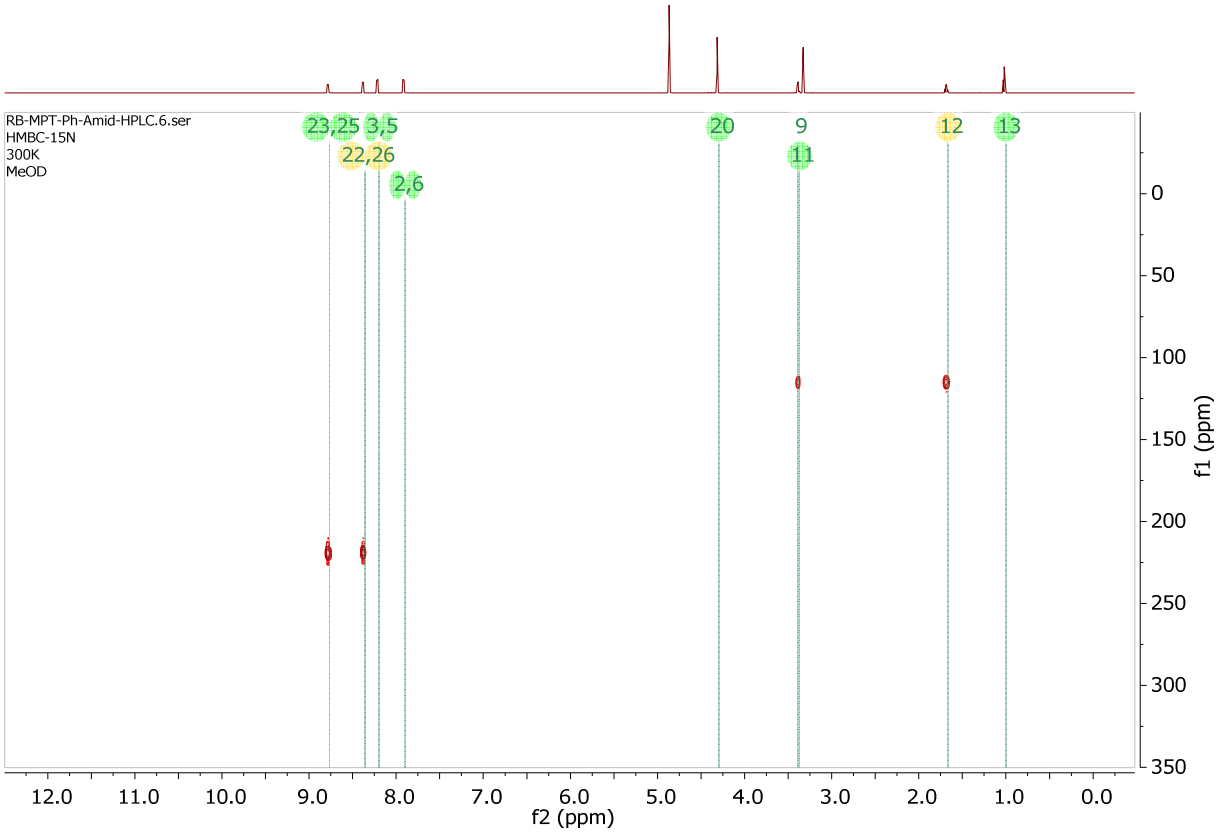

Figure S7. 1H-15N-HMBC-NMR spectrum of compound 3 MPT-Ph-amide.

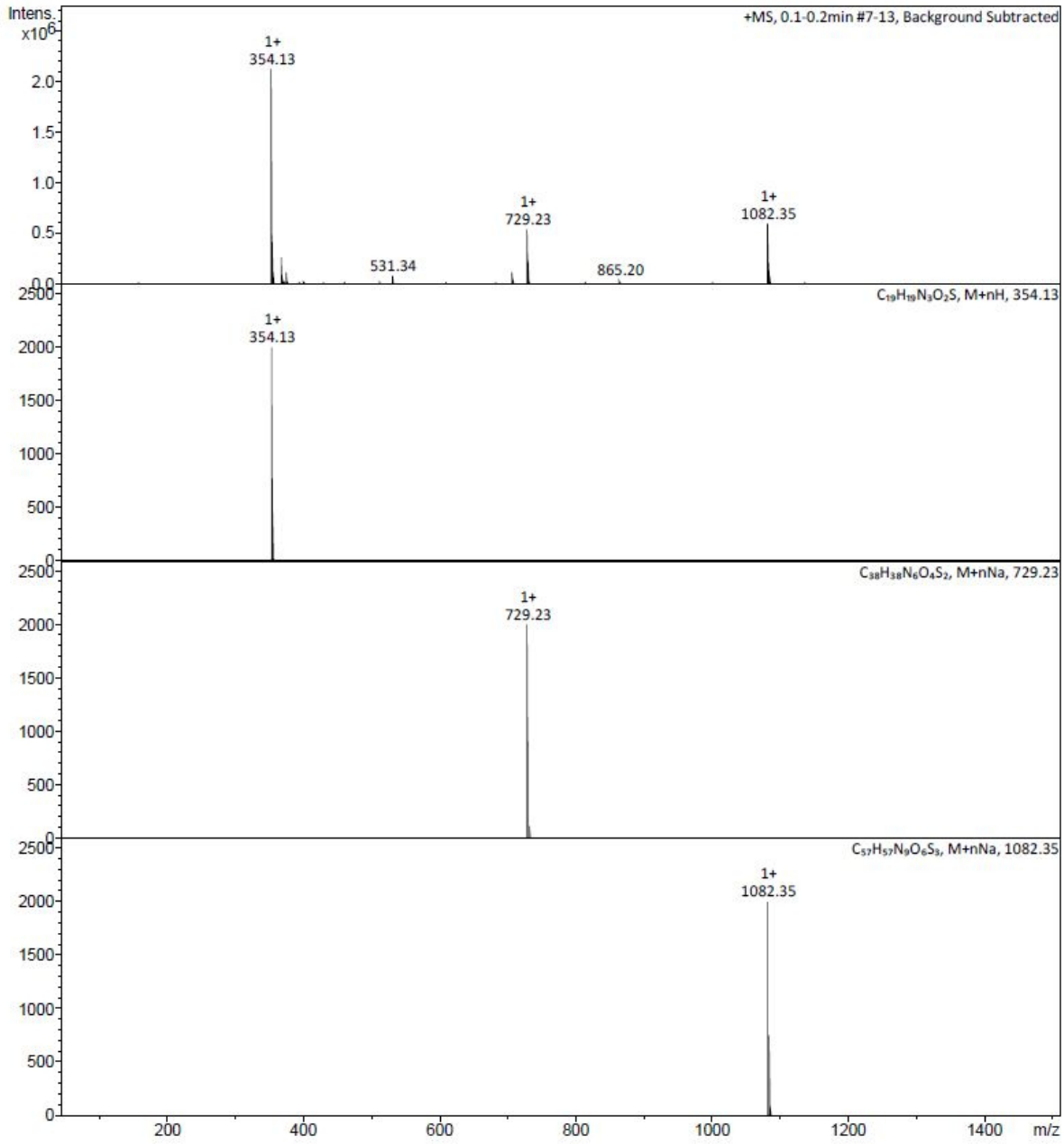

Figure S8. ESI-MS spectrum of compound 3 MPT-Ph-amide.

Optical Properties of MPT-Ph (Compound 2)

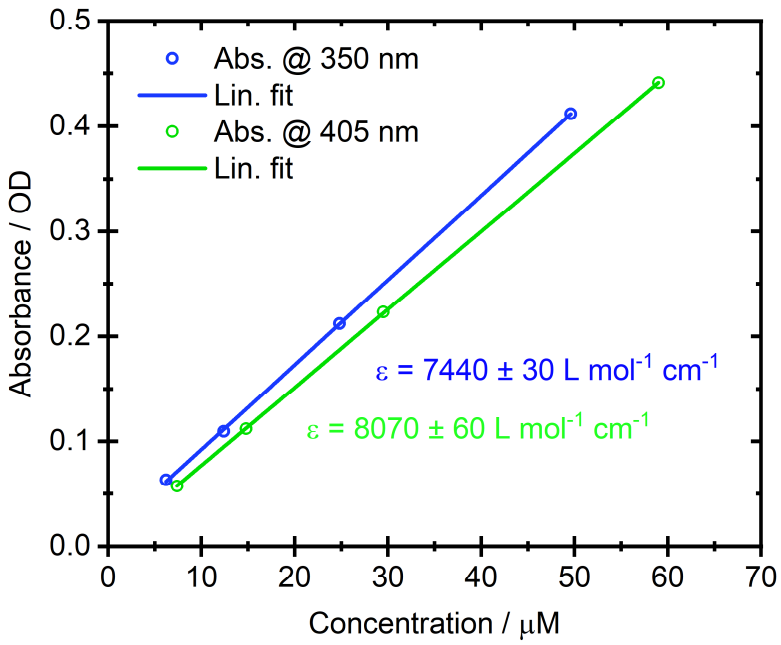

Figure S9. Plot of the absorbance values at the maximum of the UV/vis absorption band of a dilution series depending on the respective concentrations at pH 7.4 (MPT-Ph, blue) and at pH 1 (MPT-Ph-H^+, green). Datapoints (circles) were fit linearly (solid lines) and the molar extinction coefficients were determined from the slope of the fits.

To determine the molar extinction coefficients of the deprotonated (pH 7.4) and the protonated (pH 1) form of MPT-Ph, UV/vis absorbance spectra of a dilution series with known concentrations were recorded. The maximum absorbance of the sample solution was kept below 0.5 OD. According to Lambert-Beer`s law, the extinction of a sample correlates linearly to its concentration, with the path length of the cuvette and the molar extinction coefficients as proportionality factors. Hence, the extinction coefficient can be derived from the linear regression of the absorbance values plotted against the corresponding concentrations.

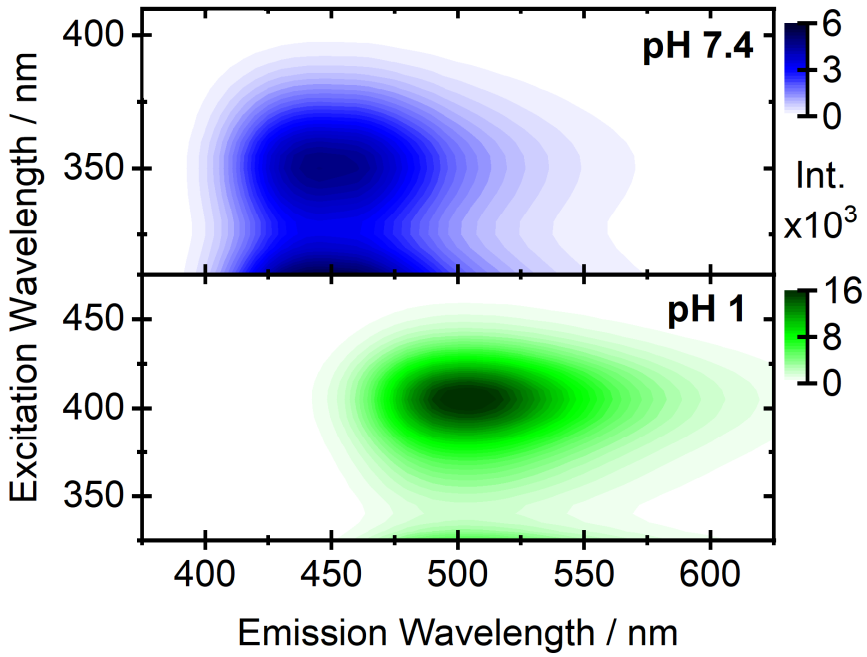

Figure S10. Excitation-wavelength dependent emission contour plots of MPH-Ph at pH 7.4 (upper panel, blue) and at pH 1 (lower panel, green).

To determine the fluorescence quantum yields, emission spectra of MPT-Ph at pH 7.4 and 1 were recorded and also spectra of the respective solvents to obtain the scattering light peak. The quantum yield is defined as the quotient $\frac{n_{em}}{n_{abs}}$, where n_{em} is the number of emitted photons and n_{abs} the number of absorbed photon. The number n_{em} is obtained by integrating the emission signal of the sample and n_{abs} corresponds to the difference of the scattering light peak intensity of the solvent and the sample measurement.

Thermogravimetric analysis (TGA)

Thermo gravimetrical analysis (TGA) was performed using a TG 209 F3 Tarsus from NETZSCH Thermal Analysis. Synthetic air was used as purge gas. The heating/cooling rates in all experiments were set to 20 K/min for all non-isothermal steps. To dry the samples, they were heated to 100°C and held at 100°C for 75 min. For organic decomposition the samples were heated to 700°C and held at this temperature for another 30 min to guarantee total decomposition.

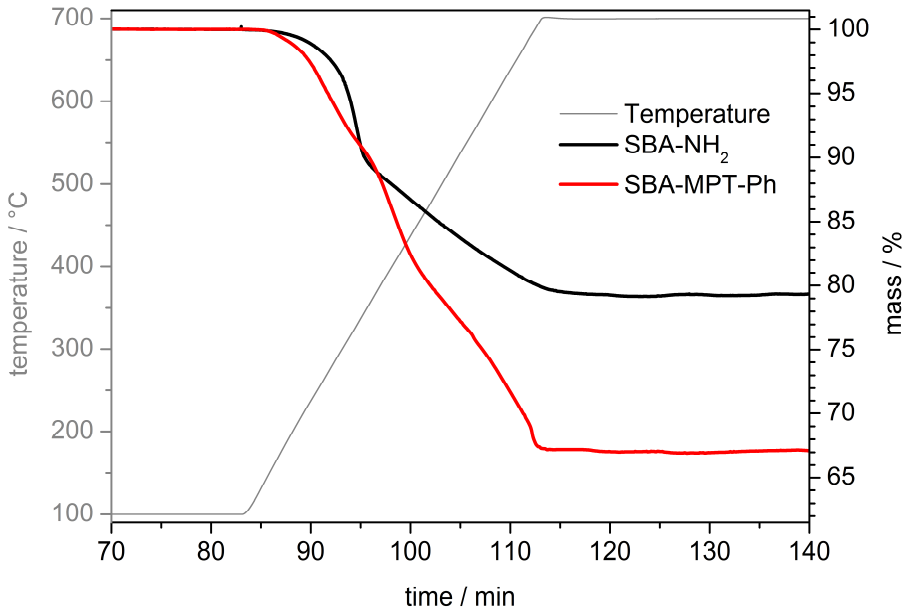

Figure S11. Comparison of the TGA curves of the NH_2-functionalized SBA-15 (black) and the MPT-Ph dye functionalized SBA-15 (red) (right axis). The temperature profile for the measurement is shown in grey (left axis).

Table S1. Weight fractions and its change (Δ) after MPT-Ph dye coupling obtained by thermogravimetric analysis.

Sample	organic content [wt%]	SiO_2 content [wt%]
SBA-NH_2	20.8 ± 0.2	79.2 ± 0.2
SBA-MPT-Ph	32.5 ± 0.5	67.5 ± 0.5
Δ	11.7 ± 0.7	11.7 ± 0.7

The organic content of the sample changes from 20.8% to 32.5% after MPT-Ph dye coupling. Assuming the mass change is only influenced by the introduced dye with a molecular mass of 353.44 g/mol the dye loading can be calculated as 0.33 mmol/g ± 0.02 by thermogravimetric analysis.

Elemental analysis (EA)

Elemental analysis was performed with a VarioEL III CHN from Elementar. 2-3 mg of the samples were combusted under O_2 atmosphere. This results in the formation of CO_2, NO_x, H_2 and H_2O. The NO_x compounds were reduced to N_2 using elemental cupper. The gases were separated by gas chromatography and detected quantitatively by a thermal conductivity detector (TCD). Acetanilide was used for calibration.

Table S2. Weight fractions of the samples obtained by elemental analysis.

Sample	N content [wt%]	C content [wt%]	H content [wt%]	Si + O content [wt%]
SBA-NH_2	2.9 ± 0.0	8.9 ± 0.1	3.7 ± 0.1	84.5 ± 0.2
SBA-MPT-Ph	4.4 ± 0.1	19.5 ± 0.2	3.1 ± 0.1	72.9 ± 0.3

Table S3. Molar nitrogen and carbon content of the samples and its change (Δ) after MPT-Ph dye coupling obtained by elemental analysis.

Sample	Nitrogen content [mmol/g]	Carbon content [mmol/g]
SBA-NH_2	2.1 ± 0.0	7.4 ± 0.1
SBA-MPT-Ph	3.2 ± 0.1	16.3 ± 0.2
Δ	1.1 ± 0.1	8.8 ± 0.3

Considering the amount of nitrogen (2) and carbon (16) atoms introduced by the MPT-Ph dye this results in a dye loading of 0.54 ± 0.05 mmol/g or 0.55 ± 0.02 mmol/g respectively obtained by elemental analysis.

Brunauer–Emmett–Teller (BET)

The porosity and specific surfaces area of the materials were characterized by nitrogen adsorption at 77 K, employing a Thermo Fisher Scientific Surfer BET analyzer using N_2 gas as adsorbent. The specific surface was obtained by the Brunauer Emmett Teller (BET) method analyzing the curve in the p/p^0 range between 0.03 and 0.3. The pore volume was obtained by the Gurvich method and the p/p^0 value at 0.95 was used. Pore size distributions were obtained by applying the Barrett-Joyner-Halenda (BJH) analyzing the adsorption-desorption isotherms in the p/p^0 range between 0.3 and 0.95 and nonlocal density functional theory (NLDFT) method.

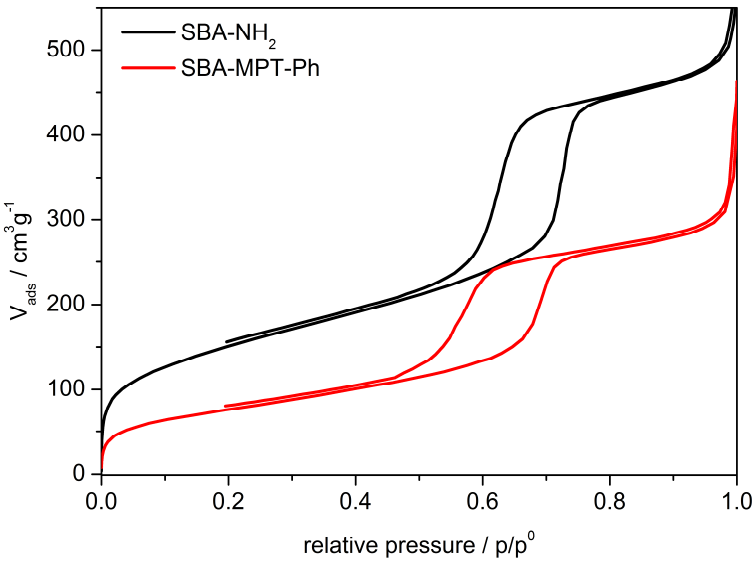

Figure S12. N_2 adsorption–desorption isotherms of the NH_2-functionalized SBA-15 (black) and the MPT-Ph dye functionalized SBA-15 (red).

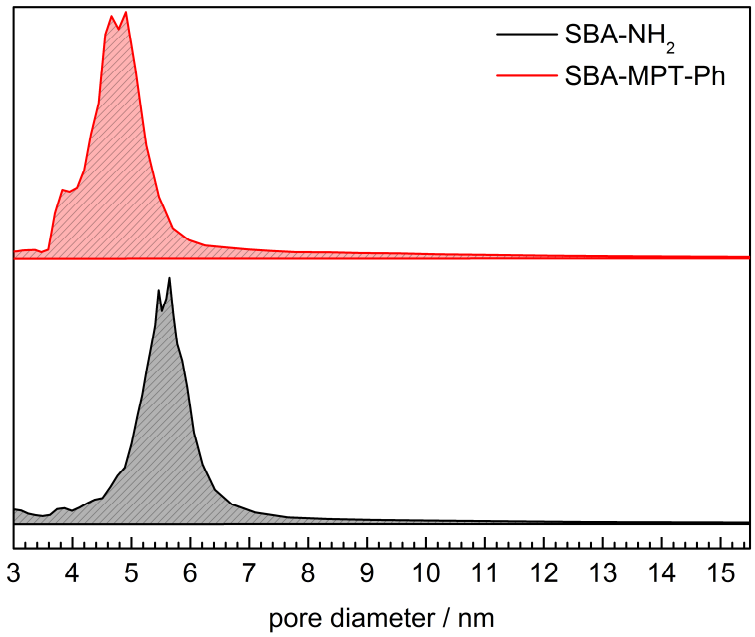

Figure S13. Normalized BJH curves calculated from the nitrogen adsorption-desorption isotherms of the NH_2-functionalized SBA-15 (black) and the MPT-Ph dye functionalized SBA-15 (red). For clarity, results for different samples are vertically shifted.

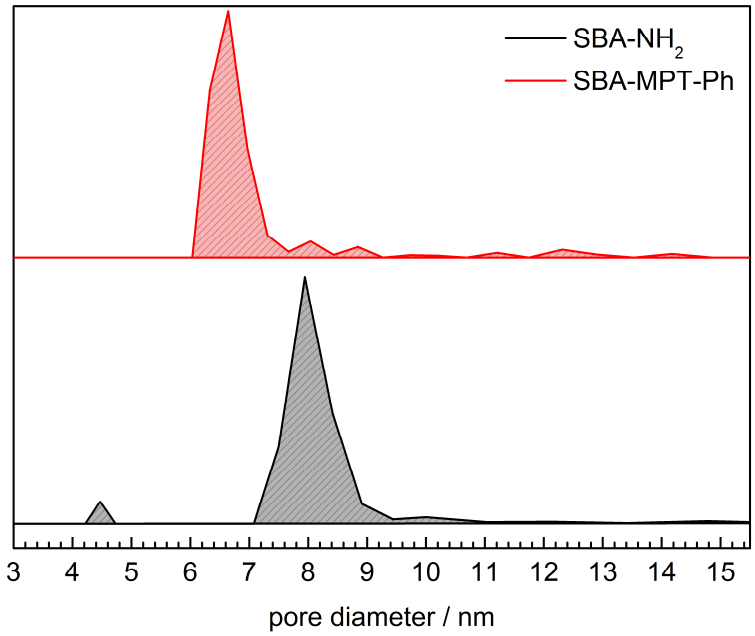

Figure S14. Normalized NLDFT curves calculated from the nitrogen adsorption-desorption of the NH_2-functionalized SBA-15 (black) and the MPT-Ph dye functionalized SBA-15 (red). For clarity, results for different samples are vertically shifted.

Table S4. Pore volume (Gurvich at p/p^0 0.95), specific surface area (BET) and median pore diameters calculated by the BJH (left) and NLDFT (right) method as obtained from BET analysis.

Sample	Pore volume [cm³/g]	Surface Area [m²/g]	Pore diameter by BJH (nm)	Pore diameter by NLDFT (nm)
SBA-NH_2	0.74 ± 0.02	545 ± 16	5.6 ± 0.2	7.9 ± 0.2
SBA-MPT-Ph	0.45 ± 0.01	271 ± 7	4.9 ± 0.3	6.6 ± 0.3

Taking into account the obtained BET surface for the functionalized SBA-15 support of 271 m²/g, and the obtained MPT-Ph dye loading obtained by elemental analysis (~0.55 mmol/g) and thermogravimetric analysis (~0.33 mmol/g), the surface grafting density can be calculated by

$$Molecules/nm^2 = \frac{dye\ loading\ [mol/g]}{specific\ surface\ area\ [m^2/g]} \times N_a. \quad (1)$$

This results in a MPT-Ph dye surface grafting density between 0.7 and 1.2 dye molecules/nm².

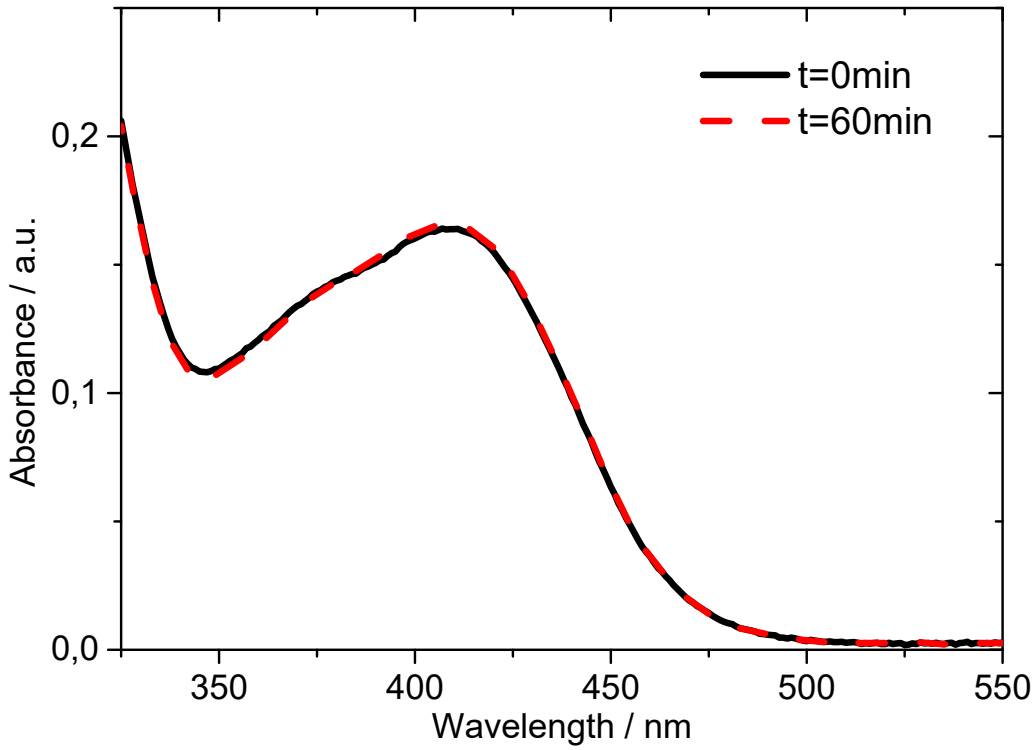

Figure S15. UV-vis measurements of a MPT-Ph functionalized mesoporous silica film that was kept in the measurement solution for 60 minutes. Measurements were taken at t t=0 minutes (black solid line) and t=60 minutes (red dashed line).

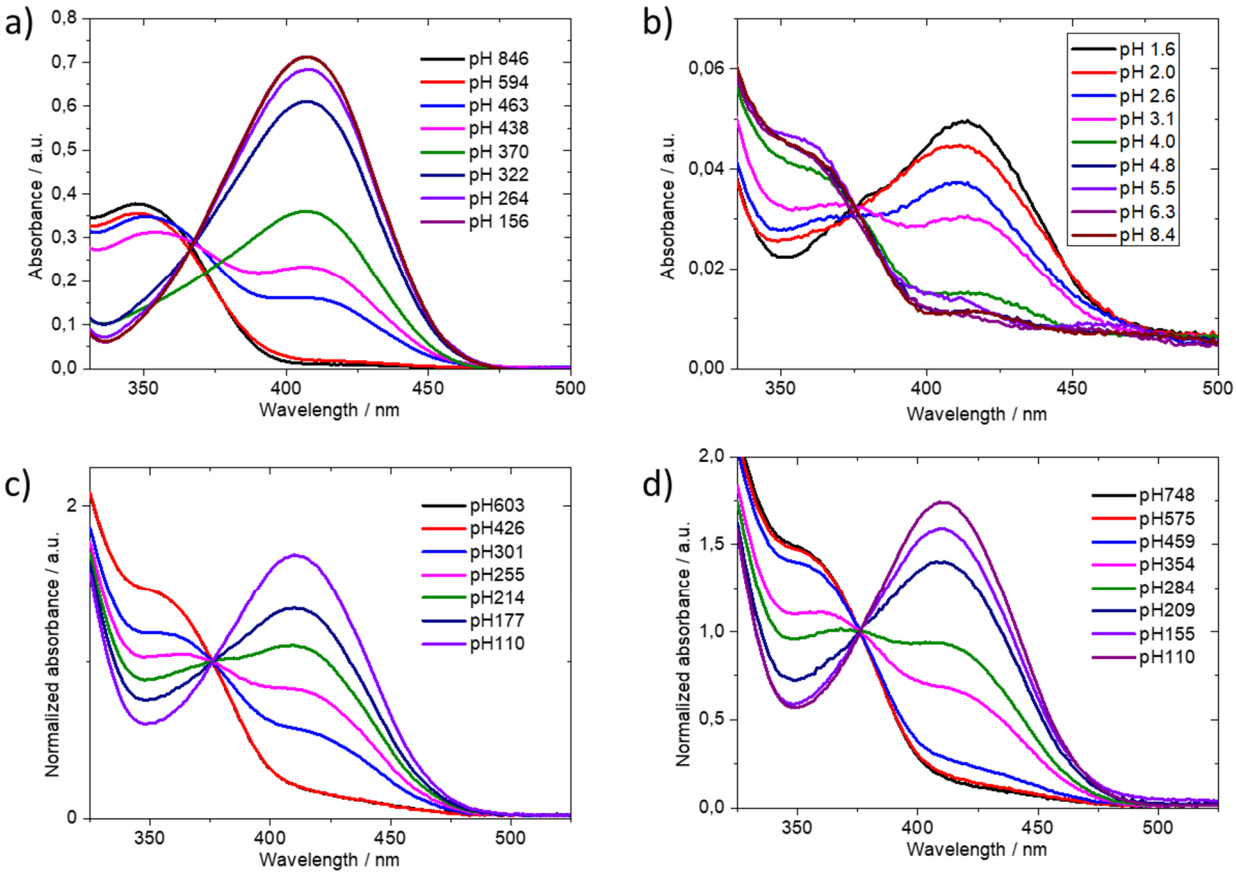

Figure S16. Measured UV-vis spectrums of MPT-Ph-Amide and MPT-Ph functionalized mesoporous silica films at different pH values. Measurements shown leads to the data shown in Figure 6 in the main manuscript. a) corresponds to Figure 5a MPT-Ph-Amide (black spheres); b) corresponds to Figure 5a MPT-Ph-Surface on a 700 nm big pore film (red spheres); c) corresponds to Figure 5b MPT-Ph grafted on a mesoporous silica thin film with big pores and a film thickness of ~500 nm. Measurements conducted at an ionic strength of 0.1xPBS (15 mM) (blue spheres); d) corresponds to Figure 5b MPT-Ph grafted on a mesoporous silica thin film. Measurements conducted at an ionic strength of 1xPBS (150 mM) (black spheres).

Microporous and Mesoporous Materials 282 (2019) 29–37

Contents lists available at ScienceDirect

Microporous and Mesoporous Materials

journal homepage: www.elsevier.com/locate/micromeso

Systematic study on FRET-pair functionalization of mesoporous thin films for correlation of pH-sensing and ionic mesopore accessibility

Mathias Stanzel[a], Robert Brilmayer[a], Markus Langhans[b], Tobias Meckel[b], Annette Andrieu-Brunsen[a,*]

[a] Ernst-Berl Institut für Technische und Makromolekulare Chemie, Technische Universität Darmstadt, Alarich-Weiss-Strasse 4, D-64287, Darmstadt, Germany
[b] Membrane Dynamics, Department of Biology, Technische Universität Darmstadt, Schnittspahnstraße 3-5, 64287, Darmstadt, Germany

ARTICLE INFO

Keywords:
Mesoporous thin films
pH-detection
Confinement effects
FRET dye pair
Ionic permselectivity
Ionic mesopore accessibility

ABSTRACT

Ordered mesoporous silica materials (OMS) are relevant in various applications such as separation, catalysis, or drug delivery. Thereby their performance is mainly dependent on mesopore accessibility and molecular transport within mesopores which is strongly influenced by the spatial confinement. This is especially relevant in case of charged mesopore walls and thus electrostatically controlled transport. Therefore, it is highly important to monitor charged states of functionalized mesopores. In this study we adapt pH-probing strategies, known from pH-monitoring e.g. in cells, to mesoporous thin films aiming to monitor mesopore charge and correlate this to mesopores ionic permselectivity. Therefore, grafting of a FRET dye pair, consisting of a pH-sensitive dye (fluorescein isothiocyanate (FITC)) and a pH-insensitive reference dye (rhodamine B isothiocyanate (RITC)), to the mesopore wall is optimized. The grafted FITC-RITC FRET pair allows to monitor mesopore "pH" over a broad range of up to six pH-units after optimization of FRET pair functionalization. Thereby, "pH" monitoring is performed based on absorption and fluorescence readout using confocal microscopy baring the potential of localized detection. The detected pH-dependent absorption and fluorescence emission is in good agreement with the pH-dependent ionic mesopore permselectivity, and thus with the influence of mesopore confinement on ionic permselectivity as detected by cyclic voltammetry. In addition, this study not only shows the possibility of using FRET dye pairs for monitoring charged states in mesopores but as well the influence of these probing dye molecules on the mesopores characteristics, such as ionic permselectivity, indicating the need of optimizing functionalization with probe molecules.

1. Introduction

Ordered mesoporous silica materials (OMS) present high specific surface area and structural stability while offering tunable pore sizes and geometries [1,2]. Due to the high number of surface silanol groups, OMS can be modified with a variety of organic functional groups [3,4]. The broad range of functionalization opportunities together with their tunable pore structure and material architecture are main reasons for OMS having attracted significant research interest and a variety of applications such as controlled drug release [5], microfluidic devices, sensing [6], lab-on-chip devices [1,7–10], bioseparation [11,12], drug delivery [13,14], oil production [15], oil-water separation or proton transport [11,16–18], e.g. in the context of energy conversion have been proposed over the last decades. Changing solution pH and thus charge density in mesopores directly affects mesopore accessibility and transport and thus the mentioned applications. Thereby, pore size as well as pore wall functional group- and thus charge density, affect "pH" within mesopores. It has been demonstrated, that mesopore "pH" might strongly differ from the measurable solution pH [3,19–22].

Inspired by natural ion channels and -pores, systematic investigation of polymer functionalization in spatially confined mesopores [23–25] resulted in a plethora of functionalized mesopores with adjustable pore accessibility and ionic transport within the last years mainly using electrostatic interaction. Gating of ionic transport as well as gradual tuning of mesopore accessibility have been achieved by incorporation of stimuli responsive functional units, often polymers, reacting to stimuli such as solution pH, potential, or light [10,26–34]. More recently, controlling polymer amount and thus charge density inside mesopores has resulted in gradual variation of ionic mesopores accessibility [23–25,35]. In case of pH-gated or gradually tuned ionic mesopore accessibility only the solution pH can be adjusted. The "pH" within the mesopores remains often unknown and cannot be directly

* Corresponding author.
E-mail address: andrieu-brunsen@smartmem.tu-darmstadt.de (A. Andrieu-Brunsen).

https://doi.org/10.1016/j.micromeso.2019.03.009
Received 24 October 2018; Received in revised form 25 February 2019; Accepted 4 March 2019
Available online 09 March 2019

monitored experimentally. In this context, only a few studies tried to correlate the resulting ionic permselectivity with gradual solution pH-changes. Doing so a difference between the measured solution pH and the expected pK_a-controlled ionic permselectivity has been observed [22]. Only after considering the influence of the spatial confinement and proximity of generated mesopore wall charges, the experimental titration curve could be theoretically reproduced [36]. Such nanoscale confinement effects on charge density and protonation-deprotonation equilibria are as well reported for hydrogels [37,38], and concave nanoparticles for which curvature plays a role [39]. This shows the need for experimental strategies to directly monitor the "pH" in spatially confined nanopores which are still missing to date. In this context, strategies enabling "pH" monitoring in mesopores, ideally with spatiotemporal control, bare the potential to directly monitor mesoporous charged states, as e.g. in smart porous materials with switchable charge density or charge density gradients. In addition, fluorescence detection bares the potential to go towards localized detection, potentially down to single pores, to get information on transport profiles of pore cross-sections. Such information with local nanoscale resolution are currently obtained using theory giving essential insights for understanding nanopore transport [22,24,40].

Local pH-read out is especially investigated in the context of tumor cells using dyes as molecular pH-probe [6,41–44]. In this context, ratiometric fluorophores such as SNARF as well as the Förster resonance energy transfer (FRET) [45] dye pairs such as fluorescein isothiocyanate (FITC) and rhodamine B isothiocyanate (RITC) are commonly used [6,41,42,46–49]. To date, FRET dye pairs have been combined with silica nanoparticles showing an influence of environmental conditions on the fluorescence emission allowing to use these materials as sensors [6,42]. This approach does not allow to differentiate between dyes attached to the external or to the pore wall surface and the potential influence of spatial confinement has not been discussed. Furthermore, dye incorporation has mostly been achieved by co-condensation techniques of functionalized dyes and inorganic precursor that results in incorporation of the dyes in the metal-organic framework and only a small amount of the functionalities are chemically available [50].

Here, we report a systematic study of FRET dye pair functionalized mesoporous silica thin films (FMSFs) to understand the influence of spatial confinement on charged state of mesopores as well as the influence of the dye functionalization on pore accessibility. The well investigated FRET dye pair FITC and RITC is immobilized in various ratios on Pluronic® F127 templated mesoporous silica thin films using post grafting. The FMSF are further analyzed with respect to their pH-dependent spectral and transport properties using UV/vis spectroscopy, fluorescence microscopy and cyclic voltammetry. Despite a possible investigation of fluorescence of FMSFs with conventional spectrometers, confocal microscopy has been applied allowing future characterization with local resolution and single pore detection. To the best of our knowledge, this is the first study systematically optimizing FRET dye pair functionalization of mesopores and correlating the resulting optical monitoring of mesopore protonated states with mesopores transport characteristics which represents a first step towards localized "pH" monitoring in mesopores.

2. Experimental

2.1. Chemicals

All materials and solvents were purchased from Sigma-Aldrich, Acros Organics, and VWR and used as received unless stated otherwise. The precursor solutions for dip-coating mesoporous films were prepared using the inorganic precursor tetraethoxysilane (TEOS, Acros Organics, 98%, Geel, Belgium) in absolute ethanol (EtOH, Merck, ≥99.5%), with hydrochloric acid as catalyst (HCl, 37%) and water. Pluronic® F127 (F127, BioReagent, Sigma-Aldrich, 12,600 g mol^{-1}) was used as structure directing agent at a molar ratio of 0.0075 relative to the silane precursor. Microscope slides (VWR, glass, cut edges) were cleaned in a mixture of detergent and water prior to rinsing with ethanol and drying under ambient conditions. Silicon wafers (Si-Mat, Kaufering, Germany, 100 mm diameter, 525 ± 25 µm thickness, type P/Bor, < 100 > orientation, CZ growth method, 2–5 W resistivity, polished on 1 side) and indium tin oxide (ITO, Delta Technologies, Ltd., Loveland, CO, USA, polished float glass, 150 × **150** × 1.1 mm, SiO_2 passivated/Indium Tin Oxide coated one surface, RS = 4–8 Ω, cut edges) were cut to desired size using a diamond cutter, cleaned using technical grade ethanol, and dried under ambient conditions prior to dip-coating of mesoporous films.

2.2. Synthesis of mesoporous thin films

Mesoporous thin films were synthesized, as described previously [10,24,27], via sol−gel chemistry and evaporation induced self-assembly [2] based on the silica precursor tetraethoxysilane (TEOS) in the presence of the template Pluronic® F127. The precursor solution was prepared using the following molar ratios: 1 TEOS : 40 EtOH : 0.0075 Pluronic® F127 : 10 H_2O : 0.28 HCl. The solutions were stirred for 24 h at room temperature prior to use for mesoporous film preparation. Mesoporous films were prepared on ITO coated glass, glass, or silicon wafer substrates at 40–50% relative humidity, 25 °C, and a withdrawal speed of 2 mm/s. Freshly deposited films were stored at 40–50% relative humidity and 25 °C in a climate chamber for 1 h. A stabilizing thermal treatment was carried out in two successive temperature steps at 60 and 130 °C for 1 h, respectively. Subsequently, the temperature was increased to 350 °C at a rate of 1 °C/min for 2 h followed by cooling down to ambient temperature, rinsing with ethanol and storage under ambient conditions. The resulting mesoporous films are characterized by a film thickness of 150–300 nm and a porosity of ~45 vol% as measured by ellipsometry (Table 1 and 2, ESI).

2.3. Dye synthesis

For grafting of fluorescein isothiocyanate (FITC) and rhodamine B isothiocyanate (RITC) to the mesoporous silica, the dyes were functionalized with 3-aminopropyltrimethoxysilane (APTMS) to form N-1-(3-trimethoxysilylpropyl)-N′-fluoreceylthiourea (APTMS-FITC) and N-1-(3-trimethoxysilylpropyl)-N′-tetramethylrhodaceylthiourea (APTMS-RITC). Therefore, 6 mg (15.4 µmol, 1 eq.) FITC or 8.3 mg (15.4 µmol, 1 eq.) RITC were dissolved in 15 mL ethanol. Then, 27.63 mg ($1.54 \cdot 10^{-4}$ mol, 10 eq.) APTMS was added. The solutions were stirred for 24 h under inert conditions and used for mesoporous film functionalization without further purification.

2.4. Synthesis of FRET dye pair functionalized mesoporous silica films (FMSFs)

Dye functionalization of mesoporous silica thin films was carried out via post-grafting. A 0.01 wt% dye solution was prepared by mixing the ethanolic solution of the modified dyes with toluene under nitrogen flow followed by purging with nitrogen for 15 min. Mesoporous thin films were placed in a flask under nitrogen flow, the dye solution was added and heated to 80 °C for 1 h under inert conditions. Subsequently, the films were rinsed with toluene and ethanol to remove unbound APTMS as well as APTMS-FITC and APTMS-RITC. The dye functionalized films were stored under ambient conditions. The molar ratio of the modified dyes in the functionalization solution was varied between 1 : 1.1 : 2.2 : 1 and 10 : 1 with respect to APTMS-FITC and APTMS-RITC in the reaction solution.

2.5. pH-dependent absorption and fluorescence

For pH-dependent measurements of absorption and fluorescence

emission, phosphate buffered solutions (PBS) were prepared for eight different pH values adjusted by either HCl or NaOH confirmed by using a pH electrode (pH 110, VWR). FMSFs were incubated into the pH adjusted phosphate buffered solution for 15 min and dried with pressured air directly before being measured. The stability of the applied mesoporous silica thin films in acidic (pH 2) and basic (pH 10) solution has been investigated using ellipsometry determining film thicknesses and refractive indices before and after incubation (Tables S4 and S5). Fluorescence spectra were recorded using a confocal microscope (CLSM TCS SP5 II, Leica Microsystems, Mannheim, Germany). For excitation monochromatic light of 458 nm (Ar-laser, 65 mW) was used. Fluorescence was recorded stepwise (5 nm) from 470 - 700 nm. Fluorescence images were analyzed using the Leica Application Suite AF Lite (V 2.6.3) software. Fluorescence spectra were obtained selecting three homogeneous regions (250 × 250 µm) of interest (ROI) on the FMSFs. The obtained spectra were then exported to OriginPro for further processing.

UV/vis spectroscopy was performed using a Varian Cary 50 SCAN UV/vis spectrometer. The UV/vis spectra were recorded from FMSFs deposited on glass substrates in a range of 300 nm–800 nm with a scan rate of 600 nm/min. All spectra were background corrected using an unmodified mesoporous silica film deposited on a glass substrate. UV/vis absorption spectra of CO_2-plasma treated dye functionalized mesoporous silica films are used to calculate the ratio of attached dyes according to Lambert-Beer's law. For calculations, extinction coefficients of FITC and RITC determined by Widmer et al. [42] are applied. Within all experiments the stability of the characterized silica films has been assured for the duration of the experiment e.g. using ellipsometry and cyclic voltammetry.

2.6. Attenuated total reflection Fourier transform infrared spectroscopy (ATR-FTIR)

Infrared spectra of the prepared mesoporous films on glass or ITO substrates were performed using a Perkin Elmer Instrument One Spectrum FT-IR Spectrometer equipped with a Universal ATR Polarization Accessory (Waltham, MA, USA). All spectra were normalized to the stretching vibration of free silanol groups at ~905 cm^{-1}. The spectra were recorded using the Spectrum Software (Version 10.5.4.738, PerkinElmer, Inc. Waltham, MA, USA, 2016) between 4000 and 650 cm^{-1} with a resolution of 4 cm^{-1}, and a background as well as baseline correction was automatically performed. Additional bands of the glass substrate are visible in the FTIR spectra: Mesoporous film signals are partially superimposed by signals originating from the glass substrate in the region of 830 - 1250 cm^{-1} depending on the penetration depth of the ATR-IR evanescent waves. Nevertheless, due to the comparable film thickness, IR-spectra of different films can be compared. All further data processing was performed in OriginPro9 (ADDITIVE Soft-und Hardware für Technik und Wissenschaft GmbH, Friedrichsdorf, Germany, 2012).

2.7. Transmission electron microscopy (TEM)

Electron micrographs were recorded using a Philips FEI CM-20 transmission electron microscope (Philips, Amsterdam, Netherlands) equipped with a LAB-6 cathode and Olympus CCD camera, and with a maximum resolution of 2.3 Å operating at an accelerating voltage of 200 kV. Samples were prepared by scratching the mesoporous films and dispersion in filtered ethanol. After 10 min of sonication scratched mesoporous films were drop cast onto 3.05 mm Cu grids (mesh size 200) with a Lacey carbon film (Plano GmbH, article number S166-2). The samples were dried under ambient conditions.

2.8. Plasma treatment

The organic functional groups present on the exterior planar mesoporous film surface were removed by applying a CO_2-plasma treatment [28] using a Diener Femto-plasma cleaner (Diener electronic, Ebhausen, Germany) at a pressure of 0.4 mbar and power of 20% for 12 s according to a previously published protocol by Babu et al. [51].

2.9. Cyclic voltammetry

The ionic permselectivity of the mesoporous materials was investigated via cyclic voltammetry (CV) using $[Fe(CN)_6]^{3-/4-}$ and $[Ru(NH_3)_6]^{2+/3+}$ as charged, redox-active probe molecules. Measurements were recorded using a Metrohm Autolab PGSTAT302N potentiostat. Mesoporous films prepared on ITO coated glass substrates (working electrode) were characterized using a 1 mM solution of either the positively- or negatively charged probe molecule in a PBS electrolyte solution. The pH-dependent permselectivity was investigated by adjusting the solution pH between 2 and 9 by the addition of either concentrated aqueous NaOH or HCl to the probe molecule containing buffer solutions. The pH was determined using a pH-meter (pH110, VWR). An Ag/AgCl reference electrode (BASi RE-6) and graphite counter electrode was used in the sample cell. The measured working electrode area was 0.21 cm^2. Pore accessibility for each pH was measured using a scan rate sequence of 200, 100, 25, 300, 1000, and 200 mV/s, with each scan rate being cycled three times.

3. Results and discussion

To enable monitoring of “pH” or, more precisely, protonation-/deprotonation equilibria in functional, spatially confined mesopores, and thus enhance understanding of confinement effects as well as to get direct and ideally spatiotemporally resolved information on “pH” allowing to predict ionic transport, FRET dye pairs are a versatile tool. To investigate their possibilities and limits, pH-sensitive FMSFs have been prepared. For the preparation and characterization of pH-sensitive FMSFs, mesoporous thin films are synthesized and subsequently functionalized with pH-reporting dyes N-1-(3-trimethoxysilylpropyl)-N′-fluoreceylthiourea (APTMS-FITC) and N-1-(3-trimethoxysilylpropyl)-N′-tetramethylrhodaceylthiourea (APTMS-RITC) by grafting them onto the mesoporous silica film pore walls (Fig. 1a).

Allowing pH-detection of such a FRET pair within the spatial confinement of mesopores requires the fluorescence emission of one dye (here APTMS-FITC, pH-sensitive donor) to overlap with the absorption of its pair dye (here APTMS-RITC, pH-insensitive acceptor) and a FRET pair distance being small to obtain sufficient FRET and to allow detection of fluorescence emission of both dyes by exclusive irradiation of the donor dye (here APTMS-FITC). As depicted in the absorption and fluorescent emission spectra in Fig. 1b FITC and RITC spectra sufficiently overlap. One common approach for dye-based pH-probing is the combination of one dye showing pH-sensitive photospectral properties while the second dye has to be pH-insensitive and serves as reference [52–54]. In this study, FITC represents the pH-sensitive dye while RITC serves as pH-independent reference [55–58]. Thus, for pH-monitoring both dyes have to be incorporated into the mesopores within a close distance to allow FRET to occur [59]. Readout is performed by monitoring the fluorescence emission of both dyes after irradiation at a single wavelength of 458 nm exciting the lower wavelength absorption of FITC. In addition, the applied functionalization strategy using post-grafting of APTMS-FITC and APTMS-RITC followed by a CO_2-plasma treatment destroying dye at the external planar film surface, enables pH-monitoring FRET dye pair attachment exclusively to the mesoporous silica pore wall inside the mesopores. Alternative co-condensation would result in dyes being as well incorporated into the inorganic matrix and thus being surrounded by very different and hard to analyze local environments.

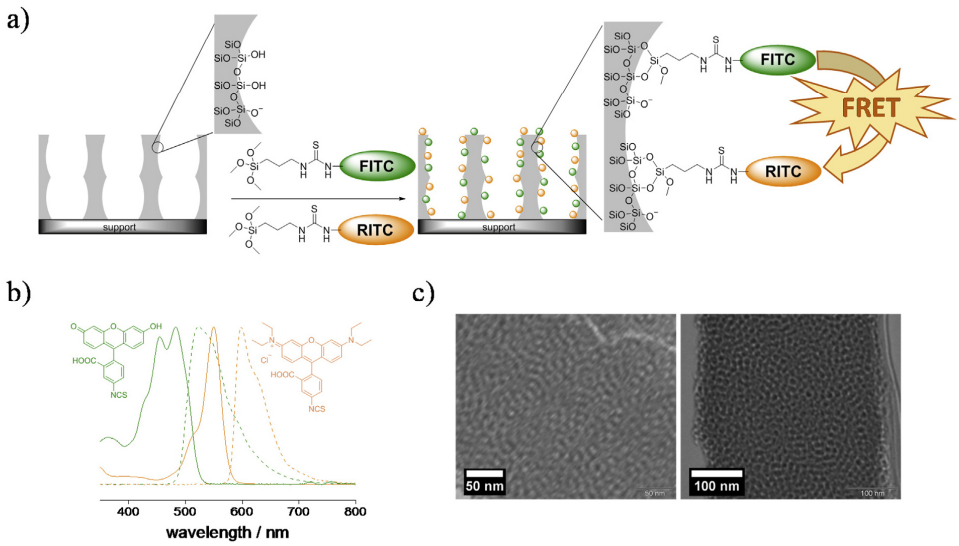

Fig. 1. a) Scheme showing the FRET dye pair (FITC, green, donor and RITC, orange, acceptor) functionalized mesoporous silica film (FMSF). **b)** Molecular structure as well as absorption (solid line) and fluorescence emission (dashed line) spectra of FITC (green) and RITC (orange) recorded in ethanol. **c)** Representative TEM image of a mesoporous silica thin film, scale bar: 50 nm (left) and 100 nm (right). (For interpretation of the references to color in this figure legend, the reader is referred to the Web version of this article.)

3.1. Structural and functional characterization of mesoporous thin films

The applied mesoporous silica thin films, prepared via sol-gel chemistry and EISA according to work of Brinker et al. [2], present an average film thickness of 160 nm and an ordered mesoporosity of 42 vol % as determined by ellipsometry and effective medium approximation [60] (Supporting Information and previous work [10,23]). As demonstrated in previous work, as prepared films display organized pore arrays with pores having an ellipsoidal shape due to uniaxial contraction [23,25] with pore connections (necks) of ~3 nm and surface area of 36 m^2 per 1 m^2 substrate surface, which corresponds to ~440 m^2/g as determined via krypton BET adsorption [23]. According to ellipso-porosimetry analysis discussed in previous reports [10], the pore size of mesoporous silica thin films using the same Pluronic® F127 template with identical molar ratio in the precursor formulation has been reported to be around 5.3 nm. TEM images of an unmodified mesoporous silica thin film (Fig. 1c) show a well ordered mesoporous structure and a pore size of about 6–7 nm which is in good agreement with previous reports [23,25] and the pore size determined in previous studies by ellipso-porosimetry [10].

Functional characterization using infrared spectroscopy shows the characteristic vibrational bands of the inorganic silica framework (Fig. 2b). The intense vibrational band at 905 cm^{-1} is related to free surface silanol groups. All infrared spectra are normalized to these vibrational bands of free silanol groups at 905 cm^{-1}. Vibrational bands at 1050 cm^{-1} and 1170 cm^{-1} can be assigned to the transverse and longitudinal Si-O-Si vibrations. In addition, transverse Si-O-Si vibrationas are observed at 768 cm^{-1}. Bending vibration and stretching vibration of adsorbed water molecules are located at 1650 cm^{-1} and 3000 - 3500 cm^{-1} respectively [61]. The vibrational band at 1595 cm^{-1}, which is overlapping with the bending vibration of water, can be assigned to the asymmetric N-H bending vibration of nitrogen containing species, particularly the thiourea group of the APTMS coupled dyes as well as remaining APTMS moieties [34] indicating successful dye functionalization. For pH-sensitive dye grafting the isothiocyanate derivates of fluorescein and rhodamine B (FITC and RITC) are modified with a silane anchor group by coupling them to 3-aminopropyltrimethoxysilane (APTMS). The resulting N-1-(3-trimethoxysilylpropyl)-N′-fluoreceylthiourea (APTMS-FITC) and N-1-(3-trimethoxysilylpropyl)-N′-tetramethylrhodaceylthiourea (APTMS-RITC) are subsequently grafted onto the silica surface (Fig. 1c). Infrared spectroscopy of functionalized FMSFs show additional bands in comparison to the unmodified mesoporous silica thin film (Fig. 2b): between 2800 - 3000 cm^{-1} C-H stretching bands are observed corresponding to the aromatic framework of the dyes. Furthermore, bands at 1350 - 1600 cm^{-1} can be correlated to the bending vibration of the aromatic framework of the dyes. Nevertheless, vibrational bands of the isothiocyanate group at around 2000 cm^{-1} are not present in the infrared of FMSFs indicating covalent binding of the dyes on the silica surface forming thiourea (Fig. S2, ESI). Comparing ellipsometric measurements (Tables S1 and S2) before and after dye functionalization reveals an increase of the refractive index of approximately 0.1 supporting the functionalization of the mesopores indicating a pore filling fraction of 68 vol% for the FMSFs with a molar ratio of 1 : 1, 1 : 2, 2 : 1 and 38 vol% for the FMSFs with a molar ratio of 10 : 1 based on effective medium calculations [10,60]. Besides using FTIR spectroscopy and ellipsometry dye attachment is indirectly proven by extraction experiments showing no stable attachment and successful extraction for unmodified dyes without APTMS anchor groups. In addition, FMSFs clearly show a color change visible by eye upon APTMS-RITC and APTMS-FITC binding. All together, reference experiments (Fig. S1) together with FTIR and ellipsometry measurements as well as the color change upon APTMS-RITC and APTMS-FITC grafting, which in addition cannot be observed for planar, non-porous dense silica thin films (Fig. 2a, Fig. S3), indicate a successful attachment of APTMS-RITC and APTMS-FITC not only on the outer mesoporous silica film surface, but also to the mesopore walls representing the much larger inner surface area.

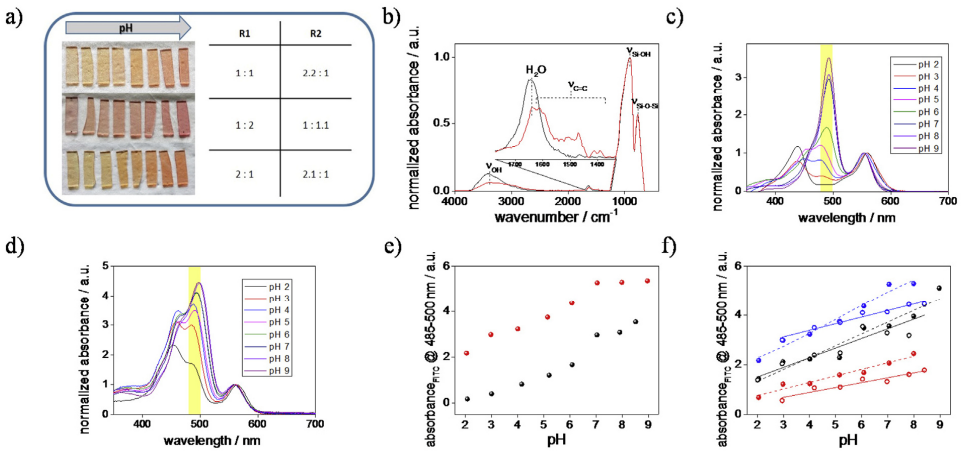

Fig. 2. a) Image of FMSF deposited on glass substrates in dependence of incubation solution pH between pH 2 and pH 9. R1: Ratio of APTMS-FITC: APTMS-RITC in the reaction solution, R2: calculated ratio of FITC: RITC on FMSFs. **b)** ATR-FTIR spectra of a FMSF with a APTMS-FITC: APTMS-RITC molar ratio of 10 : 1 in the reaction solution (red) in comparison to a bare mesoporous silica film (black). Both spectra are normalized to the stretching vibration of free silanol groups at 905 cm^{-1}. **c)** Absorption spectra of FITC: RITC = 2 : 1 in PBS buffer solution with varying pH. Absorption spectra are normalized to the absorption maxima of RITC at 560 nm. **d)** Absorption spectra of FMSF with a molar ratio of 2 : 1 with respect to APTMS-FITC and APTMS-RITC in the reaction solution in dependence of pH after CO_2-plasma treatment. Absorption spectra are normalized to the absorption maxima of RITC at 560 nm. **e)** Absorption maxima at 485–500 nm of FITC in dependence of pH of a FMSF with the molar ratio 2 : 1 (red) and in solution with a molar ratio of 2 : 1 (black). **f)** pH-dependent absorption maxima of FITC in FMSFs for molar ratios 1 : 1 (black), 1 : 2 (red) and 2 : 1 (blue) with respect to APTMS-FITC and APTMS-RITC in the reaction solution before (spheres, dashed line) and after CO_2-plasma treatment (circles, solid line). The CO_2 plasma treatment destroys attached dyes at the external planar mesoporous film surface. The absorption is recorded at a wavelength of 485–500 nm. Lines represent linear fits. (For interpretation of the references to color in this figure legend, the reader is referred to the Web version of this article.)

3.2. Spectral properties of FMSFs

The spectral properties of mesoporous thin films functionalized with APTMS-FITC and APTMS-RITC are investigated after grafting of different molar ratios APTMS-FITC: APTMS-RITC of 1 : 1, 1 : 2, 2 : 1 corresponding to the composition of the reaction solution resulting in grafted ratios between 1:1 to 2:1 (Fig. 2a). Functionalized mesoporous silica films (FMSFs) are treated with CO_2-plasma [28,51] to remove dyes attached on the outer silica surface. Spectral properties of the FMSFs are investigated via UV/vis absorption and fluorescence emission before and after CO_2-plasma treatment to compare FRET pair behavior attached exclusively on the inner mesopore wall surface with the ones attached to the planar outer surface. UV/vis absorption measurements show both absorption maxima of APTMS-FITC and APTMS-RITC at 500 nm and 560 nm (Fig. 2c and d) proving the attachment of both dyes in the inorganic framework while retaining their spectral properties.

Comparing the absorption maximum of APTMS-FITC at 500 nm before and after CO_2-plasma treatment results in a decreasing absorption of around 15% confirming that approximately 85% of the dyes are attached on the inner mesopore walls, as CO_2-plasma treatment only destroys the dyes at the outer planar surface (Fig. S6). Remarkably, most of the dyes are attached on the inner silica surface. UV/vis absorption spectra of CO_2-plasma treated dye functionalized mesoporous silica films are used to calculate the ratio of attached dyes according to Lambert-Beer's law. For calculations, extinction coefficients of FITC and RITC determined by Widmer et al. [42] are applied. The molar ratios of the dyes in the reaction solution (R1) as well as the ratios calculated from absorption spectra (R2) are compared in Fig. 2a. The attachment of APTMS-FITC is favored compared to APTMS-RITC for all applied experimental conditions.

To investigate the pH-dependence of the spectral dye properties, the FMSFs have been immersed in phosphate buffered solutions at pH between 2 and 9 for 15 min. An absorption color change of the dye functionalized silica films can be observed after incubation in different pH solutions as depicted in Fig. 2a. The spectral properties of fluorescein have been widely studied in the past. In aqueous solution fluorescein exists in four different prototropic forms depending on the solution pH [56,58]. These can be directly differentiated by pH-dependent UV/vis absorption studies of FITC in phosphate buffered solution (Fig. 2c) as described in the literature [62]. In solution the pH-dependent UV/vis spectra of FITC shown in Fig. 2c all expected forms, the cationic form at pH 2 (black spectrum), the zwitterionic chinoid or lactone form at pH 3 (red spectrum), the monoanionic form at pH 5 (magenta spectrum) and the dianionic form at pH 7 (marine spectrum), are observed. In contrast to the absorption spectra of FITC in solution, the absorption spectra of APTMS-FITC grafted to the CO_2-plasma treated mesoporous silica films do not show all prototropic forms (Fig. 2d). In the presence of buffer solution at pH 2, the cationic form cannot be observed. This probably indicates an influence of the mesopore's spatial confinement and a proton transfer between FITC and amine groups of unfunctionalized APTMS. Unfortunately, a determination of the relative amount of different prototropic forms is not possible due to overlapping absorption spectra. In addition, the absorption of APTMS-RITC reference dye at 560 nm does not change with pH (Fig. S4). This allows to use the absorption maximum of APTMS-RITC as reference. All absorption spectra are normalized to the APTMS-RITC absorption maximum at 560 nm. Comparing the evolution of the absorption maxima of FITC or APTMS-FITC at 485–500 nm an increase of the relative absorption of FITC in solution as well as of APTMS-FITC bound to the mesoporous silica film with increasing solution pH is observed. Furthermore, the pH-induced change of the relative FITC absorption shows a comparable behavior for FITC in solution and APTMS-FITC bound to the mesoporous silica film (Fig. 2e). Varying solution pH from pH 2 to pH 9 results in an almost linear increase by a factor of three of APTMS-FITC absorption at 485–500 nm relative to the

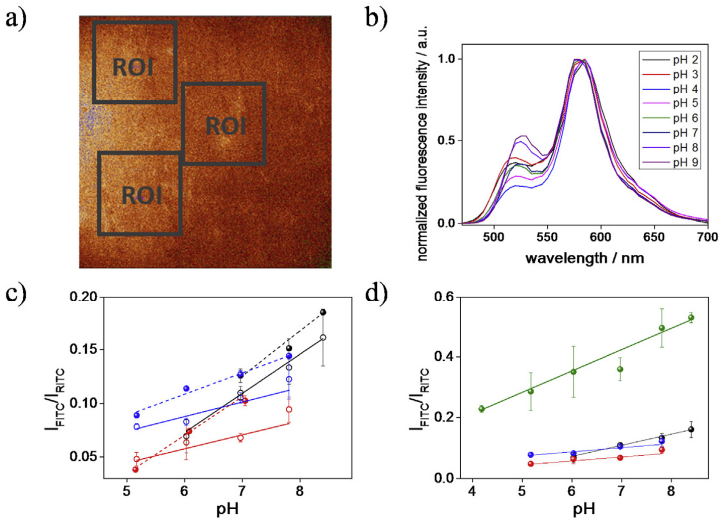

Fig. 3. a) Representative pseudocolor image (775 × 775 µm) from CLSM of a FMSF shown in a "glow over/glow under" lookup table with three chosen ROIs on homogeneous spots of the film. **b)** Fluorescence spectra of a FMSF after CO_2-plasma treatment with an APTMS-FITC: APTMS-RITC molar ratio of 10 : 1 in the reaction solution. Spectra are normalized to the emission maxima of APTMS-RITC at 585 nm. **c)** Linear dependence of fluorescence emission intensity on pH for FMSFs with APTMS-FITC: APTMS-RITC molar ratios of 1 : 1 (black), 1 : 2 (red) and 2 : 1 (blue) in the reaction solution before (spheres, dashed line) and after CO_2-plasma treatment (circles, solid line). The ratio between the fluorescence intensities of FITC at 520 nm and RITC at 585 nm is plotted in dependence of pH. **d)** Linear dependence of fluorescence emission intensity on pH detected using FMSFs functionalized with APTMS-FITC: APTMS-RITC molar ratios of 1 : 1 (black), 1 : 2 (red), 2 : 1 (blue) and 10 : 1 (green) in the reaction solution. (For interpretation of the references to color in this figure legend, the reader is referred to the Web version of this article.)

APTMS-RITC absorption at 560 nm for FMSFs showing the maintained pH-sensing properties of the FRET pair after covalent attachment. Comparing the pH-dependent absorption maxima of APTMS-FITC at 485–500 nm for FMSFs with different molar ratios of APTMS-FITC: APTMS-RITC before and after CO_2-plasma treatment (Fig. 2f), an overall decrease of the absorption intensity and a reduced change of APTMS-FITC absorption with pH is observed after destroying the dyes at the outer planar surface. This reduced relative APTMS-FITC absorption change with pH for dyes located inside the mesopores indicates a lower "pH" in the mesopores probably due to a confinement effect on local pH assuming no reduced APTMS-FITC: APTMS-RITC ratio inside the pores as compared to the outer planar surface. In any case, a pH-sensitive regime of up to six pH units for these mesopores is observed (Fig. 2).

Besides absorption, fluorescence emission based pH-detection using FRET in mesoporous thin films allows a ratiometric pH-detection inside mesopores. Fluorescence spectra are obtained using a confocal microscope, measuring three homogeneous regions of interest (ROI) on a FMSFs as depicted in Fig. 3a. Readout by confocal microscopy bares the future potential for local resolution and single pore detection. The fluorescence spectra of FMSFs show an emission maximum at 520 nm which can be attributed to APTMS-FITC as well as an emission maximum at 585 nm, attributed to APTMS-RITC (Fig. 3b). Since the excitation wavelength at 458 nm only overlaps with absorption of APTMS-FITC (donor), the observed APTMS-RITC (acceptor) fluorescence emission proofs the expected energy transfer from APTMS-FITC as the donor to APTMS-RITC as the acceptor. Additionally, the maximum fluorescence intensity of APTMS-RITC (585 nm) is significantly higher than the maximum fluorescence intensity of APTMS-FITC (520 nm) indicating an efficient energy transfer (Fig. S12). Consequently, both dyes, APTMS-FITC and APTMS-RITC, must be located close to each other within the mesopores. All fluorescence spectra recorded after immersion in buffer solution of pH 2 to pH 9 are normalized to the emission maximum of RITC at 585 nm followed by monitoring the pH-dependent evolution of the maximum emission of FITC at 520 nm. With increasing solution pH, from pH 2 to pH 9, an increasing fluorescence emission of the donor dye APTMS-FITC is observed showing a linear dependence of relative fluorescence intensity on pH as depicted in Fig. 3c. Interestingly, the pH-dependent regime is extended from two to three pH units upon changing the molar APTMS-FITC: APTMS-RITC ratio within the reaction solution from 1 : 1 to 1 : 2 (Fig. 3c). This is as well observed after CO_2-plasma treatment, indicating that the APTMS-FITC: APTMS-RITC concentration strongly determines the detectable pH-range, and that an excess of APTMS-FITC is necessary to allow FRET to occur while simultaneously detecting a broad pH-range. Comparing the fluorescence emission intensity before and after the CO_2-plasma treatment, a decrease of the overall fluorescence intensities is observed, in analogy to the observations made for the UV/vis absorption proving removal of dye from the outer planar FMSFs surface, as discussed above. After CO_2-plasma treatment a reduced change in fluorescence emission intensity upon pH-screening, in accordance with UV-vis absorption, is observed. This either indicates a higher amount of attached APTMS-FITC than of attached APTMS-RITC on the outer FMSFs surface than on the inner surface or a lower pH in the mesopores indicating a confinement effect on local pH. Overall, the fluorescence intensity of the emission maximum of APTMS-FITC at 520 nm is relatively small compared to the emission maximum of APTMS-RITC at 585 nm due to an efficient energy transfer, which limits experimental pH resolution as the donor dye is used for pH-detection. An enhanced resolution in fluorescence based pH detection is obtained improving FMSF's functionalization by using a molar ratio of APTMS-FITC: APTMS-RITC = 10 : 1 resulting in a grafted APTMS-FITC: APTMS-RITC ratio of 3 : 1 (Fig. S7). The fluorescence emission intensity of this functionalized FMSFs show a broad linear range of pH-dependent changes from pH 4 to pH 9 in fluorescence emission after CO_2-plasma (Fig. 3d). Additionally, an enhanced slope of pH-dependent relative maximum fluorescence emission intensity of APTMS-FITC is observed as compared to the FMSFs generated with APTMS-FITC: APTMS-RITC reaction solution ratios of 1 : 1, 1 : 2 and 2 : 1 resulting in a more precise determination of pH. Consequently, a higher ratio of APTMS-FITC to APTMS-RITC, achieved by increasing the APTMS-FITC ratio within the reaction solution, leads to an improved detection based on the fluorescence intensity monitoring the emission maximum of APTMS-FITC at 520 nm and the pH-detection range can be tuned varying the grafted APTMS-FITC to APTMS-RITC ratio.

In conclusion, FRET dye pair functionalization of mesoporous thin films can be used for pH-detection observing the absorption or fluorescence emission if the FRET pair consists of a pH-sensitive dye combined with a pH-insensitive reference dye both covalently grafted to the mesopore wall. Thereby, the range of pH detection by monitoring the

fluorescence emission is comparable to similar mesoporous silica nanoparticles [6], but the range of pH detection is extended to a broad range from pH 2 to pH 8 by observing the absorption of the FRET pair. An optimized detection with respect to magnitude of signal and relative ratio needs an optimization of the covalently attached dye ratio as well as consideration of preferred binding due to pore wall–dye interaction, molecular size, and competition with respect to pore accessibility and reaction with other molecules present in solution. Optimized detection is achieved by tuning the APTMS-FITC (donor, pH-sensitive) to APTMS-RITC (acceptor, reference dye) ratio such that only few APTMS-FITC (donor) molecules couple to APTMS-RITC (acceptor, reference) molecules to allow ratiometric detection but at the same time not to lose too much pH-sensitivity by FRET. In summary, 85% of the attached dyes are located within the mesopores (Fig. S6) probing "pH" in this confined space. Based on their absorption and fluorescence emission a linear detection regime of up to six pH units has been implemented after optimization of the functionalization procedure. Furthermore, comparing absorption and fluorescence with and without dyes present at the outer planar mesoporous film surface, the influence of the spatial mesopore confinement on "pH" can be observed. Finally, for these experiments only a single excitation wavelength is required and by using high resolution fluorescence microscopy techniques local information and single pore measurements are possible.

3.3. Correlation to ionic permselectivity of mesoporous thin films

The monitoring of protonation–deprotonation equilibria in mesopores is especially relevant to predict and design mesopore accessibility and transport. To the best of our knowledge, transport properties haven't been experimentally correlated with dye-based pH-sensing in mesoporous materials. To investigate the ionic transport properties of FMSFs, the diffusion of charged probe molecules through mesoporous films supported on ITO substrates is investigated using cyclic voltammetry (CV), monitoring anionic and cationic electroactive redox probes $[Fe(CN)_6]^{3-/4-}$ and $[Ru(NH_3)_6]^{2+/3+}$, respectively. The observed pH-dependent mesopore accessibility is correlated to FRET dye pair based pH-detection (Figs. 4 and 5). Due to the presence of unreacted silanol groups, amino groups, and covalently attached APTMS-RITC and APTMS-FITC at the silica pore wall, a pH-dependent charge of the pore wall, and thus ionic permselectivity of the mesoporous film is expected. In general, ionic permselectivity has been demonstrated for a variety of functionalized nanopores [1,32,33] and is mostly discussed with respect to gating of mesopore accessibility. Here, under acidic conditions,

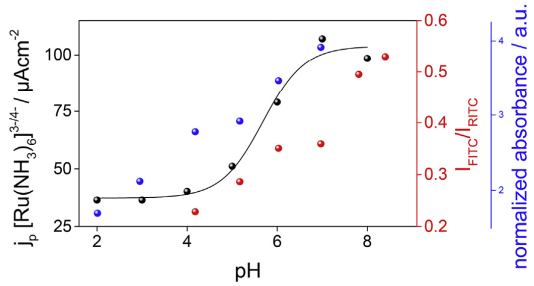

Fig. 5. pH-dependent maximum current density of the probe molecule $[Ru(NH_3)_6]^{3-/4-}$ (black spheres, sigmoidal fit) as well as pH-dependent fluorescence emission intensity (red spheres) and pH-dependent absorption maxima of FITC (blue spheres) for FMSF functionalized with a APTMS-FITC: APTMS-RITC molar ratio of 10 : 1 in the reaction solution. (For interpretation of the references to color in this figure legend, the reader is referred to the Web version of this article.)

protonated amino groups are expected to result in a positively charged mesopore wall whereas basic conditions are expected to result into deprotonated remaining silanol groups, deprotonated fluorescein, and deprotonated rhodamine B, and thus a negatively charged mesopore. As the mesopore diameter is in the range of the Debye screening length, equally charged ions should be electrostatically excluded and countercharged ions should access the pore or even be preconcentrated inside the mesopores. Redox probe molecules are oxidized and reduced below the mesoporous film at an ITO electrode and thus result in a current in the cyclic voltammogram. Cyclic voltammograms of a FMSF and unmodified mesoporous silica thin film recorded at different solution pH values are shown in Fig. 4a and b. As expected, the cyclic voltammograms of FMSFs show accessibility of negatively charged probe molecules under acidic conditions, whereas electrostatic exclusion of these negatively charged probe molecules is observed under basic conditions. The resulting pH-dependent peak current density is shown in Fig. 4b, d. Thereby, the enhanced peak current densities of the FMSF as compared to unmodified mesoporous silica and the broadened electrochemical response indicate a preconcentration of the negatively charged probe molecule $[Fe(CN)_6]^{3-/4-}$ within the functionalized mesoporous films due to attractive electrostatic interaction. At pH values above pH 5, deprotonation of remaining silanol groups as well as

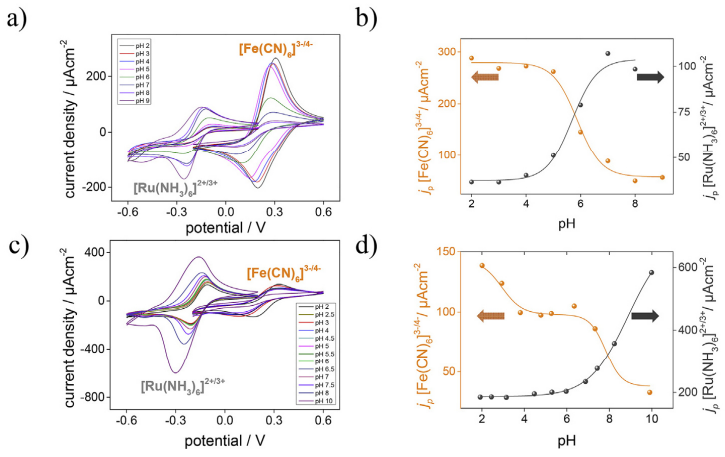

Fig. 4. a) Cyclic voltammograms (scan rate 100 mV/s) recorded in PBS buffer solution as supporting electrolyte at pH 2–10 using the redox active probe molecules $[Fe(CN)_6]^{3-/4-}$ (1 mM) and $[Ru(NH_3)_6]^{2+/3+}$ (1 mM) for a FMSF functionalized in presence of a APTMS-FITC: APTMS-RITC molar ratio of 10 : 1 in the reaction solution and **b)** its pH-dependent maximum current density of $[Fe(CN)_6]^{3-/4-}$ and $[Ru(NH_3)_6]^{2+/3+}$ reflecting mesopore accessibility. **c)** Cyclic voltammograms (scan rate 100 mV/s) recorded in PBS buffer solution as supporting electrolyte at pH 2–10 using the redox active probe molecules $[Fe(CN)_6]^{3-/4-}$ (1 mM) and $[Ru(NH_3)_6]^{2+/3+}$ (1 mM) for an unmodified mesoporous silica thin film and **d)** its maximum current density of $[Fe(CN)_6]^{3-/4-}$ and $[Ru(NH_3)_6]^{2+/3+}$ in dependence of pH reflecting mesopore accessibility. The lines in b) and c) represent sigmoidal fits.

APTMS-FITC molecules at the pore wall leads to an electrostatic repulsion of negatively charged molecules resulting in a pH-dependent decrease of peak current density down to electrostatic exclusion. Simultaneously, accessibility and preconcentration of the positively charged probe molecules are observed under these basic conditions, while an electrostatic exclusion of the positively charged probe molecule $[Ru(NH_3)_6]^{2+/3+}$ occurs in acidic environment. The peak current densities in dependence of pH result in titration curves with a sigmoidal shape (Fig. 4b). The inflection point of these curves at a pH value of 5.8 corresponds to the pK_a value which in case of mesoporous films should reflect the pK_a of the functionalized mesopores. The pK_a value of 5.8 is close to the monoanion/dianion transition of fluorescein reported in literature [57,58]. Comparing this pK_a value with the value obtained from titration of FITC with protons in buffer solution using the emission intensity at 515 nm (Fig. S11) a shift from pK_a 6.3 to 5.8 is observed. This shift of 0.5 pH units indicates the influence of the mesopore environment.

Comparing the maximum peak current density obtained from FMSFs to unmodified mesoporous silica thin films, a higher maximum peak current density is observed for FMSFs at acidic pH, whereas a lower maximum peak current density is observed for $[Fe(CN)_6]^{3-/4-}$ at basic pH. Consequently, the influence of remaining silanol groups seems to be less important for the observed transport properties of FMSFs than the free amine groups and dyes which is in accordance to the obtained pore filling after functionalization. Consistently, at pH > 5 higher $[Ru(NH_3)_6]^{2+/3+}$ peak current densities for the unmodified mesoporous silica thin film than for the FMSF are observed due to the electrostatic attraction and preconcentration of probe molecules in the negatively charged mesoporous silica film. Overall, the behavior of both probe molecules indicates, in accordance to dye-based monitoring discussed above, that the surface charge of FMSFs is dominated by the positively charged amino groups present on the wall surface at pH < 5 and remaining silanolate groups as well as deprotonated fluorescein and rhodamine B moieties at basic pH. Nevertheless, FMSFs show high ion permselectivity which can be tuned by varying pH as expected. This clearly shows that FRET dye pair functionalization is a suitable tool for “pH”-readout in mesopores, investigation of confinement effects, and its correlation to mesopores accessibility and allows application of FMSFs as sensors and membranes with gate like properties. But for pH-readout, and especially when it comes to local resolution, the influence of the dyes itself on the transport properties has to be considered as well. In this regard, a minimal functional density might be recommended as well supporting high resolution microscopy techniques for readout.

Combining the detected mesopore accessibility with FRET dye pair based pH readout shows that both pH-detection strategies, based on absorption and ratiometric FRET fluorescence emission, match the observed mesopore transport characteristics (Fig. 5). Furthermore, the confinement specific shifted pK_a value is reproduced supporting spatial influence on pore accessibility (CO_2-plasma treated films). This confirms the applicability of the installed in-situ pH-readout system based on APTMS-RITC and APTMS-FITC in silica mesopores, it represents a first step towards quantitative analysis of these shifts, and underlines the importance of knowing protonation-deprotonation equilibria and charge density of mesopores to understand their transport properties. Together with the possibility of using high resolution (confocal) microscopy techniques, single pore analysis is envisioned going beyond classical averaging information on surface pH. But it has to be noted as well, that the FRET dye pair not only serves for pH-readout but, in the applied concentration, clearly influences mesopore characteristics such as ionic permselectivity. However, molecular pH-readout based on FRET-pair absorption and fluorescence emission correlates well with the observed ionic permselectivity and thus represents optical means to detect charge state of mesopores and to optically detect transport of nanoporous materials.

4. Conclusions

With this study we provide a systematic strategy to optimally combine mesoporous silica films with a pH-sensitive FRET dye pair allowing to exclusively functionalize the mesopore wall after destroying the dyes at the external planar film surface. Thereby, approximately 85% of the dyes are located at the mesopore walls and not on the outer mesoporous film surface. Systematic variation of APTMS-RITC: APTMS-FITC ratio in the reaction solution and analysis of resulting absorption spectra indicate that grafting of APTMS-FITC is favored compared to grafting of APTMS-RITC. After optimization of dye grafting and destroying the dyes on the external mesoporous film surface, a pH-dependent linear detection regime of up to six pH units is obtained monitoring absorption or fluorescence emission of FMSFs. Thereby, the optimized pH detection range of six pH units is obtained for FMSFs prepared with a APTMS-FITC: APTMS-RITC ratio of 10 : 1 in the reaction solution resulting in a grafted ratio of 3 : 1 indicating an optimized pH detection with an access of APTMS-FITC (pH-sensitive, FRET donor). The detected “pH” by FRET dye pair absorption or fluorescence emission correlates well with the pH-dependent ionic permselectivity detected by cyclic voltammetry as well reproducing the expected confinement-based pK_a shift of mesopores as compared to solution pKa. This confirms the importance of monitoring protonation-deprotonation equilibria and charge density of mesopores to understand their transport properties especially for complex functional pores such as responsive or gradient-functionalized mesopores. In addition, this study shows the versatility of FRET dye pairs consisting of a pH-sensitive dye and a pH-insensitive reference dye to monitor protonation-deprotonation equilibria in spatially confined nanopores but as well emphasizes the need for optimization of functional density of FRET dye pairs, e.g. to reduce the influence of the dye probe molecules on the mesopores characteristics itself. For further investigation of pH differences in mesopores with respect to bulk solution, and direct monitoring of pH even in single pores, low functional dye densities and ratiometric dyes are envisioned, and are currently under investigation.

Acknowledgements

We kindly acknowledge the financial support by the LOEWE Research Cluster “iNAPO” of the Hessen State Ministry of Higher Education, Research and the Arts. Mrs. Kunz and Prof. Dr. Achim Kleebe (TU-Darmstadt) are acknowledged for their support with TEM measurements. We also thank Prof. Dr. Wolfgang Ensinger for providing access to profilometer measurements in the department of material science (TU Darmstadt).

Appendix A. Supplementary data

Supplementary data to this article can be found online at https://doi.org/10.1016/j.micromeso.2019.03.009.

References

[1] A. Walcarius, Mesoporous materials and electrochemistry, Chem. Soc. Rev. 42 (9) (2013) 4098–4140.
[2] C.J. Brinker, et al., Evaporation-induced self-assembly: nanostructures made easy, Adv. Mater. 11 (7) (1999) 579–585.
[3] I.G. Shenderovich, et al., Pyridine-15N a mobile NMR sensor for surface acidity and surface defects of mesoporous silica, J. Phys. Chem. B 107 (43) (2003) 11924–11939.
[4] N. Pal, A. Bhaumik, Soft templating strategies for the synthesis of mesoporous materials: inorganic, organic–inorganic hybrid and purely organic solids, Adv. Colloid Interface Sci. 189–190 (Supplement C) (2013) 21–41.
[5] J. Salonen, et al., Mesoporous silicon microparticles for oral drug delivery: loading and release of five model drugs, J. Control. Release 108 (2–3) (2005) 362–374.
[6] J. Lei, L. Wang, J. Zhang, Ratiometric pH sensor based on mesoporous silica nanoparticles and Forster resonance energy transfer, Chem. Commun. (Camb) 46 (44) (2010) 8445–8447.
[7] L. Malfatti, et al., Nanocomposite mesoporous ordered films for lab-on-chip intrinsic

surface enhanced Raman scattering detection, Nanoscale 3 (9) (2011) 3760–3766.
[8] A. Vaseashta, D. Dimova-Malinovska, Nanostructured and nanoscale devices, sensors and detectors, Sci. Technol. Adv. Mater. 6 (3–4) (2005) 312–318.
[9] M.H. Sun, et al., Applications of hierarchically structured porous materials from energy storage and conversion, catalysis, photocatalysis, adsorption, separation, and sensing to biomedicine, Chem. Soc. Rev. 45 (12) (2016) 3479–3563.
[10] A. Brunsen, et al., Manipulation of molecular transport into mesoporous silica thin films by the infiltration of polyelectrolytes, Langmuir 27 (8) (2011) 4328–4333.
[11] K.K. Unger, et al., Liquid chromatography-its development and key role in life science applications, Angew. Chem. Int. Ed. 49 (13) (2010) 2300–2312.
[12] K.K. Unger, A.I. Liapis, Adsorbents and columns in analytical high-performance liquid chromatography: a perspective with regard to development and understanding, J. Sep. Sci. 35 (2012) 1201–1212.
[13] C. Giménez, et al., Towards chemical communication between gated nanoparticles, Angew. Chem. Int. Ed. 53 (2014) 12629–12633.
[14] M. Benezra, et al., Multimodal silica nanoparticles are effective cancer-targeted probes in a model of human melanoma, J. Clin. Investig. 121 (2011) 2768–2780.
[15] J. Murison, et al., Wetting heterogeneities in porous media control flow dissipation, Phys. Rev. Appl. 2 (2014) 034002.
[16] R. Fan, et al., Gated proton transport in aligned mesoporous silica films, Nat. Mater. 7 (4) (2008) 303–307.
[17] L. Feng, et al., A super-hydrophobic and super-oleophilic coating mesh film for the separation of oil and water, Angew. Chem. Int. Ed. Engl. 43 (15) (2004) 2012–2014.
[18] G. Kwon, et al., On-demand separation of oil-water mixtures, Adv. Mater. 24 (27) (2012) 3666–3671.
[19] K. Leung, I.M.B. Nielsen, L.J. Criscenti, Elucidating the bimodal acid-base behavior of the water-silica interface from first principles, J. Am. Chem. Soc. 131 (2009) 18358–18365.
[20] M.L. Hair, W. Hertl, Acidity of surface hydroxyl groups, J. Phys. Chem. 74 (1970) 91–94.
[21] J.M. Rosenholm, et al., On the nature of the brønsted acidic groups on native and functionalized mesoporous siliceous SBA-15 as studied by benzylamine adsorption from solution, Langmuir 23 (2007) 4315–4323.
[22] M. Tagliazucchi, O. Azzaroni, I. Szleifer, Responsive polymers end-tethered in solid-state nanochannels: when nanoconfinement really matters, J. Am. Chem. Soc. 132 (2010) 12404–12411.
[23] L. Silies, et al., Mesoporous thin films, zwitterionic monomers, and iniferter-initiated polymerization: polymerization in a confined space, Chem. Mater. 27 (6) (2015) 1971–1981.
[24] A. Andrieu-Brunsen, et al., Mesoporous hybrid thin film membranes with PMETAC@silica architectures: controlling ionic gating through the tuning of polyelectrolyte density, Chem. Mater. 27 (3) (2015) 808–821.
[25] J. Tom, et al., Optimisation of surface-initiated photoiniferter-mediated polymerisation under confinement, and the formation of block copolymers in mesoporous films, Polymers 9 (10) (2017) 539.
[26] M.R. Banghart, et al., Photochromic blockers of voltage-gated potassium channels, Angew. Chem. Int. Ed. Engl. 48 (48) (2009) 9097–9101.
[27] A. Brunsen, et al., Proton and calcium-gated ionic mesochannels: phosphate-bearing polymer brushes hosted in mesoporous thin films as biomimetic interfacial architectures, Langmuir 28 (7) (2012) 3583–3592.
[28] F. Krohm, et al., Photochromic spiropyran- and spirooxazine-homopolymers in mesoporous thin films by surface initiated ROMP, J. Mater. Chem. C 4 (18) (2016) 4067–4076.
[29] G. Wang, et al., Photon gated transport at the glass nanopore electrode, J. Am. Chem. Soc. 128 (2006) 13553–13558.
[30] K. Xiao, L. Wen, L. Jiang, Biomimetic solid-state nanochannels: from fundamental research to practical applications, Small 12 (2016) 2810–2813.
[31] K. Xiao, et al., Construction and application of photoresponsive smart nanochannels, J. Photochem. Photobiol. C: Photochem. Rev. 26 (2016) 31–47.
[32] S. Alberti, G.J.A.A. Soler-Illia, O. Azzaroni, Gated supramolecular chemistry in hybrid mesoporous silica nanoarchitectures: controlled delivery and molecular transport in response to chemical, physical and biological stimuli, Chem. Commun. 51 (2015) 6050–6075.
[33] G.J.A.A. Soler-Illia, O. Azzaroni, Multifunctional hybrids by combining ordered mesoporous materials and macromolecular building blocks, Chem. Soc. Rev. 40 (2) (2011) 1107–1150.
[34] A. Calvo, et al., Mesoporous aminopropyl-functionalized hybrid thin films with modulable surface and environment-responsive behavior, Chem. Mater. 20 (14) (2008) 4661–4668.
[35] L. Silies, A. Andrieu-Brunsen, Programming ionic pore accessibility in zwitterionic polymer modified nanopores, Langmuir 34 (2017) 807–816 https://pubs.acs.org/doi/abs/10.1021/acs.langmuir.7b00529.
[36] F.M. Gilles, et al., Ionic conductance of polyelectrolyte-modified nanochannels: nanoconfinement effects on the coupled protonation equilibria of polyprotic brushes, J. Phys. Chem. C 120 (9) (2016) 4789–4798.
[37] G.S. Longo, M.O. de la Cruz, I. Szleifer, Molecular theory of weak polyelectrolyte thin films, Soft Matter 8 (5) (2012) 1344–1354.
[38] G.S. Longo, M. Olvera de la Cruz, I. Szleifer, Molecular theory of weak polyelectrolyte gels: the role of pH and salt concentration, Macromolecules 44 (2011) 147–158.
[39] D. Wang, et al., How and why nanoparticle's curvature regulates the apparent pK(a) of the coating ligands, J. Am. Chem. Soc. 133 (7) (2011) 2192–2197.
[40] L. Silies, et al., Insights into the role of counterions on polyelectrolyte-modified nanopore accessibility, Langmuir 34 (20) (2018) 5943–5953.
[41] H.S. Peng, et al., A nanogel for ratiometric fluorescent sensing of intracellular pH values, Angew. Chem. Int. Ed. Engl. 49 (25) (2010) 4246–4249.
[42] S. Widmer, et al., Incorporation of a FRET dye pair into mesoporous materials: a comparison of fluorescence spectra, FRET activity and dye accessibility, Analyst 140 (15) (2015) 5324–5334.
[43] C. Chiappini, et al., Mapping local cytosolic enzymatic activity in human esophageal mucosa with porous silicon nanoneedles, Adv. Mater. 27 (35) (2015) 5147–5152.
[44] C. Chiappini, et al., Biodegradable nanoneedles for localized delivery of nanoparticles in vivo: exploring the biointerface, ACS Nano 9 (5) (2015) 5500–5509.
[45] T. Förster, Zwischenmolekulare Energiewanderung und Fluoreszenz, Ann. Phys. 437 (1–2) (1948) 55–75.
[46] D. Bottenus, et al., Experimentally and theoretically observed native pH shifts in a nanochannel array, Lab Chip 9 (2) (2009) 219–231.
[47] C. Thörn, et al., A method to measure pH inside mesoporous particles using protein-bound SNARF1 fluorescent probe, Microporous Mesoporous Mater. 165 (2013) 240–246.
[48] S. Zhu, W. Lin, L. Yuan, Development of a ratiometric fluorescent pH probe for cell imaging based on a coumarin–quinoline platform, Dyes Pigment. 99 (2) (2013) 465–471.
[49] Y.-P. Chen, et al., Surface charge effect in intracellular localization of mesoporous silicananoparticles as probed by fluorescent ratiometric pH imaging, RSC Adv. 2 (3) (2012) 968–973.
[50] A. Calvo, et al., Chemical reactivity of amino-functionalized mesoporous silica thin films obtained by co-condensation and post-grafting routes, Microporous Mesoporous Mater. 121 (1–3) (2009) 67–72.
[51] D.J. Babu, et al., Carbon dioxide plasma as a versatile medium for purification and functionalization of vertically aligned carbon nanotubes, J. Phys. Chem. C 118 (22) (2014) 12028–12034.
[52] D. Dey, et al., Development of an ion-sensor using fluorescence resonance energy transfer, Sensor. Actuator. B Chem. 195 (2014) 382–388.
[53] A. Burns, H. Ow, U. Wiesner, Fluorescent core-shell silica nanoparticles: towards "Lab on a Particle" architectures for nanobiotechnology, Chem. Soc. Rev. 35 (11) (2006) 1028–1042.
[54] J. Peng, et al., Noninvasive monitoring of intracellular pH change induced by drug stimulation using silica nanoparticle sensors, Anal. Bioanal. Chem. 388 (3) (2007) 645–654.
[55] C.-J. Tsou, Y. Hung, C.-Y. Mou, Hollow mesoporous silica nanoparticles with tunable shell thickness and pore size distribution for application as broad-ranging pH nanosensor, Microporous Mesoporous Mater. 190 (2014) 181–188.
[56] M.M. Martin, L. Lindqvist, THE pH DEPENDENCE OF FLUORESCEIN FLUORESCENCE, J. Lumin. 10 (1975) 381–390.
[57] N. Klonis, et al., Spectral properties of fluorescein in solvent-water mixtures: applications as a probe of hydrogen bonding environments in biological systems, J. Photochem. Photobiol. 67 (5) (1998) 500–510.
[58] R. Sjoback, J. Nygren, M. Kubista, Absorption and fluorescence properties of fluorescein, Spectrochim. Acta A 51 (6) (1995) L7–L21.
[59] L. Stryer, Fluorescence energy transfer as a spectroscopic ruler, Ann. Rev. Biochem. 47 (1978) 819–846.
[60] C. Boissiere, et al., Porosity and mechanical properties of mesoporous thin films assessed by environmental ellipsometric porosimetry, Langmuir 21 (26) (2005) 12362–12371.
[61] P. Innocenzi, Infrared spectroscopy of sol-gel derived silica-based films: a spectra-microstructure overview, J. Non-Cryst. Solids 316 (2–3) (2003) 309–319.
[62] N. Klonis, W.H. Sawyer, Spectral properties of the prototropic forms of fluorescein in aqueous solution, J. Fluoresc. 6 (3) (1996) 147–157.

4.5. Polymerfunktionalisierung zur Herstellung von responsiven Ti_2CT_x-PDMAEMA MXen-Materialien

Neben der Funktionalisierung mesoporöser Filme stellte sich im Verlauf der Arbeit in einer Kooperation mit Minh Hai Tran (AG Birkel, TU Darmstadt) die Herstellung von stimuliresponsiven MXen-Hybridmaterialien als interessante und komplementäre Anwendung für Iniferter-initiierte Polymerisationen heraus. Neben mesoporösen Silicafilmen gibt es viele und auch relativ neue Materialien mit interessanten nanoskaligen Strukturen, deren Eigenschaften durch kontrollierte Polymerfunktionalisierung gesteuert werden können. Ein Beispiel sind die genannten MXene. Diese relativ jungen Materialien (bekannt seit ca. 10 Jahren) folgen der Zusammensetzung $M_{n+1}X_nT_x$ und zeigen z. B. interessante Leitfähigkeitseigenschaften auf (für detailliertere Informationen siehe Kapitel 2.6). Interessanterweise gibt es kaum Arbeiten zur Kombination von MXenen und kovalent angebundenen Polymerfunktionalisierungen. In Kooperation mit der AG Birkel (Arizona State University, TU Darmstadt), die Ti_2CT_x MXene herstellt und inspiriert durch Arbeiten von *Chen et al.*, denen es erstmals 2015 gelungen ist, eine kovalente Polymerfunktionalisierung auf MXenen anzubringen,[197] sollte untersucht werden, ob analog zu Polymerisationsmethoden für andere anorganische Oberflächen durch *grafting from* temperatursteuerbare MXen-Hybridmaterialien herstellbar sind.

Hierzu musste im ersten Schritt das MXen aus der korrespondierenden Ti_2AlC MAX-Phase hergestellt werden. Diese Arbeiten wurden von Minh Hai Tran (AG Birkel) durchgeführt. Im zweiten Schritt wurde die Responsivität über die Polymerfunktionalisierung eingebracht, wobei das Polymer auf der Oberfläche verankert werden sollte. Um möglichst große Mengen an Polymer aufzubringen und damit eine möglichst effiziente Schaltung zu ermöglichen, bietet sich eine *grafting from* Polymersiationsmethode wie die SI-PIMP an. Der SBDC Iniferter kann an die beim Ätzverfahren entstehenden OH-Gruppen der MXen-Oberfläche kovalent angebunden werden. Verglichen mit freien radikalischen Polymerisationsmethoden ermöglicht die SI-PIMP grundsätzlich eine besser einstellbare Polymermenge auf der Oberfläche. Für die Polymerisation wurde als Monomer DMAEMA ausgewählt, da PDMAEMA sowohl thermo- als auch pH-responsiv ist. Um die Polymerisation zu verifizieren, wurden von Karl Kopp (AG Hess, TU Darmstadt) XPS-Messungen durchgeführt, welche in Kombination mit REM- und TGA-Messungen eine vollständige Ummantelung der MXEN-*Flakes* mit Polymer nachweisen konnten. Die erhaltenen funktionalisierten MXene wurden anschließend als Film auf Glasträger aufgebracht, um bei Temperaturen unterhalb und oberhalb der *lower critical solution temperature* (LCST) von PDMAEMA (30-40 °C) die Leitfähigkeit der funktionalisierten und unfunktionalisierten MXen-Filme zu messen. Der experimentell bestimmte, starke Einfluss der Polymerfunktionalisierung auf die temperaturabhängige Leitfähigkeit der MXene konnte zusätzlich durch DFT-Kalkulationen der AG Zhuang (Arizona State University) untermauert werden.

Mein Beitrag zu dieser Veröffentlichung bestand in der Funktionalisierung der MXene zunächst mit dem Iniferter SBDC, sowie die anschließende Polymerfunktionalisierungmit PDMAEMA, deren Optimierung und Charakterisierung mittels TGA.

Die Ergebnisse dieses Abschnittes wurden bei ***ACS Applied Nano Materials*** veröffentlicht:

M. H. Tran*, R. Brilmayer*, L. Liu, H. Zhang, C. Hess, A. Andrieu-Brunsen, C. Birkel, **Synthesis of a smart hybrid MXene with switchable conductivity**, *ACS Applied Nano Materials,* **2020**.
*These authors contributed equally to this work

Die *Supporting Information* ist nicht abgedruckt, aber in der elektronischen Version dieses Artikels (DOI: 10.1016/j.micromeso.2019.03.009) verfügbar.

ACS APPLIED NANO MATERIALS

www.acsanm.org Article

Synthesis of a Smart Hybrid MXene with Switchable Conductivity for Temperature Sensing

Minh H. Tran, Robert Brilmayer, Lei Liu, Houlong Zhuang, Christian Hess, Annette Andrieu-Brunsen, and Christina S. Birkel*

Cite This: https://dx.doi.org/10.1021/acsanm.0c00118 Read Online

ACCESS | Metrics & More | Article Recommendations | Supporting Information

ABSTRACT: Inorganic−organic hybrid materials offer a wide variety of intriguing properties by combining their different characteristics and (chemical/physical) behavior, and the resulting smart materials find potential applications in areas such as energy technologies and drug delivery systems. Especially responsive two-dimensional carbides that belong to the class of MXenes benefit from this additional functionality in combination with their unique mechanical and electronic properties and bare potential for use as catalysts and sensors. Here, we therefore graft a stimuli-responsive polymer (poly(2-(dimethylamino)ethyl methacrylate (PDMAEMA)) from the surface of a Ti-based two-dimensional carbide (MXene) using the OH groups on the MXene surface as a linker for the organic molecules. Successful fabrication of the hybrid material as well as covalent bonding between the inorganic component and the thermoresponsive polymer is shown by X-ray powder diffraction, IR and X-ray photoelectron spectroscopy, thermal analysis, and electron microscopy. We further demonstrate a reversible change of conductivity of thin films of this smart hybrid material using temperature as an external stimulus and enhance the mechanistic understanding by density functional theory (DFT) calculations. Such systems could therefore be used as temperature sensors in chemical reactions or microelectronics.

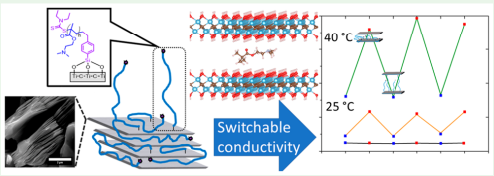

KEYWORDS: *stimuli-responsive material, switchable material, inorganic−organic hybrid, MXene, two-dimensional carbide, thermoresponsive, PDMAEMA*

INTRODUCTION

The interest in two-dimensional transition-metal-based carbides (and nitrides), so-called MXenes, has increased tremendously over the past few years due to their unique morphologies and remarkable mechanical and electronic properties. They possess good chemical stability and are hydrophilic as well as metallic and therefore very attractive candidates for several applications, such as energy storage, photo- or electrocatalysis, electromagnetic interference shielding, chemical sensors, water purification, and biomedicine.[1−4] Their potential grows significantly if these attractive intrinsic properties are coupled with additional functionalities, such as responsive/switchable ("smart") behavior.

Inorganic−organic hybrid materials possess intriguing properties since they combine characteristics and (chemical) behavior of two contrasting "worlds". While the inorganic component might be mechanically or chemically stable and therefore offers resistance toward stress or corrosion, for example, the organic component can add enhanced processability and biocompatibility to the resulting hybrid compound. As another example, polymers with stimuli-responsive properties change one of their properties in response to an external stimulus, such as light, temperature, stress, pressure, or electrical/magnetic field. If this behavior is reversible, these compounds are considered to possess switchable properties. The resulting "smart" materials have demonstrated promising behavior as catalysts, sensors, or drug carriers.[5]

Generally, MXenes are obtained by selective elimination of the A layer of the ternary parent MAX phase ($M_{n+1}AX_n$, n = 1, 2, 3). These MAX phases crystallize in a hexagonal layered crystal structure with alternating layers of M_6X octahedra and the A element along the c-axis.[6] The different bonding strength between M−X and M−A elements allows the selective etching of the A element with aqueous hydrofluoric acid. The exfoliation with hydrofluoric acid leads to two-dimensional structures whose surfaces are terminated with fluorine, oxygen, and hydroxyl groups (denoted as T_x in the general formula Ti_2CT_x, for example).[7]

These surface groups play a major role for the properties and applications of the MXenes.[8−11] Zha et al. performed DFT calculations and found that MXenes with oxygen-terminated

Received: January 14, 2020
Accepted: March 24, 2020
Published: March 24, 2020

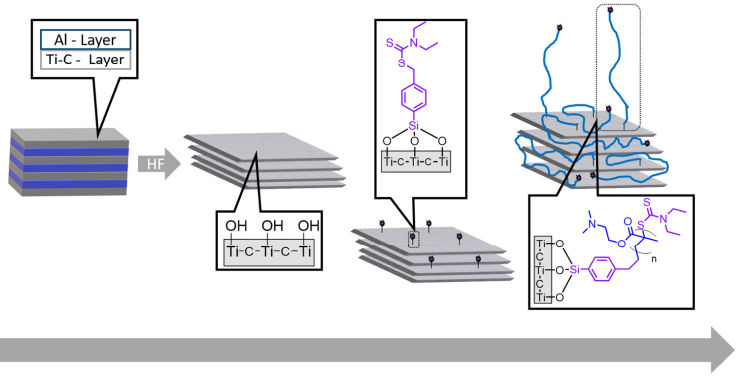

Figure 1. Schematic route to prepare a PDMAEMA/MXene hybrid material starting from the parental Ti_2AlC MAX phase. After preparation of the MAX phase Ti_2AlC, the aluminum is chemically removed to form the Ti_2CT_x MXenes. In the following step the SBDC iniferter is grafted onto the Ti−OH groups that are located on the surface of the MXen sheets. In the last step the polymerization is initiated from the SBDC-functionalized MXen surface to form the PDMAEMA-Ti_2CT_x hybrid material.

surfaces exhibit smaller lattice parameters in the *xy*-plane but have a stronger mechanical strength compared to MXenes terminated with fluorine or hydroxyl groups.[8] Besides that, Khazaei et al. performed theoretical studies on the geometric and electronic properties of MXenes in dependence of the surface functionality. In general, fully terminated MXenes are mechanically and thermodynamically stable and show semiconducting (Sc_2CF_2, $Sc_2C(OH)_2$, Sc_2CO_2, Ti_2CO_2, Zr_2CO_2, and Hf_2CO_2) or ferromagnetic (Cr_2CF_2 and $Cr_2C(OH)_2$) behavior.[10]

Furthermore, the hydroxyl surface groups can be utilized as anchors to graft organic molecules onto the MXene surface. More specifically, the 2D carbides can be functionalized with polymers which opens up the path to promising inorganic/organic hybrid structures that are mechanically stable as a result of the MXene "core". The group of Wang and Shi grafted imidazolium brushes on a $Ti_3C_2T_x$ MXene and embedded the functionalized MXene into a chitosan matrix to fabricate a hybrid alkaline anion exchange membrane with boosted thermal and mechanical stabilities and a significant increase of the ion exchange capacity.[12] Beyond that, Chen et al. successfully grafted brushes of a temperature-responsive polymer onto V_2CT_x, creating a "smart", i.e. switchable, MXene material.[13] They used the temperature-dependent behavior of poly(2-(dimethylamino)ethyl methacrylate) (PDMAEMA) and attached it through photografting and photopolymerization onto the MXene surface. Investigation of their hybrid MXene in suspension showed a reversible dependence of the transmittance and conductivity due to the thermal and CO_2 responsive behavior.

Inspired by the potential of smart MXenes, we have developed a strategy to grow the thermoresponsive PDMAEMA on a Ti-based MXene (Ti_2CT_x) through surface-initiated controlled photoiniferter polymerization (SIPIP) (see Figure 1). We demonstrate that a thin film of the MXene−PDMAEMA hybrid material exhibits a temperature-dependent change of the conductivity that is far more pronounced than the conductivity change in pristine Ti_2CT_x. These structures could therefore be used for temperature sensing during chemical reactions or for the temperature control of microelectronics.

Density functional theory (DFT) calculations further support that the PDMAEMA between the carbide sheets is responsible for the switchable conductivity of the hybrid material and therefore proves our proposed mechanism.

Hence, for the first time we combine controlled polymerization with a Ti-based MXene, prepare thin films of the resulting hybrid material, and provide a mechanistic understanding of the switchable conductivity.

EXPERIMENTAL SECTION

Synthesis of MXene Ti_2CT_x. MAX phase Ti_2AlC that served as the precursor for the MXene Ti_2CT_x was prepared by microwave heating, a technique that we have previously used for the synthesis of Cr- and V-based MAX phases.[14,15] Briefly, titanium (>99.5%, −200 mesh, Alfa Aesar), aluminum (>99.5, −325 mesh, Alfa Aesar), and carbon (99.9995%, APS 2−15 μm, Alfa Aesar) powders were mixed in a 2:1.3:1 molar ratio by using an agate mortar inside an Ar-filled glovebox. The mixture was pressed into a cylindrical pellet (5 t for 30 s, hydraulic press from Specac) with a diameter of 1.1 cm and a thickness of 0.3 cm. The resulting pellet was sealed into an evacuated quartz ampule that was surrounded by 7 g of graphite granules (Grüssing, acting as a susceptor) and placed inside an insulation housing inside the microwave chamber (CEM, Mars 6). The precursor mixture was heated at a power level of 1000 W which corresponds to 1200 °C (measured with an infrared thermometer from Optris GmbH) for 30 min. After cooling to room temperature, the pellet was ground into a fine powder by an agate mortar. For the chemical exfoliation of the MAX phase, 0.1 g of Ti_2AlC was added to 10 mL of concentrated HF (40%) and stirred for 4 h. The temperature did not increase and remained at room temperature during the exfoliation process.

The resulting product was collected by centrifugation (5000 rpm, Heraeus) and subsequently washed with deionized (DI) water until the remaining solution was neutral (six times). The resulting Ti_2CT_x was dried overnight at 80 °C inside a drying oven (Heraeus, Typ T 6030).

Note that working with hydrofluoric acid (HF) requires particular care and equipment (PTFE beakers and tubes and calcium gluconate gel needs to be accessible nearby in case of an accident).

Synthesis of *N,N*-(Diethylamino)dithiocarbamoylbenzyl-(trimethoxy)silane) (SBDC). SBDC was prepared as previously reported.[16,17] Sodium *N,N*-diethyldithiocarbamate trihydrate (STC, Sigma-Aldrich ACS reagent) was recrystallized from methanol to remove insoluble impurities. The purified STC (1.71 g, 10.00 mmol)

https://dx.doi.org/10.1021/acsanm.0c00118
ACS Appl. Nano Mater. XXXX, XXX, XXX−XXX

was dissolved in dry tetrahydrofuran (THF) (10 mL, anhydrous, Sure/Seal, Sigma-Aldrich) before being dropped to a solution of *p*-(chloromethyl)phenyltrimethoxysilane (2.12 g, 8.59 mmol, 95%, abcr GmbH) in dry THF (10 mL) under inert Schlenk line conditions. The solution was then stirred at room temperature for 4 h before being filtered to remove the sodium chloride and dried under reduced pressure to remove the THF to yield 2.41 g of SDBC as a pale yellow liquid (78% crude yield).

DMAEMA Functionalization of Ti_2CT_x. 9.8 mg of Ti_2CT_x was dried at the Schlenk line with reduced pressure (roughly 10^{-3} bar). 190 mg of SBDC was dissolved in 13 mL of dry Toluol (>99.5%, AnalaR NORMAPUR ACS, VWR GmbH) before being added to the MXene powder under a nitrogen atmosphere. The obtained suspension was stirred carefully at 80 °C for 90–120 min. After the thermal treatment the obtained product was centrifuged and washed multiple times with Toluol and THF.

For the polymer functionalization 5 mL of destabilized DMAEMA (contains 700–1000 ppm hydroquinone monomethyl ether as inhibitor, 98% Sigma-Aldrich) was dissolved in 5 mL of DMF (anhydrous, 99,8%, Sure/Seal, Sigma-Aldrich). The solution was added to the MXene powder which was dried prior under reduced pressure, and the suspension was degassed with nitrogen for 5 min. The polymerization solution was then irradiated with UV-light (320–400 nm, a Lumatec UV-Technik Superlite 410 lamp was used as the light source in a distance of 3 cm to the polymerization flask) for 30–40 min until the solution became viscous. After the treatment the hybrid MXene was centrifuged, washed multiple times with THF, and dried overnight at room temperature.

Characterization. For the X-ray powder diffraction measurements, small amounts of the powder samples were ground and loaded onto a flat plat holder. The measurement was performed in transmission using Cu radiation with a Stadi-P powder diffractometer (Stoe & Cie GmbH Darmstadt). Powder samples were prepared on carbon adhesive discs for the scanning electron microscopy (Philips, XL30 FEG) measurements.

The IR data were collected via an ATR (attenuated total reflectance) attachment on the Nicoleta 6700 FT-IR (Thermofisher Scientific). This enables the sample to be directly measured in powder form without further preparation. XP spectra were recorded on a SSX 100 ESCA spectrometer (Surface Science Laboratories Inc.) equipped with a monochromatic Al Kα X-ray source (100 W). As sample preparation, the MXene powder was pressed in an indium foil of 0.127 mm thickness (99.99%, from abcr). The XPS analysis reveals peaks at around 102, 197, 285, 401, 455, 530, 685, and 1071 eV, which are attributed to Si 2p, Cl 2p, C 1s, N 1s, Ti 2p, O 1s, F 1s, and Na 1s photoemissions, respectively.[18]

To measure the conductivity, the hybrid material was suspended with a tiny amount of distilled water until a gel-like suspension was obtained. This was used to coat a glass substrate. The resulting film was dried at room temperature. Two pin electrodes (PCE–PHD 1, PCE instrument) were brought into contact with the film surface, and the measurement setup was placed in a climate chamber (Binder APT.lineTM KBF) where a constant temperature and humidity level is assured. Prior to the measurement, the thin film was wetted with a buffer solution of pH = 9 (pK_xvalue of PDMAEMA polymer is 6.9).[19] This pH value was chosen because at pH = 9 the polymer chain is expected to be neutral, and thus the observed conductivity changes are only due to the temperature-induced conformation changes. Conductivity measurements were performed at 25 and 40 °C after holding the respective temperature for at least 5 min. All measurements were repeated several times.

DFT Calculations. We used the Vienna Ab-initio Simulation Package (VASP) to perform the density functional theory (DFT) calculations.[20,21] The exchange-correlation functional was based on the generalized gradient approximation (GGA) with the Perdew–Burke–Ernzerhof (PBE) parametrizations.[22] For the potential data sets, we treat the 1s electron of H, $2s^2$ and $2p^2$ electrons of C, $2s^2$ and $2p^3$ electrons of N, $2s^2$ and $2p^4$ electrons of O, and $3d^3$ and $4s^1$ electrons of Ti as valence electrons. These potentials were generated from the projector-augmented wave (PAW) method.[23,24] All the plane waves with a kinetic energy smaller than 500 eV were included into the basis sets. We used Γ-centered 9 × 9 × 1 and 1 × 1 × 1 Monkhorst–Pack *k*-point grids for the integrations in the reciprocal space of bilayer $Ti_2C(OH)_2$ without and with PDMAEMA, respectively.[25] To minimize the image interactions between the PDMAEMA segments, we used a 3 × 3 × 1 supercell of the bilayer $Ti_2C(OH)_2$ structure to place one PDMAEMA segment between the two layers. We also used the DFT-D3 method with the Becke–Johnson damping in the calculations to describe the interlayer van der Waals interactions.[26,27]

RESULTS AND DISCUSSION

Fabrication of the Hybrid MXene. X-ray powder diffraction data (Figure 2) show the successful exfoliation of

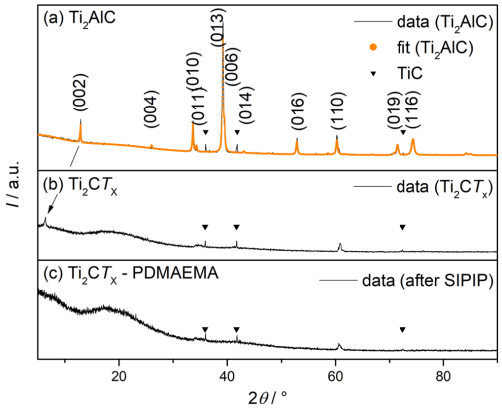

Figure 2. Powder X-ray diffraction data of the precursor MAX phase (a), the exfoliated (b), and with polymer functionalized MXene (c). Triangles indicate the peak positions of the side phase TiC. The black arrow highlights the shift of the (002) peak to smaller diffraction angles that corresponds to an increase in the lattice parameter *c* upon exfoliation. The background is the largest in (c) due to the presence of the amorphous polymer on the MXene surface.

MAX phase Ti_2AlC into MXene Ti_2CT_x. As is typical for the 2D MXenes,[2] the majority of the MAX phase peaks disappear (except for the (110) peak), and the (002) peak shifts to smaller diffraction angles as a result of the increased unit cell parameter *c* following the exfoliation of Ti_6C sheets (Figure 2b). A small amount of TiC is found in the precursor MAX phase as well as in the target MXene that is not affected by the HF treatment. X-ray powder diffraction data of the hybrid material after attachment of the polymer exhibit an even more pronounced background at low diffraction angles as a result of the amorphous polymer that now covers the surface of the MXene (Figure 2c).

Successful expansion of the layered MAX phase structure to the accordion-like morphology is also supported by electron microscopy analysis (Figure 3). While the precursor MAX phase exhibits a layered, yet dense, microstructure (Figure 3a), the layers clearly separate from one another after the selective removal of Al on the A element position (Figure 3b). EDX analysis shows the expected elemental ratios for the precursor MAX phase as well as significant loss of aluminum to a trace value upon chemical etching with HF (EDX spectra, Figures S1–S3). The electron micrograph of the MXene/PDMAEMA

https://dx.doi.org/10.1021/acsanm.0c00118
ACS Appl. Nano Mater. XXXX, XXX, XXX–XXX

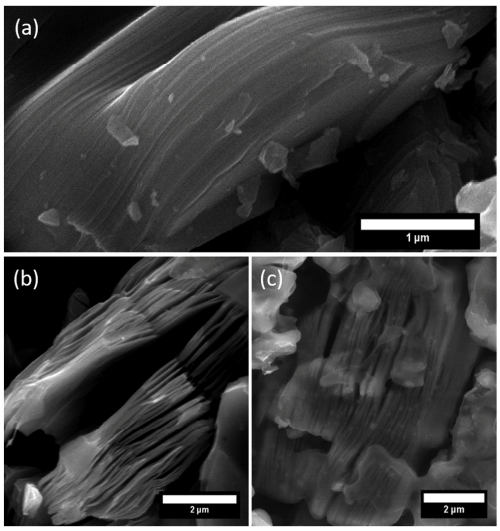

Figure 3. SEM images of MAX phase (a), MXene (b), and MXene–PDMAEMA hybrid (c). EDX results are shown in Figures S1–S3.

hybrid still shows the open 2D-type morphology of the MXene that is now covered with an amorphous organic layer.

The functionalization of the MXene surface has been performed similarly to a surface modification technique, which is known for the functionalization of silica-based materials.[16,17,28,29] The surface-initiated controlled radical polymerizations (SI-CRP) are a commonly used technique to functionalize surfaces with responsive polymer brushes.[30,31] In this study the surface-initiated photoiniferter-mediated polymerization (SI-PIMP) technique was employed. Using SI-PIMP, we needed no additives and only the iniferter and the monomer to perform the controlled polymerization. This is an advantage over other commonly used SI-CRP methods such as SI atom transfer radical polymerization (SI-ATRP) or the SI reversible addition–fragmentation chain-transfer (SI-RAFT) polymerization, especially in the context of functionalization of materials containing nanoscale pores. Additionally, photopolymerizations are readily controllable by switching on and off of the light source. After the pristine MXene material was obtained, the flakes were dried prior to adding the solution of the SBDC iniferter dissolved in toluol. The suspension was then stirred carefully at 80 °C to accelerate the condensation of the SBDC methoxy groups onto the Ti–OH surface functional groups as shown in Figure 1. This leads to the covalent attachment of the iniferter to the MXene surface. The resulting SBDC–MXene hybrid material was then immersed in a diluted solution of the PDMAEMA monomer in DMF and irradiated with UV-light (λ = 365 nm) to carry out the polymerization.

To further prove the successful covalent attachment of the polymer, ATR infrared spectroscopy measurements were conducted (Figure 4). In agreement with Li et al., the precursor MAX phase as well as the pristine MXene does not show any strong signals (the low intensity signals between 2000 and 2250 cm^{-1} are caused by the instrument). However, the hybrid material, which has been washed to remove

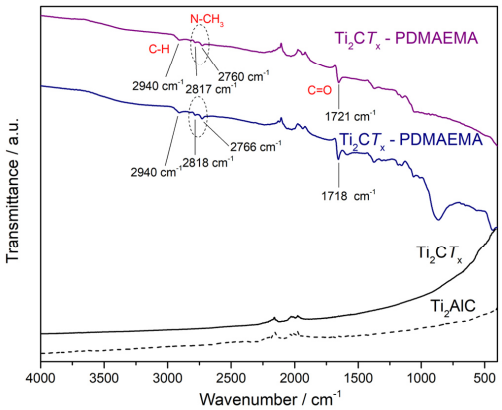

Figure 4. Infrared spectra of the hybrid material (reproduced twice) including a comparison to the pristine MXene and precursor MAX phase. Note that the signals between 2000 and 2250 cm^{-1} stem from the instrument.

unbound polymer, shows the expected carbonyl (~1700 cm^{-1}) and amide vibrational bands (2700 cm^{-1} /2800 cm^{-1}) of PDMAEMA that match the expected vibrational bands very well.[32,33] In addition, the two independent IR spectra of the hybrid MXene–PDMAEMA material confirm the reproducibility of our synthesis route and the covalent attachment of the polymer to the MXene surface which cannot be removed by washing under conditions that remove the unbound monomer (Figure S4).

Furthermore, the successful grafting from polymerization of PDMAEMA on the MXene surface was confirmed by thermal gravimetric analysis (TGA) of the hybrid material (Figure 5).

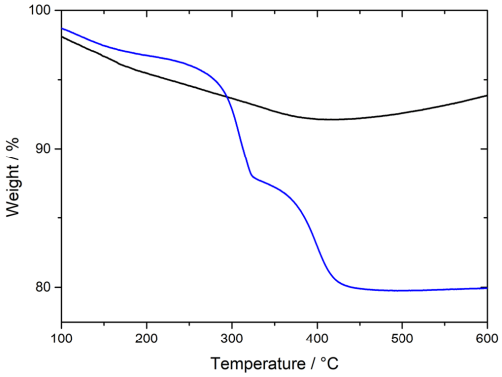

Figure 5. Thermogravimetric analysis of Ti_2CT_x hybrid material (blue curve) and the pristine MXene (black curve).

For the pristine MXene (Figure 5, black) the TG curves can be described in terms of three stages. Upon heating to about 170 °C, Ti_2CT_x experienced a weight loss of 4% due to desorption of surface bound water. In the second stage, a gradual weight loss of an additional 4% up to 400 °C was observed due to removal of oxygen and hydroxyl groups.[34] Upon further

https://dx.doi.org/10.1021/acsanm.0c00118
ACS Appl. Nano Mater. XXXX, XXX, XXX–XXX

temperature increase to 600 °C, a weight increase of 1−2% is observed. Within this temperature range Li et al. have described an exothermic process without obvious weight loss in the TG curve of pristine MXene material and interpreted it as a recrystallization or crystal structure transformation.[34] In addition, Tican form TiO_2 with oxygen in the gas phase that is responsible for the mass increase. The TG curve of the MXene−PDMAEMA hybrid (Figure 5, blue) shows a significantly different thermal behavior that can be described with a two-step degradation which is typical for PDMAEMA.[33] Between 100 and 325 °C the weight loss of ∼11% can be ascribed to the thermal degradation of the amine-containing side chains of the PDMAEMA on the MXene surface.[33] The second degradation step is clearly separated, occurring within a temperature range from 325 to 450 °C, resulting in weight loss of 8%. This weight loss can be ascribed to the decomposition of the polymer (PDMAEMA) backbone. At temperatures above 450 °C no changes in the TG curves are observed, indicating prior total decomposition of PDMAEMA.

X-ray photoelectron spectroscopy (XPS, Figure 6) was conducted to further confirm that PDMAEMA is grafted from

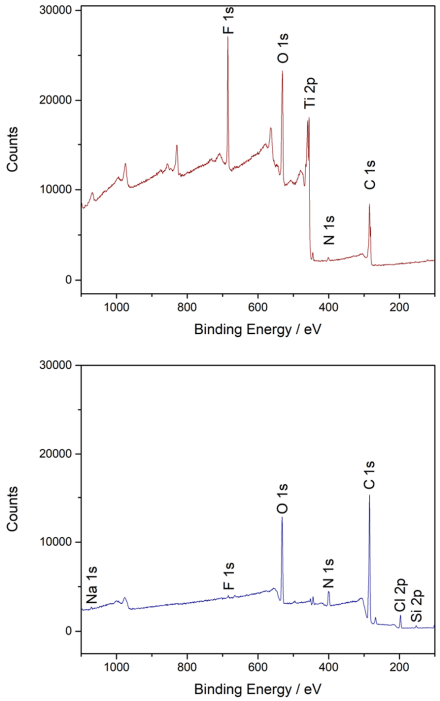

Figure 6. Results from the XPS analysis from the unmodified MXene (top) and the PDMAEMA-modified MXene (bottom).

the MXene surface. The XPS results show a clear difference between the pristine and the functionalized MXene. Beside titanium and graphite, oxygen and fluorine signals are detected, confirming the functionalization of the Ti_2CT_x surface. It is noteworthy that no aluminum was detected, which proves a successful etching process. In contrast, the XPS data of the MXene−PDMAEMA hybrid material exhibit a significantly different signature. The titanium Ti 2p signal is invisible, which demonstrates that a PDMAEMA layer thicker than ∼3 nm is completely covering the Ti_2CT_x surface. The intensity of the fluorine signal is also decreased significantly. The appearance of a silicon signal proves the successful grafting of the SBDC iniferter and together with the nitrogen signal confirms the growth of the PDMAEMA on the MXene surface.

This conclusion is further supported by a strong increase of the carbon (35 to 68 at. %) and nitrogen (1 to 6 at. %) signal (element concentrations in Table S1). Because every DMAEMA side chain contains one nitrogen atom and every SBDC iniferter molecule contains one silicon and one nitrogen atom, the ratio of the silicon to that of the nitrogen can be used to determine the PDMAEMA chain length. Depending on whether the nitrogen impurities that were found in the pristine MXene sample are taken into account, a chain length of at least 3−6 repetition units can be estimated from the XPS measurements. Because of the complete coverage of the surface, limited detection depth of XPS, and a polymer amount of 22 wt %, determined by TGA, even longer chains are very probable.

Switchable Thermoresponsive Behavior of the Hybrid MXene. To demonstrate thermoresponsive tuning of hybrid MXene conductivity, thin films of hybrid PDMAEMA-functionalized MXenes were prepared. The thin films are continuous and show varying thicknesses between 20 and 80 μm (Figure SI-4) that is the result of the deposition technique used to prepare them. The conductivity variation of hybrid MXene−PDMAEMA thin films (Figure 7, green) was

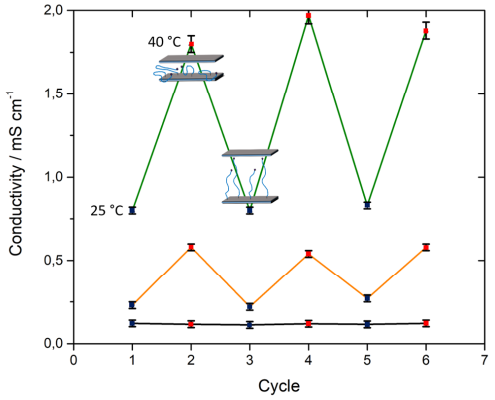

Figure 7. Conductivity results measured on thin films of hybrid MXene (green) and pristine MXene (orange) as well as a suspension of hybrid MXene (black). Blue and red dots mark the temperature range for the measurement between 25 and 40 °C, respectively. The measurements have been repeated at least three times, and the resulting variations from measurement to measurement (error bars) are relatively small.

compared to pristine MXene films (Figure 7, orange) as well as to hybrid MXene−PDMAEMA in suspension (Figure 7, black). Overall, the conductivity values are lower than reported in the literature,[35] as is to be expected since we study multilayer structures rather than single layers as done in the published work. However, the major focus is the switchable

https://dx.doi.org/10.1021/acsanm.0c00118
ACS Appl. Nano Mater. XXXX, XXX, XXX−XXX

behavior of the obtained structures. Indeed, the thermoresponsive behavior of PDAMEMA was demonstrated by the change in conductivity in dependence of the temperature (Figure 7). All samples exhibit different temperature-dependent conductivities as the temperature is cycled below and above the lower critical solution temperature (LCST) of PDMAEMA. The observed behavior is similar to the properties of water-soluble polymer described in the literature.[36−38]

The LCST is known to depend on the pH value, molecular weight, and architecture and varies around 30−40 °C. The conductivity of the suspension of the hybrid MXene−PDMAEMA did not change with the temperature and showed the lowest conductivity values. In addition, the same dark suspension turned colorless as a result of the collapse of the PDMAEMA chains above the LCST and subsequent sedimentation of the MXene−PDMAEMA hybrid (see Figure S6).

In contrast to the suspension, the thin film samples show clear and significant conductivity switching depending on the temperature, an effect that is particularly pronounced for the MXene−PDMAEMA hybrid material (green curve). For the pristine MXene thin film, the conductivity increases from 0.23 to 0.58 mS between 25 and 40 °C. In contrast, the modified hybrid material exhibits a much higher variation in conductivity ranging from 0.8 mS at room temperature to 1.9 mS at 40 °C.

The thin film of the MXene−PDMAEMA hybrid material exhibits a significant increase in conductivity at a temperature above the LCST of PDMAEMA. This is ascribed to the shrinking of the PDMAEMA that is covalently grafted from the surface of the MXene. Therefore, the metallic MXene sheets are pulled closer together, increasing the electron transport across these sheets. At temperatures below the LCST of PDMAEMA the opposite effect is observed with the expanded PDMAEMA pushing the MXene sheets away from one another. This leads to reduced electron transport between the conductive layers and lower conductivities. A similar effect is observed in the pristine MXene thin films; however, the effect is much more pronounced for the hybrid material with the covalently attached PDMAEMA on the surface.

DFT Calculations of the Pristine and Hybrid MXene. To understand the difference in switchable conductivity and to confirm our mechanism, we performed DFT calculations of the pristine MXene in comparison to the MXene−PDMAEMA hybrid material. We used a bilayer $Ti_2C(OH)_2$ sheet to model the MXenes in this work. Changing the surface groups to fluorine leads to similar results and the same overall trend. Figure 8 illustrates the structure of bilayer $Ti_2C(OH)_2$ with the presence of a PDMAEMA segment. We first determined the optimal interlayer spacings of bilayer $Ti_2C(OH)_2$ as 2.1 and 7.2 Å, corresponding to the presence and absence of PDMAEMA, respectively. Here the interlayer spacing (denoted as d in Figure 8) is defined as the nearest H−H distance between the two layers.

We computed the density of state (DOS) for these two energy-minimum structures. Because the main effects of PDMAEMA and temperatures (40 and 25 °C) are on the interlayer spacings and subsequently on the electrical conductivity, we increased the interlayer spacings to 3.0 and 9.0 Å, respectively, to examine the changes in the DOS, from which we estimated the number of electrons that participate in the electrical transport process.

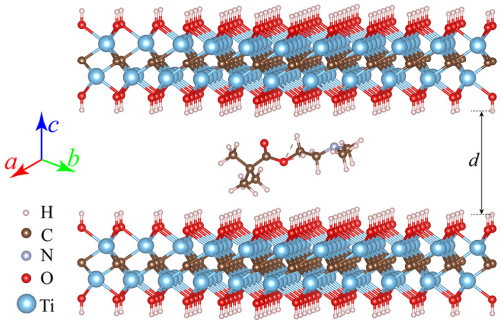

Figure 8. Schematic illustration of the atomic structure of bilayer $Ti_2C(OH)_2$ sheet with a PDMAEMA segment between the two layers.

Figure 9a shows the DOS for the case when PDMAEMA is absent. In this case, only the temperature plays a role in

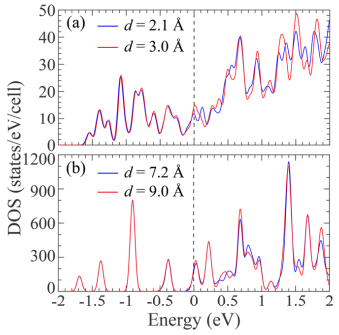

Figure 9. Interlayer-spacing-dependent density of states (DOS) of bilayer $Ti_2C(OH)_2$ (a) without and (b) with PDMAEMA.

changing the interlayer spacing. Therefore, it is expected that at 40 °C the interlayer spacing should be larger due to thermal expansion. We integrated the DOS curves for the larger spacing (d = 3.0 Å) bilayer $Ti_2C(OH)_2$ from −0.027 eV (0.027 eV is the thermal energy at 40 °C) to 0 eV (the Fermi level). We obtained 0.33 electrons per cell that could be thermally excited in electrical transport. Similarly, at 25 °C, the smaller-spacing (d = 2.1 Å) bilayer $Ti_2C(OH)_2$ has 0.30 electrons per cell contributing to the electrical conductivity. These two numbers are close, consistent with the experimental observation that without PDMAEMA the electrical conductivity is less dependent on the temperature change between 40 and 25 °C. In addition, the latter number is also slightly smaller than the former value, which also agrees well with the experiment; i.e., at the higher temperature (larger interlayer spacing), the electrical conductivity is higher.

When PDMAEMA is present between the layers, its effect on the interlayer spacing outperforms the thermal expansion effect. Namely, at a higher temperature (40 °C) the interlayer spacing is actually shorter than that at a lower temperature (25 °C). Figure 9b shows that in this case the lower-spacing (d = 7.2 Å) bilayer $Ti_2C(OH)_2$ has much more electrons (3.78 electrons per cell) than those (2.86 electrons per cell) in the

https://dx.doi.org/10.1021/acsanm.0c00118
ACS Appl. Nano Mater. XXXX, XXX, XXX−XXX

larger-spacing (d = 9.0 Å) bilayer $Ti_2C(OH)_2$, which again is consistent with our experiment; i.e., PDMAEMA functionalization makes the electrical conductivity change more sensitive to the temperature change.

■ CONCLUSION

We have covalently grafted the stimuli-responsive polymer PDMAEMA from the surface of the two-dimensional MXene Ti_2CT_x, taking advantage of the surface OH groups of the MXene which serve for covalent binding of the SBDC iniferter. This inorganic−organic hybrid material possesses unique properties that stem from the carbide "core" in combination with the flexible PDMAEMA. While the metallic MXene enables the hybrid to be electrically conductive, the thermoresponsive polymer shrinks or expands above or below the lower critical solution temperature, LCST (<40 °C, depends on pH, molecular weight, and salt concentration).[39] If processed as thin films, this smart hybrid material exhibits switchable electrical conductivity depending on the temperature that acts as the external stimulus. Hence, such structures may be used as temperature sensors during chemical reactions or serve as a temperature gauge in microelectronics. In suspension, this effect could not be observed due to the sedimentation of the hybrid material above the LCST of PDMAEMA. Based on DFT calculations, this can be understood in terms of MXene sheets getting into closer contact at temperatures above the LCST (when the PDMAEMA shrinks), thereby increasing the conductivity in between the carbide sheets. The conductivity reversibly decreases at temperatures below the LCST when the distance between the sheets is larger (due to polymer swelling).

Based on our insights into the Ti_2CT_x−PDMAEMA model system, this concept can be extended to further MXenes that are based on different transition metals, or other conductive inorganic compounds, as well as further organic molecules/polymers. The latter can also exhibit other stimuli-responsive behavior including being sensitive to other stimuli (e.g., light, pressure, and electric/magnetic field) as well as different responses (e.g., change in shape, color, and viscosity). This opens up a large toolbox for designing new smart materials with switchable properties that can be used as catalysts, sensors, or drug carriers, for example.

■ ASSOCIATED CONTENT

Supporting Information

The Supporting Information is available free of charge at https://pubs.acs.org/doi/10.1021/acsanm.0c00118.

Table of element concentrations of the MXene and MXene hybrid obtained by XPS; EDX analysis of the MAX phase, MXene and MXene hybrid material; IR spectra of the monomer and bulk polymer; SEM images of the MXene hybrid films; photographs of the MXene hybrid suspension before and after heating above the LCST (PDF)

■ AUTHOR INFORMATION

Corresponding Author

Christina S. Birkel − *Eduard Zintl Institut für Anorganische und Physikalische Chemie, Technische Universität Darmstadt, 64287 Darmstadt, Germany; School of Molecular Sciences, Arizona State University, Tempe, Arizona 85281, United States;* orcid.org/0000-0001-8979-5214; Email: christina.birkel@asu.edu

Authors

Minh H. Tran − *Eduard Zintl Institut für Anorganische und Physikalische Chemie, Technische Universität Darmstadt, 64287 Darmstadt, Germany*

Robert Brilmayer − *Ernst-Berl Institut für Technische und Makromolekulare Chemie, Technische Universität Darmstadt, 64287 Darmstadt, Germany*

Lei Liu − *School for Engineering of Matter, Transport and Energy, Arizona State University, Tempe, Arizona 85281, United States*

Houlong Zhuang − *School for Engineering of Matter, Transport and Energy, Arizona State University, Tempe, Arizona 85281, United States*

Christian Hess − *Eduard Zintl Institut für Anorganische und Physikalische Chemie, Technische Universität Darmstadt, 64287 Darmstadt, Germany;* orcid.org/0000-0002-4738-7674

Annette Andrieu-Brunsen − *Ernst-Berl Institut für Technische und Makromolekulare Chemie, Technische Universität Darmstadt, 64287 Darmstadt, Germany;* orcid.org/0000-0002-3850-3047

Complete contact information is available at: https://pubs.acs.org/10.1021/acsanm.0c00118

Author Contributions

M.H.T. and R.B. contributed equally to this work.

Notes

The authors declare no competing financial interest.

■ ACKNOWLEDGMENTS

The authors acknowledge funding from the Hessen State Ministry of Higher Education, Research and the Arts, Germany, in the frame of the LOEWE project iNAPO. This research also used computational resources of the Texas Advanced Computing Center under Contract TG-DMR170070. The authors thank Karl Kopp for performing XPS measurements. We acknowledge Nicole Herzog for sample preparation and IR measurements of Figure S4.

■ REFERENCES

(1) Anasori, B.; Lukatskaya, M. R.; Gogotsi, Y. 2D Metal Carbides and Nitrides (MXenes) for Energy Storage. *Nat. Rev. Mater.* **2017**, *2*, 16098.

(2) Alhabeb, M.; Maleski, K.; Anasori, B.; Lelyukh, P.; Clark, L.; Sin, S.; Gogotsi, Y. Guidelines for Synthesis and Processing of Two-Dimensional Titanium Carbide (Ti3C2Tx MXene). *Chem. Mater.* **2017**, *29*, 7633−7644.

(3) Lukatskaya, M. R.; Mashtalir, O.; Ren, C. E.; Dall'Agnese, Y.; Rozier, P.; Taberna, P. L.; Naguib, M.; Simon, P.; Barsoum, M. W.; Gogotsi, Y. Cation Intercalation and High Volumetric Capacitance of Two-Dimensional Titanium Carbide. *Science* **2013**, *341*, 1502−1505.

(4) Ghidiu, M.; Lukatskaya, M. R.; Zhao, M.-Q.; Gogotsi, Y.; Barsoum, M. W. Conductive Two-Dimensional Titanium Carbide 'Clay' with High Volumetric Capacitance. *Nature* **2014**, *516*, 78.

(5) Lee, W.; Kim, D.; Lee, S.; Park, J.; Oh, S.; Kim, G.; Lim, J.; Kim, J. Stimuli-Responsive Switchable Organic-Inorganic Nanocomposite Materials. *Nano Today* **2018**, *23*, 97−123.

(6) Barsoum, M. W. *MAX Phases: Properties of Machinable Ternary Carbides and Nitrides*; John Wiley & Sons: 2013.

(7) Hope, M. A.; Forse, A. C.; Griffith, K. J.; Lukatskaya, M. R.; Ghidiu, M.; Gogotsi, Y.; Grey, C. P. NMR Reveals the Surface

https://dx.doi.org/10.1021/acsanm.0c00118
ACS Appl. Nano Mater. XXXX, XXX, XXX−XXX

Functionalisation of Ti3C2MXene. *Phys. Chem. Chem. Phys.* **2016**, *18*, 5099−5102.
(8) Zha, X.-H.; Luo, K.; Li, Q.; Huang, Q.; He, J.; Wen, X.; Du, S. Role of the Surface Effect on the Structural, Electronic and Mechanical Properties of the Carbide MXenes. *Europhys. Lett.* **2015**, *111*, 26007.
(9) Peng, Q.; Guo, J.; Zhang, Q.; Xiang, J.; Liu, B.; Zhou, A.; Liu, R.; Tian, Y. Unique Lead Adsorption Behavior of Activated Hydroxyl Group in Two-Dimensional Titanium Carbide. *J. Am. Chem. Soc.* **2014**, *136*, 4113−4116.
(10) Khazaei, M.; Arai, M.; Sasaki, T.; Chung, C.-Y.; Venkataramanan, N. S.; Estili, M.; Sakka, Y.; Kawazoe, Y. Novel Electronic and Magnetic Properties of Two-Dimensional Transition Metal Carbides and Nitrides. *Adv. Funct. Mater.* **2013**, *23*, 2185−2192.
(11) Kurtoglu, M.; Naguib, M.; Gogotsi, Y.; Barsoum, M. W. First Principles Study of Two-Dimensional Early Transition Metal Carbides. *MRS Commun.* **2012**, *2*, 133−137.
(12) Wang, L.; Shi, B. Hydroxide Conduction Enhancement of Chitosan Membranes by Functionalized MXene. *Materials* **2018**, *11*, 2335.
(13) Chen, J.; Chen, K.; Tong, D.; Huang, Y.; Zhang, J.; Xue, J.; Huang, Q.; Chen, T. CO_2 and Temperature Dual Responsive "Smart" MXene Phases. *Chem. Commun.* **2015**, *51*, 314−317.
(14) Hamm, C. M.; Bocarsly, J. D.; Seward, G.; Kramm, U. I.; Birkel, C. S. Non-Conventional Synthesis and Magnetic Properties of MAX Phases (Cr/Mn)2AlC and (Cr/Fe)2AlC. *J. Mater. Chem. C* **2017**, *5*, 5700−5708.
(15) Hamm, C. M.; Schäfer, T.; Zhang, H.; Birkel, C. S. Non-Conventional Synthesis of the 413 MAX Phase V4AlC3. *Z. Anorg. Allg. Chem.* **2016**, *642*, 1397−1401.
(16) De Boer, B.; Simon, H.; Werts, M.; Van der Vegte, E.; Hadziioannou, G. Living" Free Radical Photopolymerization Initiated from Surface-Grafted Iniferter Monolayers. *Macromolecules* **2000**, *33*, 349−356.
(17) Brilmayer, R.; Hess, C.; Andrieu-Brunsen, A. Influence of Chain Architecture on Nanopore Accessibility in Polyelectrolyte Block-Co-Oligomer Functionalized Mesopores. *Small* **2019**, *15*, 1902710.
(18) Moulder, J. F. *Handbook of X-ray Photoelectron Spectroscopy*; Perkin-Elmer Corporation: 1995; pp 230−232.
(19) Cotanda, P.; Wright, D. B.; Tyler, M.; O'Reilly, R. K. A Comparative Study of the Stimuli-Responsive Properties of DMAEA and DMAEMA Containing Polymers. *J. Polym. Sci., Part A: Polym. Chem.* **2013**, *51*, 3333−3338.
(20) Kresse, G.; Hafner, J. Ab initio Molecular Dynamics for Liquid Metals. *Phys. Rev. B: Condens. Matter Mater. Phys.* **1993**, *47*, 558.
(21) Kresse, G.; Furthmüller, J. Efficient Iterative Schemes for Ab Initio Total-Energy Calculations using a Plane-Wave Basis Set. *Phys. Rev. B: Condens. Matter Mater. Phys.* **1996**, *54*, 11169.
(22) Perdew, J. P.; Burke, K.; Ernzerhof, M. Generalized Gradient Approximation Made Simple. *Phys. Rev. Lett.* **1996**, *77*, 3865.
(23) Blöchl, P. E. Projector Augmented-Wave Method. *Phys. Rev. B: Condens. Matter Mater. Phys.* **1994**, *50*, 17953−17979.
(24) Kresse, G.; Joubert, D. From Ultrasoft Pseudopotentials to the Projector Augmented-Wave Method. *Phys. Rev. B: Condens. Matter Mater. Phys.* **1999**, *59*, 1758.
(25) Monkhorst, H. J.; Pack, J. D. Special Points for Brillouin-Zone Integrations. *Phys. Rev. B* **1976**, *13*, 5188.
(26) Grimme, S.; Antony, J.; Ehrlich, S.; Krieg, H. A Consistent and Accurate Ab Initio Parametrization of Density Functional Dispersion Correction (DFT-D) for the 94 Elements H-Pu. *J. Chem. Phys.* **2010**, *132*, 154104.
(27) Grimme, S.; Ehrlich, S.; Goerigk, L. Effect of the Damping Function in Dispersion Corrected Density Functional Theory. *J. Comput. Chem.* **2011**, *32*, 1456−1465.
(28) Tom, J.; Brilmayer, R.; Schmidt, J.; Andrieu-Brunsen, A. Optimisation of Surface-Initiated Photoiniferter-Mediated Polymerisation under Confinement, and the Formation of Block Copolymers in Mesoporous Films. *Polymers* **2017**, *9*, 539.
(29) Silies, L.; Didzoleit, H.; Hess, C.; Stühn, B.; Andrieu-Brunsen, A. Mesoporous thin films, zwitterionic monomers, and iniferter-initiated polymerization: Polymerization in a confined space. *Chem. Mater.* **2015**, *27*, 1971−1981.
(30) Badoux, M.; Billing, M.; Klok, H.-A. Polymer brush interfaces for protein biosensing prepared by surface-initiated controlled radical polymerization. *Polym. Chem.* **2019**, *10*, 2925−2951.
(31) Zoppe, J. O.; Ataman, N. C.; Mocny, P.; Wang, J.; Moraes, J.; Klok, H.-A. Surface-Initiated Controlled Radical Polymerization: State-of-the-Art, Opportunities, and Challenges in Surface and Interface Engineering with Polymer Brushes. *Chem. Rev.* **2017**, *117*, 1105−1318.
(32) Huang, S.-J.; Ke, J.-H.; Chen, G.-J.; Wang, L.-F. One-Pot Synthesis of PDMAEMA-Bound Iron Oxide Nanoparticles for Magnetofection. *J. Mater. Chem. B* **2013**, *1*, 5916−5924.
(33) Stawski, D.; Nowak, A. Thermal Properties of Poly(N,N-dimethylaminoethylmethacrylate). *PLoS One* **2019**, *14*, e0217441.
(34) Li, J.; Du, Y.; Huo, C.; Wang, S.; Cui, C. Thermal Stability of Two-Dimensional Ti2C Nanosheets. *Ceram. Int.* **2015**, *41*, 2631−2635.
(35) Ying, G.; Dillon, A. D.; Fafarman, A. T.; Barsoum, M. W. Transparent, conductive solution processed spincast 2D Ti2CTx (MXene) films. *Mater. Res. Lett.* **2017**, *5*, 391−398.
(36) Bütün, V.; Armes, S. P.; Billingham, N. C. Synthesis and aqueous solution properties of near-monodisperse tertiary amine methacrylate homopolymers and diblock copolymers. *Polymer* **2001**, *42*, 5993−6008.
(37) Liu, G.; Wu, D.; Ma, C.; Zhang, G.; Wang, H.; Yang, S. Insight into the Origin of the Thermosensitivity of Poly[2-(dimethylamino)-ethyl methacrylate]. *ChemPhysChem* **2007**, *8*, 2254−2259.
(38) Plamper, F. A.; Ruppel, M.; Schmalz, A.; Borisov, O.; Ballauff, M.; Müller, A. H. E. Tuning the Thermoresponsive Properties of Weak Polyelectrolytes: Aqueous Solutions of Star-Shaped and Linear Poly(N,N-dimethylaminoethyl Methacrylate). *Macromolecules* **2007**, *40*, 8361−8366.
(39) Zheng, J. Y.; Tan, M. J.; Thoniyot, P.; Loh, X. J. Unusual Thermogelling Behaviour of Poly[2-(dimethylamino)ethyl methacrylate] (PDMAEMA)-Based Polymers Polymerized in Bulk. *RSC Adv.* **2015**, *5*, 62314−62318.

https://dx.doi.org/10.1021/acsanm.0c00118
ACS Appl. Nano Mater. XXXX, XXX, XXX−XXX

5. Zusammenfassung

Die übergeordnete Klammer und Ziel dieser Arbeit bestand darin, Ladungssituationen in nanoskaligen Poren zu verstehen und damit nutzbar zu machen. Als Vorarbeiten dazu wurden im Rahmen der vorliegenden Arbeit zunächst zwei unterschiedliche Typen von mesoporösen Silicadünnfilmen mit unterschiedlichen Porendruchmessern von 8 nm und 16 nm hergestellt. Hierbei zeigte sich, dass bei identischem Herstellungsprozess, die Silicafilme mit größeren Poren (BP-Filme), welche durch eine Erhöhung der Templatkonzentration in der Sollösung erreicht wurden, im Vergleich zu den kleinporigen Systemen (SP-Filme) unter den verwendeten Herstellungsbedingungen ungefähr doppelt so dick sind. Die Filmdicke ist vor allem für optische Untersuchungen, bei denen der Lichtstrahl durch den Film hindurchgeleitet wird, entscheidend, da in dickeren Filmen durch das größere Volumen mehr (Detektions)Moleküle pro Filmoberfläche inkorporiert werden können. Da in den verwendeten, funktionalisierten mesoporösen Silicafilmen Farbstoffkonzentrationen im nanomolaren Bereich vorliegen, ist es durch dickere Filme gelungen, aus dem Bereich der Nachweisgrenze zu gut messbaren Systemen zu gelangen. Die Schichtdicke kann im Herstellungsprozess nach bekannten Vorgehensweisen (Variation Ziehgeschwindigkeit etc.) variiert werden. Üblicherweise wurden in dieser Arbeit Schichtdicken von ca. 200 nm für die Filme mit 8 nm Poren und ca. 500 nm für die Filme mit 16 nm großen Poren verwendet. Die hergestellten Filme wurden im Anschluss im *post grafting* Verfahren so funktionalisiert, dass sie zur Untersuchung von Ladungseffekten im Confinement auf der Nanoskala verwendet werden konnten. Ladung in Nanoporen ist daher relevant, da über sie andere wichtige Parameter wie etwa der pH-Wert abgeleitet werden können. Der pH-Wert ist ein wichtiger Parameter in Anwendungen von Nanomaterialien, welcher aber durch die räumliche Begrenzung auf der Nanoskala beeinflusst wird. Um den pH-Wert in Mesoporen bestimmen und besser verstehen zu können, wurden zwei unterschiedliche Ansätze verfolgt.

In Bezug auf das Ziel Silicamesoporen über die SI-PIMP kontrolliert mit unterschiedlichen Polyelektrolyten zu modifizieren, wurden sowohl Homo- als auch Block-co-Oligomere synthetisiert. Die hergestellten funktionalen Silicadünnfilme wurden dann hinsichtlich ihres pH-abhängigen Transportverhaltens untersucht. Hierbei wurden Parameter wie Porenfüllung, Kettenlänge und Kettenarchitektur variiert, um den pH-abhängigen Ladungsaufbau in den funktionalisierten Silicamesoporen zu untersuchen und mit den bekannten pK_s-Werten aus Bulkmaterial zu vergleichen.

Neben der Herstellung komplexer Funktionalisierungen bestand der zweite Fokus der Arbeit darin,

- zu einem besseren Verständnis von nanoconfinement Einfluss auf Ladungssituation und damit auf Transport von Nanoporen zu gelangen,
- einen neuartigen und mit dem pK_s-Wert von Silicamesoporen kompatiblen Fluoreszenzfarbstoff auf Basis der MPT-Farbstoffgruppe zu synthetisieren,
- kovalent an Silicamesoporen anzubinden und
- das Potenzial dieses Ansatzes zur in-situ pH-Detektion zu evaluieren.

Der Farbstoff ist im pH-Bereich um den pK_s-Wert der Silica-Silanolgruppen von 2-4 sensitiv und ermöglicht es direkt Ladungsumschwünge in den Silicamesoporen optisch zu verfolgen.
Sowohl die Polyelektrolyt- als auch die Farbstofffunktionalisierungsstrategien wurden zur Ladungs- bzw. pH-Bestimmung in Silicamesoporen entwickelt und konnten erfolgreich eingesetzt werden. Die erhaltenen Ergebnisse basieren auf gänzlich unterschiedlichen und redundanten Detektionsmethoden. Zum einen wurden für die polyelektrolyt funktionalisierten Silicamesoporen indirekte Detektionsmethoden für die pK_s-Wert Bestimmungen verwendet, indem Permselektivitätsuntersuchungen per Cyclovoltammetrie durchgeführt wurden. Zum anderen konnten für die Farbstoff-funktionalisierten Silicamesoporen direkte pH-Messungen und pK_s-Bestimmungen durch UV-vis-Messungen durchgeführt werden. Beide Methoden zeigen pH-Verschiebungen zwischen den Polymeren in Lösung und denselben Polymeren in Nanoporen von mindestens einer pH-Einheit an. Eine pH-Verschiebung in dieser Größenordnung bedeutet, dass der Ladungsaufbau in solch kleinen Räumen energetisch so ungünstig ist, dass er erst bei einer lokalen zehnfach höheren Protonenkonzentration stattfindet als in freier Lösung. Zusätzlich konnte gezeigt werden, dass die räumliche Positionierung von Ladung innerhalb von Silicamesoporen eine Schlüsselrolle für deren Transportverhalten darstellt. Im Folgenden sind die Kernergebnisse der einzelnen Teile zusammengefasst.

Photoinferterbasierte Polymerisation zur Herstellung von Homo- und Block-co-Oligomeren in Silicamesoporen

Für die Polymerfunktionalisierung der Silicamesoporen wurden diese zunächst mit dem Photoiniferter SBDC funktionalisiert. Durch thermogravimetrische Analyse (TGA) konnte bei den verwendeten Anbindungsbedingungen eine Belegungsdichte von 0.7 Molekülen/nm^2 bestimmt werden. Eine Belegungsdichte in dieser Größenordnung liegt in dem aus Vorarbeiten in der Arbeitsgruppe bekannten Erwartungsbereich.[87] Über Variation von Polymerisationsparametern, wie der Belichtungsdauer und Monomerkonzentration, ist es gelungen Porenfüllgrade zwischen 20 % und 95 % einzustellen, was einer Kettenlänge, bestimmt über TGA und Röntgenphotoelektronenspektroskopie (XPS), von 2-6 Wiederholungseinheiten entspricht. Aus diesem Grund muss man eher von Oligomeren als von Polymeren in Mesoporen dieses Größenbereiches sprechen. Als Monomere wurden MEP und DMAEMA verwendet. DMAEMA wurde ausgewählt, da es sowohl pH- als auch temperaturresponsiv ist. MEP hingegen ist nur pH-responsiv, kann aber durch die enthaltene Ghosphatgruppe bis zu zwei Ladungen pro Monomer aufbauen. Für beide Monomere konnte die Polymermenge in den Mesoporen kontrolliert, sowohl in den SP- als auch in den BP-Filmen, eingestellt werden. In Kooperation mit der BASF SE konnte durch eine Kombination aus Kryo-TEM und EDX-Mapping zudem erstmalig die homogene Funktionalisierung mit einem Polyelektrolyten entlang der Z-Achse des mesoporösen Silicafilms nachgewiesen werden. Für die Polymerisation mit MEP konnte zusätzlich gezeigt werden, dass ein Wechsel des Lösemittels von DMF auf Wasser keinen negativen Einfluss auf die Kontrolle der

Polymerisation hat und die Polymerisation auch durch Sonnenlicht initiiert werden kann. Hinsichtlich nachhaltigerer Synthesegestaltung ist dies ein zusätzlicher Vorteil. Das hier etablierte System bietet mit Wasser als Reaktionsmedium und Sonnenlicht als Energiequelle eine gute Basis um Oberflächenpolymerisationen in Zukunft möglichst klimaneutral zu gestalten.
Auf Basis von Erkenntnissen, welche auf Computersimulationen der Szleifer-Gruppe basieren und nahelegen, dass die Kettenstruktur und Ladungsverteilung innerhalb einer Polymerkette das Transportverhalten eines funktionalisierten Nanokanals beeinflussen,[14] wurde untersucht, welchen Einfluss die räumliche Lage von Ladung innerhalb eines Polyelektrolyten auf das Transportverhalten von Silicamesoporen hat. Hierzu wurde neben den hinsichtlich der Polymermenge und Porenfüllung graduell einstellbaren Homooligomeren von PDMAEMA und PMEP, auch komplexe Kettenarchitekturen in der Form von Block-co-Oligomeren in Mesoporen <10 nm hergestelt. Über Reinitiation der Polymerisation ist es so erstmals gelungen PDMAEMA-*co*-PMEP block co-oligomere mit Blocklängen von je 2-3 Wiederholungseinheiten zu synthetisieren. Die Reinitiation und zunehmende Porenfüllung konnte hierbei über Ellipsometrie verfolgt und die Oligomerzusammensetzung über XPS bestimmt werden.

pH-abhängiger Ladungsaufbau von Polyelektrolyten in nanoskaligen Räumen

Der pH-abhängige Ionentransport durch die mesoporösen Silicafilme wurde in dieser Arbeit elektrochemisch über Cyclovoltammetriemessungen untersucht. Die Verwendung von Testmolekülen erlaubt es, durch deren Aufkonzentration an der Arbeitselektrode Rückschlüsse über die Ladungssituation des (funktionalisierten) mesoporösen Silicafilmes zu ziehen. Unter Verwendung von Messlösung mit voreingestelltem pH-Wert ist es so gelungen, den graduellen Ladungsaufbau von PDMAEMA und PMEP in den Silicamesoporen zu verfolgen. Hierbei zeigte sich, dass der Ladungsaufbau der Polyelektrolyte in extremere pH-Bereiche verschoben wird. Diese Verschiebung wird zusätzlich durch Faktoren wie Polyelektrolytmenge und Salzkonzentration des Hintergrundelektrolyten in der Messlöung beeinflusst. Verglichen mit DMAEMA in Lösung findet die Protonierung erst eine ganze pH-Einheit saurer statt. Diese Verschiebung entspricht in Lösung dem pK_s-Wert einer PDMAEMA-Kette mit >100 Wiederholungseinheiten. Für das mehrfach ladbare PMEP ist es im Rahmen dieser Arbeit und der Instabilität von Silica bei pH-Werten über 10 nicht gelungen, die doppelt geladene Spezies zu erreichen. Dies entspricht einer Verschiebung des pK_s-Wertes von mehr als zwei pH-Einheiten.
Die Relevanz des Einflusses von nanoskaliger Umgebung auf Moleküle, die für Anwendungen in Silicamesoporen inkorporiert werden konnte, wurde in Zusammenarbeit mit Adnan Khalil und Sonja Kübelbeck (BASF SE) für die Lipase *Aspergillus oryzae* demonstriert. Das Enzym zeigte nach Einlagerung in Silicamesoporen bei einem pH-Wert, bei dem das Enzym in Lösung stabil ist, einen enormen Aktivitätsverlust.
Die nanoskalige Umgebung hat jedoch nicht nur Einfluss auf den pH- und pK_s-Wert. Anhand des PDMAEMA-co-PMEP Block-co-oligomers konnte gezeigt werden, dass nicht nur Art (Ladungstyp)

und Menge die Permselektivität von funktionalisierten Silicamesoporen beeinflussen. Die orthogonal geladenen PDMAEMA und PMEP Blöcke legen einen Vergleich zu anderen heterogen geladenen Systemen, wie etwa Zwitterionen, nahe. Interessanterweise zeigten die hier untersuchten Block-co-Oligomerstrukturen im Gegensatz zu Zwitterionen keine Ausbildung von bipolaren Poren (Abstoßung von Kationen und Anionen gleichermaßen), wie es für zwitterionische Polymere beobachtet wird.[201] In pH-Bereichen, in denen beide Blöcke geladen sind, waren die Poren stattdessen auch für beide Ionenspezies zugänglich.

Synthese und Verwendung eines MPT-basierten Farbstoffes zur direkten Bestimmung des apparenten pH-Wertes in Silicamesoporen

Um die pK_s-Wert Bestimmung in Silicamesoporen zu ermöglichen, musste der hergestellte Farbstoff sowohl in den Silicamesoporen als auch in Lösung einsetzbar sein, um quantitative Vergleiche herstellen zu können, was z.B. mit FRET-Paaren ausgeschlossen ist. Deshalb eignen sich vor allem die konzentrationsunabhängigen ratiometrischen Farbstoffe, da diese quantitative pH-Sensorik in einem Molekül ermöglichen und somit die Problematik der FRET-Paare diesbezüglich umgehen. Gängige Vertreter ratiometrischer Farbstoffe, wie die SNARF-Farbstoffgruppe, verfügen jedoch über einen Sensitivitätsbreich bei pH 6,6-7,5, der für Silica (pK_s 3-4) nicht optimal ist. In dieser Arbeit stellten sich ratiometrische MPT-Farbstoffe, die je nach Derivat in einem pH-Bereich von 1-5 sensitiv sind, als sinnvolle pH-Sensoren heraus. Durch Erweiterung des π-Systems des MPT-Grundgerüstes um einen Phenylrest, ist es gelungen, das Absorptions- und Emissionsspektrum des Farbstoffes um 50 nm in das sichtbare Spektrum zu verschieben. Hierdurch ist es möglich, Ladungsveränderungen/Protonierung qualitativ mit dem Auge zu verfolgen, und der Farbstoff wird ebenfalls für laserbasierte Mikroskopiemethoden zugänglich gemacht. Bisherige MPT-Farbstoffe konnten nur umständlich über Halogen-Metallchemie an Silicaoberflächen angebunden werden. Durch das Einführen einer Carboxylgruppe ist es gelungen, den in dieser Arbeit entwickelten MPT-Ph-Farbstoff unter Verwendung von sehr milden Reaktionsbedingungen an Aminosilicamaterialien in der Form von Dünnfilmen und Partikeln anzubinden. In Kooperation mit Martin Brodrecht aus der Arbeitsgruppe Buntkowsky an der TU Darmstadt konnte die erfolgreiche Anbindung des Farbstoffes durch Festkörper-NMR-Messungen nachgewiesen werden.
Nach Synthese und Anbindung des MPT-Ph Farbstoffes an mesoporöses Silica konnte er erfolgreich genutzt werden, um pH-Verschiebungen zwischen Lösungen und Mesoporen zu bestimmen. Die hier erhaltenen Ergebnisse decken sich mit denen aus den Untersuchungen mit polyelektrolytfunktionalisierten Mesoporen und deuten auf eine pH-Verschiebung von etwa einer pH-Einheit hinzu extremeren pH-Werten.

Anhang

Abkürzungsverzeichnis

APDMS	Aminopropyldimethylmethoxysilan
APTES	3-Aminopropyltriethoxysilan
APTS	8-aminopyrene-1,3,6-trisulfonate
ATRP	*Atom-Transfer Radical Polymerization*
BDC	Benzylditethyldithiocarbamat
CBMA	Carboxybetainmethacrylat
CLCT	*Ccooperative self assembly*
CTA	*Chain Transfer Agent*
CV	Cyclovoltammetrie
DFT	Dichtefunktionaltheorie
EDX	Energiedispersive Röntgenspektroskopie
EISA	*Evaporation-Induced Self-Assembly*
FRET	Försterresonanzenergiertransfer
ITO	Indium-Zinnoxid
LCST	*Lower critical solution temperature*
MCM	Mobil Composition of Matter
MEP	2-(methacryloyloxy)ethylphosphat)
MPT	Methoxy-pyridyl-thiazol
MS	Massenspektrometrie
MSM	mesoporösen Silicamaterialien
MSS	*Modulable Steady State*
PAA	Poly(acrylsäure)
PDMAEMA	Poly(2-(Dimethylamino)ethylmethacrylat)
PVP	Poly(vinylpyridin)
RAFT	*Reversible Addition Fragmentation Chain Transfer*
REM	Rasterelektronenmikroskopie
SBA	Santa Barbara Amorphous
SBDC	(N,N(diethylamino)dithiocarbamoylbenzyl(trimethoxy)silan
SIPGP	*Self initiating photografting-photopolymerisation*
SI-PIMP	*Surface initiated photoiniferter mediated polymerization*
SNARF	Seminaphtharhodafluor
TEM	Transmissionselektronenmikroskopie
TEOS	Tetraorthoethoxysilan
TGA	Thermogravimetrische Analyse
TLCT	*True liquid crystal templating*
XPS	Röntgenphotoelektronenspektroskopie

Erklärungen

Robert Brilmayer
Detagstraße 11
58455 Witten

Erklärung

Ich erkläre hiermit, dass ich meine Dissertation selbstständig und nur mit den angegebenen Hilfsmitteln angefertigt und noch keinen Promotionsversuch unternommen habe.

Darmstadt, den

Robert Brilmayer

Erklärung zur Begutachtung der Veröffentlichungen

Prof. Dr. Annette Andrieu-Brunsen

Referentin

Prof. Dr. Markus Biesalski

Koreferent

16.04.2020

Weder Referentin (Prof. Dr. Annette Andrieu-Brunsen) noch Koreferent (Prof. Dr. Markus Biesalski) der vorliegenden kumulativen Doktorarbeit waren an der Begutachtung nachstehender Veröffentlichungen beteiligt:

[1] R. Brilmayer*, C. Förster*, L. Zhao*, A. Andrieu-Brunsen, Trends in Nanopore Polymer Funtionali-zation, Curr. Opin. Biotech., 2020. (accepted status)

[2] R. Brilmayer, S. Kuebelbeck, A. Khalil, M. Brodrecht, U. Kunz, H.-J. Kleebe, G. Buntkowsky, G. Bayer, A. Andrieu-Brunsen, Influence of nanoconfinement on the pKa of polyelectrolyte functional-ized silica mesopores, Adv. Mat. Interf., 2020.

[3] M. H. Tran*, R. Brilmayer*, L. Liu, H. Zhang, C. Hess, A. Andrieu-Brunsen, C. Birkel, Synthesis of a Smart Hybrid MXene with Switchable Conductivity for Temperature Sensing, ACS Appl. Nano Mater., 2020.

[4] R. Brilmayer, C. Hess, A. Andrieu-Brunsen, Influence of Chain Architecture on Nanopore Accessi-bility in Polyelectrolyte Block-Co-Oligomer Funtionalized Mesopores, Small, 2019.

[5] N. Herzog, R. Brilmayer, M. Stanzel, A. Kalyta, D. Spiehl, E. Doersam, C. Hess, A. Andrieu-Brunsen, Gravure printing for mesoporous film preparation, RSC Advances, 2019.

[6] M. Stanzel, R. Brilmayer, M. Langhans, T. Meckel, A. Andrieu-Brunsen, FRET-based pH sensing in mesoporous thin films with tunable detection range, Microporous and Mesoporous Materials, 2019.

[7] J. Tom, R. Brilmayer, J. Schmidt, A.Andrieu-Brunsen, Optimisation of Surface-Initiated Photoin-iferter-Mediated Polymerisation under Confinement, and the Formation of Block Copolymers in Mesoporous Films, Polymers, 2017.

*These authors contributed equally to this work

Referentin

Prof. Dr. Annette Andrieu-Brunsen

Koreferent

Prof. Dr. Markus Biesalski

Erklärung zum Eigenanteil an den Veröffentlichungen

Veröffentlichungen als Erstauthor
Mein Anteil an der folgenden Veröffentlichung beträgt 95 %.
(1) R. Brilmayer, C. Hess, A. Andrieu-Brunsen, Influence of Chain Architecture on Nanopore Accessibility in Polyelectrolyte Block-Co-Oligomer Functionalized Mesopores, Small, 2019, 15, 1902710.

Mein Anteil an der folgenden Veröffentlichung beträgt 80 %.
(2) R. Brilmayer, S. Kuebelbeck, A. Khalil, M. Brodrecht, U. Kunz, H.-J. Kleebe, G. Buntkowsky, G. Bayer, A. Andrieu-Brunsen, Influence of nanoconfinement on the pKa of polyelectrolyte functionalized silica mesopores, Adv. Mat. Interf., 2020, 1901914.

Mein Anteil an der folgenden Veröffentlichung beträgt 40 %.
(3) M. H. Tran*, R. Brilmayer*, L. Liu, H. Zhang, C. Hess, A. Andrieu-Brunsen, C. Birkel, Synthesis of a smart hybrid MXene with switchable conductivity, ACS Appl. Nano Mater., 2020, https://doi.org/10.1021/acsanm.0c00118.
*These authors contributed equally to this work

Mein Anteil an der folgenden Veröffentlichung beträgt 65 %.
(4) R. Brilmayer, M. Brodrecht, C. Kaiser, J. Wachtveitl, G. Buntkowsky, A. Andrieu-Brunsen, A new dye for ratiometric pH detection inside silica mesopores, to be submitted.

Veröffentlichungen als Coauthor
Mein Anteil an der folgenden Veröffentlichung beträgt 15 %.
(1) J. Tom, R. Brilmayer, J. Schmidt, A. Andrieu-Brunsen, Optimisation of Surface-Initiated Photoiniferter-Mediated Polymerisation under Confinement, and the Formation of Block Copolymers in Mesoporous Films, Polymers, 2017, 9(10), 539.

Mein Anteil an der folgenden Veröffentlichung beträgt 10 %.
(2) M. Stanzel, R. Brilmayer, M. Langhans, T. Meckel, A. Andrieu-Brunsen, FRET-based pH-sensing in mesoporous thin films with tunable detection range, Microporous and Mesoporous Materials, 2019, 282, 29-37.

Mein Anteil an der folgenden Veröffentlichung beträgt 10 %.
(3) N. Herzog, R. Brilmayer, M. Stanzel, A. Kalyta, D. Spiehl, E. Doersam, C. Hess, A. Andrieu-Brunsen, Gravure Printing for Mesoporous Film Preparation, RSC Adv., 2019, 9, 23570–23578.

Wissenschaftliche Publikation als Übersichtsartikel
Mein Anteil an der folgenden Veröffentlichung beträgt 34 %.
(1) R. Brilmayer*, C. Förster*, L. Zhao*, A. Andrieu-Brunsen, Trends in Nanopore Polymer Funtionalization, Curr. Opin. Biotech., accepted.
*These authors contributed equally to this work

Robert Brilmayer
Detagstraße 11
58455 Witten

Erklärung der Übereinstimmung

Ich erkläre hiermit, dass die elektronische Version der Doktorarbeit mit der schriftlichen Version übereinstimmt. Die elektronische Version liegt dem Prüfungssekretariat vor.

Darmstadt, den

Robert Brilmayer

Literaturverzeichnis

1. Mitrano, D. M.; Rimmele, E.; Wichser, A.; Erni, R.; Height, M.; Nowack, B., Presence of Nanoparticles in Wash Water from Conventional Silver and Nano-silver Textiles. *ACS Nano* **2014,** *8* (7), 7208.

2. Doyle, D. A.; Cabral, J. M.; Pfuetzner, R. A.; Kuo, A.; Gulbis, J. M.; Cohen, S. L.; Chait, B. T.; MacKinnon, R., The Structure of the Potassium Channel: Molecular Basis of K⁺ Conduction and Selectivity. *Science* **1998,** *280*, 69.

3. Walcarius, A., Mesoporous materials and electrochemistry. *Chem. Soc. Rev.* **2013,** *42* (9), 4098.

4. Yameen, B.; Ali, M.; Neumann, R.; Ensinger, W.; Knoll, W.; Azzaroni, O., Proton-regulated rectified ionic transport through solid-state conical nanopores modified with phosphate-bearing polymer brushes. *Chem Commun (Camb)* **2010,** *46* (11), 1908.

5. Weber, J.; Bergstrom, L., Mesoporous hydrogels: revealing reversible porosity by cryoporometry, X-ray scattering, and gas adsorption. *Langmuir* **2010,** *26* (12), 10158.

6. Soler-Illia, G. J.; Azzaroni, O., Multifunctional hybrids by combining ordered mesoporous materials and macromolecular building blocks. *Chem. Soc. Rev.* **2011,** *40* (2), 1107.

7. Nicole, L.; Boissière, C.; Grosso, D.; Quach, A.; Sanchez, C., Mesostructured hybrid organic–inorganic thin films. *J. Mater. Chem.* **2005,** *15* (35-36), 3598.

8. Brinker, C. J., Lu, Yunfeng, Sellinger, Alan, Fan, Hongyou, Evaporation-Induced Self-Assembly: Nanostructures Made Easy. *Adv. Mater.* **1999,** *11* (7), 579.

9. Dunphy, D. R.; Sheth, P. H.; Garcia, F. L.; Brinker, C. J., Enlarged Pore Size in Mesoporous Silica Films Templated by Pluronic F127: Use of Poloxamer Mixtures and Increased Template/SiO2Ratios in Materials Synthesized by Evaporation-Induced Self-Assembly. *Chem. Mater.* **2015,** *27* (1), 75.

10. Tagliazucchi, M.; Azzaroni, O.; Szleifer, I., Responsive Polymers End-Tethered in Solid-State Nanochannels: When Nanoconfinement Really Matters. *J. Am. Chem. Soc.* **2010,** *132*, 12404.

11. Narayan, R.; Nayak, U. Y.; Raichur, A. M.; Garg, S., Mesoporous Silica Nanoparticles: A Comprehensive Review on Synthesis and Recent Advances. *Pharmaceutics* **2018,** *10* (3).

12. Hoffmann, F.; Cornelius, M.; Morell, J.; Fröba, M., Mesoporöse organisch-anorganische Hybridmaterialien auf Silicabasis. *Angewandte Chemie* **2006,** *118* (20), 3290.

13. Brunsen, A.; Cui, J.; Ceolin, M.; del Campo, A.; Soler-Illia, G. J.; Azzaroni, O., Light-activated gating and permselectivity in interfacial architectures combining "caged" polymer brushes and mesoporous thin films. *Chem. Commun. (Camb)* **2012,** *48* (10), 1422.

14. Huang, K.; Szleifer, I., Design of Multifunctional Nanogate in Response to Multiple External Stimuli Using Amphiphilic Diblock Copolymer. *J. Am. Chem. Soc.* **2017,** *139* (18), 6422.

15. Hou, X.; Guo, W.; Jiang, L., Biomimetic smart nanopores and nanochannels. *Chem. Soc. Rev.* **2011,** *40* (5), 2385.

16. Huang, X.; Appelhans, D.; Formanek, P.; Simon, F.; Voit, B., Tailored synthesis of intelligent polymer nanocapsules: an investigation of controlled permeability and pH-dependent degradability. *ACS Nano* **2012,** *6* (11), 9718.

17. Perez-Mitta, G.; Albesa, A. G.; Knoll, W.; Trautmann, C.; Toimil-Molares, M. E.; Azzaroni, O., Host-guest supramolecular chemistry in solid-state nanopores: potassium-driven modulation of ionic transport in nanofluidic diodes. *Nanoscale* **2015,** *7* (38), 15594.

18. Qiang Fu, G. V. R. R., Linnea K. Ista, Yang Wu, Brett P. Andrzejewski, Larry A. Sklar, Timothy L. Ward, and Gabriel P. Lopez, Control of Molecular Transport Through Stimuli-Responsive Ordered Mesoporous materials. *Adv. Mater.* **2003,** *15* (15), 1262.

19. Wen, J.; Yang, K.; Liu, F.; Li, H.; Xu, Y.; Sun, S., Diverse gatekeepers for mesoporous silica nanoparticle based drug delivery systems. *Chem. Soc. Rev.* **2017,** *46* (19), 6024.

20. Yu, F.; Tang, X.; Pei, M., Facile synthesis of PDMAEMA-coated hollow mesoporous silica nanoparticles and their pH-responsive controlled release. *Microporous and Mesoporous Materials* **2013,** *173*, 64.

21. Tagliazucchi, M.; Azzaroni, O.; Szleifer, I., Responsive Polymers End-Tethered in Solid-State Nanochannels: When Nanoconfinement Really Matters. *J. Am. Chem. Soc.* **2010,** *132* (35), 12404.

22. Kuo, T.-C.; Sloan, L. A.; Sweedler, J. V.; Bohn, P. W., Manipulating Molecular Transport through Nanoporous Membranes by Control of Electrokinetic Flow: Effect of Surface Charge Density and Debye Length. *Langmuir* **2001,** *17* (20), 6298.

23. Bottenus, D.; Oh, Y. J.; Han, S. M.; Ivory, C. F., Experimentally and theoretically observed native pH shifts in a nanochannel array. *Lab Chip* **2009,** *9* (2), 219.

24. Gilles, F. M.; Tagliazucchi, M.; Azzaroni, O.; Szleifer, I., Ionic Conductance of Polyelectrolyte-Modified Nanochannels: Nanoconfinement Effects on the Coupled Protonation Equilibria of Polyprotic Brushes. *J. Phys. Chem. C* **2016,** *120* (9), 4789.

25. Zoppe, J. O.; Ataman, N. C.; Mocny, P.; Wang, J.; Moraes, J.; Klok, H. A., Surface-Initiated Controlled Radical Polymerization: State-of-the-Art, Opportunities, and Challenges in Surface and Interface Engineering with Polymer Brushes. *Chem. Rev.* **2017,** *117* (3), 1105.

26. Li, X.; Mastan, E.; Wang, W.-J.; Li, B.-G.; Zhu, S., Progress in reactor engineering of controlled radical polymerization: a comprehensive review. *Reaction Chemistry & Engineering* **2016,** *1* (1), 23.

27. Brilmayer, R.; Hess, C.; Andrieu-Brunsen, A., Influence of Chain Architecture on Nanopore Accessibility in Polyelectrolyte Block-Co-Oligomer Functionalized Mesopores. *Small* **2019**, 1902710.

28. Brunsen, A.; Diaz, C.; Pietrasanta, L. I.; Yameen, B.; Ceolin, M.; Soler-Illia, G. J.; Azzaroni, O., Proton and calcium-gated ionic mesochannels: phosphate-bearing polymer brushes hosted in mesoporous thin films as biomimetic interfacial architectures. *Langmuir* **2012,** *28* (7), 3583.

29. Yameen, B.; Mubarak, A.; Neumann, R.; Ensinger, W.; Knoll, W.; Azzaroni, O., Single Conical Nanopores Displaying pH-Tunable Rectifying Characteristics. Manipulating Ionic Transport With Zwitterionic Polymer Brushes. *J. Am. Chem. Soc.* **2009,** *131*, 2070.

30. Park, S. H.; Kwon, N.; Lee, J. H.; Yoon, J.; Shin, I., Synthetic ratiometric fluorescent probes for detection of ions. *Chem. Soc. Rev.* **2020,** *49* (1), 143.

31. Ajayaghosh, A.; Carol, P.; Sreejith, S., A ratiometric fluorescence probe for selective visual sensing of Zn2+. *J. Am. Chem. Soc.* **2005,** *127* (43), 14962.

32. Li, L. I.; Yun, S.; Yuan-Hui, Z.; Lan, M. U.; Xi, Z.; Redshaw, C.; Gang, W. E. I., A single chemosensor for multiple analytes: Fluorogenic and ratiometric absorbance detection of Zn2+, Mg2+ and F−, and its cell imaging. *Sensors and Actuators B: Chemical* **2016,** *226*, 279.

33. Li, S.; Zhang, D.; Xie, X.; Ma, S.; Liu, Y.; Xu, Z.; Gao, Y.; Ye, Y., A novel solvent-dependently bifunctional NIR absorptive and fluorescent ratiometric probe for detecting Fe3+/Cu2+ and its application in bioimaging. *Sensors and Actuators B: Chemical* **2016,** *224*, 661.

34. Maity, D.; Govindaraju, T., A differentially selective sensor with fluorescence turn-on response to Zn2+ and dual-mode ratiometric response to Al3+ in aqueous media. *Chem. Commun. (Camb)* **2012,** *48* (7), 1039.

35. Qu, L.; Yin, C.; Huo, F.; Chao, J.; Zhang, Y.; Cheng, F., A pyridoxal-based dual chemosensor for visual detection of copper ion and ratiometric fluorescent detection of zinc ion. *Sensors and Actuators B: Chemical* **2014,** *191*, 158.

36. Wang, L.; Yan, J.; Qin, W.; Liu, W.; Wang, R., A new rhodamine-based single molecule multianalyte (Cu2+, Hg2+) sensor and its application in the biological system. *Dyes and Pigments* **2012,** *92* (3), 1083.

37. Chiappini, C.; Martinez, J. O.; De Rosa, E.; Almeida, C. S.; Tasciotti, E.; Stevens, M. M., Biodegradable Nanoneedles for Localized Delivery of Nanoparticles in Vivo: Exploring the Biointerface. *ACS Nano* **2015,** *9* (5), 5500.

38. Chiappini, C.; Campagnolo, P.; Almeida, C. S.; Abbassi-Ghadi, N.; Chow, L. W.; Hanna, G. B.; Stevens, M. M., Mapping Local Cytosolic Enzymatic Activity in Human Esophageal Mucosa with Porous Silicon Nanoneedles. *Adv. Mater.* **2015,** *27* (35), 5147.

39. E.A. AbouAitah, K.; A. Farghali, A., Mesoporous Silica Materials in Drug Delivery System: pH/Glutathione- Responsive Release of Poorly Water-Soluble Pro-drug Quercetin from Two and Three-dimensional Pore-Structure Nanoparticles. *Journal of Nanomedicine & Nanotechnology* **2016,** *07* (02).

40. Song, Y.; Li, Y.; Xu, Q.; Liu, Z., Mesoporous silica nanoparticles for stimuli-responsive controlled drug delivery: advances, challenges, and outlook. *Int. J. Nanomedicine* **2017,** *12*, 87.

41. Liu, X.; Cheng, J.; Lu, X.; Wang, R., Surface acidity of quartz: understanding the crystallographic control. *Phys. Chem. Chem. Phys.* **2014,** *16* (48), 26909.

42. Sulpizi, M.; Gaigeot, M. P.; Sprik, M., The Silica-Water Interface: How the Silanols Determine the Surface Acidity and Modulate the Water Properties. *J. Chem. Theory. Comput.* **2012,** *8* (3), 1037.

43. Rosenholm, J. M.; Czuryszkiewicz, T.; Kleitz, F.; Rosenholm, J. B.; Lindén, M., On the Nature of the Brønsted Acidic Groups on Native and Functionalized Mesoporous Siliceous SBA-15 as Studied by Benzylamine Adsorption from Solution. *Langmuir* **2007,** *23* (8), 4315.

44. Stanzel, M.; Brilmayer, R.; Langhans, M.; Meckel, T.; Andrieu-Brunsen, A., Systematic study on FRET-pair functionalization of mesoporous thin films for correlation of pH-sensing and ionic mesopore accessibility. *Micropor. and Mesopor. Mat.* **2019,** *282*, 29.

45. Lei, J.; Wang, L.; Zhang, J., Ratiometric pH sensor based on mesoporous silica nanoparticles and Forster resonance energy transfer. *Chem. Commun. (Camb)* **2010,** *46* (44), 8445.

46. Zheng, M.-H.; Jin, J.-Y.; Sun, W.; Yan, C.-H., A new series of fluorescent 5-methoxy-2-pyridylthiazoles with a pH-sensitive dual-emission. *New Journal of Chemistry* **2006,** *30* (8).

47. Zdravkov, B.; Čermák, J.; Šefara, M.; Janků, J., Pore classification in the characterization of porous materials: A perspective. *Open Chemistry* **2007,** *5* (2).

48. Davis, M. E., Zeolites and molecular sieves: not just ordinary catalysts. *Industrial & Engineering Chemistry Research* **1991,** *30* (8), 1675.

49. Puppe, L., Zeolithe - Eigenschaften und technische Anwendungen. *Chemie in unserer Zeit* **1986,** *20* (4), 117-127.

50. Nisticò, R.; Scalarone, D.; Magnacca, G., Preparation and physico-chemical characterization of large-mesopore silica thin films templated by block copolymers for membrane technology. *Micropor. and Mesopor. Mat.* **2014,** *190*, 208.

51. Kresge, C. T.; Leonowicz, M. E.; Roth, W. J.; Vartuli, J. C.; Beck, J. S., Ordered mesoporous molecular sieves synthesized by a liquid-crystal template mechanism. *Nature* **1992,** *359* (6397), 710.

52. Dunphy, D. R.; Sheth, P. H.; Garcia, F. L.; Brinker, C. J., Enlarged Pore Size in Mesoporous Silica Films Templated by Pluronic F127: Use of Poloxamer Mixtures and Increased Template/SiO2 Ratios in Materials Synthesized by Evaporation-Induced Self-Assembly. *Chem. Mater.* **2014,** *27* (1), 75.

53. Attard, G. S.; Glyde, J. C.; Göltner, C. G., Liquid-crystalline phases as templates for the synthesis of mesoporous silica. *Nature* **1995,** *378* (6555), 366.

54. Hoffmann, F.; Cornelius, M.; Morell, J.; Froba, M., Silica-based mesoporous organic-inorganic hybrid materials. *Angew. Chem. Int. Ed. Engl.* **2006,** *45* (20), 3216.

55. Steel, A.; Carr, S. W.; Anderson, M. W., 14N NMR study of surfactant mesophases in the synthesis of mesoporous silicates. *J. Chem. Soc., Chem. Commun.,* **1994**, 1571.

56. Ying, J. Y.; Mehnert, C. P.; Wong, M. S., Synthesis and Applications of Supramolecular-Templated Mesoporous Materials. *Angew. Chem. Int. Ed. Engl.* **1999,** *38* (1-2), 56.

57. Firouzi, A.; Atef, F.; Oertli, A. G.; Stucky, G. D.; Chmelka, B. F., Alkaline Lyotropic Silicate−Surfactant Liquid Crystals. *J. Am. Chem. Soc.* **1997,** *119* (15), 3596.

58. Firouzi, A.; Kumar, D.; Bull, L. M.; Besier, T.; Sieger, P.; Huo, Q.; Walker, S. A.; Zasadzinski, J. A.; Glinka, C.; Nicol, J.; et al., Cooperative organization of inorganic-surfactant and biomimetic assemblies. *Science* **1995,** *267* (5201), 1138.

59. Grosso, D.; Cagnol, F.; Soler-Illia, G. J. d. A. A.; Crepaldi, E. L.; Amenitsch, H.; Brunet-Bruneau, A.; Bourgeois, A.; Sanchez, C., Fundamentals of Mesostructuring Through Evaporation-Induced Self-Assembly. *Adv. Funct. Mater.* **2004,** *14* (4), 309.

60. Robertson, C.; Beanland, R.; Boden, S. A.; Hector, A. L.; Kashtiban, R. J.; Sloan, J.; Smith, D. C.; Walcarius, A., Ordered mesoporous silica films with pores oriented perpendicular to a titanium nitride substrate. *Phys. Chem. Chem. Phys.* **2015,** *17* (6), 4763.

61. Brinker, C. J.; Lu, Y. F.; Sellinger, A.; Fan, H. Y., Evaporation-induced self-assembly: Nanostructures made easy. *Adv. Mater.* **1999,** *11* (7), 579.

62. Alberti, S.; Soler-Illia, G. J.; Azzaroni, O., Gated supramolecular chemistry in hybrid mesoporous silica nanoarchitectures: controlled delivery and molecular transport in response to chemical, physical and biological stimuli. *Chem. Commun. (Camb)* **2015,** *51* (28), 6050.

63. Grosso, D.; Babonneau, F.; Albouy, P.-A.; Amenitsch, H.; Balkenende, A. R.; Brunet-Bruneau, A.; Rivory, J., An in Situ Study of Mesostructured CTAB−Silica Film Formation during Dip Coating Using Time-Resolved SAXS and Interferometry Measurements. *Chem. Mater.* **2002,** *14* (2), 931.

64. Innocenzi, P.; Falcaro, P.; Grosso, D.; Babonneau, F., Order−Disorder Transitions and Evolution of Silica Structure in Self-Assembled Mesostructured Silica Films Studied through FTIR Spectroscopy. *J. Phys. Chem. B* **2003,** *107* (20), 4711.

65. Meynen, V.; Cool, P.; Vansant, E. F., Verified syntheses of mesoporous materials. *Micropor. Mesopor. Mater.* **2009,** *125* (3), 170..

66. Grosso, D., How to exploit the full potential of the dip-coating process to better control film formation. *J. Mater. Chem.* **2011,** *21* (43).

67. Kim, T.-W.; Chung, P.-W.; Lin, V. S. Y., Facile Synthesis of Monodisperse Spherical MCM-48 Mesoporous Silica Nanoparticles with Controlled Particle Size. *Chem. Mater.* **2010,** *22* (17), 5093.

68. Herzog, N.; Brilmayer, R.; Stanzel, M.; Kalyta, A.; Spiehl, D.; Dörsam, E.; Hess, C.; Andrieu-Brunsen, A., Gravure printing for mesoporous film preparation. *RSC Advances* **2019,** *9* (41), 23570.

69. Low, Z.-X.; Chua, Y. T.; Ray, B. M.; Mattia, D.; Metcalfe, I. S.; Patterson, D. A., Perspective on 3D printing of separation membranes and comparison to related unconventional fabrication techniques. *J. Membr. Sci.* **2017,** *523*, 596.

70. Lee, J.-Y.; An, J.; Chua, C. K., Fundamentals and applications of 3D printing for novel materials. *Applied Materials Today* **2017,** *7*, 120.

71. Khoo, Z. X.; Teoh, J. E. M.; Liu, Y.; Chua, C. K.; Yang, S.; An, J.; Leong, K. F.; Yeong, W. Y., 3D printing of smart materials: A review on recent progresses in 4D printing. *Virtual and Physical Prototyping* **2015,** *10* (3), 103.

72. Kotz, F.; Arnold, K.; Bauer, W.; Schild, D.; Keller, N.; Sachsenheimer, K.; Nargang, T. M.; Richter, C.; Helmer, D.; Rapp, B. E., Three-dimensional printing of transparent fused silica glass. *Nature* **2017,** *544* (7650), 337.

73. Femmer, T.; Kuehne, A. J.; Wessling, M., Print your own membrane: direct rapid prototyping of polydimethylsiloxane. *Lab Chip* **2014,** *14* (15), 2610.

74. Khripin, C. Y.; Pristinski, D.; Dunphy, D. R.; Brinker, C. J.; Kaehr, B., Protein-directed assembly of arbitrary three-dimensional nanoporous silica architectures. *ACS Nano* **2011,** *5* (2), 1401.

75. Nasir, T.; Herzog, G.; Hebrant, M.; Despas, C.; Liu, L.; Walcarius, A., Mesoporous Silica Thin Films for Improved Electrochemical Detection of Paraquat. *ACS Sens.* **2018,** *3* (2), 484.

76. Walcarius, A.; Sibottier, E.; Etienne, M.; Ghanbaja, J., Electrochemically assisted self-assembly of mesoporous silica thin films. *Nat. Mater.* **2007,** *6* (8), 602.

77. Wang, K.; He, J., One-Pot Fabrication of Antireflective/Antibacterial Dual-Function Ag NP-Containing Mesoporous Silica Thin Films. *ACS Appl. Mater. Interf.* **2018,** *10* (13), 11189.

78. Alothman, Z., A Review: Fundamental Aspects of Silicate Mesoporous Materials. *Materials* **2012,** *5* (12), 2874.

79. Kruk, M., Surface-Initiated Controlled Radical Polymerization in Ordered Mesoporous Silicas. *Israel J. Chem.* **2012,** *52*, 246.

80. van der Heyden, F. H.; Bonthuis, D. J.; Stein, D.; Meyer, C.; Dekker, C., Electrokinetic energy conversion efficiency in nanofluidic channels. *Nano Lett.* **2006,** *6* (10), 2232.

81. Stein, A., Advances in Microporous and Mesoporous Solids—Highlights of Recent Progress. *Adv. Mater.* **2003,** *15* (10), 763.

82. Nicole, L.; Boissière, C.; Grosso, D.; Quach, A.; Sanchez, C., Mesostructured hybrid organic–inorganic thin films. *J. Mater. Chem.* **2005,** *15,* 35.

83. Park, J. W.; Park, Y. J.; Jun, C. H., Post-grafting of silica surfaces with pre-functionalized organosilanes: new synthetic equivalents of conventional trialkoxysilanes. *Chem. Commun. (Camb)* **2011,** *47* (17), 4860.

84. Anwander, R.; Nagl, I.; Widenmeyer, M.; Engelhardt, G.; Groeger, O.; Palm, C.; Röser, T., Surface Characterization and Functionalization of MCM-41 Silicas via Silazane Silylation. *J. Phys. Chem. B* **2000,** *104* (15), 3532.

85. Der Voort, P. V.; Vansant, E. F., Silylation of the Silica Surface A Review. *Journal of Liquid Chromatography & Related Technologies* **1996,** *19* (17-18), 2723.

86. Huang, X.; Wirth, M. J., Surface-Initiated Radical Polymerization on Porous Silica. *Anal. Chem.* **1997,** *69* (22), 4577.

87. Silies, L.; Didzoleit, H.; Hess, C.; Stühn, B.; Andrieu-Brunsen, A., Mesoporous Thin Films, Zwitterionic Monomers, and Iniferter-Initiated Polymerization: Polymerization in a Confined Space. *Chem. Mater.* **2015,** *27* (6), 1971.

88. Turgman-Cohen, S.; Genzer, J., Computer Simulation of Controlled Radical Polymerization: Effect of Chain Confinement Due to Initiator Grafting Density and Solvent Quality in "Grafting From" Method. *Macromolecules* **2010,** *43* (22), 9567.

89. Elliott, I. G.; Mulder, D. E.; Träskelin, P. T.; Ell, J. R.; Patten, T. E.; Kuhl, T. L.; Faller, R., Confined polymer systems: synergies between simulations and neutron scattering experiments. *Soft Matter.* **2009,** *5* (23).

90. Xue, Y. H.; Zhu, Y. L.; Quan, W.; Qu, F. H.; Han, C.; Fan, J. T.; Liu, H., Polymer-grafted nanoparticles prepared by surface-initiated polymerization: the characterization of polymer chain conformation, grafting density and polydispersity correlated to the grafting surface curvature. *Phys. Chem. Chem. Phys.* **2013,** *15* (37), 15356.

91. Cheesman, B. T.; Neilson, A. J.; Willott, J. D.; Webber, G. B.; Edmondson, S.; Wanless, E. J., Effect of colloidal substrate curvature on pH-responsive polyelectrolyte brush growth. *Langmuir* **2013,** *29* (20), 6131-40.

92. Kalb, J.; Dukes, D.; Kumar, S. K.; Hoy, R. S.; Grest, G. S., End grafted polymernanoparticles in a polymeric matrix: Effect of coverage and curvature. *Soft Matter.* **2011,** *7* (4), 1418.

93. Pasetto, P.; Blas, H. l. n.; Audouin, F.; Boissière, C. d.; Sanchez, C. m.; Save, M.; Charleux, B., Mechanistic Insight into Surface-Initiated Polymerization of Methyl Methacrylate and Styrene via ATRP from Ordered Mesoporous Silica Particles. *Macromolecules* **2009,** *42* (16), 5983.

94. Liu, H.; Zhu, Y.-L.; Zhang, J.; Lu, Z.-Y.; Sun, Z.-Y., Influence of Grafting Surface Curvature on Chain Polydispersity and Molecular Weight in Concave Surface-Initiated Polymerization. *ACS Macro Letters* **2012,** *1* (11), 1249.

95. Otsu, T.; Yoshida, M., Role of initiator-transfer agent-terminator (iniferter) in radical polymerizations: Polymer design by organic disulfides as iniferters. *Die Makromolekulare Chemie, Rapid Communications* **1982,** *3* (2), 127.

96. Otsu, T., Iniferter concept and living radical polymerization. *J. Poly. Sci. Part A: Poly. Chem.* **2000,** *38* (12), 2121.

97. Banerjee, S.; Paira, T. K.; Mandal, T. K., Surface confined atom transfer radical polymerization: access to custom library of polymer-based hybrid materials for speciality applications. *Poly. Chem.* **2014,** *5,* 14.

98. Hui, C. M.; Pietrasik, J.; Schmitt, M.; Mahoney, C.; Choi, J.; Bockstaller, M. R.; Matyjaszewski, K., Surface-Initiated Polymerization as an Enabling Tool for Multifunctional (Nano-)Engineered Hybrid Materials. *Chem. Mater.* **2013,** *26* (1), 745.

99. Xu, F. J.; Neoh, K. G.; Kang, E. T., Bioactive surfaces and biomaterials via atom transfer radical polymerization. *Progress in Polymer Science* **2009,** *34* (8), 719.

100. Fristrup, C. J.; Jankova, K.; Hvilsted, S., Surface-initiated atom transfer radical polymerization—a technique to develop biofunctional coatings. *Soft Matter.* **2009,** *5,* 23.

101. Matyjaszewski, K.; Tsarevsky, N. V., Macromolecular engineering by atom transfer radical polymerization. *J. Am. Chem. Soc.* **2014,** *136* (18), 6513.

102. Matyjaszewski, K.; Tsarevsky, N. V., Nanostructured functional materials prepared by atom transfer radical polymerization. *Nat. Chem.* **2009,** *1* (4), 276.

103. Perrier, S.; Takolpuckdee, P., Macromolecular design via reversible addition-fragmentation chain transfer (RAFT)/xanthates (MADIX) polymerization. *J. Poly. Sci. Part A: Poly. Chem.* **2005,** *43* (22), 5347.

104. Chiefari, J.; Chong, Y. K.; Ercole, F.; Krstina, J.; Jeffery, J.; Le, T. P. T.; Mayadunne, R. T. A.; Meijs, G. F.; Moad, C. L.; Moad, G.; Rizzardo, E.; Thang, S. H., Living Free-Radical Polymerization by Reversible Addition−Fragmentation Chain Transfer: The RAFT Process. *Macromolecules* **1998,** *31* (16), 5559..

105. Moad, G.; Rizzardo, E.; Thang, S. H., Living radical polymerization by the RAFT process. *Aust. J. Chem.* **2005,** *58* (6), 379.

106. Matyjaszewski, K., Atom Transfer Radical Polymerization (ATRP): Current Status and Future Perspectives. *Macromolecules* **2012,** *45* (10), 4015.

107. Matyjaszewski, K.; Dong, H.; Jakubowski, W.; Pietrasik, J.; Kusumo, A., Grafting from surfaces for "everyone": ARGET ATRP in the presence of air. *Langmuir* **2007,** *23* (8), 4528.

108. Christopher, B. K.; P., D. T.; A., H. J. P.; H., S. M.; Philipp, V.; Michael, W., RAFTing down under: Tales of missing radicals, fancy architectures, and mysterious holes. *J. Poly. Sci. Part A: Poly. Chem.* **2003,** *41* (3), 365.

109. Otsu, T.; Yoshida, M., A model for living radical polymerization. *Die Makromolekulare Chemie, Rapid Communications* **1982,** *3* (2), 133.

110. Rubens, M.; Latsrisaeng, P.; Junkers, T., Visible light-induced iniferter polymerization of methacrylates enhanced by continuous flow. *Poly. Chem.* **2017,** *8* (42), 6496..

111. B. de Boer, H. K. S., M. P. L. Werts, E. W. van der Vegte, and G. Hadziioannou, "Living" Free Radical Photopolymerization Initiated from Surface-Grafted Iniferter Monolayers. *Macromolecules* **2000,** *33*, 349.

112. Khalil, A.; Zimmermann, M.; Bell, A. K.; Kunz, U.; Hardt, S.; Kleebe, H. J.; Stark, R. W.; Stephan, P.; Andrieu-Brunsen, A., Insights into the interplay of wetting and transport in mesoporous silica films. *J. Coll. Interf. Sci.* **2020**, 560, 369.

113. Vivek, R.; Nipun Babu, V.; Thangam, R.; Subramanian, K. S.; Kannan, S., pH-responsive drug delivery of chitosan nanoparticles as Tamoxifen carriers for effective anti-tumor activity in breast cancer cells. *Coll. Surf. B Biointerf.* **2013,** *111*, 117.

114. Feng, Y.; Zhu, W.; Guo, W.; Jiang, L., Bioinspired Energy Conversion in Nanofluidics: A Paradigm of Material Evolution. *Adv. Mater.* **2017,** *29,* 45.

115. Xie, G.; Wen, L.; Jiang, L., Biomimetic smart nanochannels for power harvesting. *Nano Research* **2016,** *9* (1), 59.

116. Xia, F.; Jiang, L., Bio-Inspired, Smart, Multiscale Interfacial Materials. *Adv. Mater.* **2008,** *20* (15), 2842.

117. Ulbricht, M., Advanced functional polymer membranes. *Polymer* **2006,** *47* (7), 2217..

118. Adiga, S. P.; Brenner, D. W., Stimuli-Responsive Polymer Brushes for Flow Control through Nanopores. *J. Funct. Biomater.* **2012,** *3* (2), 239.

119. Zhang, H.; Hou, X.; Zeng, L.; Yang, F.; Li, L.; Yan, D.; Tian, Y.; Jiang, L., Bioinspired artificial single ion pump. *J. Am. Chem. Soc.* **2013,** *135* (43), 16102.

120. Tom, J.; Brilmayer, R.; Schmidt, J.; Andrieu-Brunsen, A., Optimisation of Surface-Initiated Photoiniferter-Mediated Polymerisation under Confinement, and the Formation of Block Copolymers in Mesoporous Films. *Polymers* **2017,** *9* (10), 539.

121. Stamatialis, D. F.; Papenburg, B. J.; Gironés, M.; Saiful, S.; Bettahalli, S. N. M.; Schmitmeier, S.; Wessling, M., Medical applications of membranes: Drug delivery, artificial organs and tissue engineering. *J.Membr. Sci.* **2008,** *308* (1-2), 1.

122. Hegazy, M.; Zhou, P.; Rahoui, N.; Wu, G.; Taloub, N.; Lin, Y.; Huang, X.; Huang, Y., A facile design of smart silica nanocarriers via surface-initiated RAFT polymerization as a dual-stimuli drug release platform. *Colloids and Surfaces A: Physicochemical and Engineering Aspects* **2019,** *581*.

123. Zheng, Y. B.; Zhao, S.; Cao, S. H.; Cai, S. L.; Cai, X. H.; Li, Y. Q., A temperature, pH and sugar triple-stimuli-responsive nanofluidic diode. *Nanoscale* **2017,** *9* (1), 433.

124. Wang, Z.; Yang, X.; Cheng, Z.; Liu, Y.; Shao, L.; Jiang, L., Simply realizing "water diode" Janus membranes for multifunctional smart applications. *Mater. Horiz.* **2017,** *4* (4), 701.

125. Zhang, Z.; Sui, X.; Li, P.; Xie, G.; Kong, X. Y.; Xiao, K.; Gao, L.; Wen, L.; Jiang, L., Ultrathin and Ion-Selective Janus Membranes for High-Performance Osmotic Energy Conversion. *J. Am. Chem. Soc.* **2017,** *139* (26), 8905.

126. Cheng, H.; Zhou, Y.; Feng, Y.; Geng, W.; Liu, Q.; Guo, W.; Jiang, L., Electrokinetic Energy Conversion in Self-Assembled 2D Nanofluidic Channels with Janus Nanobuilding Blocks. *Adv. Mater.* **2017,** *29,* 23.

127. Gong, P.; Wu, T.; Genzer, J.; Szleifer, I., Behavior of Surface-Anchored Poly(acrylic acid) Brushes with Grafting Density Gradients on Solid Substrates: 2. Theory. *Macromolecules* **2007,** *40* (24), 8765.

128. Schepelina, O.; Zharov, I., Poly(2-(dimethylamino)ethyl methacrylate)-modified nanoporous Colloidal films with pH and ion response. *Langmuir* **2008,** *24* (24), 14188.

129. Yamaguchi, A.; Namekawa, M.; Kamijo, T.; Itoh, T.; Teramae, N., Acid-base equilibria inside amine-functionalized mesoporous silica. *Anal. Chem.* **2011,** *83* (8), 2939.

130. Yameen, B.; Ali, M.; Neumann, R.; Ensinger, W.; Knoll, W.; Azzaroni, O., Synthetic proton-gated ion channels via single solid-state nanochannels modified with responsive polymer brushes. *Nano Lett.* **2009,** *9* (7), 2788.

131. Hiemstra, T.; Van Riemsdijk, W. H., A Surface Structural Approach to Ion Adsorption: The Charge Distribution (CD) Model. *J. Coll. Interf. Sci.* **1996,** *179* (2), 488.

132. Hiemstra, T.; Van Riemsdijk, W. H., On the relationship between charge distribution, surface hydration, and the structure of the interface of metal hydroxides. *J. Coll. Interf. Sci.* **2006,** *301* (1), 1.

133. Weiß, D.; Brandl, H., Fluoreszenzfarbstoffe in der Natur. *Chemie in unserer Zeit* **2013,** *47* (1), 50.

134. Peter Atkins, J. d. P., Atkins´Physical Chemistry. **2006**, 492f., 852f.

135. Deckwer, M., Biotechnologie und Gentechnik. *RÖMPP Lexikon, 2. Auflage* **1999**, 658f.

136. Lakowicz, J. R., Principles of Fluorescence Spectroscopy. *Springer* **1999**, 278f.

137. Hippchen, H., Konfokale Einzelpartikel-Detektion von Fluoreszenz-kodierten Nanospheres. *Dissertation* **2008**.

138. Li, L.-L.; Sun, H.; Fang, C.-J.; Xu, J.; Jin, J.-Y.; Yan, C.-H., Optical sensors based on functionalized mesoporous silica SBA-15 for the detection of multianalytes (H+ and Cu2+) in water. *J. Mater. Chem.* **2007,** *17,* 4492.

139. Shen, L.; Zhao, P.; Zhu, W., A ratiometric hydrophilic fluorescent copolymer sensor based on benzimidazole chromophore for microbioreactors. *Dyes and Pigments* **2011,** *89* (3), 236.

140. Widmer, S.; Reber, M. J.; Muller, P.; Housecroft, C. E.; Constable, E. C.; Rossi, R. M.; Bruhwiler, D.; Scherer, L. J.; Boesel, L. F., Incorporation of a FRET dye pair into mesoporous materials: a comparison of fluorescence spectra, FRET activity and dye accessibility. *Analyst* **2015,** *140* (15), 5324.

141. Gao, F.; Tang, L.; Dai, L.; Wang, L., A fluorescence ratiometric nano-pH sensor based on dual-fluorophore-doped silica nanoparticles. *Spectrochim. Acta A Mol. Biomol. Spectrosc.* **2007,** *67* (2), 517.

142. Thörn, C.; Carlsson, N.; Gustafsson, H.; Holmberg, K.; Åkerman, B.; Olsson, L., A method to measure pH inside mesoporous particles using protein-bound SNARF1 fluorescent probe. *Micropor. Mesopor. Mater.* **2013,** *165*, 240.

143. Tian, M.; Peng, X.; Fan, J.; Wang, J.; Sun, S., A fluorescent sensor for pH based on rhodamine fluorophore. *Dyes and Pigments* **2012,** *95* (1), 112.

144. Moerner, S. B. a. W. E., Fluorescence Behavior of Single-Molecule pH-Sensors. *Single Mol. 1* **2000,** (1), 17.

145. Wan, S.; Zheng, Y.; Shen, J.; Yang, W.; Yin, M., "On-off-on" switchable sensor: a fluorescent spiropyran responds to extreme pH conditions and its bioimaging applications. *ACS Appl. Mater. Interf.* **2014,** *6* (22), 19515.

146. Martínez-Máñez, R.; Sancenón, F.; Biyikal, M.; Hecht, M.; Rurack, K., Mimicking tricks from nature with sensory organic–inorganic hybrid materials. *J. Mater. Chem.* **2011,** *21,* 12588.

147. Han, J.; Loudet, A.; Barhoumi, R.; Burghardt, R. C.; Burgess, K., A ratiometric pH reporter for imaging protein-dye conjugates in living cells. *J. Am. Chem. Soc.* **2009,** *131* (5), 1642.

148. Lee, H. L.; Lord, S. J.; Iwanaga, S.; Zhan, K.; Xie, H.; Williams, J. C.; Wang, H.; Bowman, G. R.; Goley, E. D.; Shapiro, L.; Twieg, R. J.; Rao, J.; Moerner, W. E., Superresolution imaging of targeted proteins in fixed and living cells using photoactivatable organic fluorophores. *J. Am. Chem. Soc.* **2010,** *132* (43), 15099.

149. Ji, J.; Rosenzweig, N.; Griffin, C.; Rosenzweig, Z., Synthesis and application of submicrometer fluorescence sensing particles for lysosomal pH measurements in murine macrophages. *Ana.l Chem.* **2000,** *72* (15), 3497.

150. Hornig, S.; Biskup, C.; Gräfe, A.; Wotschadlo, J.; Liebert, T.; Mohr, G. J.; Heinze, T., Biocompatible fluorescent nanoparticles for pH-sensoring. *Soft Matter* **2008,** *4,* 1169.

151. Li, L.-L.; Sun, H.; Fang, C.-J.; Xu, J.; Jin, J.-Y.; Yan, C.-H., Optical sensors based on functionalized mesoporous silica SBA-15 for the detection of multianalytes (H+ and Cu2+) in water. *Journal of Materials Chemistry* **2007,** *17* (42), 4492.

152. Richter, C.; Schneider, C.; Quick, M. T.; Volz, P.; Mahrwald, R.; Hughes, J.; Dick, B.; Alexiev, U.; Ernsting, N. P., Dual-fluorescence pH probe for bio-labelling. *Phys. Chem. Chem. Phys.* **2015,** *17* (45), 30590.

153. Kurishita, Y.; Kohira, T.; Ojida, A.; Hamachi, I., Rational design of FRET-based ratiometric chemosensors for in vitro and in cell fluorescence analyses of nucleoside polyphosphates. *J. Am. Chem. Soc.* **2010,** *132* (38), 13290.

154. Förster, T., Zwischenmolekulare Energiewanderung und Fluoreszenz. **1948**.

155. Simkova, E.; Stanek, D., Probing nucleic acid interactions and pre-mRNA splicing by Forster Resonance Energy Transfer (FRET) microscopy. *Int. J. Mol. Sci.* **2012,** *13* (11), 14929.

156. Dennis, A. M.; Rhee, W. J.; Sotto, D.; Dublin, S. N.; Bao, G., Quantum dot-fluorescent protein FRET probes for sensing intracellular pH. *ACS Nano* **2012,** *6* (4), 2917.

157. Whitaker, J. E.; Haugland, R. P.; Prendergast, F. G., Spectral and photophysical studies of benzo[c]xanthene dyes: Dual emission pH sensors. *Anal. Biochem.* **1991,** *194* (2), 330.

158. Beane, W. S.; Adams, D. S.; Morokuma, J.; Levin, M., Live imaging of intracellular pH in planarians using the ratiometric fluorescent dye SNARF-5F-AM. *Biol. Methods Protoc.* **2019,** *4* (1), bpz005.

159. Golda-VanEeckhoutte, R. L.; Roof, L. T.; Needoba, J. A.; Peterson, T. D., Determination of intracellular pH in phytoplankton using the fluorescent probe, SNARF, with detection by fluorescence spectroscopy. *J Microbiol Methods* **2018,** *152*, 109.

160. Hunter, R. C.; Beveridge, T. J., Application of a pH-sensitive fluoroprobe (C-SNARF-4) for pH microenvironment analysis in Pseudomonas aeruginosa biofilms. *Appl. Environ. Microbiol.* **2005,** *71* (5), 2501.

161. Mori, K.; Kuhn, B., Imaging Ca(2+) Concentration and pH in Nanopores/Channels of Protein Crystals. *J. Phys. Chem. B* **2018,** *122* (42), 9646.

162. Shenderovich, I. G.; Buntkowsky, G.; Schreiber, A.; Gedat, E.; Sharif, S.; Albrecht, J.; Golubev, N. S.; Findenegg, G. H.; Limbach, H.-H., Pyridine-15NA Mobile NMR Sensor for Surface Acidity and Surface Defects of Mesoporous Silica. *J. Phys. Chem. B* **2003,** *107* (43), 11924.

163. Mabbott, G. A., An introduction to cyclic voltammetry. *J. Chem. Edu.* **1983,** *60* (9).

164. Evans, D. H.; O'Connell, K. M.; Petersen, R. A.; Kelly, M. J., Cyclic voltammetry. *J. Chem. Edu.* **1983,** *60* (4).

165. Elgrishi, N.; Rountree, K. J.; McCarthy, B. D.; Rountree, E. S.; Eisenhart, T. T.; Dempsey, J. L., A Practical Beginner's Guide to Cyclic Voltammetry. *J. Chem. Edu.*, *95* (2), 197..

166. Goux, A.; Ghanbaja, J.; Walcarius, A., Prussian Blue electrodeposition within an oriented mesoporous silica film: preliminary observations. *J. Mater. Sci.* **2009,** *44* (24), 6601.

167. Calvo, A.; Yameen, B.; Williams, F. J.; Soler-Illia, G. J. A. A.; Azzaroni, O., Mesoporous Films and Polymer Brushes Helping Each Other To Modulate Ionic Transport in Nanoconfined Environments. An Interesting Example of Synergism in Functional Hybrid Assemblies. *J. Am. Chem. Soc.* **2009,** *131* (31), 10866.

168. Silies, L.; Gonzalez Solveyra, E.; Szleifer, I.; Andrieu-Brunsen, A., Insights into the Role of Counterions on Polyelectrolyte-Modified Nanopore Accessibility. *Langmuir* **2018,** *34* (20), 5943.

169. Naguib, M.; Kurtoglu, M.; Presser, V.; Lu, J.; Niu, J.; Heon, M.; Hultman, L.; Gogotsi, Y.; Barsoum, M. W., Two-dimensional nanocrystals produced by exfoliation of Ti3 AlC2. *Adv. Mater.* **2011,** *23* (37), 4248.

170. Xiao, X.; Wang, H.; Urbankowski, P.; Gogotsi, Y., Topochemical synthesis of 2D materials. *Chem. Soc. Rev.* **2018,** *47* (23), 8744.

171. Hantanasirisakul, K.; Gogotsi, Y., Electronic and Optical Properties of 2D Transition Metal Carbides and Nitrides (MXenes). *Adv. Mater.* **2018,** *30* (52), e1804779.

172. Hong Ng, V. M.; Huang, H.; Zhou, K.; Lee, P. S.; Que, W.; Xu, J. Z.; Kong, L. B., Recent progress in layered transition metal carbides and/or nitrides (MXenes) and their composites: synthesis and applications. *J. Mater. Chem. A* **2017,** *5* (7), 3039.

173. Naguib, M.; Mochalin, V. N.; Barsoum, M. W.; Gogotsi, Y., 25th anniversary article: MXenes: a new family of two-dimensional materials. *Adv. Mater.* **2014,** *26* (7), 992.

174. Anasori, B.; Lukatskaya, M. R.; Gogotsi, Y., 2D metal carbides and nitrides (MXenes) for energy storage. *Nat. Rev. Mater.* **2017,** *2*, 16098.

175. Hantanasirisakul, K.; Zhao, M.-Q.; Urbankowski, P.; Halim, J.; Anasori, B.; Kota, S.; Ren, C. E.; Barsoum, M. W.; Gogotsi, Y., Fabrication of Ti3C2TxMXene Transparent Thin Films with Tunable Optoelectronic Properties. *Adv. Electronic Mater.* **2016,** *2*, 1600050.

176. Dillon, A. D.; Ghidiu, M. J.; Krick, A. L.; Griggs, J.; May, S. J.; Gogotsi, Y.; Barsoum, M. W.; Fafarman, A. T., Highly Conductive Optical Quality Solution-Processed Films of 2D Titanium Carbide. *Adv. Funct. Mater.* **2016,** *26* (23), 4162.

177. Kim, S. J.; Koh, H. J.; Ren, C. E.; Kwon, O.; Maleski, K.; Cho, S. Y.; Anasori, B.; Kim, C. K.; Choi, Y. K.; Kim, J.; Gogotsi, Y.; Jung, H. T., Metallic Ti3C2Tx MXene Gas Sensors with Ultrahigh Signal-to-Noise Ratio. *ACS Nano* **2018,** *12* (2), 986.

178. Cai, Y.; Shen, J.; Ge, G.; Zhang, Y.; Jin, W.; Huang, W.; Shao, J.; Yang, J.; Dong, X., Stretchable Ti3C2Tx MXene/Carbon Nanotube Composite Based Strain Sensor with Ultrahigh Sensitivity and Tunable Sensing Range. *ACS Nano* **2018,** *12* (1), 56.

179. Ma, Y.; Liu, N.; Li, L.; Hu, X.; Zou, Z.; Wang, J.; Luo, S.; Gao, Y., A highly flexible and sensitive piezoresistive sensor based on MXene with greatly changed interlayer distances. *Nat. Commun.* **2017,** *8* (1), 1207.

180. Srimuk, P.; Halim, J.; Lee, J.; Tao, Q.; Rosen, J.; Presser, V., Two-Dimensional Molybdenum Carbide (MXene) with Divacancy Ordering for Brackish and Seawater Desalination via Cation and Anion Intercalation. *ACS Sustainable Chemistry & Engineering* **2018,** *6* (3), 3739.

181. Srimuk, P.; Kaasik, F.; Krüner, B.; Tolosa, A.; Fleischmann, S.; Jäckel, N.; Tekeli, M. C.; Aslan, M.; Suss, M. E.; Presser, V., MXene as a novel intercalation-type pseudocapacitive cathode and anode for capacitive deionization. *J. Mater. Chem. A* **2016,** *4* (47), 18265.

182. Ren, C. E.; Hatzell, K. B.; Alhabeb, M.; Ling, Z.; Mahmoud, K. A.; Gogotsi, Y., Charge- and Size-Selective Ion Sieving Through Ti3C2Tx MXene Membranes. *J- Phys- Chem. Lett.* **2015,** *6* (20), 4026.

183. Handoko, A. D.; Fredrickson, K. D.; Anasori, B.; Convey, K. W.; Johnson, L. R.; Gogotsi, Y.; Vojvodic, A.; Seh, Z. W., Tuning the Basal Plane Functionalization of Two-Dimensional Metal Carbides (MXenes) To Control Hydrogen Evolution Activity. *ACS Applied Energy Materials* **2017,** *1* (1), 173.

184. Seh, Z. W.; Fredrickson, K. D.; Anasori, B.; Kibsgaard, J.; Strickler, A. L.; Lukatskaya, M. R.; Gogotsi, Y.; Jaramillo, T. F.; Vojvodic, A., Two-Dimensional Molybdenum Carbide (MXene) as an Efficient Electrocatalyst for Hydrogen Evolution. *ACS Energy Letters* **2016,** *1* (3), 589.

185. Cambaz, G. Z.; Yushin, G. N.; Gogotsi, Y.; Lutsenko, V. G., Anisotropic etching of SiC whiskers. *Nano Lett.* **2006,** *6* (3), 548.

186. Sun, Z.; Music, D.; Ahuja, R.; Li, S.; Schneider, J. M., Bonding and classification of nanolayered ternary carbides. *Phys. Rev. B* **2004,** *70, 092102*.

187. Ghidiu, M.; Lukatskaya, M. R.; Zhao, M. Q.; Gogotsi, Y.; Barsoum, M. W., Conductive two-dimensional titanium carbide 'clay' with high volumetric capacitance. *Nature* **2014,** *516* (7529), 78.

188. Du, F.; Tang, H.; Pan, L.; Zhang, T.; Lu, H.; Xiong, J.; Yang, J.; Zhang, C., Environmental Friendly Scalable Production of Colloidal 2D Titanium Carbonitride MXene with Minimized Nanosheets Restacking for Excellent Cycle Life Lithium-Ion Batteries. *Electrochimica Acta* **2017,** *235*, 690.

189. Liu, F.; Zhou, A.; Chen, J.; Zhang, H.; Cao, J.; Wang, L.; Hu, Q., Preparation and methane adsorption of two-dimensional carbide Ti2C. *Adsorption* **2016,** *22* (7), 915.

190. Li, T.; Yao, L.; Liu, Q.; Gu, J.; Luo, R.; Li, J.; Yan, X.; Wang, W.; Liu, P.; Chen, B.; Zhang, W.; Abbas, W.; Naz, R.; Zhang, D., Fluorine-Free Synthesis of High-Purity Ti3 C2 Tx (T=OH, O) via Alkali Treatment. *Angew. Chem. Int. Ed. Engl.* **2018,** *57* (21), 6115.

191. Alhabeb, M.; Maleski, K.; Anasori, B.; Lelyukh, P.; Clark, L.; Sin, S.; Gogotsi, Y., Guidelines for Synthesis and Processing of Two-Dimensional Titanium Carbide (Ti3C2Tx MXene). *Chem. Mater.* **2017,** *29* (18), 7633.

192. Halim, J.; Cook, K. M.; Naguib, M.; Eklund, P.; Gogotsi, Y.; Rosen, J.; Barsoum, M. W., X-ray photoelectron spectroscopy of select multi-layered transition metal carbides (MXenes). *Appl. Surf. Sci.* **2016,** *362*, 406.

193. Persson, I.; Näslund, L.-Å.; Halim, J.; Barsoum, M. W.; Darakchieva, V.; Palisaitis, J.; Rosen, J.; Persson, P. O. Å., On the organization and thermal behavior of functional groups on Ti3C2 MXene surfaces in vacuum. *2D Materials* **2018,** *5*, 015002.

194. Mashtalir, O.; Lukatskaya, M. R.; Kolesnikov, A. I.; Raymundo-Pinero, E.; Naguib, M.; Barsoum, M. W.; Gogotsi, Y., The effect of hydrazine intercalation on the structure and capacitance of 2D titanium carbide (MXene). *Nanoscale* **2016,** *8* (17), 9128.

195. Ling, Z.; Ren, C. E.; Zhao, M. Q.; Yang, J.; Giammarco, J. M.; Qiu, J.; Barsoum, M. W.; Gogotsi, Y., Flexible and conductive MXene films and nanocomposites with high capacitance. *Proc. Natl. Acad. Sci. USA* **2014,** *111* (47), 16676.

196. Naguib, M.; Saito, T.; Lai, S.; Rager, M. S.; Aytug, T.; Parans Paranthaman, M.; Zhao, M.-Q.; Gogotsi, Y., Ti3C2Tx(MXene)–polyacrylamide nanocomposite films. *RSC Advances* **2016,** *6* (76), 72069.

197. Chen, J.; Chen, K.; Tong, D.; Huang, Y.; Zhang, J.; Xue, J.; Huang, Q.; Chen, T., CO2 and temperature dual responsive "Smart" MXene phases. *Chem. Commun. (Camb)* **2015,** *51* (2), 314.

198. Ye, Q.; Xiao, P.; Liu, W.; Chen, K.; Chen, T.; Xue, J.; Du, S.; Huang, Q., Exploring the potential of exfoliated ternary ultrathin Ti4AlN3 nanosheets for fabricating hybrid patterned polymer brushes. *RSC Advances* **2015,** *5* (86), 70339.

199. Tao, N.; Zhang, D.; Li, X.; Lou, D.; Sun, X.; Wei, C.; Li, J.; Yang, J.; Liu, Y.-N., Near-infrared light-responsive hydrogels via peroxide-decorated MXene-initiated polymerization. *Chem. Sci.* **2019,** *10* (46), 10765.

200. Tran, M. H.; Brilmayer, R.; Liu, L.; Zhuang, H.; Hess, C.; Andrieu-Brunsen, A.; Birkel, C. S., Synthesis of a Smart Hybrid MXene with Switchable Conductivity for Temperature Sensing. *ACS Applied Nano Materials* **2020**, *3, 5*, 4069.

201. Silies, L.; Andrieu-Brunsen, A., Programming Ionic Pore Accessibility in Zwitterionic Polymer Modified Nanopores. *Langmuir* **2018**, *34, 3*, 807.

202. Soler-Illia, G. J.; Sanchez, C.; Lebeau, B.; Patarin, J., Chemical strategies to design textured materials: from microporous and mesoporous oxides to nanonetworks and hierarchical structures. *Chem. Rev.* **2002,** *102* (11), 4093.

203. Sun, M. H.; Huang, S. Z.; Chen, L. H.; Li, Y.; Yang, X. Y.; Yuan, Z. Y.; Su, B. L., Applications of hierarchically structured porous materials from energy storage and conversion, catalysis, photocatalysis, adsorption, separation, and sensing to biomedicine. *Chem. Soc. Rev.* **2016,** *45* (12), 3479.

204. Buckler, K. J.; Vaughan-Jones, R. D., Application of a new pH-sensitive fluoroprobe (carboxy-SNARF-1) for intracellular pH measurement in small, isolated cells. *Pflugers Arch.* **1990,** *417* (2), 234.

205. Zheng, M.-H.; Jin, J.-Y.; Sun, W.; Yan, C.-H., A new series of fluorescent 5-methoxy-2-pyridylthiazoles with a pH-sensitive dual-emission. *New J. Chem.* **2006,** *30* (8), 1192.